Phase Transformation Kinetics and Oxygen Transport in the Relaxor Ferroelectric $Na_{1/2}Bi_{1/2}TiO_3$ studied by First-Principles Calculations

Untersuchung von Phasentransformationskinetik und Sauerstofftransport im Relaxorferroelektrikum $Na_{1/2}Bi_{1/2}TiO_3$ mittels *ab initio* Rechnungen

Zur Erlangung des Grades eines Doktors der Naturwissenschaften (Dr. rer. nat.)
genehmigte Dissertation von M.Sc. Kai-Christian Meyer aus Frankfurt am Main
Tag der Einreichung: 8.5.2017, Tag der Prüfung: 19.6.2017
Darmstadt — D 17

1. Gutachter: Prof. Dr. rer. nat. Karsten Albe
2. Gutachter: Prof. Dr. rer. nat. Doru Lupascu
3. Prüfer: Prof. Dr. rer. nat. Wolfgang Donner
4. Prüfer: Prof. Dr. rer. nat. Michael Vogel

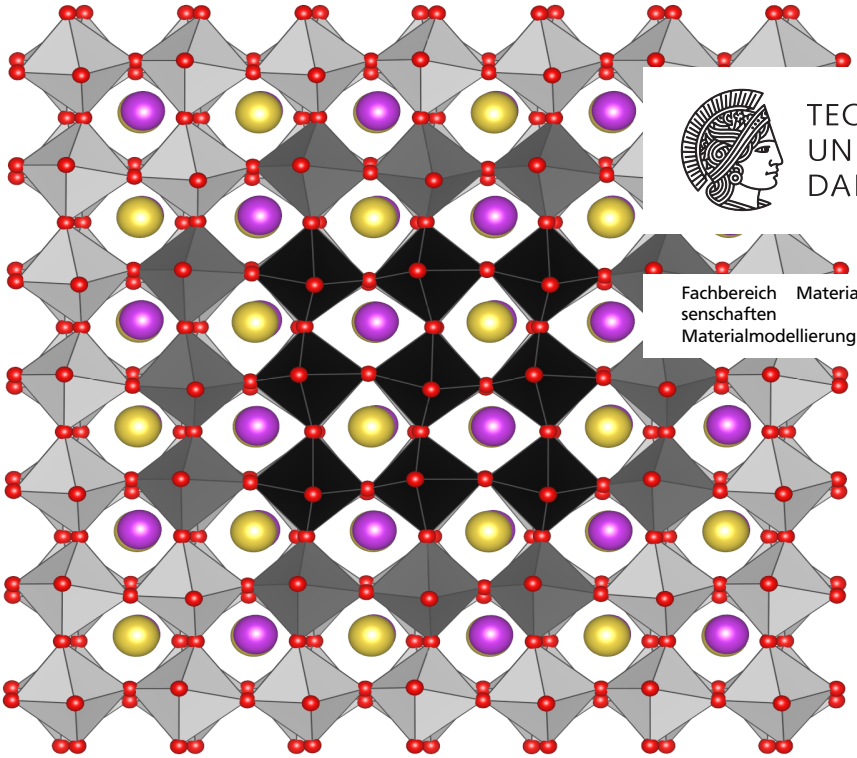

TECHNISCHE UNIVERSITÄT DARMSTADT

Fachbereich Material- und Geowissenschaften
Materialmodellierung

Phase Transformation Kinetics and Oxygen Transport in the Relaxor Ferroelectric $Na_{1/2}Bi_{1/2}TiO_3$ studied by First-Principles Calculations
Untersuchung von Phasentransformationskinetik und Sauerstofftransport im Relaxorferroelektrikum $Na_{1/2}Bi_{1/2}TiO_3$ mittels *ab initio* Rechnungen

Genehmigte Dissertation von M.Sc. Kai-Christian Meyer aus Frankfurt am Main

1. Gutachter: Prof. Dr. rer. nat. Karsten Albe
2. Gutachter: Prof. Dr. rer. nat. Doru Lupascu
3. Prüfer: Prof. Dr. rer. nat. Wolfgang Donner
4. Prüfer: Prof. Dr. rer. nat. Michael Vogel

Tag der Einreichung: 8.5.2017
Tag der Prüfung: 19.6.2017

Darmstadt — D 17
Darmstadt 2017

Bitte zitieren Sie dieses Dokument als:
URN: urn:nbn:de:tuda-tuprints-65179
URL: http://tuprints.ulb.tu-darmstadt.de/6517

Dieses Dokument wird bereitgestellt von tuprints,
E-Publishing-Service der TU Darmstadt
http://tuprints.ulb.tu-darmstadt.de
tuprints@ulb.tu-darmstadt.de

This work is licensed under the Creative Commons Attribution 4.0 Unported License.:
Attribution – NonCommercial – ShareAlike
https://creativecommons.org/licenses/by-nc-sa/4.0/

Acknowledgements – Danksagung

Zuallererst möchte ich mich bei meiner engsten Familie bedanken. Dazu gehören Doris, Bernfried, Erik, Annemarie und Martin. Ihr habt mir nicht nur das Studium ermöglicht und mich dabei unterstützt, sondern mich auch nach den Ereignissen im Jahr 2011 aufgefangen. Dafür bin ich euch unendlich dankbar.

Als nächstes danke ich meinem Doktorvater Prof. Dr. Karsten Albe für die Möglichkeit, diese Arbeit in seiner Arbeitsgruppe schreiben zu können. Sehr bedeutend waren dabei die gewährten Freiheiten bezüglich der wissenschaftlichen Arbeit, aber auch bei privaten Angelegenheiten.

Außerdem gebührt ihm auch der Dank für das Zusammenstellen der Arbeitsgruppe, die es eine Freude gemacht hat, die gesamten Jahre in einer sehr angenehmen Arbeitsatmosphäre zu arbeiten. Auch wenn die Arbeit mal nicht laufen wollte oder die Stimmung aus anderen Gründen im Keller war, konnte man sich auf die Unterstützung und Aufmunterung der anderen MMs verlassen, seien es aufbauende Worte, die ein oder andere Kuchenpause oder abendliche Aktivitäten. Insbesondere möchte ich mich bei Sabrina bedanken: Du hast mir bei wissenschaftlichen und bei privaten Angelegenheiten sehr weiter geholfen. Dafür bin ich dir sehr dankbar.

Als nächstes möchte ich Prof. Dr. Doru Lupascu für das Begutachten dieser Arbeit, und der damit einhergehenden zeitlichen Beanspruchung, danken. Zudem danke ich Prof. Dr. Wolfgang Donner und Prof. Dr. Michael Vogel, die als weitere Prüfer fungieren.

Ich danke zudem unseren fleißigen Helferlein Renate und Gabi, die sich immerzu zuverlässig um den reibungslosen Ablauf aller bürokratischen Angelegenheiten kümmern. Ohne euch hätten die MMs ein riesiges Problem!

Diese Arbeit wurde von der DFG über das Schwerpunktsprogramm "Ferroic Cooling" finanziert. Die Rechnungen wurden auf dem Hessischen Hochleistungsrechner (HHLR) in Darmstadt und auf den Hochleistungsrechnern am Forschungszentrum Jülich durchgeführt.

Copyright Notice

Results of this thesis were published in articles of scientific journals:

1. Sec. 5 are partly reprinted from article:

   K.-C. Meyer, M. Gröting and K. Albe.
   Octahedral tilt transitions in the relaxor ferroelectric $Na_{1/2}Bi_{1/2}TiO_3$.
   J. Solid State Chem. 227, 117-122 (2015).

2. Sec. 6 and 7 are partly reprinted from article:

   K.-C. Meyer and K. Albe,
   Influence of phase transitions and defect associates on the oxygen migration in the ion conductor $Na_{1/2}Bi_{1/2}TiO_3$,
   J. Mater. Chem. A 5, 4368-4375 (2017).

3. Sec. 7 are partly reprinted from article:

   L. Koch, S. Steiner, **K.-C. Meyer**, I.-T. Seo, K. Albe and T. Frömling,
   Ionic conductivity of acceptor doped sodium bismuth titanate: influence of dopants, phase transitions and defect associates,
   J. Mater. Chem. C, (2017)

4. Sec. 5 are partly reprinted from article:

   K.-C. Meyer, L. Koch and K. Albe,
   Phase transformations in the relaxor $Na_{1/2}Bi_{1/2}TiO_3$ studied by means of density functional theory calculations,
   J. Am. Ceram. Soc. (2017).

Contents

1 Abstract **4**

2 Introduction **6**

3 NBT and its properties: State of the art **8**
3.1 Phases and phase transitions of NBT . . . 11
3.2 Structure of perovskites . . . 12
3.2.1 Chemical order . . . 14
3.2.2 Octahedral tilts . . . 15
3.2.3 Ferroelectric distortions . . . 15
3.2.4 Displacive Disorder . . . 16
3.3 Relaxors . . . 16
3.4 NBT as an ionic conductor . . . 20
3.5 Theoretical work on NBT . . . 23
3.6 The electrocaloric effect . . . 24
3.7 Comparison of NBT to other important perovskites . . . 27
3.8 Open questions . . . 28

4 Methods **30**
4.1 Density functional theory . . . 31
4.1.1 Transition state theory . . . 36
4.1.2 Nudged elastic band method . . . 37
4.2 Molecular dynamics . . . 38
4.3 Monte Carlo simulations . . . 42

5 Kinetics of phase transformations **44**
5.1 NBT structures . . . 44
5.2 Octahedral tilt transformations – Tetragonal . . . 45
5.3 Octahedral tilt transformations – All phases . . . 51
5.4 Octahedral tilt transformations – Molecular dynamics . . . 55
5.5 Octahedral tilt defects . . . 57
5.6 A-cation displacements . . . 62
5.7 Summary . . . 63

6 Oxygen vacancy migration **66**
6.1 Rhombohedral phase . . . 68
6.2 Orthorhombic phase . . . 71
6.3 Tetragonal phase . . . 72
6.4 Thermal expansion . . . 74
6.5 Summary . . . 77

7 Defect associates **80**
7.1 Mg dopants . . . 82
7.2 Ni dopants . . . 84
7.3 Bi vacancies . . . 85

7.4 Summary 87

8 Electrocaloric effect in $BaTiO_3$ 90
8.1 Monte Carlo simulations 90
8.1.1 Defect-free 91
8.1.2 Polar defects 94
8.2 Molecular dynamics simulations 97
8.3 Summary 100

9 Conclusions 102

10 Discussion 106

11 Outlook 108

12 Appendix 110
12.1 Structures 110
12.1.1 Structure parameters 110
12.1.2 Wyckoff positions of irreducible cells 111
12.2 Input files 117
12.2.1 VASP 117
12.2.2 feram 122

List of figures 123

List of tables 124

List of symbols, abbreviations and constants 125

References 128

Curriculum Vitae 153

1 Abstract

Health and environmental-friendly aspects of daily life have increased in importance over the last decades. As materials scientists, we are able to develop non-hazardous materials, which can replace toxic materials that are currently used in piezoelectric devices. Also, the efficiencies of cooling and energy conversion devices can be improved by new materials, which are especially important in industrialized countries. In this work, we tackle these aspects from a computer-aided modeling point of view.

A major aim of this work is to study the kinetic processes of the relaxor ferroelectric sodium bismuth titanate $Na_{1/2}Bi_{1/2}TiO_3$ (NBT) on a fundamental level by first-principles density functional theory (DFT) calculations. This material is of particular interest since its solid solutions are viable candidates to replace the toxic, however yet indispensable, lead zirconium titanate (PZT) in various piezoelectric and cooling applications. Within this thesis we investigate the influence of chemical A-cation order, octahedral tilts and cation displacements on the macroscopic properties. In particular, we study phase transformations, try to identify the origins of the relaxor ferroelectric properties, investigate oxygen migration and polar defect associates. Further, we employ Ising-like Monte Carlo (MC) simulations and *ab initio* based effective molecular dynamics (MD) simulation to study the electrocaloric effect (ECE) in ferroelectrics, anti-ferroelectrics and relaxor ferroelectrics. The ECE describes the increase in temperature of a material when an electric field is applied. Although the effect is rather small, it might be possible to utilize it in solid-state cooling devices in the future. Relaxor ferroelectrics are expected to increase the achievable temperature change compared to conventional ferroelectrics. It is also investigated how polar defects, which are unavoidable in devices, influence the ECE.

We find that the energy landscape of NBT for octahedral tilts is very flat, thus different kinds of octahedral tilt patterns can easily be introduced and the underlying order of the A-cations is very important. These local deviations in tilt pattern then can lead to locally varying A-cation displacements which result in different polarizations, leading to the observable relaxor properties. The phase and symmetry transitions also influence the ionic conductivity and defect associates. Further, our employed MC and MD calculations could not show any increase of the ECE for relaxors, compared to conventional ferroelectrics. However, the simple Ising-like model proved to be sufficient to explain the negative electrocaloric temperature change observed in anti-ferroelectrics and ferroelectrics containing polar defects.

Zusammenfassung

Über die letzten Jahrzehnten haben Gesundheits- und Umweltaspekte erheblich an Bedeutung zugenommen. Als Materialwissenschaftler können wir nicht-toxische Materialien entwickeln, welche die bisher verwendeten umweltschädlichen Materialien ersetzen. Ein anderer Ansatzpunkt ist die Erhöhung der Effizienz von Kühlzyklen und Systemen zur Energieumwandlung, welche insbesondere für Industrienationen wichtig sind. In dieser Arbeit befassen wir uns mit diesen Problemen mit Hilfe von computergestützter Modellierung.

Der Hauptteil dieser Arbeit beschäftigt sich mit der Untersuchung der kinetischen Prozesse im Relaxorferroelektrikum Natrium Bismut Titanat $Na_{1/2}Bi_{1/2}TiO_3$ (NBT) durch *ab initio* Dichtefunktionaltheorie (DFT) Simulationen. Dieses Material ist von besonderer Bedeutung, da seine Mischkristalle mögliche Kandidaten für das Ersetzen des toxischen, aber bisher unverzichtbaren, Blei-Zirkonat-Titanats (PZT) in verschiedenen piezoelektrischen Anwendungen und in neuen Kühltechnologien sind. Wir untersuchen den Einfluss von lokaler A-Kationenordnung, Oktaederverkippung und Kationenverschiebung, die maßgeblich die makroskopischen Eigenschaften beeinflussen. Im speziellen werden Phasentransformationen analysiert, nach den Gründen für die Eigenschaften des Relaxorferroelektrikums gesucht, die Sauerstoffmigration und polare Defektassoziate untersucht. Im zweiten Teil werden Monte Carlo (MC) und Molekulardynamik (MD) Simulationen verwendet um den elektrokalorischen Effekt (ECE) zu untersuchen. Dieser Effekt beschreibt den Anstieg der Temperatur, wenn ein elektrischen Feld angelegt wird. Auch wenn dieser Effekt relativ klein ist, kann dieser Effekt in Zukunft möglicherweise in Festkörperkühlgeräten eingesetzt werden. Es wird angenommen, dass Relaxorferroelektrika den erreichbaren Temperaturunterschied im Vergleich zu konventionellen Ferroelektrika erhöhen könnten. Außerdem wird der Einfluss von polaren Defekten, welche in praktischen Anwendungen unvermeidbar sind, auf den ECE untersucht.

Wir zeigen, dass die Energielandschaft für Oktaederverkippungen in NBT sehr flach ist, diese also leicht auftreten können. Die Anordnung der A-Kationen spielt jedoch eine entscheidende Rolle. Die lokalen Abweichungen in den Verkippungen der Oktaeder ermöglichen eine lokale Variation der A-Kationverschiebungen, was zu unterschiedlichen Polarizationen führt und damit die beobachtbaren Relaxoreigenschaften erklären kann. Die Phasen- und Symmetrieübergänge beeinflussen zusätzlich die ionische Leitfähigkeit und das Bilden von Defektassoziaten. Außerdem konnten mit wir mit den verwendeten MC und MD Modellen keine Steigerung des ECE in Relaxoren im Vergleich zu typischen Ferroelektrika feststellen. Jedoch konnte ein einfachen Modell, basierend auf dem Ising Modell, den negativen ECE beschreiben, der in Antiferroelektrika und Ferroelektrika mit polaren Defektassoziaten auftritt.

2 Introduction

Over the last decades, health and environmental issues have increased in importance and have become a general concern for politics and industries. One of the aspects that has to be considered to reach a sustainable and environmental-friendly way of living, is the reduction and replacement of toxic lead. Lead is used in various different materials and applications, ranging from batteries, alloys, gasoline to paint, as shown in **Fig. 2.1a** [1].
In the early 2000s the European Union announced directives, which restrict "the use of certain hazardous substances in electrical and electronic equipment" and regulate the "waste of electrical and electronic equipment". These directives were renewed in 2011 and 2012 [3–5]. Still, the amount of mined lead has increased by more than 60% since 2005 [6] and ways to prevent a further raise are of urgent need.
Even though the largest amount of lead is contained in lead-acid batteries [1], also other devices are strongly dependent on lead containing components. Lead-free substitutes are of particular interest in piezoceramic materials. These type of materials are mainly used for sensors and actuators and are thus included in many different applications, such as cars and medical equipment [1] and in the future possibly in advanced cooling technologies [7]. Conventional vapor compression technology is responsible for a large portion of the consumed energy in households, as it can be seen from **Fig. 2.1b** [2]. Air conditioning alone consumes electricity worth of more than 11 billion $ in US households per year [8]. Mischenko *et al.* [9] showed that by application of an electric field to a $Pb(Zr,Ti)O_3$ (PZT) thin-film, a large temperature change of 12 K of the sample can be obtained. The inverse of this electrocaloric effect (ECE) could be used to cool devices efficiently.
The main task of improving the life cycle sustainability of piezoceramic products can be condensed to the task of replacing PZT by lead-free alternatives. Throughout the history of piezoceramic technology, PZT was one of the most widely used materials [10, 11].

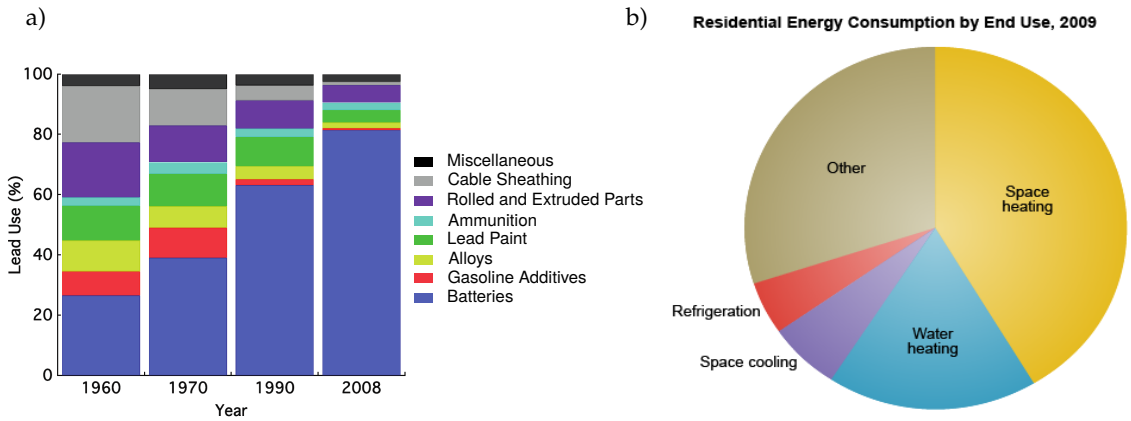

FIGURE 2.1: **a)** Usage of lead in various applications since 1960. Reprinted from Journal of the European Ceramic Society 35, 1659-1681, J. Rödel, K. G. Webber, R. Dittmer, W. Jo, M. Kimura and D. Damjanovic, Transferring lead-free piezoelectric ceramics into application, Copyright (2015), with permission from Elsevier [1]. **b)** Energy consumption in US households. Taken from Ref. [2] with permission from the United States Environmental Protection Agency.

One of the first reports on a lead-free material that could compete with the piezoelectric properties of PZT was given by Saito *et al.* in 2004 [12]. They studied the system $(K_{0.5}Na_{0.5})_{1-x}Li_x(Nb_{1-y}\ Ta_y)O_3$ and from then on more and more studies were conducted on lead-free alternatives [1]. Within a few years, various different systems were studied and first review articles were published that summarized the findings [13–18]. It turns out that several classes of materials are able to be mayor competitors to the still ubiquitous PZT. The first interesting class is based on Bi, which includes materials such as $Na_{0.5}Bi_{0.5}TiO_3$ (NBT), $Na_{0.5}Bi_{0.5}TiO_3$–$BaTiO_3$ (NBT-BT) and $(Na_xK_{1-x})_{0.5}Bi_{0.5}TiO_3$ (NKBT). The second class is based on the long known and widely used $BaTiO_3$ (BT). One important material is $Ba(Zr_xTi_{x-1})O_3$ (BZT) [19] and recently the often studied $(Ba_xCa_{x-1})(Zr_yTi_{y-1})O_3$ (BCZT) [20]. A third class of materials is based on Nb such as $(K_xNa_{x-1})NbO_3$ (KNN) [21]. So far these material still do not reach the necessary properties to fully compete with PZT [1]. Either the piezoelectric coefficients are inferior to the values of PZT or their temperature range for applications is far from the desired room temperature [16]. Therefore, the quest to find a suitable replacement for PZT is still ongoing.

Part of the task of finding new materials, is to understand why certain materials have superior properties over others. The search for new materials can be simplified and accelerated, when the underlying physics and chemistry, that give rise to the macroscopic properties, are understood.

The aim of this work is to deepen the knowledge on the so-called relaxor ferroelectric materials (short relaxors), and in particular of NBT, which is one of the most important basis of materials that are able to compete with PZT and other utilized materials. Relaxor materials (to which NBT, BCZT, KNN and the lead containing $Pb(Mg_{1/3}Nb_{2/3})O_3$ (PMN) belong) have good piezoelectric properties [22–24], similar to conventional ferroelectrics, but are not limited to a narrow temperature range close to the Curie temperature T_C, as standard ferroelectrics such as PZT and BT [1, 13, 25, 26]. Relaxors are expected to show an even larger ECE than conventional ferroelectrics due to increased number of degrees of freedom on the microscopic level [27, 28]. Additionally, in the materials PMN-PT [29] and NBT [30] a peculiar negative temperature change was observed, which might increase the obtainable temperature change for an entire electrocaloric cycle even further [31]. Recently, it has been discovered that NBT exhibits a high ionic conductivity [32] and could be used in solid oxide fuel cells (SOFC), which become increasingly important in a world that is ever more dependent on efficient energy conversion methods [33]. Investigating the unusual high conductivity in NBT is another part of this work.

Although NBT has been thoroughly studied since its discovery in 1961 [34], many aspects of this material are still not well understood [35]. Here, we study the kinetics of phase transitions, polar defect associates and oxygen migration, that lead to the (often desired) relaxor ferroelectric properties. The complex behavior of NBT is related to the differences in local and average structure and the many degrees of freedom that are present, but no final conclusions have yet been drawn.

This work is part of the Priority Program "1599: Caloric Effects in Ferroic Materials [7, 36]: New Concepts for Cooling" of the Deutsche Forschungsgemeinschaft (DFG).

All of the materials mentioned in the introduction (BT, KNN, NBT, PZT and solid-solutions thereof) belong to the same type of crystal structure, the perovskite structure. Perovskite is the abundant mineral $CaTiO_3$, which lends its name to a whole structure type with the chemical formula of ABX_3, short perovskites.
Perovskites exhibit a vast variety of different properties, depending on the used elements and their composition [37–39]. The properties range from superconductors (e.g. $Ba_{1-x}K_xBiO_3$), antiferromagnetic insulators (e.g. $LaMnO_3$), colossal magnetoresistance (e.g. $La_{1-x}Ca_xMnO_3$), multiferroics (e.g. $TbMnO_3$), ferroelectrics (e.g. $BaTiO_3$), ionic conductors (e.g. $La_{0.67-x}Li_{3x}TiO_3$, $BaCeO_{3-x}$) and the already mentioned piezoelectrics (e.g. PZT). However, some of these materials (especially the superconductors) require doping to induce the desired properties. The materials of interest for this work are those which show (relaxor) ferroelectric behavior, especially NBT.
NBT has some peculiar properties that distinguish it from other ferroelectric perovskites. **Fig. 3.1** depicts the real part of the dielectric permittivity of NBT and Bi-deficient NBT ($Na_{0.48}Bi_{0.52}TiO_{2.98}$) measured by Hidaka *et al.* [40]. It can be seen that the peak of the permittivity is very broad and spans over several hundred Kelvin. The permittivity is also slightly dependent on the frequency of the external electric field. The situation becomes even more interesting when Bi-deficient NBT ($Na_{0.48}Bi_{0.52}TiO_{2.98}$) is measured, as seen in **Fig. 3.1b**. Now, the permittivity becomes strongly dependent on the frequency. This is typical for a relaxor ferroelectric (see Sec. 3.3). As we will see later, the introduction of Bi and O vacancies can lead to polar defect associates, which can alter the properties substantially. Further, structural details on the microscopic scale of NBT are still under debate. **Fig. 3.2** shows the X-ray diffuse scattering pattern of NBT of Kreisel *et al.* [41]. The rod-like asymmetry next to the Bragg peaks indicates two-dimensional (polar) planar defects. This suggests that the average and local structure of NBT are different. The structural origin of this observation is, however, not well understood. In Secs. 3.1 and 3.2 we look at the phase tran-

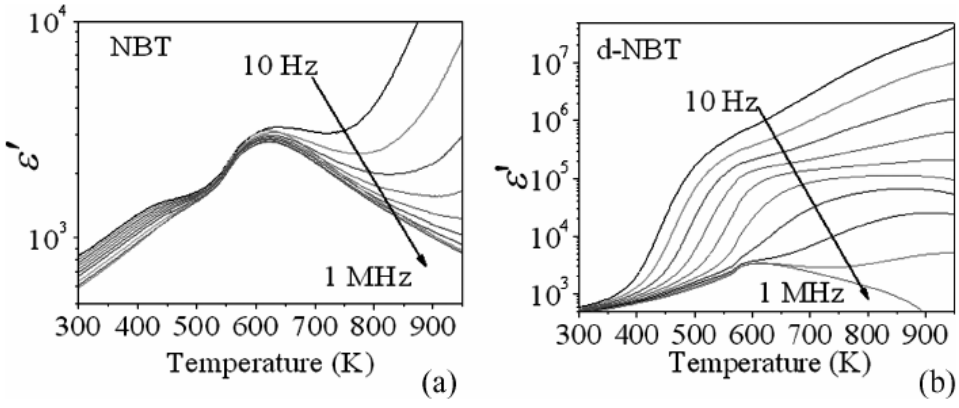

FIGURE 3.1: Measured real part of the dielectric permittivity ϵ' of **a)** NBT and **b)** Bi-deficient NBT ($Na_{0.48}Bi_{0.52}TiO_{2.98}$). Reprinted from Y. Hidaka, S. Tsukada and S. Kojima, Aging of Dielectric Properties in $Na_{0.5}Bi_{0.5}TiO_3$ Ceramics, Ferroelectrics 376, 134-139 (2008) with the permission of Taylor & Francis Publishing [40].

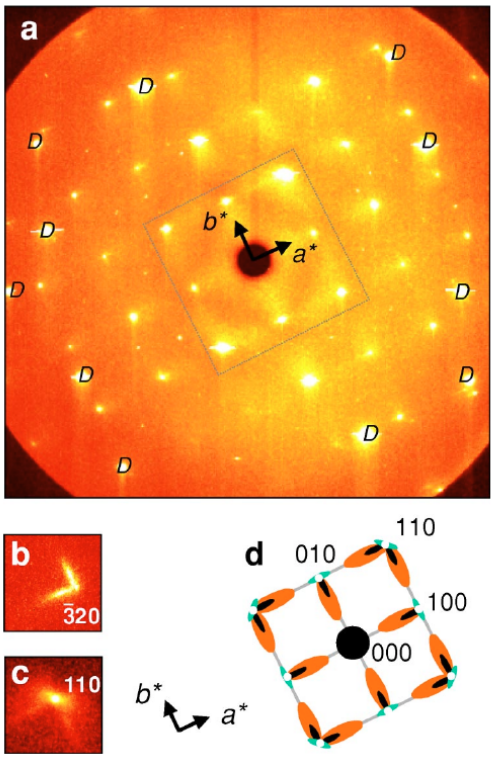

FIGURE 3.2: X-ray diffuse scattering pattern of NBT at hydrostatic pressure of 0.6 GPa. Reprinted figure with permission from J. Kreisel, P. Bouvier, B. Dkhil, B. Chaabane, A. M. Glazer, P. A. Thomas and T. R. Welberry, Effect of High Pressure on the Relaxor Ferroelectrics $Na_{1/2}Bi_{1/2}TiO_3$ (NBT) and $PbMg_{1/3}Nb_{2/3}O_3$ (PMN), Ferroelectrics 302, 293-298 (2004), Copyright 2004 by the American Physical Society [41].

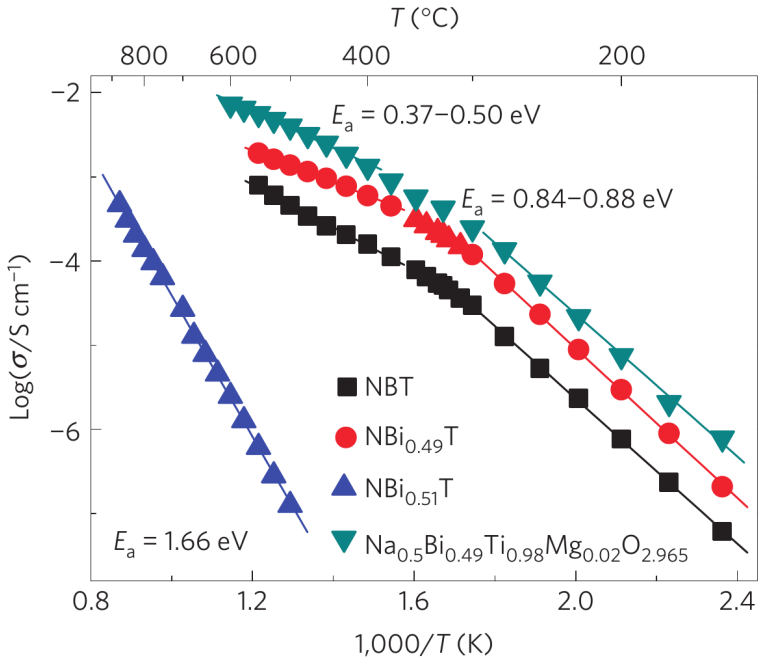

FIGURE 3.3: Arrhenius-type plots of bulk conductivity of stoichiometric NBT, non-stoichiometric NBT and Mg-doped $NBTi_{0.98}Mg_{0.02}$. Reprinted by permission from Macmillan Publishers Ltd: Nature Materials (M. Li, M. J. Pietrowski, R. A. De Souza, H. Zhang, I. M. Reaney, S. N. Cook, J. A. Kilner and D. C. Sinclair, Nat. Mater. 13, 31-35), copyright (2014) [32].

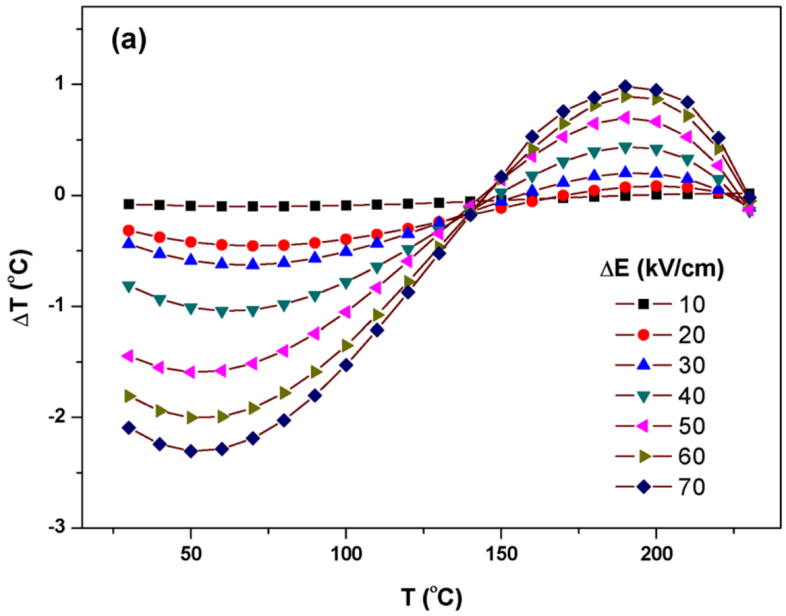

FIGURE 3.4: Electric field and temperature dependences of the electrocaloric temperature change ΔT in NBT-6BT. Reprinted from Journal of Applied Physics 114, S. Uddin, G.-P. Zheng, Y. Iqbal, R. Ubic and J. Yang, Unification of the negative electrocaloric effect in $Bi_{1/2}Na_{1/2}TiO_3$-$BaTiO_3$ solid solutions by $Ba_{1/2}Sr_{1/2}TiO_3$ doping (2013) with the permission of AIP Publishing [30].

sitions of NBT and the perovskite structure in general. The kinetics of the phase transitions are studied in Sec. 5.

Additionally, doped and non-stoichiometric NBT exhibits a high ion conductivity, as was shown by Li *et al.* [32] and can be seen in **Fig. 3.3**. Interestingly, at around 300 °C the slope of the conductivity changes, which implies that the activation energy for the oxygen migration changes. A deeper insight on the conductivity of NBT is given in Sec. 3.4 and investigated in Secs. 6 and 7.

NBT has also been investigated as a potential candidate material for the ECE. Electrocaloric temperature changes measured by Uddin *et al.* [30] are given in **Fig. 3.4**. Instead of the conventional positive temperature change, a negative change of the temperature is observed below 150 °C. The ECE is explained in more detail in Sec. 3.6 and studied in Sec. 8.

From these four examples we can see that many aspects of NBT require a deeper investigation for a proper understanding. We have to answer questions like: Are polar defects responsible for the frequency dependent permittivity? What is the underlying structural origin of polar nanoregions (PNR)? How do PNRs come into existence and in what way are they temperature dependent? Why has NBT a negative ECE? To answer these questions one first needs to take a closer look at the knowledge on NBT that was gathered so far.

NBT has been studied with respect to its structural and electric properties since its discovery in 1961 [34]. Pronin *et al.* [42] were the first to study the phase transitions in NBT by dielectric and differential scanning calorimetry (DSC) measurements. The first neutron scattering experiments to resolve the structure were performed by Vakhrushev *et al.* in the 1980s [43–45], in which they observed a transition from the room temperature rhombohedral phase into a tetragonal phase at 600 K and a second transition to cubic phase at 800 K. Later many other studies employing neutron scattering followed [46–58], in which the same phase transition sequence was found. These findings were confirmed by X-ray diffraction studies [41,48,53,54,59–65] and other characterization techniques [42,54,59,66–79]. However in 2008, Dorcet and Trolliard performed transmission electron microscopy (TEM) studies [80,81], in which they reported an intermediate orthorhombic phase, that was later also considered in other studies [82–84]. All proposed structures and phase transitions are listed in **Fig. 3.5** [35]. The most prominent feature of these phases are the differences in the octahedral tilts. Below 470 K, in the low temperature regime, NBT has been reported to be rhombohedral [47,54], monoclinic [53,85] or a mixture of both [61,63], depending on thermal, electric and mechanical treatments. Moreover, it was found that the application of an electric field transforms the structure from the monoclinic to the rhombohedral state, which is reversible by heating the sample [63]. Above 470 K the symmetry starts to deviate from the rhombohedral/monoclinic symmetry, but the origin of this deviation is still under debate. Two possible phase transformations were suggested. Originally, a "direct" transition from the rhombohedral to the tetragonal phase was reported [44,47]. Later a "indirect" transition via an intermediate orthorhombic phase was proposed from TEM studies [80,81,83] and also reported in a neutron powder diffraction study on Ca-doped NBT [50]. At 670 K the phase is purely tetragonal [47]. At very high temperatures ($T > 790$ K) the structure becomes cubic. As it can be seen in **Fig. 3.5** the phase transition temperatures are not fixed values, but vary over a broad temperature range of more than 50 K. This effect is sometimes called a "diffuse" phase transition and is connected to the so-called relaxor-like behavior of NBT, which is further described in the next sections. Within this transition range the fraction of each phase varies, as it was reported by Jones and Thomas [47], Siny *et al.* [86] and Pforr *et al.* in NBT-4BT [87], where the rhombohedral, tetragonal and cubic phase are present simultaneously. At the lowest temperatures, rhombohedral NBT is ferroelectric (FE) and transforms to an antiferroelectric (AFE) in the orthorhombic phase [88]. For temperatures higher than 590 K the structure NBT is paraelectric (PE) [88].
The kinetics of the phase transitions, in particular whether the transition is a nucleation or a collective process, is studied in Sec. 5. We also investigate whether one of the proposed phase transition sequences can be observes in *ab initio* molecular dynamics simulations (Sec. 5.4) and we study tilt defect energies to estimate the size of stable tilt defect clusters in Sec. 5.5.

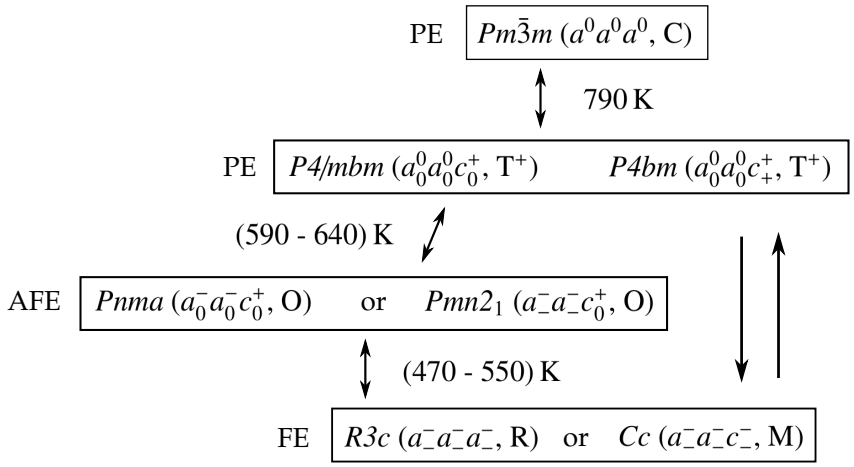

FIGURE 3.5: Reported phases in NBT, their respective oxygen tilt patterns and possible phase transitions. The two parallel arrows indicate a large temperature hysteresis. [47, 54, 63, 75, 77, 80, 89]

3.2 Structure of perovskites

Of the ABX_3 perovskite the A and B elements are positively charged cations and X are negatively charged anions, which in most cases are oxygen ions [90,91]. The crystal structure of a model perovskite BT is shown in two different representations in **Fig. 3.6**. **Fig. 3.6a** gives BT with the Ti-ion (blue) in the center of the cell at the Wyckoff position (0.5,0.5,0.5). The position for Ba (green) is on the corner of the cube (0,0,0) and the oxygen ions (red) sit on the faces of the cube at (0.5,0.5,0.0), (0.0,0.5,0.5), (0.5,0.0,0.5). However, for all upcoming figures we choose the representation as in **Fig. 3.6b** with the following Wyckoff positions: Ti: (0,0,0), Ba: (0.5,0.5,0.5), O: (0.5,0.0,0.0), (0.0,0.5,0.0), (0.0,0.0,0.5). Ti has thus six oxygen ions as neighbors and these oxygen ions form an octahedron with the Ti ion in the center. This oxygen octahedron is visualized in each structure figure for easier identification of the structure symmetry.
Within this structure type various different distortions are possible, which are called degrees of freedom. As it was mentioned in the introduction, NBT exhibits many degrees of freedom, which are listed in **Fig. 3.7**. From left to right we need to consider: ferroelectric distortions of the octahedra, octahedral tilts, lattice strain, chemical order and displacive disorder of the A-cations. These degrees of freedom are often not independent of each other, but are coupled. This coupling can either be promotive or competitive [92, 93]. $PbTiO_3$ (PT) is a typical example in which the ferroelectric distortion and the octahedral tilts compete. It exhibits ferroelectricity, but no octahedral tilts [94].
Chemical order, octahedral tilting, ferroelectric distortion and displacive disorder are described in more detail in the following sections.

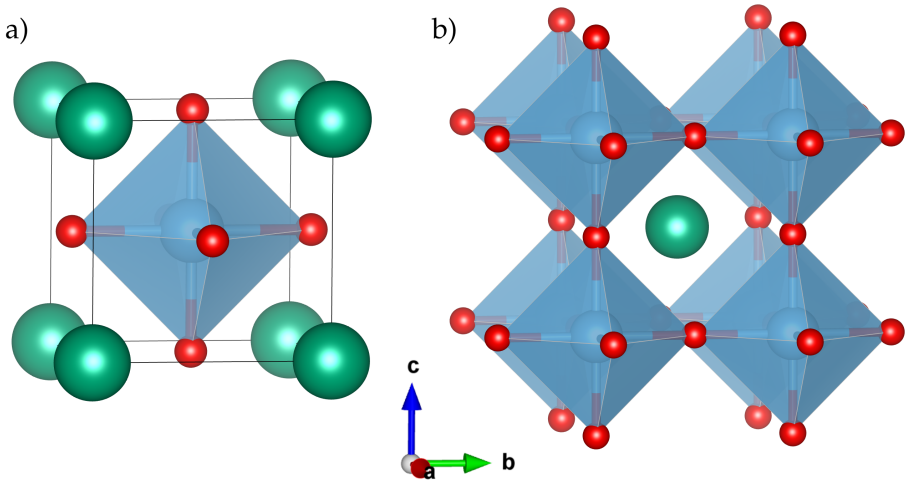

FIGURE 3.6: Two different representations of the perovskite $BaTiO_3$. **a)** The B-cation Ti is located at the center (0.5,0.5,0.5) of the cubic cell and **b)** on the corner of the cell (0,0,0). The oxygen ions (red) form an octahedron around the Ti ions. The Ba ions (green) are situated between the octahedra and have 12-fold coordination (a cuboctahedron). For all following figures the right representation is used.

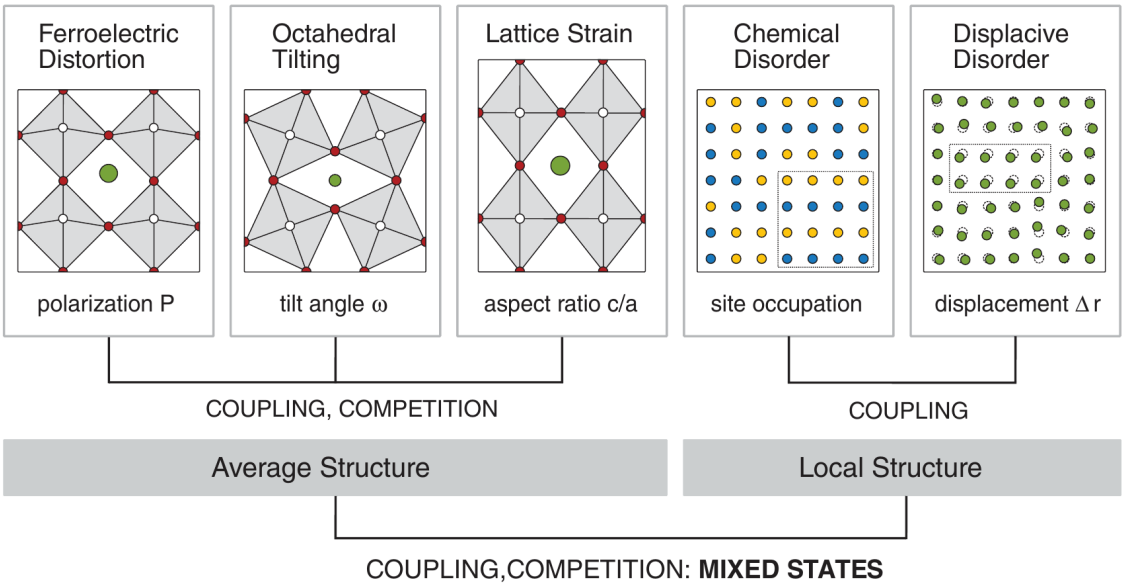

FIGURE 3.7: The different degrees of freedom in NBT and their interactions (from left to right): ferroelectric distortions of the oxygen octahedra, octahedral tilts, lattice strain, chemical order and displacive disorder of the A-cations. Reprinted figure with permission from M. Gröting, I. Kornev, B. Dkhil and K. Albe, Physical Review B, 86, 134118 (2012). Copyright (2012) by the American Physical Society [89].

3.2.1 Chemical order

The spatial arrangement of cations (called chemical order) is an important factor concerning the properties of a perovskite, if two different A- or B-cations with the chemical formula $A_xA'_yBO_3$ or $AB_xB'_yO_3$ are present. When the A and A' or B and B' cations are heterovalent (as Na^{+1} and Bi^{+3} in NBT) a fixed amount of cations has to be present to achieve charge neutrality of the system ($x = y = 0.5$ in $Na_{0.5}Bi_{0.5}TiO_3$ and $x = 1/3, y = 2/3$ in $Pb(Mg_{1/3}Nb_{2/3})O_3$). For homovalent cations (as Zr^{+4} and Ti^{+4} in BZT) a continuous change in composition is possible ($x = 1 - y$).
If the amount of the two cations is equal (as in NBT), one important configuration is the rock-salt order, in which the cations are placed alternatingly on the A-site sublattice [38]. When the two A-cations are charged differently, this configuration has the lowest electrostatic energy. This configuration is named "111-order" and is shown in **Fig. 3.8a**.
Another important arrangement is the alternating stacking of layers of the two cations. This order is named 001-order in this work and is shown in **Fig. 3.8b**. However, in most materials the A-cations are not ordered and are randomly distributed [38]. If the A-cations have any kind of order, the 001-order is preferred.
For a long time the chemical order for NBT was and is still under debate, since different works suggested different orders. In the two studies from Park *et al.* [77] and from Levin and Reaney [83] it was stated from X-ray diffraction that the A-cation order should be on a local nano-scale dimension (if present at all). From Raman spectroscopy a local order of the Na- and Bi-ions was suggested by Petzelt *et al.* [68]. Yenoda *et al.* stated from fitting of pair distribution functions that a local order is present [95]. *Ab initio* calculations from Gröting *et al.* [96] showed that the layered order is preferred, but the energetic differences to the other orders are so small, that during sintering temperatures all orders should be present and the final structure should not experience a long-range order. All these results lead to the conclusion that the chemical order of NBT is mostly disordered and an order of the A-cations exists only within small nm-sized regions. This makes it difficult to observe the local order by the various available spectroscopic techniques, which can measure only spatially averaged configurations.

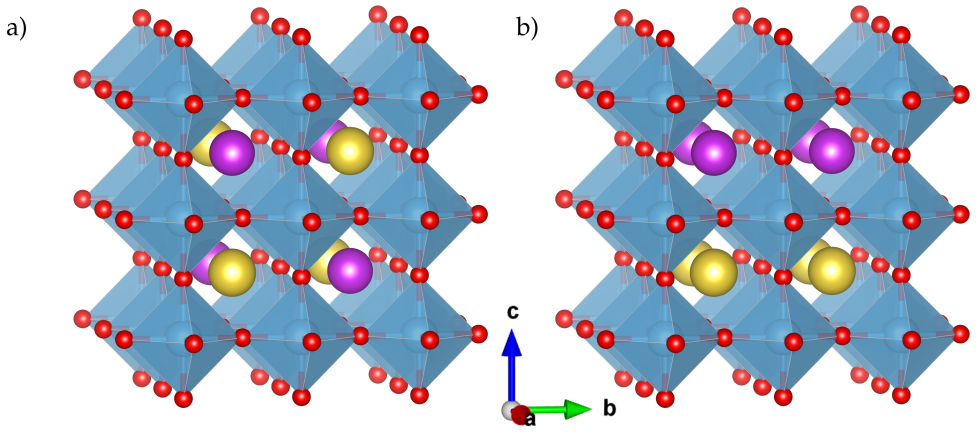

FIGURE 3.8: Two different A-cation orders. **a)** Rock-salt order (111-order) of the Na and Bi ions. **b)** Alternating stacking of Na and Bi layers along the [001]-direction (001-order).

3.2.2 Octahedral tilts

Many perovskite materials show a tilt of the oxygen octahedral network, which lowers the symmetry of the structure. This is usually due to the size mismatch of the A, B and X ions, but can also be affected by the lone-pair effect of some elements [39]. A rule of thumb to determine whether a structure will exhibit tilts or not, can be given by the Goldschmidt tolerance factor [97]

$$g = \frac{r_A + r_X}{\sqrt{2}(r_B + r_X)}\,, \tag{3.1}$$

where r_A, r_B and r_X are the ionic radii of the three ions in the ABX_3 perovskite. If the value g is slightly below unity ($0.9 < g \leq 1$), no tilt of the octahedra is observed (as in $BaTiO_3$ or $SrTiO_3$, ST), because the sizes for the A- and B-cations fit optimal into the structure. If g is larger than unity (A-ions are too large) or smaller than 0.8 (A and B have similar sizes) the structures transform into completely different lattice types. For the range of $0.8 < g < 0.9$ (A-ions are too small) the octahedra tilt.
The tilt patterns are given in the Glazer notation [98], e.g. $a^+b^-c^0$. The superscripts describe the tilt along the respective axes, where "+" means an in-phase tilt, "-" an anti-phase tilt and "0" no tilt, as will be visualized later. The letters a, b and c sometimes are used to denote the angle of the tilting. Thus, same letters correspond to equal tilt angles and different letters to unequal tilt angles. In some cases the polarization of the structure is given as a subscript, again respective for each axis as in $a_0^0a_0^0a_0^0$. This notation is referred to as the modified Glazer notation [99].
Depending on the tilt patterns the symmetry of the structure differs. The non-tilted structure $a^0a^0a^0$ has a cubic symmetry, when no displacement of the A- or B-cation are present. Tilting along one direction (e.g. $a^0a^0a^+$) transforms the cell to a tetragonal symmetry. Additionally, when the tilts have an anti-phase pattern (e.g. $a^0a^0a^-$) the cell size of the irreducible cell is doubled along the respective axis. Often observed tilt patterns include rhombohedral or orthorhombic symmetries, with $a^-a^-a^-$ and $a^-a^-c^+$ tilt patterns [39, 100].
However, at least in NBT-BT, it seems that a certain phase consists of an average over different tilt patterns, with sizes of the octahedral tilt domains on the nanometer scale [101].

3.2.3 Ferroelectric distortions

Polarization in perovskites arises often by the displacement of the positively charged B-site ion relative to the surrounding negatively charged oxygen ions. Depending on the direction of the displacement, the structure adopts different symmetries, as it is well known from the prototype perovskite BT. The symmetry is tetragonal for a Ti displacement along [001]-, orthorhombic for the [110]- and rhombohedral for the [111]-direction. B-site displacements and octahedral tilts are often competitive and suppress each other [39]. This can be seen for example in PZT, where Zr replaces Ti on the B-site. Zr does not show any ferroelectric displacements [102] and thus small amounts of tilts of the octahedra are possible [102, 103].

3.2.4 Displacive Disorder

Another important degree of freedom is the displacive disorder of the A-cations. When two differently charged A-cations are present (as in NBT), unequal displacements of the A-cations can lead to a polarization [39, 92]. This type of displacement is strongly dependent on the chemical order and the octahedral tilts [39]. As it will be shown later, no A-cation displacements are present in the tetragonal tilted structures. The orthorhombic and rhombohedral structures exhibit different kind of shifts of the A-cations. In the orthorhombic phase, with $a^-a^-c^+$ tilt pattern, a polarization is present, which arises from the displacement of the A-cations along the [110]- and [$\overline{1}$10]-direction. In the rhombohedral $a^-a^-a^-$ structure the displacements of the A-cations along the [111]-direction lead to a polarization along the diagonal of the pseudo-cubic cell.
The displacement of the A-cations is affected by the lone-pair of Bi, which tends to have an asymmetric arrangement with its surrounding [104–106]. This leads to an A-site driven polarization in PZT [107]. However, the A-cation displacements can be competitive with B-site displacements and suppress the ferroelectric distortion at the B-site [39].

3.3 Relaxors

As it was seen in Fig. 3.1, NBT does not show a conventional temperature dependent behavior of the permittivity, but one that is known from a different class of ferroelectrics, from relaxor ferroelectrics (RFE). RFEs can be distinguished from regular ferroelectrics (FE) by three characteristics:

- pinched hysteresis,
- no Curie-temperature,
- broad peak of the dielectric constant over a large temperature range and a frequency dependent peak maximum.

As it can be seen on the right side in **Fig. 3.9a** (after Ref. [25]), RFEs show a much narrower polarization-electric field hysteresis as FEs, which sometimes resembles the hysteresis of antiferroelectrics (which shows a double hysteresis loop with a polarization that goes to zero for a vanishing electric field). Moreover, in RFEs a polarization persists above the temperature at which the dielectric permittivity ϵ peaks. In comparison, in FEs the polarization vanishes completely above the narrow peak in ϵ, at the Curie temperature T_C. Last, the peak of the permittivity in RFEs depends on the frequency, whereas in FEs it is frequency independent.
Over the time, several temperatures have been defined, which describe certain temperature ranges in which the observable features of RFEs can be observed. In the following these are listed and explained from high to low temperatures [109, 110]. The most important temperatures are then sketched in **Fig. 3.9b**.

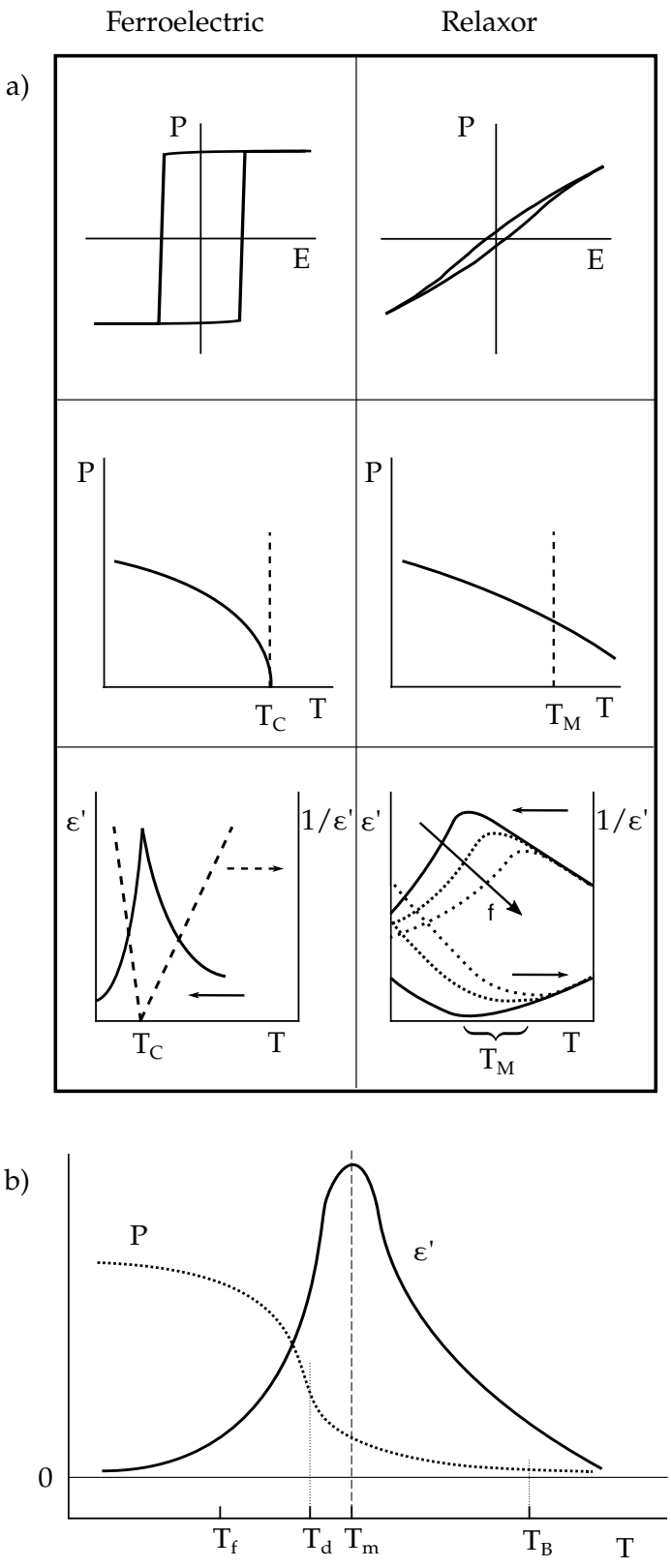

FIGURE 3.9: **a)** Comparison between conventional ferroelectrics (left) and relaxor ferroelectrics (right), redrawn after Ref. [25]. For a ferroelectric material the polarization P vs. electric field E hysteresis loop has a large rectangular shaped area, a steep decrease of the polarization at the Curie temperature T_C and a sharp maximum of the dielectric permittivity at T_C. Here a second order phase transition is shown. In contrast, for a relaxor the hysteresis is pinched and the polarization persists far above the temperature T_m, which denotes the temperature with the maximum of the dielectric permittivity. Additionally, the temperature T_m is frequency dependent in a relaxor, but not in a ferroelectric. **b)** Important temperatures defining special properties in relaxor ferroelectrics: Burns temperature T_B, temperature of the maximum dielectric permittivity T_m, depolarization temperature T_d and freezing temperature T_f. Redrawn and adapted from Ref. [108].

Burns temperature T_B

Above the Burns temperature T_B the material is in a paraelectric state [111, 112]. Below T_B the relaxor starts to become polar. These polar nanoregions show ergodic behavior, meaning that the mobility is fast enough to reach any polar configuration within a certain measurement time.

Temperature of the maximum dielectric permittivity T_m

At this temperature the dielectric permittivity shows a maximum, but it is frequency dependent. For FEs the maximum in permittivity is at T_C, however, no large change in the polarization is observed at T_m in RFEs [26].

Intermediate temperature T*

At the intermediate temperature T* first static (correlated) polar regions appear and the origin of these was suspected to stem from the polar displacements of Pb^{2+} [113]. The intermediate temperature T* is rarely used in literature.

Depolarization temperature T_d

At the depolarization temperature T_d RFEs experience the steepest decrease in polarization [114]. This temperature is therefore comparable to T_C of normal FEs.

Freezing temperature T_f

Below the freezing temperature T_f (sometimes called the percolation temperature [26]) the material gets into a non-ergodic state and the polar nanoregions become completely immobile [115]. At the freezing temperature the relaxation time of the polarization reorientation tends to infinity.

Different explanations and models for the appearance of these features have been formulated. Recently, Ahn *et al.* summarized the most important models [116]:

1. Diffuse phase transition

   Most studies adopt the idea of a diffuse phase transition (DPT) which was formulated by Kirilov and Isupov and Smolenskii in the 1970ies [117, 118]. The DPT model suggests that polar nanoregions (PNR) with different sizes are embedded in a non-polar matrix. All of these PNRs have different Curie temperatures and therefore this distribution of phase transitions leads to the broad peak of the dielectric constant. The differences in the PNRs arise from variations in the local chemical order. This model however fails to explain the frequency dependent positions of the permittivity maxima.

2. Superparaelectric model

   The superparaelectric model [119] describes the polarization flipping processes of each individual PNR, similar to the superparamagnetic model [120]. When the PNR

size is lower than a certain value, the polarization can flip between different states just because of thermal energy. The polarization of the PNRs do not vanish, but cancel each other out on a macroscopic scale. In this model there is no stable remanence polarization.

3. Dipolar glass

   The idea of a relaxation time in a dipolar glass are the same as in a regular glass. It specifies the timescale which is required to flip a polarization. These relaxation times, which can be fitted by a Vogel-Fulcher-Tammann equation, depend on the correlation lengths between the PNRs [121, 122]. At lower temperatures the polarizations begin to frustrate (cannot switch freely) and the correlation lengths and relaxation times increase (long-range order starts to persist). Therefore, the dipolar glass model is able to describe the kinetics of the PNR [123]. Despite this success, the disadvantage of this model is that it does not describe why some materials behave as relaxors and some as regular ferroelectrics.

4. Random fields

   Another important model is based on the so-called random fields. Westphal *et al.* [124] applied the idea of random fields to relaxors (which was adapted from Imry and Ma [125]). They suggested that these fields lead to local deviations of the polarizations. The origin of the random fields can either stem from charge disorder (e.g. when ions with different charge share sites on one sublattice) or strain disorder (ions with different volumes) [126, 127]. Recently, Phelan *et al.* [128] suggested that homovalent (BZT) and heterovalent (PMN) relaxors belong to different types of relaxors, as they show either weak or strong random fields, respectively.

5. Feedback model

   Similar to the aforementioned superparaelectric model, a feedback model has been recently formulated [129, 130]. It describes the relaxation processes of polarizations flipping between basins of a double-well potential. A main difference to the superparaelectric model is the temperature dependent asymmetry of the double-well potential.

6. Spherical random-bond–random-field model

   In 1999 Pirc and Blinc formulated the spherical random-bond–random-field (SRBRF) model that describes the interaction between polar clusters by a Hamiltonian of interacting spins [131]. These spins can have any orientation and couple to external electric fields and internal random electric fields. However, it again does not describe any dynamics, which are needed to explain the frequency dispersion.

Over the years many review articles on the various relaxors and their properties have been published [25, 75, 108, 109, 119, 132–134]. Explanations for the structural origin of polar nanoregions, which are used in many of the above mentioned models, are not yet conclusive. Hlinka [135] stressed that only when a full geometrical description of the PNRs can be given, the topic of relaxors can be understood ultimately.
It was long believed that some kind of polar regions are embedded in an unpolar (cubic) matrix or differently polarized nanodomains (PND) [109]. Also a competition between AFE and FE domains was proposed [136]. However, the exact structural features were

only explained on a speculative basis. To grasp a better understanding of the local structures of PNRs several studies have been performed. Kreisel *et al.* [41] and Xu *et al.* [137] observed rod-like patterns from X-ray measurements in NBT and $PbZn_{1/3}Nb_{2/3}O_3$–$xPbTiO_3$. They assigned these patterns to planar defects, which Xu *et al.* called "pancake-like". In a proceeding study Kreisel *et al.* [138] suggested that the diffuse scattering originates from different chemical orders within and outside of the PNRs. In 2010 Ganesh *et al.* [139] proposed that the diffuse scattering in the RFE system $PbSc_{1/2}Nb_{1/2}O_3$ arises from local concentration fluctuations of the B-site ordering, which induces shifts of the Pb ions due to locally varying electric fields. Later Ge *et al.* [55] compared the A-site mixed NBT and the B-site mixed PMN relaxors by neutron scattering and stated that the diffuse scattering may be a feature specific to RFEs, independent of the origin of the relaxor properties. Generally, correlated and uncorrelated shifts of the Pb ions are often held responsible for the observed diffuse scatterings in Pb containing relaxors [140]. Recently, Manley *et al.* [24] suggested that PNRs are just some kind of localized phonons with correlated Pb displacements. The wavelength of the resonant ferroelectric phonons would thus describe the size of the PNRs. Molecular dynamics (MD) simulations based on an effective Hamiltonian (explained in detail in the methods Sec. 4.2) for B-site mixed relaxors of the type $Pb(B_xB'_{1-x})O_3$ showed the relative strength between random electric fields and the ferroelectric interaction determine, whether a system is a RFE or FE [141, 142]. Additionally, the characteristic length scales of PNRs and chemical ordered regions are similar. Studies from the Bellaiche group [143, 144] and Rappe group [145, 146] focused on the relaxation times of the polarization switching in PMN and PMN-PT. In a different MD study Akbarzadeh *et al.* [147] showed that relaxor behavior could be found in disordered BZT, just from the smallest length scale deviations in the Ti/Zr distributions. In other studies a core-shell model [148–150] or a Pauli master equation for the polarization switching [151] was applied to investigate the time and temperature dependence of the dielectric response.
From what we have learned so far about the definition of relaxors, we have to say that NBT can not fully be characterized as a relaxor, since the peak of the dielectric permittivity does not show a shift with temperature [40]. Nevertheless, it is often referred to as a relaxor or to be relaxor-like.

3.4 NBT as an ionic conductor

Generally, when non-stoichiometry of a material is induced intentionally, by doping or unintentionally by contamination, new interesting properties can emerge. One just has to think of semiconductors, where small doping concentrations create electric conductivity [152]. NBT is similar in this regard. Perfectly stoichiometric NBT is an insulator and does not show any noteworthy electrical conductivity [153]. However, ionic conductivity, which results from oxygen vacancy migration, can be induced [32]. Since during processing of NBT the reaction

$$2Bi_{Bi}^{\times} + 3O_O^{\times} \rightarrow 2V_{Bi}^{'''} + 3V_O^{\bullet\bullet} + Bi_2O_3 \tag{3.2}$$

can lead to a loss of Bi_2O_3, it is expected that in nominally stoichiometric NBT Bi and oxygen vacancies are present [32].

Interestingly, the conductivity of Bi-deficient and acceptor-doped NBT is in the order of other important oxide ion conductors, like yttria stabilized zirconia (YSZ) [32]. A plot of the conductivity of stoichiometric, Bi-deficient and Mg- and Ni-doped NBT is given in **Fig. 3.10**. The drawn lines show different slopes and serve as guide for the eyes. The Arrhenius plot of the conductivity shows a peculiar temperature dependent non-linearity, i.e. a change in the activation energy E_a at around 600 K. Above 600 K the activation energy is around (0.4-0.5) eV and below at (0.8-1.2) eV, depending on the chosen segment to be fitted. The huge difference in activation energies for high and low temperature is in contrast to former studies on ionic conductivity of various different perovskites and oxides, in which straight lines in the Arrhenius plot have been reported [154, 155].
Understanding the underlying processes and how to maximize the conductivity of doped and non-stoichiometric NBT (and other perovskite) is an active field of research. Already in 2009 Ranjan *et al.* [50] studied Ca substituted NBT via neutron scattering, however with a focus on the rhombohedral to orthorhombic phase transition. One of the first studies on doped NBT regarding the ferroelectric properties was performed by Aksel *et al.* They investigated Fe, La and Mn dopants with a concentration of 1% [156, 157]. Although no significant changes in the piezoelectric properties were observed, they found a structural transformation on a local scale. A portion of the structure transforms from an initial monoclinic Cc symmetry into a cubic symmetry with space group $Pm\bar{3}m$. Many more studies on doped NBT have been carried out since the work of Li *et al.* was published in 2014 [32], primarily to enhance the piezoelectric properties. For example, binary phases were found in cerium doped NBT [158]. Further, the processing behavior [159], Cc phase stabilization [160] and piezoelectric properties of Co doped NBT [161] were studied. Other investigated dopants and their influence on the piezoelectric properties were Hf and Zr [162] and Rb [163]. Recently, other groups have investigated Ag and Ga doped NBT [164] or other Mg concentrations [165]. Modelling of the oxygen vacancy migration

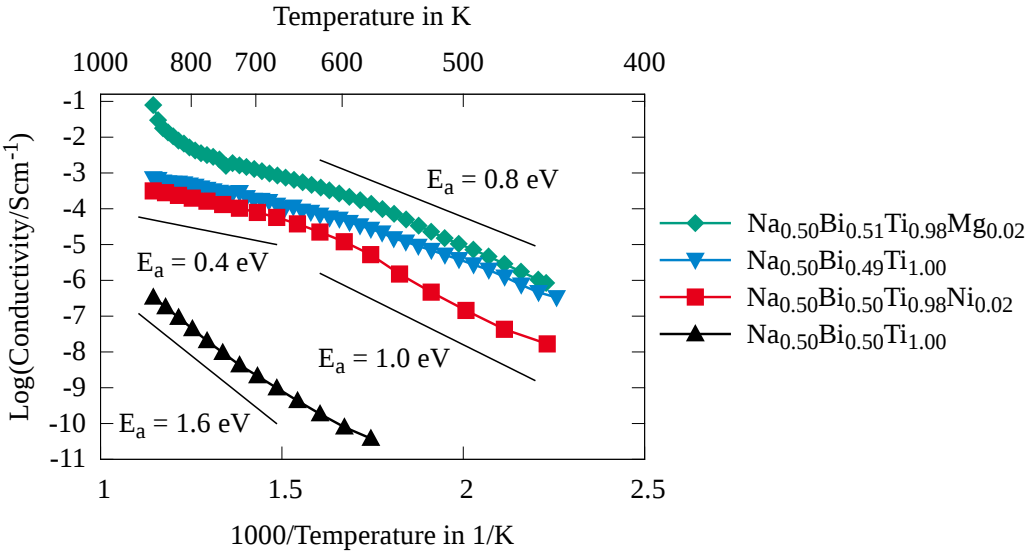

FIGURE 3.10: Electronic and ionic conductivity of stoichiometric, Bi-deficient, Ni-doped ($NBTi_{0.98}Ni_{0.02}$) and Mg-doped $NBTi_{0.98}Mg_{0.02}$ (with permission of Sebastian Steiner and Till Frömling).

was done by different methods. Classical MD calculations were performed on ST [166] and *ab initio* MD calculations on NBT [167]. Chemical defect models have been used to describe the conductivity of ST [168, 169] and BT [170, 171], which are going to be extended for the more complex NBT in the future [172]. Yet, no definite answer could be given to the question, why a kink in the activation energy was observed in conductivity measurements (as shown in **Fig. 3.10**).
The diffusion of oxygen vacancies in a crystalline lattice depends on different factors. First of all, only "free" vacancies $V_O^{\bullet\bullet}$ contribute to the overall conductivity. When oxygen vacancies are bound to the dopant ion (e.g. Mg) or other defects the concentration of free oxygen vacancies $[V_O^{\bullet\bullet}]$ is reduced. The amount of free vacancies depends on the association energy ΔH_{asso}:

$$K = \frac{[Mg_{Ti}'' - V_O^{\bullet\bullet}]}{[Mg_{Ti}''][V_O^{\bullet\bullet}]} = \exp\left[\frac{-\Delta H_{\text{asso}}}{k_B T} + \frac{\Delta S_{\text{asso}}}{k_B}\right], \tag{3.3}$$

where K is the equilibrium constant and ΔS_{asso} the configuration entropy of the associate [173, 174]. The diffusion coefficient is then given by

$$D = c_{\text{cor}} c_{\text{geo}} a^2 \nu \exp\left[\frac{\Delta S_{\text{mig}} + \Delta S_{\text{asso}}/2}{k_B}\right] \exp\left[\frac{\Delta H_{\text{mig}} + \Delta H_{\text{asso}}/2}{k_B T}\right], \tag{3.4}$$

with a correlation factor c_{cor}, a geometry factor c_{geo}, the jump distance a and the attempt frequency ν. Note that only half of the association energy enters the equation. This results from the fact that the dopant concentration and concentration of the oxygen vacancies is equal $[Mg_{Ti}''] = [V_O^{\bullet\bullet}]$, because of charge neutrality.
Via the Nernst-Einstein equation [175] this leads to a total conductivity of

$$\sigma = \frac{[V_O^{\bullet\bullet}] D q^2}{k_B T}, \tag{3.5}$$

where q is the charge of the migrating particle. For a single migration and association energy this equation gives a straight line in an Arrhenius plot and has no kink.
Yang *et al.* [176] modeled the change in activation energy by assuming a two-phase composite of a tetragonal and rhombohedral phase between 520 K and 670 K. They were able to fit the change in slope by employing the Maxwell model with extrapolated low and high temperature conductivities. However, they did not provide any explanation for the different activation energies, which can have different origins.

In the following, we study the influence of phase dependent effects on the activation energies. First, in Sec. 6 we study whether a change in the migration energy arises, when a transition from the low temperature rhombohedral to the high temperature tetragonal symmetry via the intermediate temperature orthorhombic symmetry is taken into account. Related to this explanation of phase transitions is the increase in the cell volume from thermal expansion, which could affect the migration barriers. The effect of the increased cell volume is investigated at the end of Sec. 6. Secondly, in Sec. 7 we study the association of an oxygen vacancy with a dopant and an intrinsic Bi-vacancy. For a long-range diffusion of an oxygen ion, the associate first has to be separated. Thus, this association energy has to

be overcome additional to the migration energy, which leads to an increase of the activation energy at lower energies. Since the kink in the slope is even present in non-doped NBT, we also study whether the association of the two $V_O^{\bullet\bullet}$ and a $V_{Bi}^{'''}$ vacancies is energetically favorable.
Furthermore, associates, especially polar associates, can alter the properties in ferroelectric materials in a negative manner, e.g. influence the domain switching behavior and lead to fatigue [177–181]. Therefore, polar defects also influence the ECE, which will be studied in Sec. 8. Another import aspect of polar defects is not of static nature, but of kinetic. Erhart *et al.* [179] calculated the switching time scales of polar $(Fe_{Zr,Ti}^{'}–V_O^{\bullet\bullet})^{\bullet}$ and $(Cu_{Zr,Ti}^{''}–V_O^{\bullet\bullet})^{\times}$ associates in PT by calculating their binding energies. These timescales are of importance since they might be of the same order as the timescales of the switching of the electric field in the ECE, which is in the order of seconds. In 2014, Zannen *et al.* [182] studied the ECE of NBT, doped with different lanthanide elements, indirectly by measuring the polarization and using the Maxwell's relation of Eq. 3.8. Interestingly, they observed that not only the magnitude and the temperature range of the ECE change with the used element, but also the sign. For Nd and Ho dopants a negative ECE was determined at temperatures lower than 320 K. As these defects can only be avoided to a certain extent [178, 183], it is important to study their properties.

3.5 Theoretical work on NBT

Since the beginning of this century, more and more *ab initio* based studies have been performed to investigate the various properties of NBT. The theoretical works started with Xu and Ching in 2000 on the electronic structure, who found a strong covalent binding in NBT [184]. Burton and Cockayne studied the A-cation order in 2001 [185] and found that the 111-order is the one with the highest energy. Later more complex features like elastic constants [186], electrical and optical properties were studied, including the electronic band structure and band gap [187–189]. Gröting *et al.* investigated the octahedral tilt phase stability dependent on the chemical order [96] and pressure [89]. They concluded that a chemical order should be present only on a local scale. Further, a phase transition from a rhombohedral to an orthorhombic phase with increasing pressure was observed. Kitanaka *et al.* studied the polarization in NBT (displacement of Ti ions along one of the pseudo-cubic diagonals). They found that 71° polarization switching (from one corner to a neighboring corner in the pseudo-cubic cell) is preferred over the 180° inversion [190]. Phonon frequencies were investigated in Refs. [191–193] and assigned the different frequency ranges to the ones observed in experimental Raman studies. Oxygen octahedral tilt defects and tilt phase transitions were studied by Meyer *et al.* [194]. Ju *et al.* studied the magnetoelectric coupling, who observed that Na vacancies can induce a magnetic moment [195]. Also studies on the tilt phase stability of NBT solid-solutions were carried out [196]. Recently, the vacancy defect chemistry in NBT and doped-NBT was studied [167, 197, 198], especially in respect to the oxygen migration, which is also part of this work. He and Mo performed *ab initio* MD simulations on pure NBT and Mg, Zn and Cd doped NBT [167]. They focused on the oxygen migration at very high temperatures (1200 K to 2800 K). Most of these studies focused on the ground state rhombohedral phase and a single chemical order. However, regarding the relaxor properties of NBT many questions are still unanswered.

3.6 The electrocaloric effect

The endeavor to replace conventional vapor-based cooling techniques by new more sustainable ones has lead to an increase of studies on a specific cooling effect, which was discovered and reported more than 80 years ago, the electrocaloric effect [199]. These earliest studies were performed on Rochelle salt by Kobeko in 1930 [199]. A large amount of different materials was investigated in the 1960ies and 70ies, like the ceramics $BaTiO_3$ [200] and $BaTiO_3$-$SrTiO_3$ [201] and $PbTiO_3$-solid solutions [202] and other salts like KCl [203]. However, the possible temperature changes for all materials were about 1 K (2.6 K was the highest in 1981 [204]) and for a long time the electrocaloric effect (ECE) was disregarded as too small for any applications. Only from 2006 on, when Mischenko *et al.* discovered the "giant electrocaloric effect" in thin-film PZT ($\Delta T > 10 K$) [9], the quest to search for new materials with large ECE was reawakened.
Since then many different ceramics have been measured, among some are BT- and ST-based: BT [205,206], BCZT [207], BZT [208,209] and KNB-ST [210]. Others are lead-free NBT-based materials such as NBT-BT [211], La-doped-NBT [182] and NBT-KBT-BT [212]. The largest set of materials however still belongs to the lead containing materials: Ca-doped NBT-ST-PT [213] PMN-PT, [29, 214], $Pb(Zn_{1/3}Nb_{2/3})O_3$-$PbTiO_3$ (PZN-PT) [215], $(PbLa)(ZrTi)O_3$ (PLZT) [216] and $Pb_{0.8}Ba_{0.2}ZrO_3$ (PBZ) with a ΔT of up to 43 K [217].
Interestingly, in some studies a negative ECE was found. Thereby, the temperature of the material decreases when the electric field is applied (instead of increased). Peräntie *et al.* found a negative electrocaloric (EC) temperature change in PMN-PT by indirect measurements (determination of ΔT by measuring the change in polarization) [218]. Shortly after, a negative ECE was reported in NBT and other NBT-based solid solutions by indirect measurements [30,211,212,219]. Recently, even a "giant negative ECE" of 5 K was observed in La-doped PZT [220].
The negative EC temperature change was investigated theoretically by different approaches. In 2012, Ponomareva and Lisenkov used first-principles based simulations on $Ba_{0.5}Sr_{0.5}TiO_3$ (BST) [221]. Although they could not observe a negative ECE, they attributed the experimentally observed ECE to the misalignment of an external electric field to the internal polarizations. In general, the ECE is strongly anisotropic, meaning the direction of the applied electric field strongly influences the temperature change [222]. Two years later, Pirc *et al.* studied the negative ECE in antiferroelectric PZ within a Kittel model [223]. A simple uniaxial model of polarizations situated on two sublattices were sufficient to obtain a negative temperature change. Another way to achieve a negative ECE is the introduction of polar defects into a ferroelectric material. The effect of polar defects on the ECE was studied experimentally [224] and theoretically [31, 225, 226]. However, the usefulness or harmfulness of polar defects is still under debate and is studied in Sec. 8.
Over time, several review articles have been published, which give an overview of all the studied materials, ranging from ceramics (mostly lead-based) to polymers [227–230]. In 2012 Lu and Zhang dedicated a review article solely on the ECE in relaxors [28]. Since relaxor materials provide several advantages over common ferroelectrics, they are an interesting type of material to study [231]. As already mentioned, RFE experience a broad phase transition temperature range and a narrow hysteresis, which can lead to smaller work losses and a better reversibility of cooling/heating of the material.

An important factor for good ECE materials is their geometry, which can either be bulk, thick-film or thin-film [227]. The advantage of thin-films over thick-films and bulk are the high electric breakdown voltage and therefore a very large electric field can be applied (776 kV/cm in the work of Mischenko [9]). Since the EC temperature change is proportional to the applied ΔE, as we will see soon, a large dielectric strength is desirable. However, the disadvantages of thin-films (with a thickness of usually less than 500 nm) are the low heat capacity because of the small amount of mass involved. This problem must be considered for applications and when the EC cooling cycle is discussed.
The EC cycle depicted in **Fig. 3.11** (after Ref. [232]) shows a possible scenario where heat can be transfered from a heat source to a heat sink by a periodic application and removal of an electric field. At the initial stage A (top left) the sample has an initial temperature (usually room temperature) and an initial electric field is applied (usually the electric field

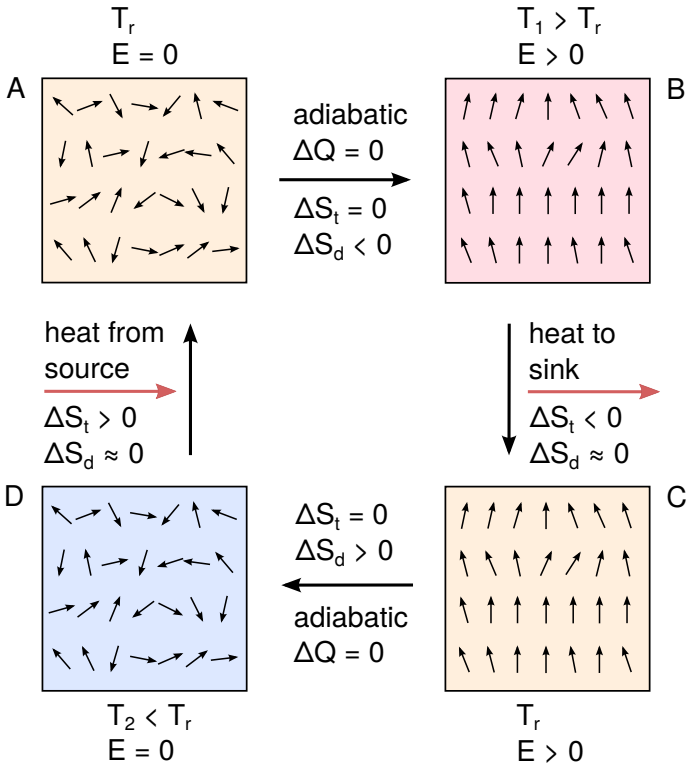

FIGURE 3.11: The adiabatic electrocaloric cycle. In the initial state A the sample has room temperature T_r and no electric field E is applied. The dipoles within the sample show a certain degree of disorder. When an electric field $E > 0$ is applied the dipoles align along the external field. If the field is applied fast enough the process happens adiabatically and the total energy and entropy stays constant. However, since the dipolar (configurational) entropy decreases, because of the alignment of the dipoles, the lattice entropy (i.e. the temperature) increases. If state B rests for some time it can transfer its gained temperature to a sink and reaches room temperature after some time. During this process the total entropy is reduced, but the dipolar entropy is approximately constant, since the electric field is still applied. From state C to state D the removal of the electric field reverses the effect and the temperature decreases.

is turned off). In a first step (A→B) an electric field E is switched on adiabatically (i.e. fast), so that no heat can be exchanged with the surrounding ($\Delta Q = 0$).
At stage B the dipoles residing within the sample align along the external field, which lowers the dipolar entropy S_d. Since the total entropy S_t stays constant [233], the vibrational entropy of the lattice increases, which means that the temperature of the sample increases (indicated by the red color). At elevated temperatures, the sample is brought into contact with a heat sink (which can be at room temperature) and the temperature of the sample equilibrates with temperature of the heat sink. During this process the vibrational entropy decreases and the sample reaches the third stage C.
From stage C to D the electric field is removed and the dipoles reorient randomly (when the temperature is above the Curie temperature). This leads to an increase of the dipolar entropy and a decrease of temperature. Heat can then be absorbed from a heat source and the sample is again at stage A.
The achievable EC temperature change can be quantified with the help of Maxwell's relations. If an electric field is applied to a ferroelectric material, the internal dipoles try to align along the external field. The reorientation of these dipoles leads to a change of the structural (dipolar) entropy. When the external field is applied adiabatically (no exchange of heat with the surrounding) the temperature change can be determined using the following Maxwell's relation [234]:

$$\left(\frac{\partial S}{\partial E}\right)_T = \left(\frac{\partial P}{\partial T}\right)_E , \tag{3.6}$$

where S is the dipolar entropy, E the electric field, P the polarization and T the temperature. When the electric field is switched from the initial value E_1 (usually =0) to E_2, the entropy change can be determined to be

$$\Delta S = \int_{E_1}^{E_2} \left(\frac{\partial P}{\partial T}\right)_E dE . \tag{3.7}$$

Since the change in entropy of a system is related to the temperature and the heat capacity c by $\Delta S = c\Delta T/T$, one can write

$$\Delta T = -\frac{1}{\rho} \int_{E_1}^{E_2} \frac{T}{c(E,T)} \left(\frac{\partial P}{\partial T}\right)_E dE , \tag{3.8}$$

where ρ is the density of the material.
The pyroelectric coefficient $\partial P/\partial T$ is often used as a measure to quantify the ECE of a material, see e.g. [202]. Another important parameter is the relation of the temperature change to the applied electric field $\Delta T/\Delta E$, since it is a better figure of merit than ΔT, which depends on the strength of the applied electric field.
Eq. 3.8 is called the "indirect" approach to determine ΔT, since only knowledge of the polarization, and the heat capacity is required. In contrast, the temperature change can also be obtained directly by different techniques [235]. The two most important ones are DSC (e.g. Ref. [209]) or infrared cameras [236, 237].
Some studies reported that the indirect determination of ΔT is not applicable [238, 239], especially close to the first order phase transition of ferroelectrics, at which the heat ca-

pacity diverges. However, in a theoretical study Kalcher *et al.* showed that the direct and indirect measurements should give similar results, if the integration of Eq. 3.8 is carried out carefully [240]. Also Goupil *et al.* compared and found a strong agreement between the direct and indirect measurement of the ECE in PMN-PT [27]. Although the debate on the validity of the indirect approach is still ongoing, it is a convenient starting point for different models, which aim to describe the EC temperature change.
Simultaneously to the experimental studies, various theoretical works have been published. One of the earlier works was published by Kutnjak *et al.* in 1999 [241]. They described the polarization of the system with a Landau-Devonshire expansion of the free energy [242], which then could be used together with Eq. 3.8 to determine the EC temperature change. Similar Landau-type formulations for the free energy where later chosen by other authors, which also take into account stresses [243–246], compositional variance [247] or deal with relaxors [233, 248]. Other approaches include statistical thermodynamics to describe the properties of the system: a Gibbs-Shannon equation for the entropy was formulated by Pirc *et al.* [249], the canonical partition function $Q(N, V, T, E)$ [250, 251], the time-dependent phase field model [252] or mean-field models [253].
In Sec. 8 we study the difference of the ECE between ferroelectrics, antiferroelectric and relaxors. Further, we study the impact of polar defects, arising from associates, since these defects reduce the available dipolar entropy of Eq. 3.7, which decreases the obtainable EC temperature change.

3.7 Comparison of NBT to other important perovskites

As described in Sec. 3.2, NBT exhibits many different degrees of freedom, from polar ferroelectric displacements of the A and B cations, octahedral tilts and chemical disorder. Mechanical strain fields of the heterovalent Bi^{+3} and Na^{+1} are small due to the similar ionic radii of Bi (1.45 Å) and Na (1.39 Å) [254]. In comparison, most other mentioned perovskites lack certain degrees of freedom.

- **BT** is a ferroelectric material, that undergoes phase transitions from the rhombohedral to orthorhombic and further to a tetragonal and then cubic symmetry [255]. These different symmetries arise from the displacement of the Ti ion along different directions. However, it neither shows any octahedral tilts, nor does it have any chemical order (as it only has a single A- and B-cation).
- **PZT** has a morphotropic phase boundary at 45 mol% Zr from the rhombohedral to tetragonal phase [103]. It experiences small octahedral tilts for higher Zr concentrations [100, 256]. However, PZT is not a relaxor, but a ferroelectric [180].
- The recently more studied material **BCZT** does not show any tilts of the oxygen octahedra [257]. It is also only a relaxor-like material, since it has no significant shift in the dielectric permittivity peak.
- **PMN** has a diffuse phase transition, a frequency dependence of T_M and octahedral tilts. Thus PMN is a model relaxor material [258].
- **KNN** is a ferroelectric material that exhibits octahedral tilts, but becomes a relaxor only when doped [259, 260].

3.8 Open questions

From all the information we have gathered so far, we can pose several questions about unresolved aspects of NBT and the ECE, which we try to answer in this work.

NBT

1. **What are the kinetics of the phase transitions?**

   Local phase transitions may cause the difference between the local and the average structure seen in experimental studies. Different degrees of freedom can account for these phase transitions.

2. **What is the size of polar nanoregions?**

   Since it is known that the size of PNRs is smaller than the resolution of different scattering methods, one can only say so far that the diameter of a PNR has to be smaller than 500 Å. It is expected that the size of PNRs is equal to the size of the chemically ordered regions, which is restricted to very small sizes of several nm. Octahedral tilt defects might account for these polar nanoregions in NBT.

3. **Does the chemical order influence the phase transitions?**

   If PNRs are due to ordering of the A-cations, the question remains, why the different chemical orders lead to local phase transitions? To answer this, one has to investigate whether the different chemical orders exhibit different local energy landscapes for octahedral tilts and cation displacements or not.

4. **Why is the activation energy of the ionic conductivity temperature dependent?**

   The large change of up to 0.5 eV in the activation energy for the oxygen migration at low and high temperatures might have several origins. Phase transitions from the rhombohedral to the tetragonal symmetry could change the oxygen migration energy barriers. Further, volume changes due to thermal expansion can influence the migration. Defect associates could further increase the activation energy.

5. **Do oxygen vacancies associate with dopants and Bi vacancies?**

   Different oxygen vacancy defect associates can be thought of. Oxygen vacancies can associate with dopants, but also with other vacancies, such as Bi vacancies. If an association energy exists, the activation energy for oxygen migration will be influenced. Further, the associates are polar defects, which can influence the ECE.

1. **How does the ECE differ in ferroelectrics, antiferroelectrics and relaxor ferroelectrics?**

   Is the ECE in relaxors superior to ferroelectrics or antiferroelectrics, as it is suggested? Two aspects can be considered, the overall achievable temperature change and temperature range, which can be tuned to be close to room temperature.

2. **How do polar defects influence the ECE?**

   Can polar defects enhance the EC temperature change or shift the ECE to temperature suitable for application? Further, how do parallel and antiparallel oriented polar defects influence the ECE? How important is fatigue, that is related to reorientation of polar defects, for the ECE?

3. **Do different methods (molecular dynamics and Monte Carlo) give similar results for the ECE?**

   How sophisticated do different models have to be to give qualitative and quantitative agreements for the ECE? This includes the question, which terms in the Hamiltonian are the most relevant ones and which are less important.

4 Methods

Throughout this work three different computational methods are used: density functional theory (DFT), molecular dynamics (MD) and Monte Carlo (MC) (see **Fig. 4.1**).
In the first part of this section, DFT is explained, which is used for the major part of this work to investigate the system NBT. These first-principles (or *ab initio*) calculations are carried out without any experimental input data. Everything that is needed to set up and run calculations is set by the choice of the potentials, which describe the electronic configuration of each element. DFT is able to describe systems with N electrons accurately by solving the Schrödinger equation. The obtained wave function and electron density contain the full information on the system. However, DFT is computational demanding. Thus, only rather small system sizes of up to 10 000 electrons can be investigated, since the computational demand increases with the factor N^3. Another restriction of DFT calculations is that only the electronic ground state is considered, as if the system is at $T = 0\,\mathrm{K}$. Excited electronic states can not be studied in a straightforward manner. Therefore, the free energy F of the electronic ground state structure contains only the internal energy U.
Next, a short introduction on transition state theory and the nudged elastic band method is given. Therein it is described how to obtain energy barriers and the transition path of a process, which take a structure from one state in an energetic minimum to a different energetic minimum state.
The last two parts of this section deal with molecular dynamics (MD) and Monte Carlo (MC) methods. Both methods are used to model the electrocaloric effect (ECE). *Ab initio* MD simulations are employed to investigate the temperature dependent dynamics of the phase transitions in NBT.
Molecular dynamics simulations allow to study the time evolution of a system at finite temperatures by solving Newton's equations of motion for a given set of potentials. The

Methods	General equation	Statistical Physics
DFT	$H\Psi = E\Psi$	$F_0(T=0\,K) = U(T=0\,K)$
Molecular dynamics	$\vec{F} = m\vec{a} = -\vec{\nabla}U_{pot}(\vec{R}_i)$	$U_{tot} = U_{kin} + U_{pot}$
Monte Carlo simulations	$p = \exp\left[\frac{-\Delta U_{conf}}{k_B T}\right]$	U_{conf}

FIGURE 4.1: The employed computational methods of this work. Density functional theory (DFT) is based on the Schrödinger equation. Molecular dynamics use Newton's equations of motion to describe the dynamics of particles. Monte Carlo simulations model the configurational energy from statistical approaches.

trajectories of all particles are determined by forces that act on each atom. These forces accelerate the particles and change their velocities. In *ab initio* MD simulations the forces are determined from density functional theory.
The Monte Carlo method is based on the stochastic occurrence of events that change the configurational arrangement of a system. Here, a lattice-based Ising-like Hamiltonian is used to describe the response of the polarization of the system as a response to an external field. The MC method does not contain any information on the kinetics and time-evolution of the system, but allows to obtain macroscopic entities, such as the polarization.

4.1 Density functional theory

The solution to non-relativistic quantum mechanical problems can be obtained by solving the time dependent Schrödinger equation (SE) [261]

$$\left[i\hbar\partial_t + \hat{H}\right]\Psi(r,t) = 0\ , \tag{4.1}$$

where ∂_t is the time differential and $\hat{H}$ is the Hamilton operator, which determines all energy contributions of the investigated system. The solution to this differential equation is given by the wave function $\Psi(r,t)$. However, for most problems it is sufficient to solve the stationary (time-independent) SE

$$\hat{H}\Psi(r) = E\Psi(r)\ , \tag{4.2}$$

with the time independent Hamilton operator $\hat{H}$ that contains all energy contributions. E is the energy of the system with the eigenstate wave function $\Psi(r)$. For a solid, $\hat{H}$ takes the following form (in atomic units: $e = \hbar = m_e = 1/4\pi\epsilon_0 = 1$):

$$\hat{H} = -\sum_k \frac{\boldsymbol{\nabla}_k^2}{2m_c} - \sum_i \frac{\boldsymbol{\nabla}_i^2}{2m_e} + \sum_{k\neq l} \frac{Q_k Q_l}{|R_k - R_l|} + \sum_{i\neq j} \frac{q^2}{|r_i - r_j|} + V_{\text{ext}}(r)\ . \tag{4.3}$$

$-i\hbar\boldsymbol{\nabla}$ is the momentum operator and thus the first term contains the kinetic energies of all cores with the mass m_c. The second term sums the kinetic energies of all electrons with the mass m_e. The Coulomb interaction between the cores is considered in the third term and is therefore a two body sum. Of course the interaction of one core with itself is excluded by summing over $k \neq l$. R_k and R_l are the coordinates of the two cores. Identically to the core coulomb interaction the forth term sums the Coulomb interactions between all electrons. Again, self-interaction is excluded. The last term describes the interaction of the electrons with the cores.
Fortunately, this Hamiltonian can be simplified and some terms can be neglected. In the Born-Oppenheimer approximation the kinetic energy of the cores is disregarded since the mass of the cores is about 2000 times higher than the ones of the electrons, which leads to much slower velocities of the cores than the ones of the electrons. Therefore, the positions of the cores are static (which also reduces the complexity of the fifth term in the Hamiltonian). In a next step we can neglect the Coulomb interaction between the cores as they do

not change the energies of the electronic system (which we are interested in). Hence, we can rewrite our Hamiltonian in a shorter and simpler form:

$$\hat{H} = -\sum_i \frac{\nabla_i^2}{2m_e} + \sum_{i \neq j} \frac{q^2}{|r_i - r_j|} + V_{\text{ext}}(r) \,. \tag{4.4}$$

This equation describes all energy contributions to the electronic system and it can be solved for different simplifications.

Hartree method

The first simple approach to solve Eq. 4.4 was given by Hartree shortly after the introduction of the SE in the late 1920s. The solution of the SE (the total wave function with N electrons) is given as a product of all single particle wave functions [261]:

$$\Psi(r_1, r_2, \ldots, r_N) = \phi_1(r_1)\phi_2(r_2)\ldots\phi_N(r_N) = \Pi_i \phi_i(r_i) \,. \tag{4.5}$$

By this ansatz the SE for the individual orbitals can be rewritten in two ways:

$$\left[-\nabla_i^2 + v_{\text{ext}} + v_{\text{H}}(r)\right]\phi_i(r_i) = \epsilon_i \phi_i(r_i) \tag{4.6}$$

and

$$\left[-\nabla_i^2 + v_{\text{ext}} + v_{\text{H, SIC}}(r)\right]\phi_i(r_i) = \epsilon_i \phi_i(r_i) \,. \tag{4.7}$$

Equation 4.6 contains the Hartree potential

$$v_{\text{H}}(r) = \int d^3r' \frac{n(r')}{|r - r'|} = \sum_j \left\langle \phi_j \middle| w_{ij} \middle| \phi_j \right\rangle \,, \tag{4.8}$$

which includes the self-interaction of each electron. Here we introduce the electron density $n(r)$. A correction to this ansatz is the self-interaction corrected Hartree potential

$$v_{\text{H,SIC}}^k(r) = \int d^3r' \frac{n_i'(r')}{|r - r'|} = \sum_{j \neq k} \left\langle \phi_j \middle| w_{ij} \middle| \phi_j \right\rangle \,, \tag{4.9}$$

as in Eq. 4.7, in which the sum of all electron-electron interaction does not include the self-interaction. The self-interaction corrected approach is "more" correct, however, the computational time increases a lot, because the electron density $n_i'(r)$ is different for each electron. However, for large systems with several thousands of electrons the difference in energies for the two sums (self-interaction corrected or not) is negligible. The major problem of this ansatz is that the solution does not fulfill the requirement of a fermion, i.e. the wave function is not antisymmetric.

Hartree-Fock method

The antisymmetric property of the wave function can be included by a Slater determinant

$$\Psi = \frac{1}{\sqrt{N}} \begin{vmatrix} \phi_1(r_1) & \phi_1(r_2) & \dots & \phi_1(r_N) \\ \phi_2(r_1) & \phi_2(r_2) & \dots & \phi_2(r_N) \\ \dots & & & \\ \phi_N(r_1) & \phi_N(r_2) & \dots & \phi_N(r_N) \end{vmatrix} \tag{4.10}$$

of all individual wave functions [261]. By using this wave function, the resulting SE for one orbital for the case of a system with two electrons looks as follows:

$$\begin{aligned} &-\frac{\nabla^2}{2}\phi_1(r) + V(r)\phi_1(r) + \int d^3r \phi_2^*(r')\phi_2(r')\frac{1}{|r-r'|}\phi_1(r) \\ &-\int d^3r \phi_2^*(r')\phi_1(r')\frac{1}{|r-r'|}\phi_2(r) = \epsilon_1\phi_1(t)\,. \end{aligned} \tag{4.11}$$

The difference to the Hartree approach is the exchange potential

$$V_x(r)\phi_k(r) = -\sum_l \int d^3r \phi_l^*(r')\phi_k(r')\frac{1}{|r-r'|}\phi_l(r)\,, \tag{4.12}$$

which has purely quantum mechanical origins. This potential can be computed directly only for simple cases such as the spherically symmetric atoms or for the free electron gas.

Exchange-correlation potential

The Hartree-Fock approximation introduced the exchange potential $V_x(r)$ and its corresponding exchange energy E_x, which is however often not sufficient to give the exact energy of a system [262]. The difference of the Hartree-Fock energy to the exact value is called the correlation energy E_c. Since both E_x and E_c have quantum mechanical origins (and E_x is usually not directly calculable) they are often treated as one single term, called the exchange-correlation energy (E_xc). There are two different ways to determine this energy contribution:

- **Local density approximation (LDA)**
  The LDA is based on the assumption (and simplification) that the electron density is distributed homogeneously in space, for which the exchange potential is known. Even though this assumption is far from reality (covalent bonds have a strong direction dependent electron density), it gives rather good agreements with exact potentials [263, 264].
- **Generalized gradient approximation (GGA)**
  The GGA exchange-correlation potentials describe an electron density that changes spatially. Different implementations of the GGA are possible, but the most widely used one is the one from Perdew, Burke and Ernzerhof (PBE) [265].

LDA and GGA potentials generally give slightly different results. The LDA usually underestimates lattice parameters, whereas GGA tends to overestimate those [266]. Furthermore, the ferroelectric distortion of the B-site ions in perovskites depend on the potentials [267, 268]. Within this work the LDA is used exclusively to sustain the comparability with the work of Gröting [92].

Thomas-Fermi-Dirac

In the late 1920ies, Thomas, Fermi and Dirac (TFD) proposed a scheme to solve the SE which is similar to modern DFT. They introduced the electron density (instead of individual orbitals), but used the free electron gas for the kinetic and the exchange energy parts of the Hamiltonian. The Hamiltonian reads [261]:

$$E_{\mathrm{TFD}}[n] = T_{\mathrm{HEG}}[n] + E_{\mathrm{ext}}[n] + E_{\mathrm{H}}[n] + E_{\mathrm{LDA-x}}[n]\,, \tag{4.13}$$

with

$$T_{\mathrm{HEG}}[n] = \frac{3}{10}(3\pi^2)^{2/3} \int d^3r n^{5/3}(r) \tag{4.14}$$

and

$$E_{\mathrm{LDA-x}}[n] = -\frac{3}{4}\frac{3}{\pi}^{1/3} \int d^3r n^{4/3}(r) \tag{4.15}$$

and $E_{\mathrm{H}}[n]$ as in Eq. 4.8.
This Hamiltonian however fails to reproduce correct values, since the error of the kinetic part is too large. Therefore this ansatz is not used in today's DFT calculations.

Hohenberg-Kohn theorems

In 1964 Hohenberg and Kohn derived the two basic theorems of DFT [261]:

- **Theorem I**

  The ground state electron density $n_0(\mathbf{r})$, which is obtained from the ground state wave function $\Psi_0(\mathbf{r})$, uniquely determines the external potential $V_{\mathrm{ext}}(r)$.

- **Theorem II**

  For any external potential $V_{\mathrm{ext}}(r)$ an energy functional $E[n(r)]$ can be given that minimizes the energy globally for the ground state with the density $n_0(\mathbf{r})$.

These theorems state that the ground state electron density $n_0(\mathbf{r})$ determines the whole system (including the external potential $V_{\mathrm{ext}}(r)$) and vice versa that $V_{\mathrm{ext}}(r)$ can be related to the ground state energy E_0 of the ground state $n_0(\mathbf{r})$ by minimizing the energy functional $E[n(r)]$.

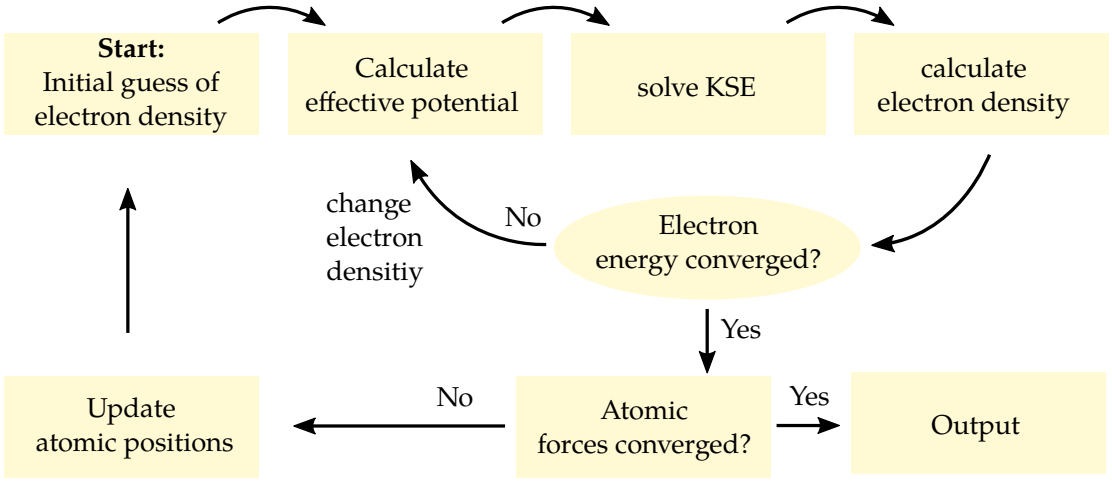

FIGURE 4.2: Electronic and atomic self-consistency cycle in DFT.

Kohn-Sham equation

The Kohn-Sham equation (KSE) is similar to the TFD equation, but the kinetic energy is replaced by the general term $-\boldsymbol{\nabla}^2/2$ and the correlation potential is added to the exchange potential:

$$\left[-\frac{\boldsymbol{\nabla}^2}{2} + V_{\text{ext}}(r) + V_{\text{H}}(r) + V_{\text{xc}}(r)\right]\psi_{\text{KS},i}(r) = \epsilon_i \psi_{\text{KS},i}(r)\,, \tag{4.16}$$

where $\psi_{\mathbf{KS},i}$ are the Kohn-Sham orbitals and the electron density is given by:

$$n(r) = \sum_i \left|\psi_{\text{KS},i}(r)\right|^2\,. \tag{4.17}$$

Solution to the KSE and important parameters

Solutions to the KSE are obtained by electronic self-consistency cycles (**Fig. 4.2**). The initially guessed set of wave functions creates an electron density that interacts with itself and with the surrounding cores. Subsequently, a new set of waves is created, that lowers the electronic energy, until the total electronic energy is converged. In the next step, the positions of the cores are updated according to the forces acting upon them. This scheme is also referred to as "molecular statics", since particles are moving, but without any velocities.
The computational time of the calculations can be reduced when the core electrons are replaced by pseudopotentials, which decrease the total number of electrons in the system and additionally smoothens the electron density close to the core. This reduces the number of waves needed to fit the core electron density. For molecular systems, atomic orbital wave functions are often the preferred choice as initial guesses of the wave functions. Electrons in extended crystals (as in this study) are more easily described with plane waves. Projector-augmented waves [269,270] (which are employed in VASP) are used to keep the

TABLE 4.1: Valence electrons used in the DFT calculations of this work.

Element	Valence electrons
O	$2s^2\ 2p^4$
Na	$2p^6\ 3s^1$
Mg	$2p^6\ 3s^2$
Ti	$3s^2\ 3p^6\ 4s^2\ 3d^2$
Ni	$3p^6\ 3d^8\ 4s^2$
Bi	$5d^{10}\ 6s^2\ 6p^3$

all electron information, but still reduce the roughness of the core electrons. An energy cut-off can be set that determines the number of plane waves that are used as basis set. The higher the energy cut-off, the larger the number of plane waves and thus the more accurate are the results. However, the computational demand increases with the number of plane waves and therefore a trade-off between accuracy and computational time has to be made.
To obtain certain properties, like the electronic density of states, a summation over a certain number of k-points within the first Brillouin-zone has to be evaluated [271]. The higher the number of k-points, the more accurate the resulting values become. But again the computational demand increases (approximately linear) with the number of k-points. The smallest system size that is used in this work consists of 40 atoms, i.e. 8 $A_{1/2}B_{1/2}O_3$ formula units, as was seen in Fig. 3.8. The largest cells consist of 360 atoms. Specific computational parameters are given in each results section and input files for the VASP code (INCAR and KPOINTS) for each individual calculation type are given in the Appendix 12.2.1.

4.1.1 Transition state theory

A major part of this work deals with the kinetics of transitions. These are treated in the framework of transition state theory (TST) [173]. It describes the diffusion or reaction process of individual atoms (or other particles) that require a certain energy barrier E_t to be overcome. For example, Eq. 4.18 gives the jump rate Γ for a particle with mass m in a harmonic minimum with a prefactor of the quadratic energy term (spring constant) of β to jump over a barrier with the height E_t:

$$\Gamma = \frac{1}{2\pi}\sqrt{\frac{k}{m}}\exp\left[\frac{-E_t}{k_B T}\right] . \tag{4.18}$$

The picture of an individual particle jumping from one harmonic minimum to the next is applicable in many cases, such as diffusion of a vacancy within a crystal lattice. For this kind of analysis the energy barrier E_t has to be known, which usually is not. However, energy barriers also exist for processes in which whole structural transitions occur, as sketched in **Fig. 4.3**. The figure shows the reaction path of an octahedral tilt transition in NBT, which switches from an in-phase tetragonal octahedral tilt at R_0 to an anti-phase tilt at R_6. The structure at R_3, which has a tilt angle of 0° has the highest energy E_{max}. To map the reaction path and obtain E_t one often applied method is the "nudged elastic band method", which is explained next.

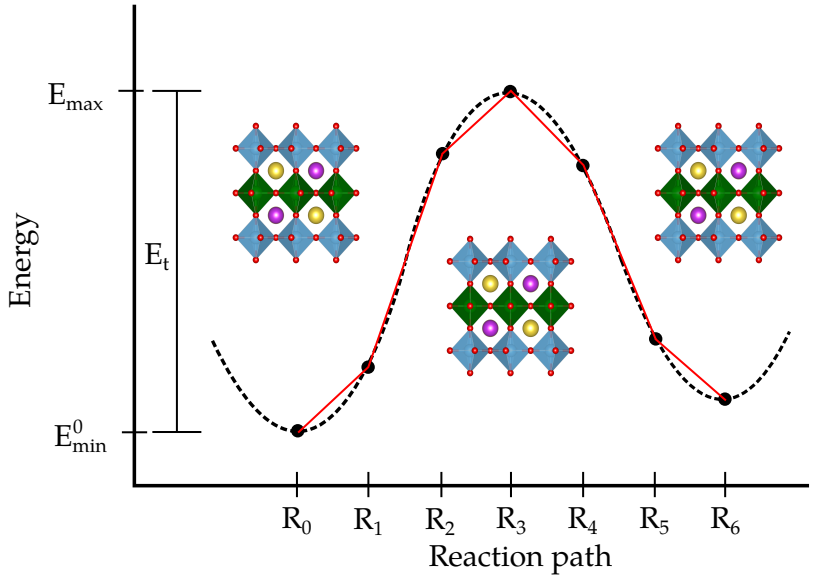

FIGURE 4.3: Sketch of the transition path of an octahedral tilt transformation. The difference between E_{min} and E_{max} gives the transition energy E_{t}.

4.1.2 Nudged elastic band method

The nudged elastic band (NEB) method is a way to determine a transition energy of a certain process. Mapping the reaction can be done by evaluating the energy of different structures along the reaction path, which in the example of **Fig. 4.3** is a stepwise rotation of the oxygen octahedra within the green colored layer. Along the reaction path coordinates R_0 to R_6 the structure transforms from tetragonal anti-phase to tetragonal in-phase. However, a relaxation of the structures at any coordinate along the reaction path would end in one of the ground state structures at R_0 and R_6 (a structure at exactly R_3 would be stable, since no forces are acting). To avoid this undesired relaxation, the NEB method is employed. [272, 273] Virtual springs (red in **Fig. 4.3**) between the structures (also called images) introduce a force upwards the energy gradient and keeps the structures equally spaced along the reaction path.
Fig. 4.4 is taken from Sheppard *et al.* [273] and gives an energy landscape that explains the concept of the NEB method in more detail. Additional to the force $\boldsymbol{F}_i^{\nabla}$ that drives image i down the gradient of the energy landscape, new forces are introduced. The spring force $\boldsymbol{F}_i^{s\parallel}$ is directed along the spring towards the neighboring structure with the higher energy. The calculation is converged when the total NEB force

$$\boldsymbol{F}_i^{\text{NEB}} = \boldsymbol{F}_i^{s\parallel} + \boldsymbol{F}_i^{\nabla\perp} \tag{4.19}$$

becomes zero for each image. $\boldsymbol{F}_i^{\nabla\perp}$ is the gradient force perpendicular to the path, defined as

$$\boldsymbol{F}_i^{\nabla\perp} = \boldsymbol{F}_i^{\nabla} - (\boldsymbol{F}_i^{\nabla} \cdot \hat{\boldsymbol{\tau}}_i)\hat{\boldsymbol{\tau}}_i \,, \tag{4.20}$$

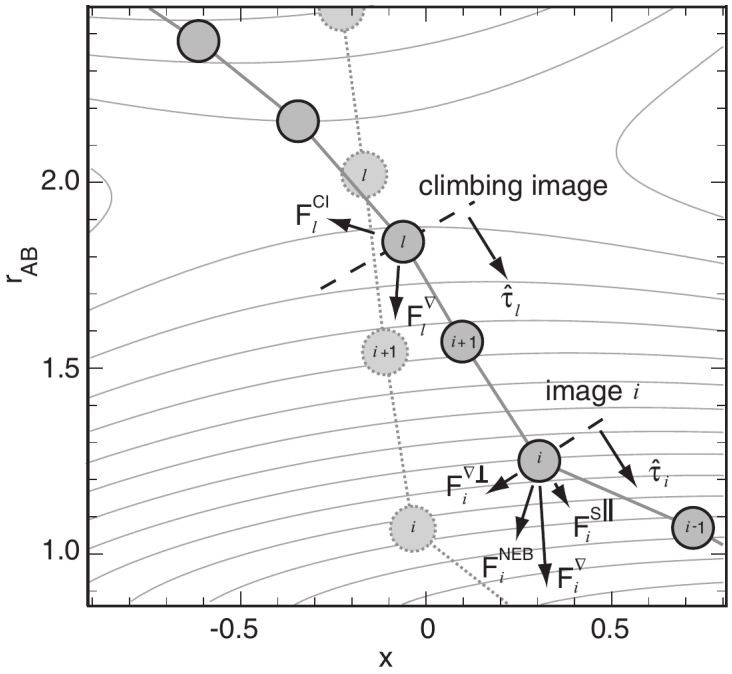

FIGURE 4.4: Sketch of the nudged elastic band method for determination of the transition path. Reprinted from the Journal of Chemical Physics 136, D. Sheppard, P. Xiao, W. Chemelewski, D. D. Johnson and G. Henkelman, A generalized solid-state nudged elastic band method (2012) with the permission of AIP Publishing [273].

where $\hat{\boldsymbol{\tau}}$ is an unit vector upwards the reaction path. The force $\boldsymbol{F}_i^{\nabla\perp}$ drags the image down the energy landscape. The image can, however, not relax into the energetic minimum, since the distances between the images is kept constant via the spring force

$$\boldsymbol{F}_i^{s\parallel} = s(|\Delta\boldsymbol{R}_+| - |\Delta\boldsymbol{R}_-|)\hat{\tau}_i \,, \tag{4.21}$$

with $\Delta\boldsymbol{R}_+ = \boldsymbol{R}_{i+1} - \boldsymbol{R}_i$ and $\Delta\boldsymbol{R}_- = \boldsymbol{R}_i - \boldsymbol{R}_{i-1}$ being the distance to the neighboring images. Thus, the NEB method not only provides E_t, but also gives detailed information on the energy landscape for the whole transition path. This method is often used in molecular statics and molecular dynamics simulations.

4.2 Molecular dynamics

Molecular dynamics simulations are used to study the time evolution of a system at finite temperatures. It it used to investigate the kinetics of NBT , but also the ECE. The idea of this technique is to solve the equation of motion of classical mechanics. To set up the equation of motion, the energetic contributions U (potentials) have to be known, from which the forces

$$\mathbf{F}_i = -\boldsymbol{\nabla}_i U(\mathbf{R}_i) = m\mathbf{a}_i \tag{4.22}$$

on the particles at positions R_i of the system can be calculated. The particles can either be atoms, molecules, chemical groups or more abstract objects, like polarization vectors, as used for determining the ECE.

Ab initio molecular dynamics

Ab initio molecular dynamics simulations are performed in a similar way as classical molecular dynamics simulations. However, the forces acting on the cores are calculated from the Hellman-Feynman forces [261]:

$$\mathbf{F}_I = -\frac{\partial E}{\partial \lambda} = -\langle \Psi_\lambda \left| \frac{\partial H}{\partial \lambda} \right| \Psi_\lambda \rangle - \frac{\partial E_{cc}}{\partial \lambda} \,, \tag{4.23}$$

where λ is any parameter of the Hamilton (such as atomic coordinates) and E_{cc} is the Coulomb energy between cores. For a given configuration of atoms, the forces on each atom are calculated by solving the SE, which then results in a change of the respective velocities. This type of molecular dynamics is called Born-Oppenheimer MD.

Effective Hamiltonian

A perovskite ABO_3 material has five atoms within its unit cell. Therefore, the number of degrees of freedom of this unit cell is $5 \times 3 = 15$ (in three dimensions). To reduce the number of degrees of freedom, an effective Hamiltonian can be set up. This approach was developed by King-Smith, Rabe, Vanderbild, Waghmare and Zhong in the 90ies [274–277]. The idea is to replace the five atoms of the unit cell by one polarization vector (a ferroelectric soft mode) and one acoustic vector (for all displacements that do not produce any polarization), each with tree coordinates. Therefore, the number of degrees of freedom are therefore reduced from 15 to 6. One possible way of writing the total energy of the system is, as implemented in the code "feram" (developed by Nishimatsu [278–280]):

$$\begin{aligned} U(\mathbf{R}_i) \rightarrow U^{\text{eff}}(\{\mathbf{u}\},\{\mathbf{w}\},\eta_1,\ldots,\eta_6) = {} & \frac{M^*_{\text{dipole}}}{2}\sum_{i,\alpha}\dot{\mathbf{u}}^2_{i,\alpha} + \frac{M^*_{\text{acoustic}}}{2}\sum_{i,\alpha}\dot{\mathbf{w}}^2_{i,\alpha} \\ & + V^{\text{self}}(\{\mathbf{u}\}) + V^{\text{dpl}}(\{\mathbf{u}\}) + V^{\text{short}}(\{\mathbf{u}\}) \\ & + V^{\text{elas, homo}}(\eta_1,\ldots,\eta_6) + V^{\text{elas, inho}}(\{\mathbf{w}\}) \\ & + V^{\text{coup, homo}}(\{\mathbf{u}\},\eta_1,\ldots,\eta_6) + V^{\text{coup, inho}}(\{\mathbf{u}\},\{\mathbf{w}\}) \,, \end{aligned} \tag{4.24}$$

with the polarization vector $\boldsymbol{u}$ and the acoustic vector $\boldsymbol{w}$. The parts of the effective Hamiltonian are: the (self) energy of the ferroelectric soft mode, the long- and short-range dipole-dipole interaction energy, the elastic energy and the energy due to the coupling between the local soft modes and the strain. Parameters for this Hamiltonian are obtained from DFT calculations and thus this MD approach can be called first-principles effective MD. Details on the Hamiltonian and its parameters are given in the studies of Paul *et al.* and Nishimatsu *et al.* [278,279,281]. feram simulation are currently restricted to simple ferroelectrics (like BT), without octahedral tilts.
The conventional choices for interatomic potentials include two-body or many-body potentials. These however to not include any electrostatic contributions to the total energy.

To describe more complex systems, other potentials can be used. The "shell model" takes electrostatic interactions of charged atoms into account [282]. Therein a spring between the charged (ionic) core and (electron) shell is implemented and thus this model allows to simulate polar entities. The parameters that are needed can be obtained from DFT calculations. However, the equation of motion for each spring introduces new degrees of freedom and therefore the computational cost is increased. Another more sophisticated description of the energetic contributions is implemented in the bond-valence model, as explained in Refs. [283–287]. This model is able to describe complex systems like $PbTiO_3$ and $BiFeO_3$, which exhibit octahedral tilts and displacements of the A-cations due to the lone-pair of Bi and Pb. It has so far been used to study phase transitions, but in theory would be able to provide information about the ECE even in more complex systems, which exhibit octahedral tilting.
The probability of the initial velocities are chosen from the Maxwell-Boltzmann-distribution

$$p(v) \propto \exp(-mv^2/2k_\mathrm{B}T)\ . \tag{4.25}$$

The evolution in time can be calculated by the integration of the equation of motions with a time step of Δt. Several implementations of the time integration exist [288, 289].

1. **Verlet**

   The atom positions are calculated from the current position, the positions at the last time step and the current forces acting on the atoms. However, only when the coordinates of the new positions $\mathbf{r}(t+\Delta t)$ are known, the velocities $\mathbf{v}(t)$ are computed:

$$\mathbf{r}(t+\Delta t) = 2\mathbf{r}(t) - \mathbf{r}(r-\Delta t) + (\Delta t)^2\mathbf{a}(t)\ , \tag{4.26}$$

$$\mathbf{v}(t) = \frac{\mathbf{r}(t-\Delta t) - \mathbf{r}(t+\Delta t)}{2\Delta t}\ . \tag{4.27}$$

2. **Leap-frog**

   The leap-frog method (which is implemented in the MD code feram [280]) evaluates the positions and velocities at different points in time, separated by half a time step. This still does not give the velocities at the current time step, but allows for a simpler code implementation [288]:

$$\mathbf{r}(t+\Delta t) = \mathbf{r}(t) + \Delta t\mathbf{v}(t+\Delta t/2)\ , \tag{4.28}$$

$$\mathbf{v}(t+\Delta t/2) = \mathbf{v}(t-\Delta t/2) + \Delta t\mathbf{a}(t)]\ . \tag{4.29}$$

3. **Velocity Verlet**

   The velocity Verlet method is one of the most widely used integration schemes, as it enhances the numerical stability:

$$\mathbf{r}(t+\Delta t) = \mathbf{r}(t) + \Delta t\mathbf{v}(t) + (\Delta t^2)\mathbf{a}(t)/2\ , \tag{4.30}$$

$$\mathbf{v}(t+\Delta t) = \mathbf{v}(t) + \Delta t[\mathbf{a}(t+\Delta t) + \mathbf{a}(t)]/2\ . \tag{4.31}$$

Simulations can be run in different ensembles, with different constant thermodynamic variables. The most natural ensemble from a computational side is the "microcanonical" one, in which the sum of kinetic and potential is kept fixed. Within this ensemble the energy ratio between the vibrational to the potential part can vary and thus the temperature of the system is not constant.
In reality, usually the temperature is the variable that is kept fixed, not the energy. This scenario is achieved in a "canonical" ensemble. To maintain the desired temperature in a canonical ensemble, a thermostat has to be used. Again various implementations have been developed over time and some of those are described here shortly [289]:

- **Andersen-thermostat**

  At each n^{th} time-step, the velocity of a random particle is replaced by one drawn from the Maxwell-Boltzmann distribution of Eq. 4.25 at the target temperature [290]. The disadvantage of this stochastic type of thermostat is its bad efficiency and that dynamic quantities, like diffusion coefficients cannot be determined [289].

- **Nosé-Hoover-thermostat**

  In contrast to the stochastic rescaling of the velocities after some time, like in the Andersen thermostat, a friction term $\xi(r, v)$ is added to the real system Hamiltonian to obtain the Nosé-Hoover thermostat [289,291]. The Lagrangian of the Nosé-Hoover thermostat is given by [292, 293]:

$$H_{\text{NH}} = \sum_i \frac{\mathbf{p}_i^2}{2m_i} + V(r) + \frac{\xi_s^2 m_v}{2} + 3Nk_{\text{B}}T \ln s \ , \tag{4.32}$$

  where the first two terms are the real system and the last two terms belong to a fictional oscillator with the virtual mass m_v and the degree of freedom s. This formulation leads to a new (non-Hamiltonian) set of equations of motion, which can be solved by a modified velocity Verlet integration [294].

For the investigation of the ECE, first-principles based molecular dynamics simulations have been used in many studies. The studied materials included PZT [295], BZT [296], BST [221, 297] and PZ [298]. Recently, the ECE of BT, PT, $KNbO_3$ (KN) was studied in nanowires [299]. These nanoscale systems reduced the achievable ECE, but shifted the phase transition temperature and therefore the temperature with the maximum EC temperature change. The feram code was used to study the ECE in BT [300–302]. Marathe *et al.* showed with help of the feram code that the indirect and direct method give the same temperature changes, when the temperature at which the first order phase transition appears is excluded [303]. Further was the feram code used to inspect the influence of strain on the phase transitions of BT [225, 304]. First computational studies on the influence of defect dipoles on the ECE have been performed, where a negative EC temperature change could be observed [31]. Additionally, Ma *et al.* showed that a qualitative agreement between the MD and MC models (explained in the next section) of the ECE exists [31].

The "feram" code allows for the direct and indirect calculation of the ECE (see next section). Since the indirect method is very sensitive to the chosen heat capacity and the numerical integration of Eq. 3.8 [240], only the direct method is used. The ECE temperature change is obtained by removing an external field. The system is equilibrated at a fixed temperature and fixed electrical field in the canonical ensemble. After the adiabatic removal or application of the electrical field the temperature change is calculated in a microcanonical ensemble. An instantaneous switching of the electric field is used in the MD simulations. Although switching rates in reality take a finite time, the results of different ramping rates are in good qualitative agreement [303]. By ramping the field and long equilibration times, the system can overcome possible energy barriers due to domain switching. The applied electric field of $100\,\mathrm{kV\,mm^{-1}}$ of this study is high compared to studies on bulk materials [227]. These high fields are comparable to fields used in studies on thin or thick films, which have large dielectric strengths [227]. An input file for a canonical run at $E = 100\,\mathrm{kV\,mm^{-1}}$ is taken and modified from Ref [280] and given in Appendix 12.2.2.

4.3 Monte Carlo simulations

Monte Carlo (MC) simulations are used in this work to study the ECE. In MC simulations the properties of a system are obtained after a large number of occurring events that result in an equilibrated configuration. The system can consist of atoms, but also other more abstract entities (like polarization vectors in this work). During the simulations the events occur with a certain probability. From MC simulations it is easy to obtain properties that arise from the configurational arrangement of the investigated entities. However, it is not straightforward to gather any information of the dynamics of the system. The configurational energy of the system is a sum of all energetic contributions, similar to the Hamiltonian in the case of molecular dynamics, as seen in Sec.4.2.
In our case, we employ a simple lattice-based model that is similar to the Ising model of interacting neighboring spins [305]. The configurational energy

$$U_{\mathrm{conf}} = -\sum_{ij} J_{ij}\boldsymbol{P}_i\boldsymbol{P}_j - \sum_i \boldsymbol{E}\boldsymbol{P}_i - \sum_i \boldsymbol{h}_i\boldsymbol{P}_i \tag{4.33}$$

depends on the polarization P_i at lattice site i, the external electric field $\boldsymbol{E}$, the strength of the random field h_i at lattice site i, and the interaction strength J_{ij} (the Ising parameter) between the two sites i and j. The lattice extends in three dimensions (N×N×N). In contrast to the original Ising model that limits the polarization to be along one direction, the polarization vectors in this model can align along the six directions $\pm x, \pm y$ and $\pm z$. Therefore, this model is referred to as Ising-like. Additionally, random fields can be introduced, which are electric fields that vary for each individual lattice site. These random fields thus add an extra inhomogeneity to the system, as was already discussed in Sec. 3.3, and should allow to model relaxor-like properties. From this setup the EC temperature change can be obtained in three different ways [240], from which two (Metropolis and Creutz) are explained in more detail.

- **Metropolis algorithm (indirect method)**

  The indirect method uses Eq. 3.8 to obtain the temperature change ΔT. Changes of the polarization vectors are determined by the Metropolis algorithm. The probability p of an event to happen is related to the Boltzmann-statistics [289]:

$$p = \begin{cases} 1 & \text{if } \Delta U \leq 0 \\ \exp\left(\frac{-\Delta U_{\text{conf}}}{k_B T}\right) & \text{if } \Delta U > 0 \end{cases}, \tag{4.34}$$

  where $\Delta U = U_\beta - U_\alpha$ is the difference in energy between an initial α and final configuration β, before and after the event. This algorithm was first described by Metropolis *et al.* [306] and it fulfills the requirements of statistical physics that every possible configuration of a system can be reached with a certain probability.

  A simple Metropolis Monte Carlo scheme was set up by Alexander Stukowski and continued by Constanze Kalcher [240]. This code allows to calculate the EC temperature change of a lattice-based system containing electric dipoles. Since the polarization is a direct output of the simulations, the difficult part is to find the right value for the heat capacity c and the integration of Eq. 3.8. Often a constant heat capacity is chosen, which however gives an overestimation of the temperature change [240]. The capacity is calculated from the derivative of the energy with respect to the temperature. The calculations are performed in a canonical ensemble, in which the temperature is kept fixed.

  A substantial problem of the indirect method is that it fails at the first order phase transition, where the heat capacity of the material becomes infinite.

- **Creutz algorithm (direct method)**

  To avoid the difficulty of first order phase transitions and the determination of the heat capacity, the direct method to obtain the ECE can be applied. For this, the simulation is switched to a microcanonical constant energy ensemble and an additional energy term is introduced. This term is called "demon"-energy and mimics the kinetic energy of the lattice [307]. Since the kinetic energy of one lattice site is proportional to $f k_B T/2$, the number of demons is $15/2 \cdot \text{N}\times\text{N}\times\text{N}$ and each demon contains $k_B T$ in energy. The simulations will then run as usual, however when a polarization flip occurs, instead of checking the Metropolis equation 4.34, one demon is chosen randomly and when the energy of the demon is higher than the energy required for the flip, it is performed. The energy of the demon is lowered according to the used energy. At the end of the simulations one obtains a distribution of demon energies, which allows to determine the temperature change.

  During the simulations the total energy (energy of the system containing the polarizations and energy of the demons) is constant. The energy is only transferred between the demons and and the polarizations, thus the algorithm runs within a microcanonical ensemble.

As a side note, many equations and explanations from above can also be used to model the magnetocaloric effect (MCE) [308–310]. The MCE has been studied more extensively than the electrocaloric effect and recently two books have been published, dedicated purely to the MCE [311, 312].

5 Kinetics of phase transformations

Parts of this chapter have been published in Journal of Solid State Chemistry [194] and in Journal of the American Ceramic Society [313].

This chapter deals with the kinetics of NBT on an atomistic scale. We want to find out what PNRs consist of and how they come into existence. This involves the question, whether PNRs appear as nuclei within a matrix or the structural transition is a collective transformation process of an extended region. To investigate this aspect it is important to explore the energy landscape of NBT for the various tilt phases and the transformations between those. This is also interesting in the context of phase transformations, which are still a topic of debate in literature. We expect to learn why NBT acts differently on a local scale and on an averaged long-range scale, which ultimately results in a macroscopic relaxor behavior. Also of interest is to investigate how it is possible that different phase transition paths have been suggested over time.
The term "phase transition" that is used in literature, typically refers to the context of differences in the free energy of the individual phases. However, from here on we use the term "phase transformation" to stress that the focus of this work is on the kinetic pathway and atom movements that are involved in a phase transition.
First, we study the transformation energies to transform one phase to another by static and nudged elastic band calculations. These calculations are complemented by *ab initio* molecular dynamics simulations. By obtaining these information, we are able to get a picture of the energy landscape related to the octahedral tilts. In a second step, the picture of the global energy landscape is further enlightened by studying the displacement of A-cations. In the last step, we investigate tilt defect clusters, especially their defect formation energies and how they act as onsets for phase transformations.

5.1 NBT structures

Chemical order

One of the first tasks to be solved when investigating NBT, is to decide which A-site chemical order should be used in the following calculations. Gröting *et al.* studied all six possible A-cation configurations in **Fig. 5.1** with a cell size of eight f.u. [92, 96]. It turned out that the rock salt arrangement (111-order) has the highest energy and the layered arrangement (001-order) has the lowest energy for all octahedral tilt configurations. The four other A-cation orders have energies which lie in between the values of the 111- and 001-order [96]. Within this work only the 111- and 001-order are investigated and compared.

Tilt phases

Figs. 5.2 and **5.3** depict the four tilt configurations which are used within this study, with view along the [100]-direction and [001]-direction. In the top left the tetragonal structure with an in-phase tilt along the [001]-direction is shown. For easier description all phase are labeled with single letters and the tetragonal in-phase tilt structure is labeled as (T^+).

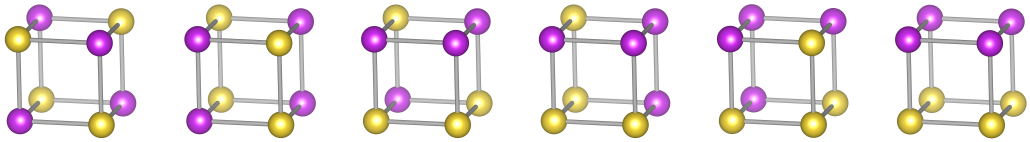

FIGURE 5.1: The six possible orderings of Bi and Na on the A-cation sublattice in NBT, after Ref. [96].

The top right figures show the tetragonal anti-phase tilt structure $a_0^0a_0^0c_0^-$ (T^-) which has an anti-phase tilt along the [001]-direction. Again, the structure does not have any polarization. The third structure is orthorhombic (O) with the tilt configuration $a^-a^-c_0^+$ (bottom left in **Figs. 5.2** and **5.3**). Along the [100]- and [010]-direction the tilts are in anti-phase, but along the [001]-direction they are in-phase. This structure exhibits a polarization, because of the off-centering of the Ti ion and the displacement of the A-cations along the [110]-direction. The last structure, which is shown in the bottom right of **Figs. 5.2** and **5.3**), has a rhombohedral (R) symmetry and the tilt configuration $a^-a^-a^-$. It, too, has a polarization, which is along the [111]-direction. Detailed information on the used structures are given in Appendix 12.1. All space groups (T^+: *P4/mbm*, T^-: *I4/mcm*, O: $Pmn2_1$ and R: *R3c*) are given in the high symmetry configuration (no A-cation order). The superscripts of the labels of the tetragonal T^+ and T^- phases indicate the in-phase and anti-phase tilt patterns. A tetragonal anti-phase T^- structure has not been reported in literature, but our calculations suggest that this tilt configuration is equally likely to occur as the in-phase tetragonal T^+ structure.

5.2 Octahedral tilt transformations – Tetragonal

Computational setup

A 600 eV plane wave energy cut-off was set and ionic positions were optimized until the forces reached less than 0.01 eV/Å. For the calculations an 8×8×8 Γ-centered Monkhorst-Pack k-point mesh [271] per one formula unit (f.u., $A_{1/2}A'_{1/2}BO_3$, i.e. one octahedra) was used, which results in a 4×4×4 mesh for a 40 atoms supercell (eight octahedra). For determination of the transition energies the NEB method was used, with five images in the section for the simple tetragonal case and eleven images for the comprehensive case with all tetragonal, orthorhombic and rhombohedral phases. The electronic valance configurations are given in **Tab. 4.1**.

Tilts of individual oxygen octahedra layers

The most simple implementation of a tilt transformation is to tilt a complete layer of octahedra in a 2×2×2 supercell. As a first variant tilt transformations from the tetragonal in-phase T^+ (**Fig. 5.4a**) to the anti-phase T^- (**Fig. 5.4c**) structure are examined. **Fig. 5.4b** shows an intermediate tilt configuration where the layer of tilted octahedra (green highlighted layer) has a tilt angle of 0°. By stepwise tilting of the octahedra from 13° of the T^+ to -13° of the T^- phase transformation energies are obtained that are plotted in **Fig. 5.5**. It

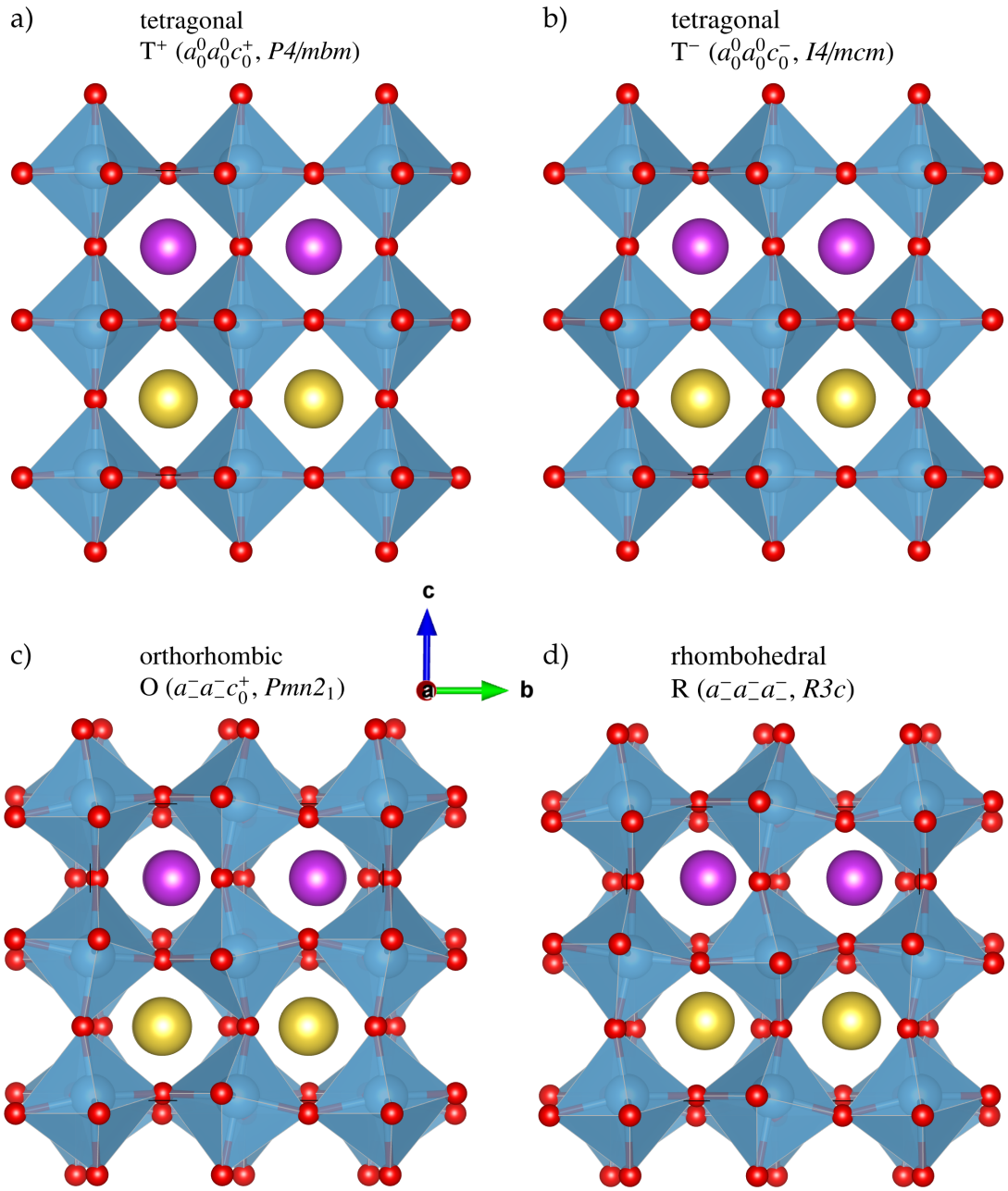

FIGURE 5.2: The four investigated tilt configurations, viewed along the [100]-direction. **a)** tetragonal $a^0_0a^0_0c^+_0$ (T^+), **b)** tetragonal $a^0_0a^0_0c^-_0$ (T^-), **c)** orthorhombic $a^-_-a^-_-c^+_0$ (O) and **d)** rhombohedral $a^-_-a^-_-a^-_-$ (R).

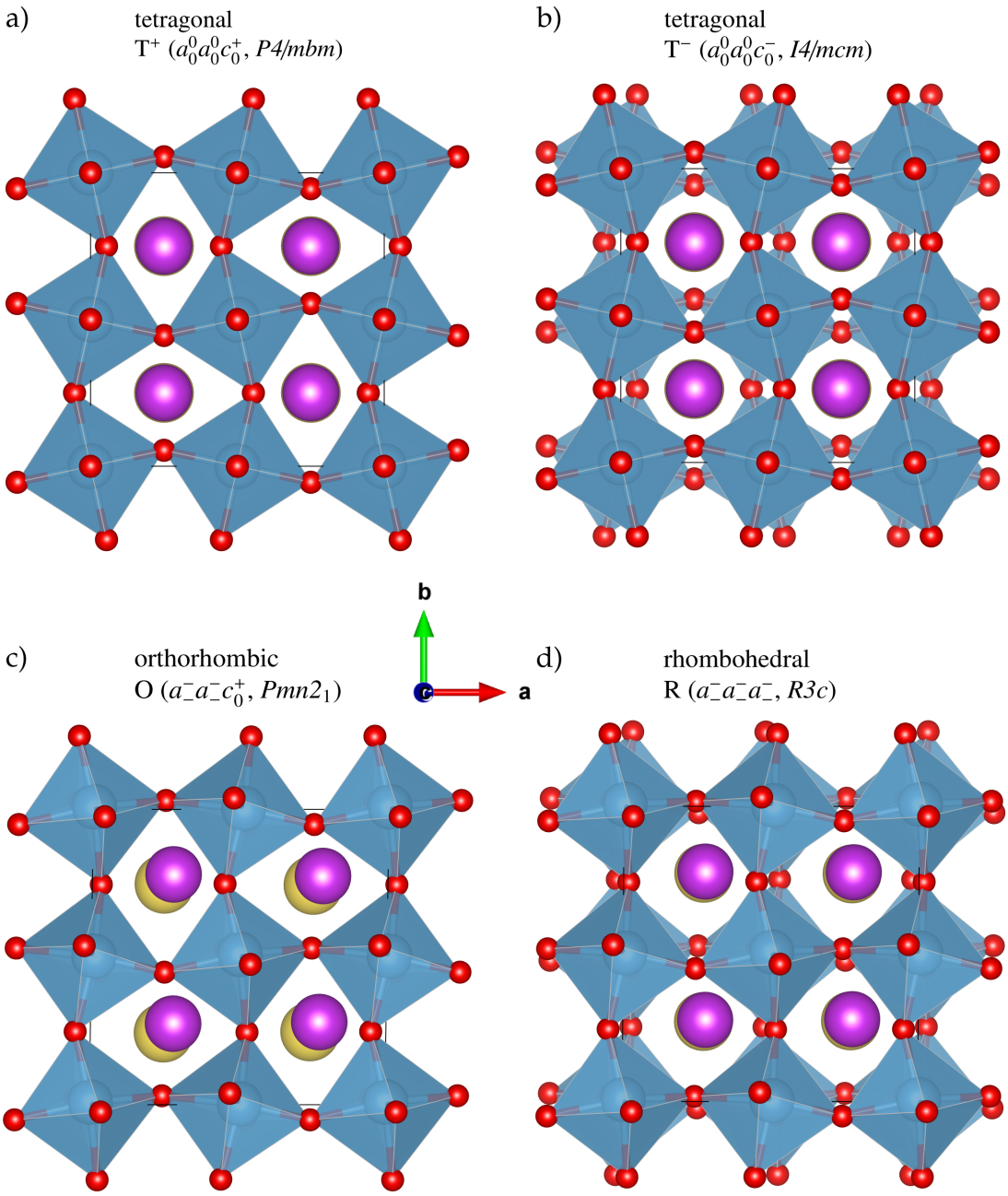

FIGURE 5.3: The four investigated tilt configurations, viewed along the [001]-direction. **a)** tetragonal $a_0^0a_0^0c_0^+$ (T^+), **b)** tetragonal $a_0^0a_0^0c_0^-$ (T^-), **c)** orthorhombic $a^-a^-c_0^+$ (O) and **d)** rhombohedral $a^-a^-a^-$ (R).

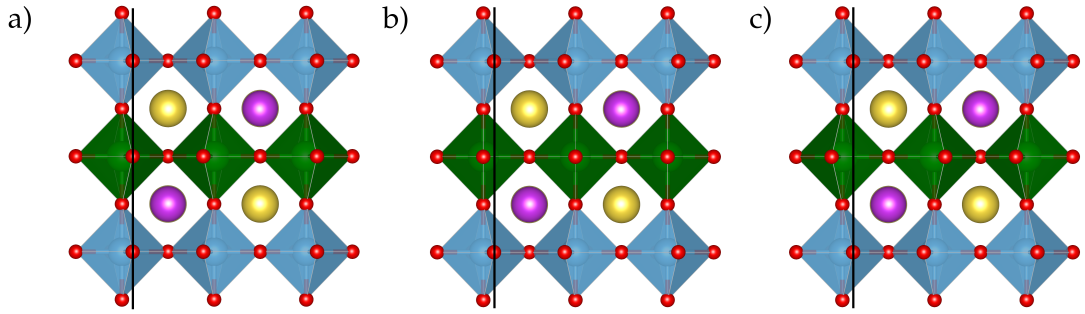

FIGURE 5.4: Illustration of the stepwise transformation from the **a)** tetragonal $a^0a^0c^+$ in-phase to the **c)** tetragonal $a^0a^0c^-$ anti-phase tilt configuration via an **b)** intermediate mixed tilt configuration. Lines are a guide to the eyes for an easier comparison of the tilt angles.

depicts the energies per formula unit (with one octahedron per f.u.) relative to the T^+ energy. This calculation can be done statically (no ion relaxation) and within NEB calculation (ion relaxation is constrained, but allowed). Additionally, the 111-order and 001-order are compared. Several conclusions can be drawn:

1. The ground state energies of both T^+ and T^- structures with 001-order are lower than the 111-order configurations, which has already been reported by Gröting *et al.* [96].
2. The energy barriers in the structures with 001-order are lower for the ones for 111-order by about 20% in the unrelaxed case (76 meV and 97 meV) and about 30% in the relaxed NEB case (43 meV and 65 meV).
3. The NEB calculations decrease the value of the energy barrier by about 30% compared to the unrelaxed calculations, but the shape of the curve does not change.

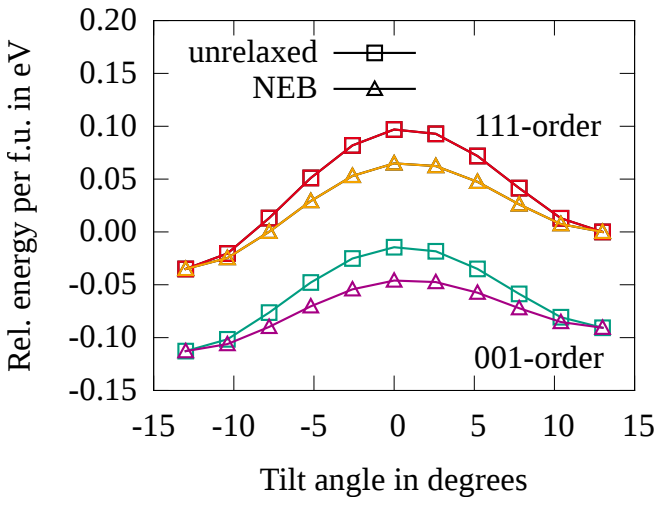

FIGURE 5.5: Comparison of the transformation barriers for the tetragonal $a^0a^0c^+$ in-phase (at 13°) to the tetragonal $a^0a^0c^-$ anti-phase (at -13°) tilt configuration, as displayed in Fig. 5.4, for 111- and 001-order and unrelaxed and NEB calculations. The transformation barriers for the structure with 001-order is smaller than for the one with 111-order by 33%. Relaxed structures exhibit a 30% smaller barrier than the unrelaxed barriers.

The maximum value at 0° is due to the shortened bond length between the titanium and oxygen ions, which leads to an unfavorable packing of the A, B and oxygen ions, as was explained in Sec. 3.2.2 on the Goldschmidt tolerance factor [97].

Tilts of several oxygen octahedra layers

In the previous calculations we have seen that the chemical order plays a role on the height of the tilt transformation energy barrier. Now we investigate whether the energy barrier is influenced by the Bi and the Na-layers. For this set of calculations two adjacent oxygen octahedra layers are tilted simultaneously in a 4×2×2 supercell. In the first case, as it can be seen in **Fig. 5.6a**, the two octahedra layers (green) enclose a Na-layer. In the second case the two layers enclose a Bi-layer, as shown in **Fig. 5.6b**. Again, a transformation between two tetragonal phases is studied. The initial structure is the T^+ tilt phase, however the final states consists of in-phase and anti-phase tilts (mixed tilt configuration).
The transformation energies are given in **Fig. 5.7** for the unrelaxed and NEB relaxed structures. The following conclusions can be drawn:

1. The mixed state configuration is energetically favorable if the enclosed layer consists of Na ions (green and purple).
2. Relaxed NEB calculation again decrease the energies of all structures along the transformation path compared to the unrelaxed structures.
3. Energy barriers at 0° are lower when the enclosed layer is a Na-layer.

Conclusion 1 and 3 can be understood from the point of view that Na and Bi react differently on volume constrains. In the T^+ phase the undisturbed 12-fold bismuth-oxygen cuboctahedron shows bond lengths between 2.38 Å and 2.99 Å. As part of the enclosed

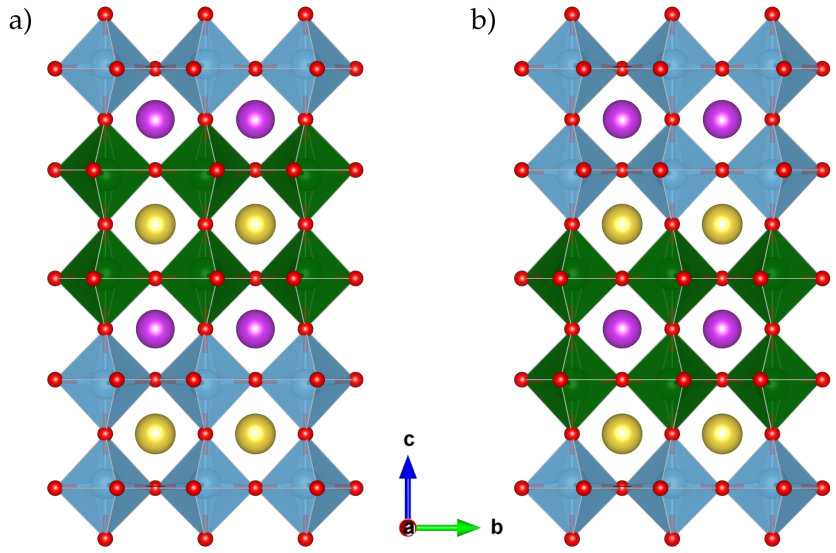

FIGURE 5.6: Tilting of two adjacent layers of oxygen octahedra in a 2×2×4 structure with 001-order. **a)** The two octahedra layers enclose a Na-layer. **b)** The two octahedra layers enclose a Bi-layer.

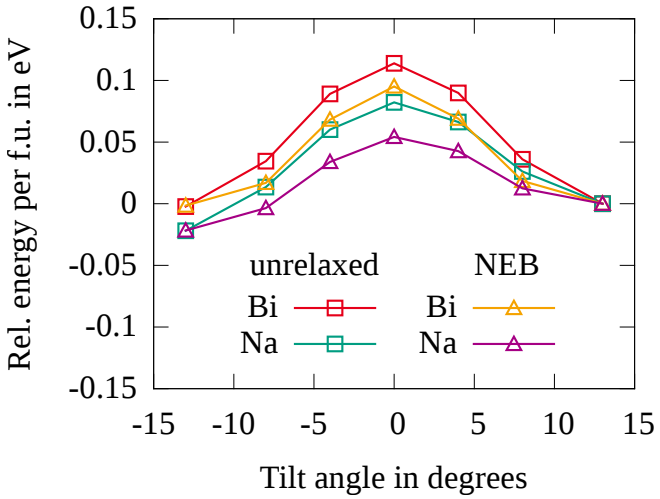

FIGURE 5.7: Transformation energies for two adjacent layers as displayed in Fig. 5.6. Energy barriers are smaller when the enclosed layer is a Na-layer.

layer all bond length are close to 2.66 Å with no deviation from the average bond length and the volumes of the cuboctahdra decrease from 45.97 Å^3 to 44.39 Å^3. A similar effect can be seen for the sodium-oxygen cuboctahdra, where the bond lengths change from (2.48 to 3.07) Å to (2.65 to 2.76) Å. The volumes of the Na cuboctahdra decrease from 49.25 Å^3 to 47.55 Å^3. However, since Bi prefers an asymmetric displacement within the 12-fold cuboctahedron, because of the existence of the 6*s* lone-pair, the energy is higher

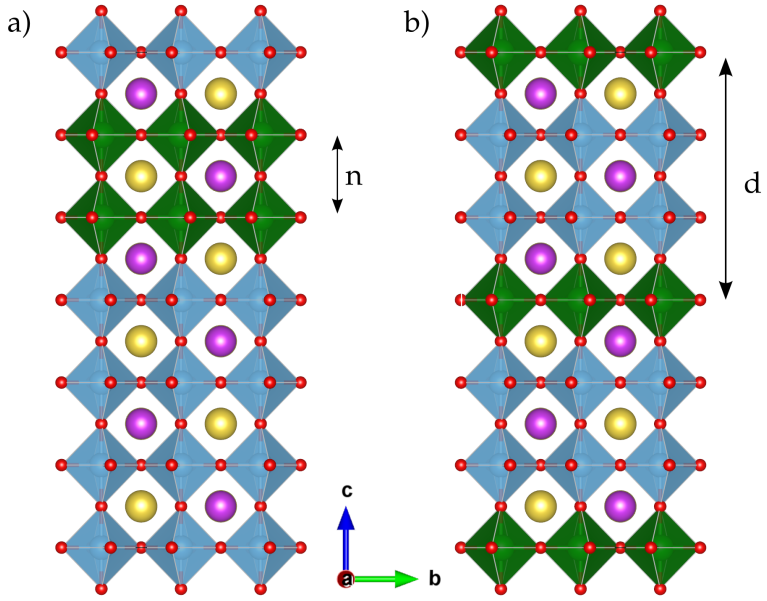

FIGURE 5.8: **a)** 2×2×6 supercell with n simultaneously tilted adjacent layers (green). **b)** 2×2×6 supercell with simultaneously tilted layers (green) which are separated by a distance d. For $d = 2$ the tilt configuration becomes the tetragonal T$^-$ anti-phase pattern.

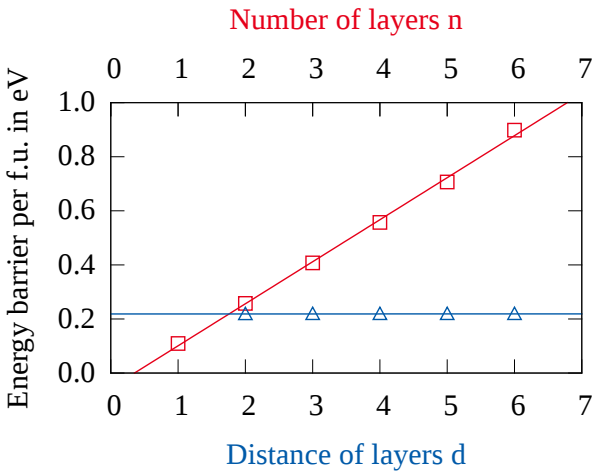

FIGURE 5.9: Energy barrier per f.u. for the 2×2×6 supercells displayed in Fig. 5.8. The red squares show that energy barrier is approximately linear with the number of adjacent tilted layers (Fig. 5.8a). The blue triangles show the independence of the energy barrier on the distance between the simultaneous tilted layers (Fig. 5.8b). The solid lines are a guide for the eyes.

for the Bi enclosed layer. This difference between Bi and Na will reoccur in Sec. 5.6 on the investigations of the A-cation displacements.
To study the transformation energy barriers further, two additional variants of coupled tilted octahedra layers are investigated. We check whether the tiltings of the layers can happen independent of each other, or if the arrangement of neighboring octahedra affect the energy barriers, first by tilting n (from two to six) adjacent octahedral layers simultaneously, as shown in **Fig. 5.8a**. Second, **Fig. 5.8b** depicts two layers of octahedra which are tilted simultaneously, but are separated by d number of layers (also from two to six). Both calculations are performed without ion relaxation.
The energy barriers of these calculation are shown in **Fig. 5.9**. The lines are guides for the eyes. The red squares show a linear dependence of the energy barrier with the number of tilted layers n. By looking at the blue triangles it can be seen that the value of the energy barrier is independent of the distance d between two tilted layers. No additional contributions can be seen, and thus the conclusion is that the tilting of octahedral layers in the tetragonal phases can happen independent of each other and the only contribution to the energy barrier is due to the shortening of the Ti-O bond length.

5.3 Octahedral tilt transformations – All phases

A 600 eV plane wave energy cut-off was set and ionic positions were optimized until the forces reached less than 0.01 eV/Å. For all calculations an 8×8×8 Γ-centered Monkhorst-Pack k-point mesh [271] per one formula unit (f.u., $A_{1/2}A'_{1/2}BO_3$, i.e. one octahedra) was used, which results in a 4×4×4 mesh for a 40 atoms supercell (eight octahedra). For determination of the transition energies the NEB method was used, with five images in the section for the simple tetragonal case and eleven images for the comprehensive case with all phases. The electronic valance configurations are given in Tab. 4.1.

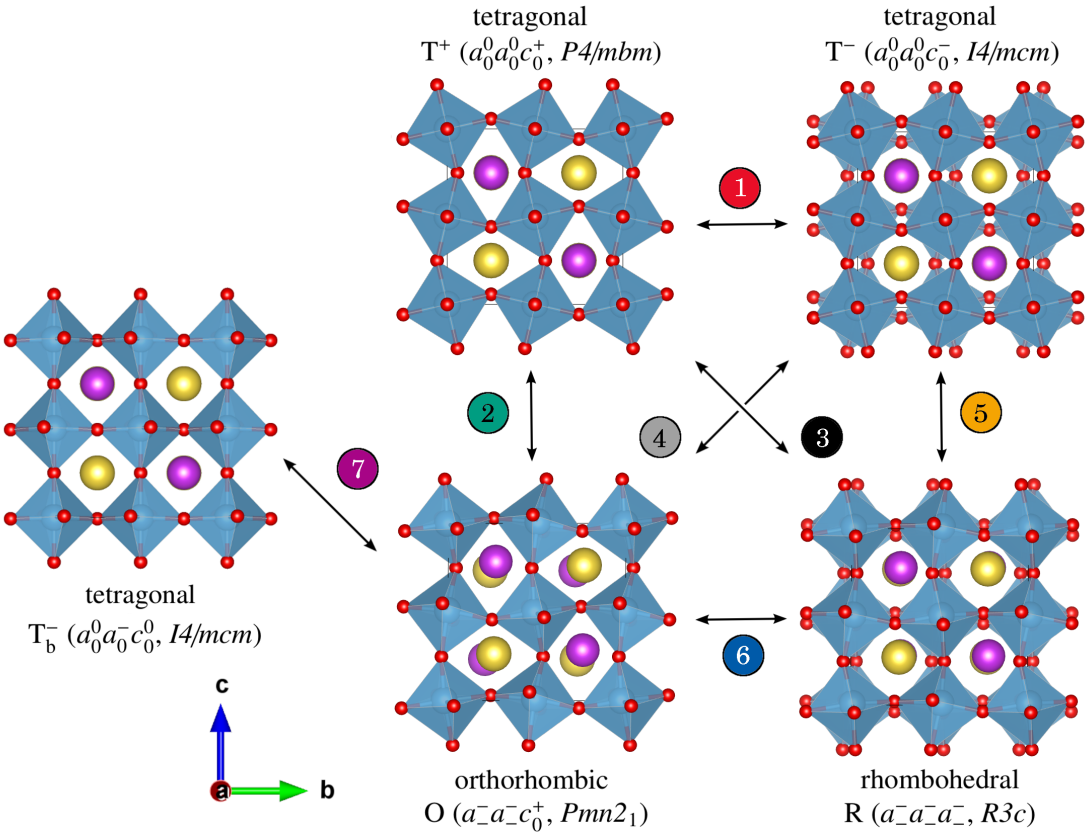

FIGURE 5.10: The five investigated structures (four phases) and transformations between those: tetragonal in-phase T^+ (top-middle), tetragonal anti-phase T^- (top-right), tetragonal anti-phase T_b^- with tilt along the b-axis (left), orthorhombic O (bottom-middle) and rhombohedral R (bottom-right). The phase transformations are marked with numbers: 1) $T^+ \longleftrightarrow T^-$ 2) $T^+ \longleftrightarrow$ O 3) $T^+ \longleftrightarrow$ R 4) $T^- \longleftrightarrow$ O 5) $T^- \longleftrightarrow$ R 6) O $\longleftrightarrow$ R 7) $T_b^- \longleftrightarrow$ O. Colors in the circles correspond to the colors in Figs. 5.11 and 5.17. View along [001]-direction for an 111-order of the A-cations.

In the last section we have seen that the transformation energies in the tetragonal phases are sensitive to the local chemical order, but tilts of separated layers can happen independent of each other. Here, in this section, we extent the study on these energy barriers to the tetragonal, orthorhombic and rhombohedral phases. These structures are depicted in **Fig. 5.10**, with the high temperature tetragonal phases at the top, the intermediate temperature orthorhombic phase at the bottom and the low temperature rhombohedral phase in the bottom right. At the left side a fifth structure is shown with a tetragonal $a_0^0c_0^-a_0^0$ tilt pattern. The subscript of the T_b^- of this structure specifies the axis of the anti-phase tilt, which is along the b-axis, not the c-axis. Each transformation path is labeled with numbers from 1 to 7 and with individual colors for easier recognition. The color coding is consistent with the one from Figs. 5.11 and 5.17. Both 111- and 001-order are studied.
Fig. 5.11 shows the energies of the seven transformation paths of **Fig. 5.10** for both 111- (a) and 001-order (b) relative to the energy per f.u. of the structures with the lowest energy, which is rhombohedral for the 111-order and orthorhombic for the 001-order (see Ref. [89]). The red line (path 1) is the energy barrier between the T^+ and T^- phases have

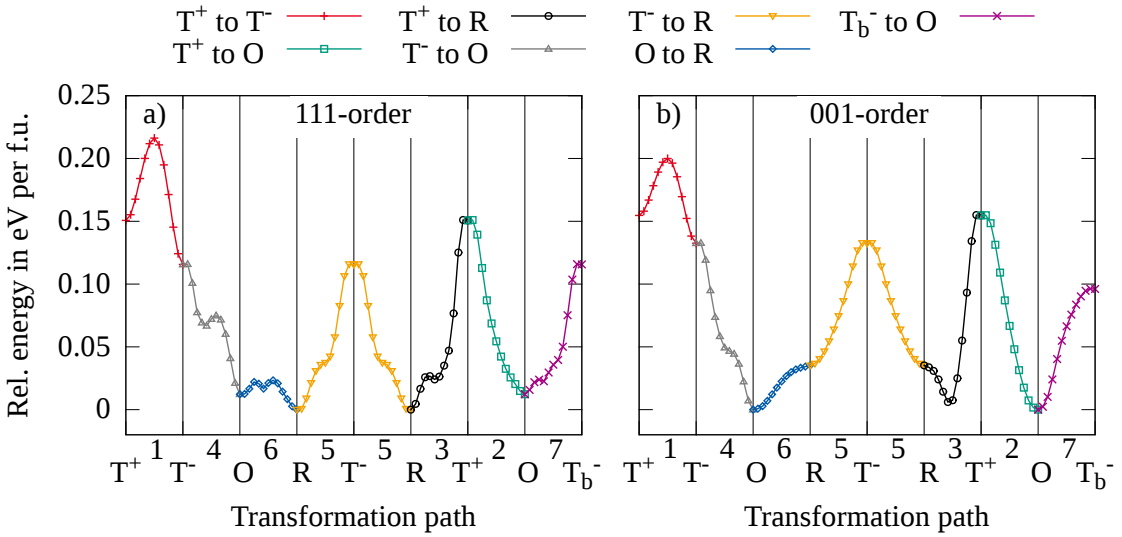

FIGURE 5.11: Energies of the seven transformation paths for **a)** 111-order and **b)** 001-order. Energies are relative to the structure with the lowest energy, which is rhombohedral for 111-order and orthorhombic for 001-order. Colors are the same as in Figs. 5.10 and 5.17. Metastable structures are marked with arrows.

already been shown in Sec. 5.2. Interestingly, path 1 is the only one with a high energy barrier of about 0.065 eV. Most of the other paths show a monotonic decrease or increase in energy when moving along the transformation path. Five paths show exceptions from this monotonic behavior. The first four paths with 111-order in **Fig. 5.11a** are: $T^- \longleftrightarrow O$ (gray, path 4, point A), $O \longleftrightarrow R$ (blue, path 6, point B), $T^+ \longleftrightarrow R$ (black, path 3, point C) and $T_b^- \longleftrightarrow O$ (purple, path 7, point D). These paths show metastable intermediate configurations with $P2_1$, Pm, P_1 and Pm symmetry, respectively. The $P2_1$ (A) structure has a tilt configuration of $a^-a^-c^-$, where the tilt angles for the a- and b-axes are smaller than for the c-axis (a<c) and with an A-cation displacement similar to the O phase. The Pm (B) structure has an $a^-b^-c^+$ tilt system with tilt angles a>b and the Na ions are in the orthorhombic configuration, while the Bi ions are still in the rhombohedral configuration. The P_1 (C) is similar to the Pm (B), but slightly differently displaced A-cations and smaller tilt angles. The fourth intermediate structure Pm (D) has a similar tilt pattern compared to the structures B and C, but differently displaced A-cations. The fifth intermediate structure lies along the path $T^+ \longleftrightarrow R$ (black, path 3, point E in **Fig. 5.11b**) for the 001-order. However, this state (space group Pc) is very similar to the energetic lowest orthorhombic phase. Thus, metastable configurations are only present in 111-ordered structures.
The transformations of the paths with the metastable states consists of two steps. For example. the displacements of the ions for the $O \longleftrightarrow R$ transformation with 111-order (blue, path 6) can be described as follows: 1.) The angle of the tilt around the b-axis decreases and simultaneously the A-cations shift closer to the rhombohedral configuration (displacement in [111]-direction]. 2.) The transformation from the in-phase to anti-phase tilt around the c-axis occurs simultaneously with a small final shift of the Na ions. The Ti-ions shift in the first step relative to the surrounding oxygen octahedron from a rather small displacement in the orthorhombic phase through an $[\bar{1}\bar{1}0]$- and in the second step to an $[\bar{1}\bar{1}\bar{1}]$-displacement in the rhombohedral phase. Both steps show similar energy barrier heights.

In path $T^- \longleftrightarrow O$, when going from the energetically low orthorhombic phase to the metastable $P2_1$ structure at point B, the positions of the A-cations are still very close to the ones in the orthorhombic structure and the oxygen octahedra have already tilted into the tetragonal tilt pattern. Therefore, the transformation seems to be a two-step process, consisting of an octahedral tilting and a subsequent A-cation shift. We will return to this finding in Sec. 5.4 on the *ab initio* MD simulations.
Two other paths profiles exhibit a shoulder: $T^- \longleftrightarrow R$ (orange, path 5) for 111-order in **Fig. 5.11a** and $T^- \longleftrightarrow O$ (gray, path 4) for 001-order in **Fig. 5.11b**. The existence of this shoulder can be attributed again to the two processes, tilting of the octahedra and displacement of the A-cations. Nevertheless, no energetic minimum can be observed.
Noteworthy are the tiny barriers of about $\cong 0.02\,\text{eV}$ (0.16 eV per eight f.u.) close to the metastable structures. For a single octahedron this barrier is lower than the room temperature thermal energy. This finding agrees with the statement of Cross, who mentioned already in 1987 that micro polar regions are "dynamical disordered by thermal motion" [119]. Our calculations, however, are limited to a small cell size, which mimics an infinitely large transformation of the whole macroscopic sample. In reality, nuclei of different tilt patterns can appear on a local scale which are separated by interfaces from a matrix. These interfaces are only two unit cells wide and strongly affect the energy by the deformation of the oxygen octahedra (see Secs. 5.6 and 5.5 and Ref. [89]). Thus, as already mentioned in Ref. [314], the interaction (or distance) between these regions plays an important role for the phase transformations. Since the rhombohedral, monoclinic, orthorhombic and intermediate lower symmetry structures have similar energies, it can be expected that a mixture of these symmetries is present at all times. We investigate the low symmetry structures in further detail by molecular dynamics in Sec. 5.4.
Attention should be paid to the two transformation paths $T^- \longleftrightarrow O$ (gray, path 4, $a^0a^0c^- \longleftrightarrow a^-a^-c^+$) and $T_b^- \longleftrightarrow O$ (purple, path 7, $a^0c^-a^0 \longleftrightarrow a^-a^-c^+$) with 111-order (in **Fig. 5.11a**), which both have the same initial and final structure and energy. The difference between the two tetragonal structures is the direction of the anti-phase tilt, which is along the c-axis in T^- and along the b-axis in T_b^-. It can be seen that the energies for the $T_b^- \longleftrightarrow O$ transformation are lower for all points along this transformation path. This observation can be explained as follows: for the $T_b^- \longleftrightarrow O$ transformation a close group $\longleftrightarrow$ subgroup relation exists [92], since the anti-phase tilt pattern along the b-axis is the same for both structures. This implies that only few displacements of the oxygen ions (and for the cations) are required to transform one structure into the other. To get from the T^- phase to the orthorhombic phase more displacements are needed. This leads to stronger deformation of the octahedra and thus an increase in energy for all structures. We will come back to the group $\longleftrightarrow$ subgroup relation in Sec. 5.6 about tilt defect clusters.
Another aspect, which can be investigated from these calculations is improper ferroelectricity. In contrast to the 111-order, the $O \longleftrightarrow R$ phase transformation with 001-order (blue, path 6) does not show an energy barrier and all displacements and tilts occur simultaneously. This indicates that the coupling between the different degrees of freedom (or modes, such as tilts around different axes and cation shifts) changes with the A-cation order. Therefore, improper ferroelectric behavior is possible in the 001-order as three different modes (polar displacement, tilt $a^-a^-a^0$ and tilt $a^0a^0c^+$) coexist [92, 315]. The criterion that 001-order is a prerequisite to induce improper ferroelectricity has already been deduced by Rondinelli and Fennie [316].

From these calculations we can conclude that the energy surface of NBT is very flat and that octahedral tilts and A-cation displacements have energy barriers which are close to the room temperature thermal energy. Therefore, we expect that several different tilt patterns emerge in chemical differently ordered regions just due to thermal motion. Next, we take a closer look at the kinetics of the phase transformations from an *ab initio* MD point of view.

5.4 Octahedral tilt transformations – Molecular dynamics

As it was seen in the previous chapter, octahedral tilts and A-cation displacements can be easily introduced, since energy barriers for structural transitions are small. We employ *ab initio* MD simulations to investigate which of these transitions occur more often. In this section we study the dynamics of all ions during the phase transformations in the temperatures range from 300 K to 1000 K. The initial structures are the ground state rhombohedral (111-order) and orthorhombic phases (001-order).
For the *ab initio* MD simulations the energy cut-off was reduced to 500 eV and the number of k-points was set to one. Further, a time step of 1 fs was used and time spans of at least 10 ps were simulated in both a microcanonical and a canonical ensemble with a Nosé-Hoover thermostat (see Sec. 4.2).
For structures with 111-order the rhombohedral tilt pattern is retained up to temperatures of 500 K, as it can be seen in **Fig. 5.12a**, which gives the root mean square displacement (RMSD) of each ion from the average position. At 500 K the thermal displacements of oxygen (and to a certain degree of Bi) has a sharp increase and other tilt patterns emerge. One of these patterns has the orthorhombic $a^-a^-c^+$ tilt, but also other tilts are observed, such as $a^-b^+c^+$ and $a^+b^+c^+$. However, the structures can not be assigned to a certain tilt configuration at all time steps, as can be seen in **Fig. 5.13**. It shows a snapshot of the simulation cell at 700 K along the a-, b- and c-directions. Along the a- and b-direction the tilts are in-phase and anti-phase, respectively (**Figs. 5.13a** and **5.13b**). Along the c-axis a mixture of in- and anti-phase tilts coexist (**Fig. 5.13c**). Therefore it can be concluded that in a first step a small fraction of the oxygen ions jump into an in-phase tilt configuration and then the whole structure follows into the in-phase configuration (and vive versa from in-phase to anti-phase).
As soon as the temperature is sufficiently high to allow for tilt transformations the time averaged structure (mean positions of the ions at the end of the simulation) gets close to a cubic $a^0a^0a^0$ phase without tilts. The higher the temperature, the faster the average tilt $a^0a^0a^0$ is observed. Nevertheless, the displacements of the A-cations are still close to the low temperature rhombohedral configuration. Only for higher temperatures ($T > 900$ K) the average positions of the A-cations shift towards the high-symmetry values. It again seems that the octahedral tilts occur at lower temperature than the shift of the A-cations because of the high mobility of the oxygen ions, as was seen in Sec. 5.3.
For structures with 001-order the results are similar, as can be deduced from Fig. 5.12b. The orthorhombic structure (which is the ground state structure) is stable up to a temperature of 600 K. Again, at temperatures higher than 600 K other tilt configurations start to exist. However, the most often observed tilt transformation in the structures with 001-order are along the [001]-direction (the stacking direction), which transform the orthorhombic $a^-a^-c^+$ tilt to the rhombohedral $a^-a^-a^-$ tilt. Tilt transformations along the other directions appear less often. This can be also be seen in **Fig. 5.14**, which gives the RMSD of the

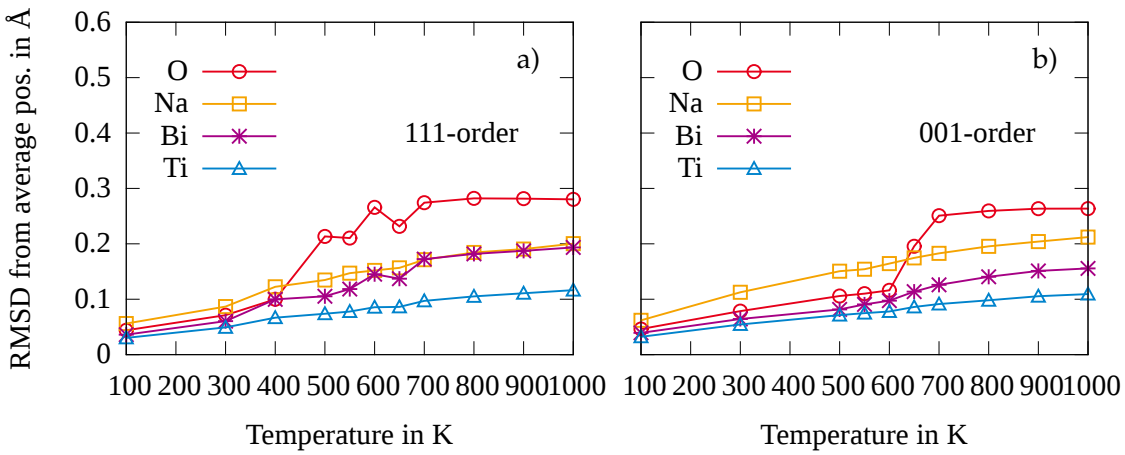

FIGURE 5.12: **a)** Root mean square displacement (RMSD) of Bi, Na, Ti and O ions at several temperatures in an 111-ordered structure. **b)** RMSD of Bi, Na, Ti and O ions at several temperatures in an 001-ordered structure.

oxygen ions along the individual axes. Within the a-b-plane (parallel to the A-cation layers) oxygen ions have a larger displacement than along the c-axis.
From these MD calculations we conclude that transformations from one phase to the next start locally by jumps of a few oxygen ions, which leads to a mixed tilt pattern. When the number of switched oxygen ions is sufficiently large, in a second step the whole cell (consisting of eight octahedra) follows. Additionally, in structures with 001-order a tilt transformation along the [001]-direction (which is along the stacking direction) is preferred over other tilt directions.
Thus, these calculations suggest that the phase transformations are very localized and a nucleation of phases can be expected. However, the cell sizes of all calculation so far were restricted to 40 atoms and no distinction between a nucleus and a matrix can be made. Therefore, in the next section we increase the size of the investigated system, in which it is possible to introduce tilt defects with varying size.

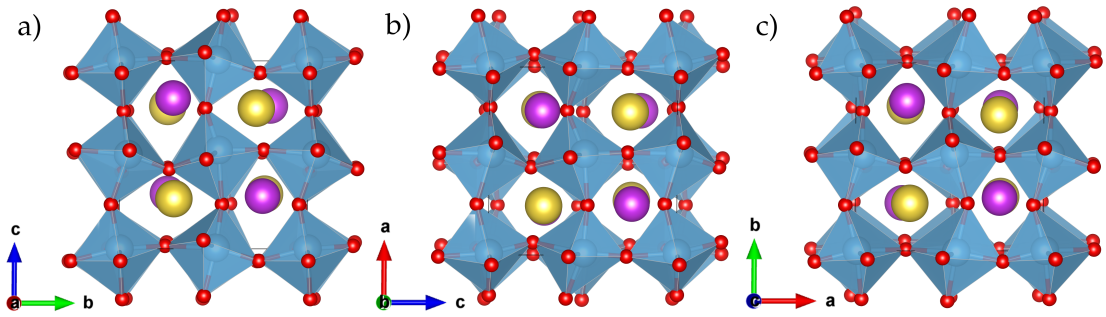

FIGURE 5.13: Snapshot of an *ab initio* molecular dynamics run at 700 K. Along the a-direction **a)** an in-phase tilt and along the b-direction **b)** an anti-phase is present. Along the c-direction **c)** both in-phase and anti-phase tilts are present simultaneously.

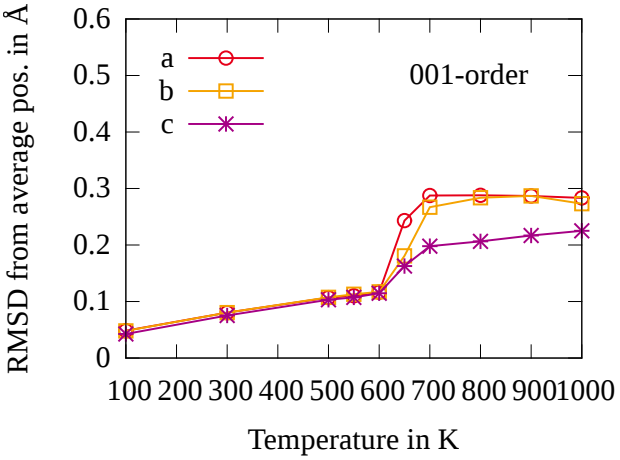

FIGURE 5.14: Root mean square displacement of oxygen ions at several temperatures along different directions in an 001-ordered structure.

5.5 Octahedral tilt defects

Supercell sizes of 6×6×2 oxygen octahedra are used, of which one to nine octahedra are titled into a different tilt pattern [41, 137]. These flat supercells are sufficient, because tilt defects are introduces as planar defects. The energy cut-off is again set to 600 eV and a single k-point is used. Energies were calculated again by selective dynamics relaxations in which all ions were allowed to relax except for the oxygen ions of the tilt defects.
The calculations of the last subsections focused on structural transformations of the whole investigated cells. Here, we study the energetic cost to introduce octahedral tilt defects in supercells with tetragonal, orthorhombic or rhombohedral symmetry.
The arrangement of the tilt defect octahedra is depicted in **Fig. 5.15**, where the numbers give the positions of the respective tilted octahedra. It shows the example configuration of nine orthorhombic tilt defect octahedra (green) in a rhombohedral matrix (light blue octahedra). At the interface deformed octahedra occur, which are colored orange. A cluster of nine defects has a cluster diameter of three octahedra, which corresponds to a cluster dimension of about 12 Å which is the largest cluster that is computational feasible and without having severe finite size effects. Most of the possible tilt combinations of the four symmetries are studied.

Stability of tilt defect clusters

First, the sizes of stable tilt defect clusters are being examined. For this, two sets of calculations are prepared. To study the stability of tilt defect clusters we choose tilt defect patters for the clusters that are lower in energy than the tilt pattern of the matrix. In the first set, we examine the emergence of one, four, six and nine T^- defects in a T^+ supercell (with 111-order). In a second set, an orthorhombic tilt defect cluster in a rhombohedral matrix (as was proposed by Levin and Reaney [83]) is used (with 001-order).
The energies of the tilt defects are plotted in **Fig. 5.16** as red squares for the T^+ matrix (111-order) and blue triangles for the R matrix (001-order). The inset enlarges the part for

smaller cluster dimensions. The energies are given relative to the defect-free matrix. As it can be seen, the energy of the cluster increases with the number of tilt defects (i.e. the size of the clusters). However, for the tetragonal structures the tilt defect energies are much larger than for the R/O combination. But since T^- is energetically more favorable than T^+ (and O lower in energy than R for 001-order), it can be expected that the tilt defect energy will decrease at a certain size of the defect clusters. Since larger clusters can not be computed, the values have to be extrapolated from the obtained data. To estimate the energy of the clusters two models are set up:

$$E_{\mathrm{sq}}(N) = 4E_{\mathrm{def}}N + E_{\mathrm{diff}}\left[\frac{1}{2}\left(8 + 12(N-2) + 4(N-2)^2\right) + 4N\right], \tag{5.1}$$

$$E_{\mathrm{disk}}(N) = E_{\mathrm{def}}\pi N + 2E_{\mathrm{diff}}\frac{\pi}{4}N^2. \tag{5.2}$$

Equation 5.1 describes a quadratic cluster, which we use in our calculations. Equation 5.2 models a disk-shaped cluster. N is either the number of octahedra in one dimension for the square or the diameter of the disk in the number of octahedra. The total energy of the system has two contributions. First, the energy of the deformation of the octahedra at the interface, which is larger than zero ($E_{\mathrm{def}} > 0\,\mathrm{eV}$). Second, the energy difference between the tilt configurations of the tilt defect and the matrix (T^- to T^+ and O to R), which is smaller than zero ($E_{\mathrm{diff}} < 0\,\mathrm{eV}$). The energy difference E_{diff} is given per single oxygen ion. This value can be used more easily than for a whole octahedron, since the octahedra at the interface consist of both, oxygen ions that belong to the cluster, but also oxygen ions

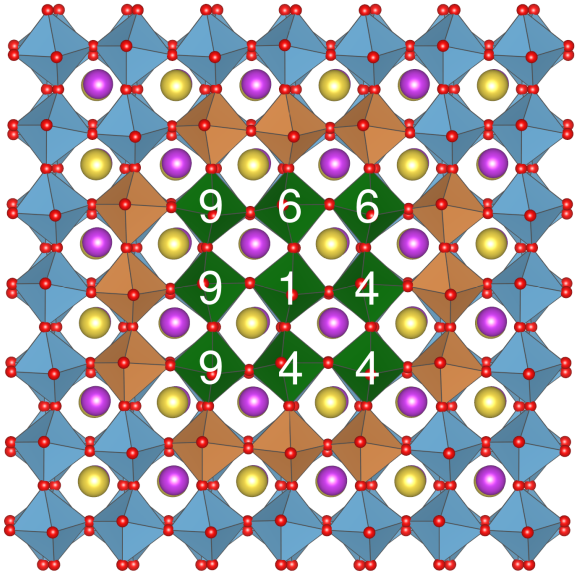

FIGURE 5.15: 6x6x2 supercell with 111-order and an orthorhombic tilt phase defect (green octahedra) in a rhombohedral tilted matrix (light blue). The number of defects is set to 1, 4, 6 and 9 and the positions are indicated by numbers (octahedra with higher numbers are added to the lower numbered octahedra). Deformed interface octahedra are colored orange.

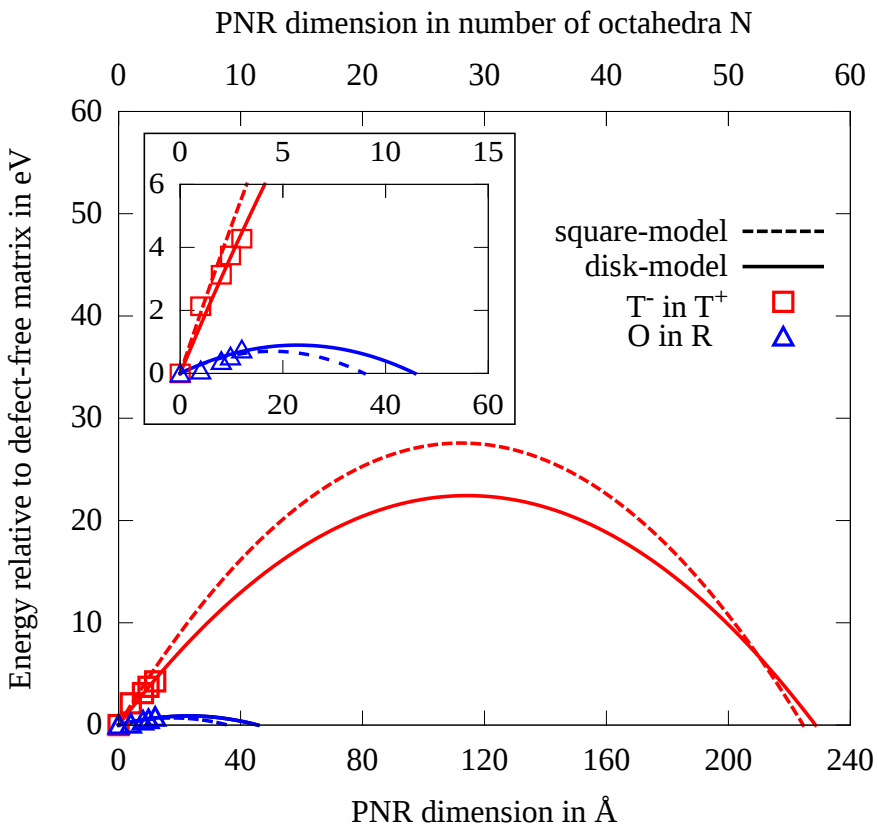

FIGURE 5.16: Energies for two tilt defect clusters of different sizes as sketched in Fig. 5.15. Tilt combinations are T^{-} tilt defects in a T^{+} matrix (red, 111-order) and O tilt defects in a R matrix (blue, 001-order). Energies for larger cluster sizes are extrapolated by two approximate models: a quadratic cluster (dotted line, Eq. 5.1) and a disk-shaped cluster (solid line, Eq. 5.2). The cluster tend to grow further for sizes larger than 120 Å in the tetragonal matrix and between about 20 Å in the rhombohedral matrix.

that belong to the matrix and thus do not contribute to the tilt defect energy. **Tab. 5.1** lists the values of E_{diff}, which are obtained from the differences in ground state energies of the individual structures. The T^{-} phase is lower in energy for both 111- and 001-A-cation-order, thus E_{diff} is negative. Also the orthorhombic phase is lower in energy than the rhombohedral phase, but only for 001-order. For 111-order the rhombohedral structure is lower in energy than the orthorhombic one (positive E_{diff}), thus orthorhombic tilt defect clusters are not stable in a rhombohedral tilted matrix. The equation for the quadratic clusters can attribute all oxygen ions of the tilt defect, whereas for the disk shape cluster an approximation was chosen. Since the values of E_{diff} are known from the tilt transformation calculations, only E_{def} needs to be fitted. This fitted values of E_{def} give an estimate for the energy (drawn in **Fig. 5.16** as dotted lines for the square model and full line for the disk-model). A comparison of the blue and red curves shows that in the tetragonal structure the clusters have to become larger than in the rhombohedral one to become stable, independent of the model. The maximum of the curves (the point at which the clusters tend to increase in size) are at 120 Å for the T^{-} and 20 Å for the orthorhombic tilt clusters. In case of the tetragonal structures the stability of the clusters versus the initial configurations is

TABLE 5.1: Summary of the calculated values from the tilt defect section: difference in energy between the two different tilt configurations E_{diff} normalized for a single oxygen ion, the cost to deform an octahedron when defects are introduced E_{def} and the sizes of the clusters at which they have a lower energy than the defect-free 6x6x2 supercell.

	T^- in T^+		O in R	
	111	001	111	001
E_{diff} in eV per oxygen ion	-0.018	-0.011	0.006	-0.018
E_{def} in eV per octahedron	0.4 - 0.54	0.25 - 0.27	—	0.08 - 0.12
Cluster dimension in Å	230	233	—	35 - 42

reached at sizes of circa 225 Å. For the orthorhombic clusters the stable size is about 40 Å. This is due to the fact that the octahedral deformation energy is much smaller in the rhombohedral structures than in the tetragonal structures (0.08 to 0.12 eV for R/O and 0.4 to 0.54 eV for T^+/T^-). Noteworthy is the fact that the energy to deform an octahedra is much larger than the energy gain from switching to the favorable tilt configuration, by a factor of 25 for both structures, tetragonal and rhombohedral. However, the energy to deform an octahedra in the O/R interface is rather small. This observation was also made by Gröting *et al.* [89], where a two dimensional interface between an orthorhombic and rhombohedral tilted structure was studied. It was reported that only one intermediate layer is needed to stabilize the two tilt configuration of thicknesses of three layers.
The tetragonal clusters with 001-order (not plotted) show approximately the same size as the 111-ordered tetragonal cluster. Although the 001-order deformation energy E_{def} is about half the value of the 111-order, the energy difference E_{diff} is also about half. All values are summarized in **Tab. 5.1**.

Formation energy of tilt defect clusters

We just investigated a few combinations of tilts of the defect cluster and the matrix. One of them was an orthorhombic cluster within a rhombohedral matrix. However, also other tilt patterns, like the T^+ or T^- phase, can be introduced into the rhombohedral matrix. This is of interest, when we recall the phase diagram of NBT. The transition from the rhombohedral to the orthorhombic phase was only one of the suggested phase transitions at lower temperatures. The direct transition to the tetragonal state is another possible phase transition sequence. Therefore, here we study how large the energetic differences of the chosen tilt defect pattern are. We however do not restrict us to the rhombohedral tilted matrix, but study six of the seven possible phase transitions that were already studied in Sec. 5.3 and depicted in Fig. 5.10.
Fig. 5.17 shows the defect energies of several tilt defect sizes relative to the energy of the matrix without defects for an 111-ordered (a) and an 001-ordered system (b). The red and blue lines show respectively the T^- defects in T^+ matrices and orthorhombic defects in a rhombohedral matrix, which were already shown in Fig. 5.16. In **Fig. 5.17a** it can be seen that there is a pronounced difference from the red and black (T^+ in R) lines to the other lines. The difference for the T^+ in R matrix combination to the other combinations is similar to the $T^- \leftrightarrow$ O and $T_b^- \leftrightarrow$ O situation from Sec. 5.3. To get from the $a^0a^0c^+$ to the

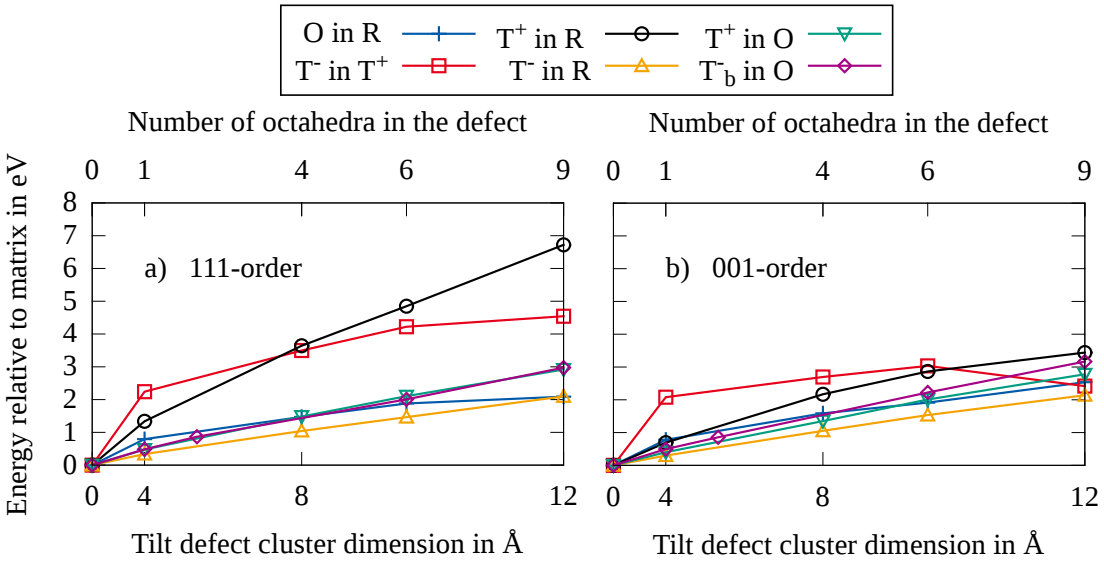

FIGURE 5.17: Energies for various defect and matrix tilt combinations for different sizes relative to the energy of the defect-free matrix for **a)** 111-order and for **b)** 001-order. Color coding is the same as in the Figs. 5.10 and 5.11.

$a^-a^-a^-$ phase the two $a^-a^-a^0$ and $a^0a^0c^-$ tilt modes have to be applied, which results in a strong deformation of the octahedra at the interfaces. The T^+ and T^- phases require only a single mode, but the deformation of the octahedra at the interface very large, which leads to high formation energies.

The lowest formation energies are seen for the T^- in R configuration (orange). Yet, when the deformation of the octahedra at the interface is small, the defect energies are very similar for each combination [89]. Fig. 5.15 shows the orthorhombic defects in rhombohedral matrix combination and it can be seen that the interface octahedra (dark gray) are hardly deformed. For the 001-order in **Fig. 5.17b** the results are similar, however all defect energies are slightly reduced compared to the 111-order.

For tilt defects which consist of four octahedra, defect energies are around 0.5 eV for most of the 111- and 001-ordered structures, which is well above the room temperature thermal energy. However, in a real system the positions of the oxygen octahedra of the tilt defect cluster are not constrained. Therefore, the energies obtained from these calculations can be seen as upper limits to the real defect energies.

As said, all tilt defect and matrix combinations which show a small deformations of the octahedra are equally likely. This means that within the rhombohedral phase different kind of tilt defect clusters can exist (also simultaneously). Either the anti-phase tilts along two axes disappear (the resulting structure is T^-) or the tilt along one axis becomes in-phase (resulting structure is orthorhombic). This would lead to a simultaneous appearance of rhombohedral, orthorhombic and tetragonal symmetries. The results of the *ab initio* MD simulations from Sec. 5.4 even suggest that other kind of tilt configurations (without any symmetry) can exist. Additionally, chemical 001-ordered regions enhance the effect of different tilt configurations, because of their lower tilt defect formation energies. The 001-ordered regions prefer an orthorhombic tilt configuration with an in-phase tilt along the stacking sequence. As we have seen, the sizes of these tilt defect clusters can be small (less

than 100 Å) and therefore might explain the origin of the polar nanoregions, since different tilt phases exhibit different polarizations [109].
Therefore, two different phase transformation routes with simple group ⟷ subgroup relations from the low rhombohedral to the high temperature tetragonal phase seem to be plausible. The transformations can either occur on the "direct" route from the rhombohedral phase to the tetragonal anti-phase one: (R/M ⟷ T^-) or via the orthorhombic phase to the tetragonal in-phase one: R/M ⟷ O ⟷ T^+. The experimentally observed tetragonal phase thus might consist of a mixture of in-phase and anti-phase tilts, which result in an observed averaged tetragonal phase with small in-phase tilt angle [47].

5.6 A-cation displacements

So far we have focused on the oxygen octahedra. Here we change the topic slightly and concentrate solely on the A-cation displacements, which play also play an important role in the relaxor properties of NBT, as they couple to the ferroelectric distortions of the B-cations [39]. We have already seen in Sec. 5.2 that Bi and Na react differently on the volume reduction of the 12-fold A-O cuboctahedron. Now we study the energetic cost to displace Bi and Na from their ideal ground state position.
We use selective dynamics relaxations, in which the respective Na or Bi ion were displaced by a certain distance from its ground state position and kept fixed, surrounding ions were allowed to relax. However, all ions being third nearest neighbors or further away from the respective Bi or Na ion were fixed additionally to avoid a translational shift of the entire cell.
In Refs. [48,51–53,60,65] it is reported that, although the Bi and Na ions occupy the same 12-fold oxygen environment, bond lengths for Bi and Na to the neighboring oxygen ions differ. Kreisel *et al.* [41] were the first to suggest that Bi exhibits an off-[111]-direction displacement in NBT because of its lone-pair (similar to Pb in lead-containing relaxors). Keeble *et al.* [52] showed that Bi experiences several distinct displacements along the tetragonal, orthorhombic, rhombohedral and monoclinic directions depending on temperature. Na in contrary, displaces more uniformly along all directions, especially at temperatures close to room temperature. Jeong *et al.* [51] and Aksel *et al.* [53] showed by reversed Monte Carlo

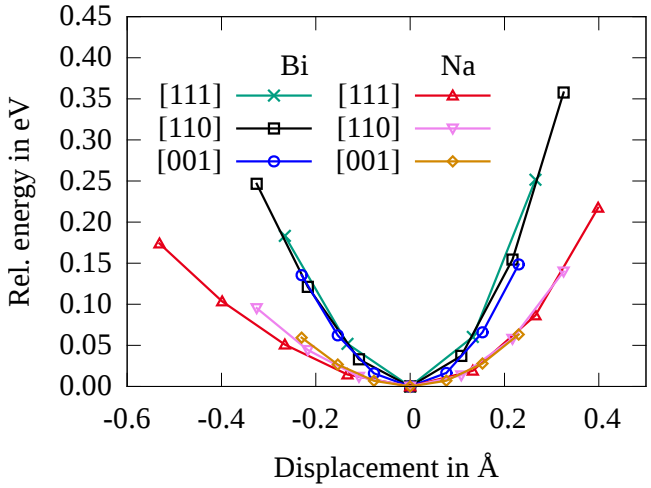

FIGURE 5.18: Displacements of Bi and Na along three different directions: [001], [111] and [110] for a system with 111-order. The minimum corresponds to the ground state position of the Bi and Na ions.

modeling of neutron and X-ray data that the Na ion prefers to displace into the center of the Na-O polyhedron along the [111]-direction. Instead, Bi ions tends to displace towards the face of the closest oxygen octahedron along the [001]-direction. Usher *et al.* reported that an application of en electric field led to an ordering of the Bi ions along the external field [65]. These different kinetic behaviors of Bi and Na are suspected to be due to the lone-pair of Bi [106].
In this section we study the local energetic environments of Bi and Na close to the ground state position in the rhombohedral phase, especially for displacements along the [111]-, [110]- and [001]-directions. The ground state positions are shifted along the [111]-direction from the high symmetry position (the center of the 12-fold oxygen cuboctahedron) by 0.23 Å for Bi and 0.16 Å for Na, which is in agreement with an earlier study [46]. The results of the displacements are shown in **Fig. 5.18**. Negative displacements imply that the A-cations move closer to the center of the oxygen polyhedron. Positive displacements denote they get close to the edge of the oxygen polyhedron and closer to one face of a Ti-O octahedron.
First of all, it can be seen that the (approximately) quadratic displacement curves for Na are flatter than for Bi. The curvatures for the Bi-displacements are much steeper and therefore Bi displaces less than Na (which is also seen in the MD simulations of Sec. 5.4). For Na the displacement towards the center is slightly preferred when it is along the [111]-direction (red curve), but positive displacements for Na do not show an energetic difference for any of the directions. In contrast, Bi has no directional preference when displaced towards the center, but a positive displacement along the [001]-direction (blue curve) is slightly preferred over other displacement directions. A displacement in the [001]-direction leads to a deformation of the cell to a tetragonal symmetry. The reason for this behavior might be the lone-pair of the Bi ion, which tends to stabilize asymmetric arrangements of Bi and its surrounding [106]. These findings are in agreement with the results of Keeble *et al.* [52] and Aksel *et al.* [53] who see a transition at room temperature towards a displacement along the tetragonal direction for Bi.

5.7 Summary

From the various calculations of this chapter on the kinetics of the phase transformations in NBT we can conclude several points:

- As was seen in Sec. 5.2, it is necessary to perform NEB calculations when transformation barriers are investigated, since the reduction of the obtained energy are about 30% compared to static (unrelaxed) calculations. This huge reduction in energy arises from the structural relaxation of oxygen and Bi. The large energy gain from the ion relaxation was also observed by Gröting *et al.* [96]. One of the driving factors of the structural relaxation is the asymmetric displacement of the Bi 6s lone-pair.

- In Secs. 5.2, 5.3 and 5.4 we found that the chemical order not only influences the ground state phases and ground state energies [89], but also the octahedral tilt transformation paths. Tilt transformation barriers which exist in structures with 111-order completely vanish for structures with 001-order (Fig. 5.11).

- The experimentally observed distinct kinetic behaviors of Bi and Na [52,53] was also observed in our calculations. Bi and Na influence octahedral tilt barriers differently (Sec. 5.2) and have different thermal displacement behaviors within the 12-fold A-O cuboctahedron (Secs. 5.4 and 5.6). This effect can be attributed to the active lone-pair of the Bi ion, which tends to displace its Bi core asymmetrically within its surrounding [104].

- A very flat energy landscape for octahedral tilts and A-cation displacements was found in Secs. 5.3, 5.4 and 5.6. Energy barriers per f.u. for octahedral tilts and A-cation displacements are close to room temperature, which leads to the conclusion that above room temperature regions with different tilt patterns are present simultaneously, just as reported for NBT-based materials [47,87]. Therefore, deviations from the global average symmetry can easily be introduced on a local scale.

- Similar, in Sec. 5.5 we saw that the energetic difference of various octahedral tilt defect patterns is small, as long as the deformations of the octahedra at the interface between tilt defect cluster and matrix remain small. From this follows that in a rhombohedral tilted phase, both orthorhombic and tetragonal tilt clusters can emerge with similar energetic cost. Tilt defect clusters are stable for sizes much smaller than 200 Å. The size of PNRs might be of the same order.

- Although the energy barriers for tilt transformation and A-cation displacements are of similar magnitude, it appears from the results of Secs. 5.3 and 5.4 that the oxygen ions have larger thermal displacements than the other elements. This suggests that the phase transformations are initialized by the vibration and hopping of oxygen ions and only then the A-cation displacements follow in a subsequent step. This explanation is in line with experimentally obtained vibrational frequencies [71,191].

- When the structure has 001-order, several degrees of freedom (octahedral tilting and A-cation displacements) can occur simultaneously. Thus, the possibility of improper ferroelectricity is dependent on the chemical order, as was seen in Sec. 5.3 and reported earlier [316].

6 Oxygen vacancy migration

Parts of this chapter have been published in Journal of Materials Chemistry A [317].

Now that we have dealt with the phase transitions of NBT, in this chapter we focus on the migration of oxygen, which leads to the observed ionic conductivity. We are especially interested in the question why the huge difference in activation energies exists (see Fig. 3.10) between the high temperature and room temperature regime. The first step is to look at oxygen migration in the tetragonal, orthorhombic and rhombohedral phase and then to look at the influence of volume changes on the migration barrier. The next chapter will then deal with associates of oxygen vacancies and dopants or Bi vacancies.

Computational setup

In the last chapter, which dealt with the kinetics of the phase transformations in NBT, we focused on cells with perfect stoichiometry. In this chapter we introduce oxygen vacancy point defects $V_O^{\bullet\bullet}$ and study their migration barriers. The energy cut-off for the oxygen vacancy migration calculations was set to 600 eV. Most cells have a size of 4×4×4≙ 64 $A'_{0.5}A_{0.5}BO_3$ unit cells (i.e 64 octahedra) and were thus large enough to reduce finite size effects [318]. A single k-point was set for all relaxations and the electric density of states were calculated with a doubling of the k-point density along each direction, resulting in a 2×2×2 k-point mesh. All migration barrier calculations were performed in supercells with one $V_O^{\bullet\bullet}$ defect and therefore contain 319 atoms. All migration barriers were obtained by NEB calculations with either five or seven images between the initial and final configurations.
Energies for the migration barriers in the tetragonal and orthorhombic structures were calculated by a constrained relaxation, which excluded specific atoms from the relaxation. Thereby, a relaxation from the tetragonal and orthorhombic structures into the ground state rhombohedral configuration was prevented. For the orthorhombic phase, fixing of several oxygen octahedra remote from the migrating oxygen ion was sufficient to avoid a phase transformation. However, for the tetragonal phase, all ions which were further away than the third nearest neighbors from the vacancy, were kept fixed. Especially, a relaxation of the A-cations into the configuration of the rhombohedral phase leads to a drastic drop of the energy of the cell, which made it impossible to observe migration barriers.
Since the oxygen vacancy can be charged, the charge of the cell has to be taken into account. The charge of the cells of the rhombohedral phase were either neutral (removal of one neutral oxygen atom) or charge compensated In the the case labeled "charged", one neutral oxygen atom and two electrons are removed. In the neutral case two unbound electrons are present in the system, which in reality would not be there, since they are removed with the oxygen ion that has a charge of -2. This neutral setup does not correspond to the realistic picture of a defect, but is studied here for comparison to the compensated states. In a third case (labeled "substituted") the cell was charge compensated by substitution of one neutral Bi by one neutral Na atom. This substitution compensates the charge and no unbound electrons are present in the system, since the Bi^{3+} ion is replaced by a Na^{1+} ion. For the orthorhombic and tetragonal cells the "charged" case is studied, exclusively.
We saw in Fig. 3.10 that a kink in the slope of the conductivity appears around 600 K, which relates to a change in the activation energy of the oxygen migration process. As it

was described above, deviations from the rhombohedral symmetry start to occur at 470 K, at which orthorhombic and tetragonal phases appear (see Fig. 3.5). A purely tetragonal phase is reached only at 640 K. Therefore, the change in the slope of the conductivity appears in the same temperature range as the diffuse phase transition. This leads to the idea that the change in activation energy is related to the present phases.
We study the three phases, rhombohedral, orthorhombic and tetragonal and additionally increase the volume of the rhombohedral and tetragonal phases as is expected from thermal expansion. For the tetragonal phase the T^{-} anti-phase tilt was chosen and not the in-phase tilt phase T^{+}, since it is lower in energy and the structures were more stable versus relaxation toward other tilt configurations. However, the migration barriers of the two tetragonal phases should be comparable, since we have seen in Sec. 5.2 that the coupling between layers of octahedra along the [001]-direction in the tetragonal phase is negligible. The migration of an oxygen ion is characterized by squeezing of an oxygen ion through an A-A-B-cation triangle [319]. Four different migration paths are investigated and are displayed in **Fig. 6.1** and **Fig. 6.2**. It can be seen that the paths labeled with 1 and 2 are along the [001]-direction and 3 and 4 are along the [010]-direction. Again, the two chemical A-cation 111- and 001-orders are studied, since we have seen that large energetic differences can be expected for these two chemical orders. Also, chemical order dependent migration barriers have already been observed by Uberuaga and Pilana [320] and He and Mo [167]. First, **Fig. 6.1a** and **6.2a** show the 001-order. Therefore, paths 1 and 2 take the oxygen vacancy from the Bi-layer with four neighboring Bi ions (position A in **Fig. 6.1**) via the mixed layer with two neighboring Bi and Na ions (position B) into the Na-layer with four neighboring Na ions (position C). Paths 3 and 4 keep the vacancy within the mixed layer at all steps (positions B, B' and B"). Second, we use the 111-order, as shown in **Fig. 6.1b** and **6.2b**. For 111-ordered A-cations the oxygen vacancy is in a mixed layer in every position. Because of the displacements of the A- and B-cations and the tilt of the oxygen octahedra

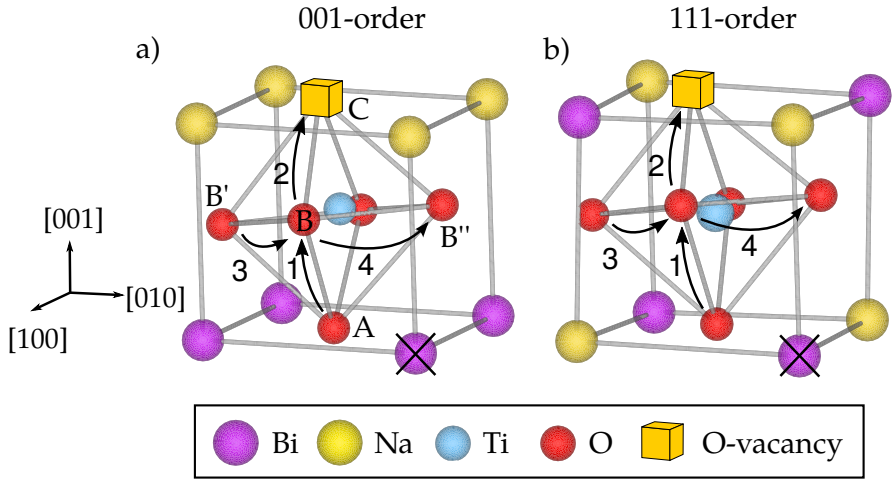

FIGURE 6.1: Investigated migration paths "1, 2, 3 and 4" of an oxygen vacancy (orange cube) within one oxygen octahedron. The A-cations Bi (purple) and Na (yellow) are either stacked along **a)** the [001]-direction or **b)** arranged in a rock salt order (111-order). Positions of the oxygen vacancy are labeled by letters "A", "B" and "C". The Bi atom marked with an "×" is replaced by a Na atom in the "compensated" case.

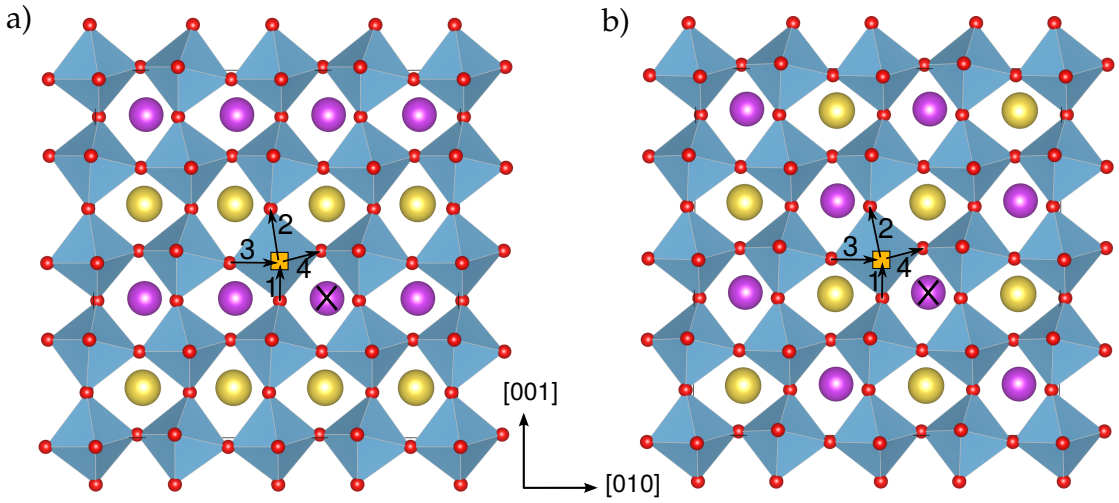

FIGURE 6.2: The two used A-cation chemical orders and the oxygen vacancy migration paths: **a)** 001-order **b)** 111-order. The migration paths are labeled as in Fig. 6.1. The Bi atom marked with a "×" is replaced by a Na atom in the "compensated" case.

the B positions have different surroundings and thus lead to four different possibilities for path 1 and path 2, yet the differences in energies for these paths are small. The position of the Bi atom, which is substituted by a Na atom, is marked by a "×" in **Figs. 6.1** and **6.2**. **Fig. 6.2** depicts one layer of the whole cell of the rhombohedral phase (with 001- and 111-order, respectively).

6.1 Rhombohedral phase

The migration barriers in the rhombohedral phase for the "charged", "compensated" and "neutral" case are shown in **Fig. 6.3**. For most paths, the barrier heights are around 0.6 eV. The unphysical case with neutral cells has migration barriers of around 1.0 eV to 1.5 eV. Thus, the presence of two residual electrons leads to a doubling of the migration barrier height. This agrees with the findings of Zhang *et al.* that a neutral cell increases the barrier height, compared to charged cells [318].
Of particular importance is the completely different shape of the migration barrier for path 1 in the structure with 001-order (green) for both the "charged" and the "compensated" case. The migration path is not symmetric and has only one barrier for the jump from the Bi to the mixed layer. The calculated barriers for this path vary between 0.45 eV and 0.54 eV, depending on the different possibilities the vacancy can take from the A to one of the {B} positions. However, no barriers or small barriers of 0.1 eV are present for the back-hopping from the {B} to the A position. From this one can draw an interesting conclusion. If a long-range (percolating) 001-order would exist in the sample, the measured ionic conductivity should mainly originate from the migration of the oxygen vacancies along the Bi-layer as indicated in **Fig. 6.4**. The diffusion along the Bi-layers within the 001-ordered regions are highlighted in red and blue. Because of the energetic favorable back-hopping from B to A positions, the vacancies can easily jump between the Bi and mixed layer until the 001-ordered region ends. Therefore, from the experimental conduc-

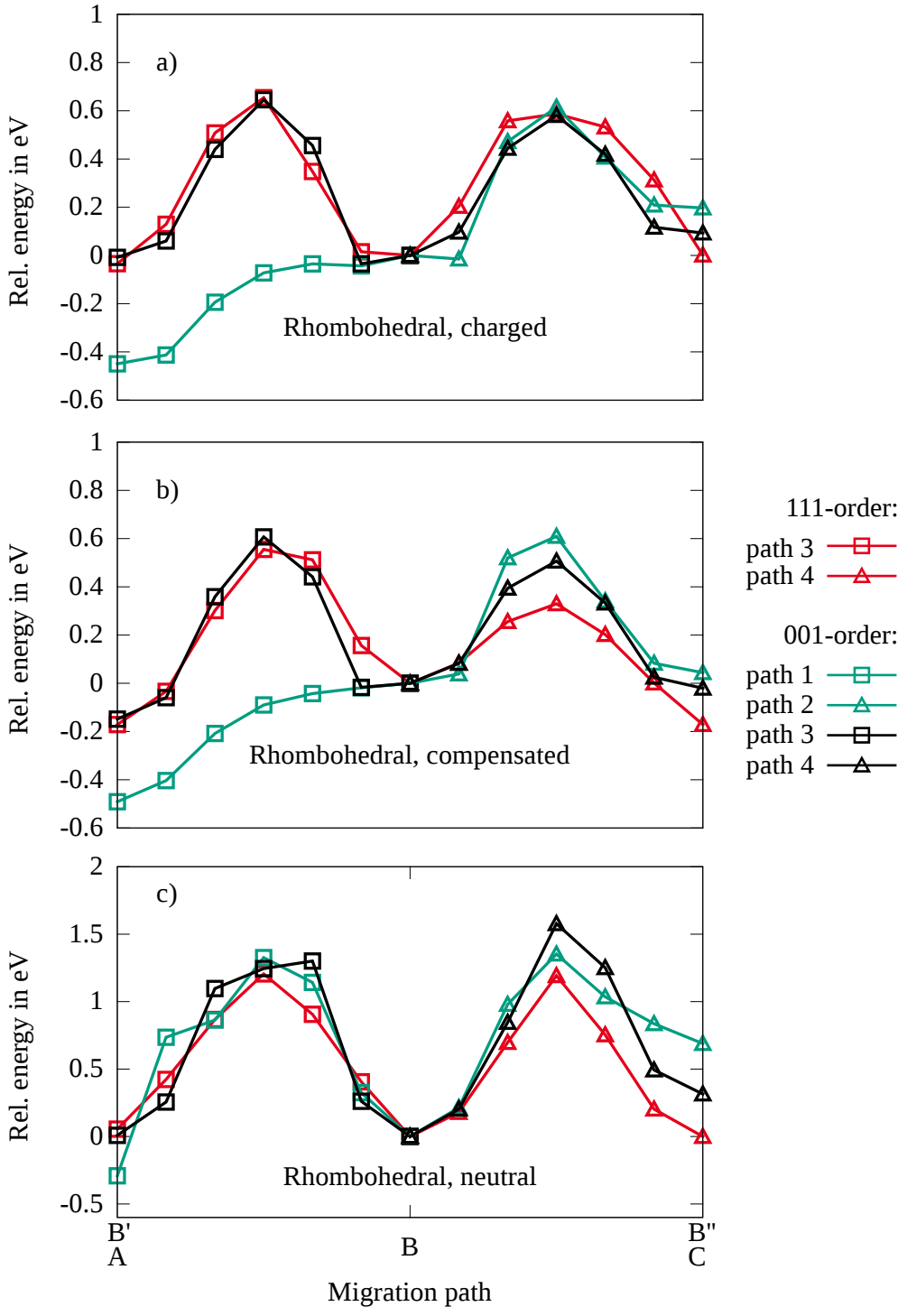

FIGURE 6.3: Oxygen vacancy migration barriers in the rhombohedral phase for three different scenarios: **a)** charge compensated cell and **b)** "compensated" cell with one Bi atom replaced by a Na atom and **c)** no charge compensation ("neutral"), as sketched in Fig. 6.1.

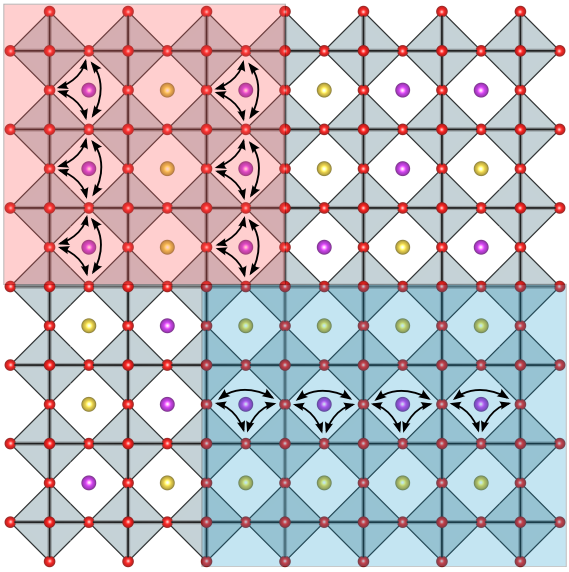

FIGURE 6.4: Sketch of NBT with few unit cell sized regions with 001-order (highlighted by a red and a blue mask). According to Fig. 6.3 these regions exhibit a very fast oxygen vacancy diffusion with only a small migration barrier along the Bi-layers (indicated by arrows).

tivity measurements and our barrier calculations we rule out a long-range 001-order of the A-cations in NBT.

Additionally, in **Fig. 6.3** it can be seen that the defect formation energy is the smallest when the vacancy is situated in the Bi-layer (green, position A) and the highest when it is in the Na-layer (green, position C). The energy gain when an oxygen vacancy migrates from the mixed layer to the Bi-layer is about 0.5 eV. When the oxygen vacancy resides within the Na-layer the energy is increases by 0.4 eV compared to the mixed layer. These formation energies were already reported by Dawson *et al.* [198] and He *et al.* [167]. The lowering of the energy for oxygen vacancies within the Bi-layer can be attributed to the Bi 6*s* lone-pair electrons, which leads to a relatively weak Bi-O binding energy that often results in an asymmetric coordination [104–106]. Therefore, short-range 001-order would trap vacancies within the Bi-layers, as they have the lowest formation energy.

The "compensated" case in **Fig. 6.3b** shows a feature that is not present for the purely "charged" cell of **Fig. 6.3a**. Path 4 has a reduced energy barrier compared to path 3 for both the 111- and 001-ordered structures. After replacing a Bi atom by a Na atom, position B″ (see **Fig. 6.1**) in the 111-order no longer has two Na neighbors, but three and only one Bi atom. This leads to a reduction of the energy barrier from 0.55 eV of path 3 to 0.3 eV. Similar, but less pronounced, the migration barrier is reduced from 0.6 eV to 0.5 eV for the 001-ordered structure. Interestingly, the shape of the migration path 1 is not affected, when compared with the one in **Fig. 6.3a** for the "charged" case. A reduction of four to three Bi neighbors at position A neither changes the formation energy nor the migration barrier. From these calculations we find that the charge of the cell and the local electronic configuration massively affects the oxygen vacancy formation energies and migration barriers.

The energy barriers for the oxygen migration in the intermediate temperature orthorhombic phase are shown in **Fig. 6.5**. It is easily visible that the migration barrier heights vary between 0.33 eV and 1.11 eV for the different paths and chemical orders. Further, the migration barriers are asymmetric along one direction for path 1 and 2 (or 3 and 4). The larger variation and asymmetry in barriers arises from the lower symmetry of the orthorhombic compared to the rhombohedral phase, which is because of the more complex octahedral tilt pattern and displacements of the A and B-cations. In contrast to the rhombohedral phase with 001-order in Fig. 6.3, the one-sided barrier of path 1 (both green) has vanished and now the barrier height is 0.36 eV to 0.4 eV for both hopping and back-hopping. The highest barrier of 1.11 eV is found for path 4 in the 001-ordered structure, where the oxygen vacancy migrates within the mixed layer. For 111-order the barriers decrease from around 0.6 eV in the rhombohedral phase to 0.33 eV to 0.55 eV in the orthorhombic phase. As was found in the rhombohedral structure the vacancy prefers to be located within the Bi-layer (position A), but the energetic difference to the mixed layer is smaller. In contrary, the defect formation energy for the vacancy in the Na-layer (position C) increases compared to the mixed layer. Therefore, it can be concluded that the formation vacancy energy does not depend only on the number and type of the neighboring atoms, but also on the local arrangement of these. Thus, we find that the migration barriers in the orthorhombic phase vary by a factor of three and a total of about 0.8 eV.

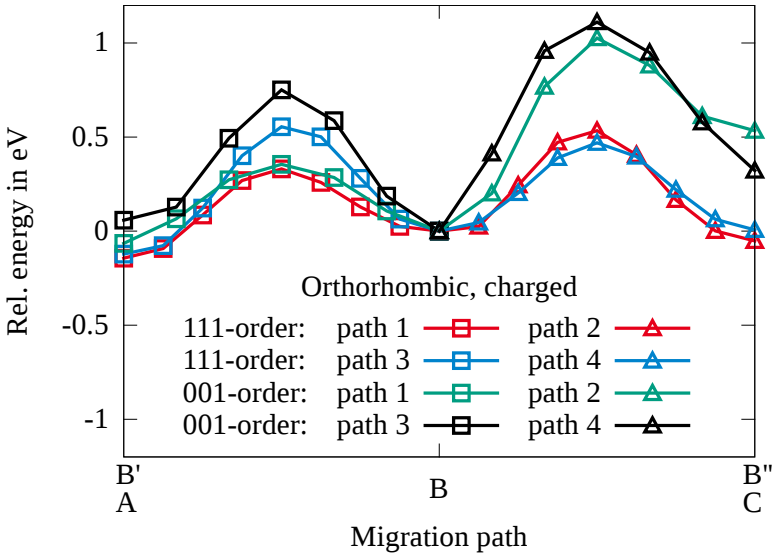

FIGURE 6.5: Oxygen vacancy migration barriers for the orthorhombic phase in a "charged" cell. Chemical orders are 111 and 001 and the migration is along the [001]- and [010]-direction, as sketched in Fig. 6.1.

Finally, we investigate the high temperature tetragonal phase with 111-order and $a^0a^0c^-$ tilt pattern. The [001]-migration direction is along the axis around which the octahedra are tilted. The [010]-migration-direction is along one of the axis without tilts. Therefore, these two migration direction are different from each other, despite the 111-order.
Fig. 6.6 shows the migration barriers of the 111-ordered tetragonal structures for two directions. For paths 3 and 4, along the [010]-direction the migration barriers are about 0.87 eV. However, for path 1 and 2 the migration along the [001]-direction has a substantially lower migration barrier of about 0.38 eV. All paths exhibit a symmetric shape.
To understand why the migration barrier are so different, we take the two structures at the maxima of paths 1 and 3 (marked as I and II in **Fig. 6.6**) and look at the electronic density of states (DOS). **Fig. 6.7a** displays the DOS of selected ions of the structures I. The DOS of structure II is given in **Fig. 6.7b**. The labels at the top of each column describe whether the specific ion is "close" (a direct neighbor) or "remote" (not a direct neighbor) from the migrating oxygen. Below the ion label the distance to the migrating oxygen ion is given. The column labeled with "O mig." depicts the DOS of the migrating oxygen ion. Na ions are neglected, as they do not show any interesting features. The most striking feature in the DOS of the structure with the high energy barrier (**Fig. 6.7a**) can be seen for some ions at the Fermi level at $E = 0\,\text{eV}$. These defect states are a dangling bond belonging to the migrating oxygen ion. The oxygen-oxygen distance of 3.47 Å of the migration oxygen to its second closest neighbor is much longer than the distance in structure II with the low barrier (**Fig.6.7b**). For the low migration barrier structure the distance is 2.86 Å (which is the average oxygen-oxygen distance). Therefore, the change of the migration barrier in the

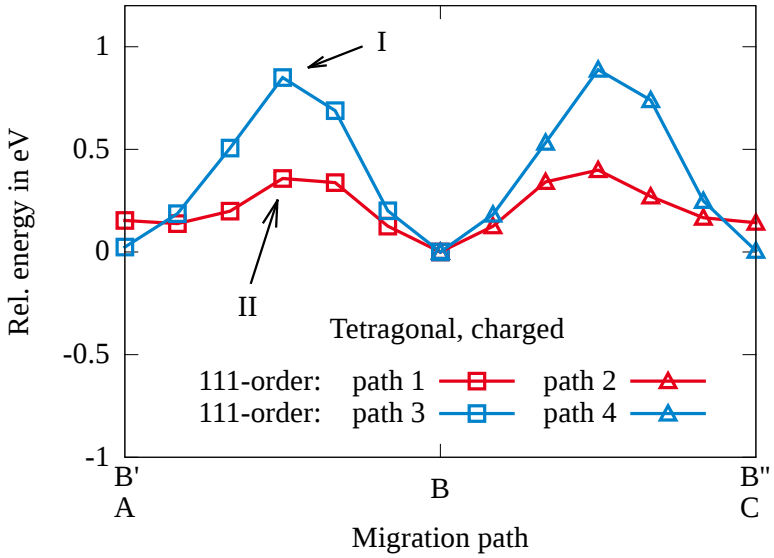

FIGURE 6.6: Oxygen vacancy migration barriers for the tetragonal $a_0^0a_0^0c_0^-$ phase in a "charged" cell. Chemical order is 111 and the migration is along the [001]- and [010]-direction. For path 1 and 3 at positions I and II the electronic density of states is displayed in Fig. 6.7.

a) I Tetragonal path 3 (010) (high barrier)

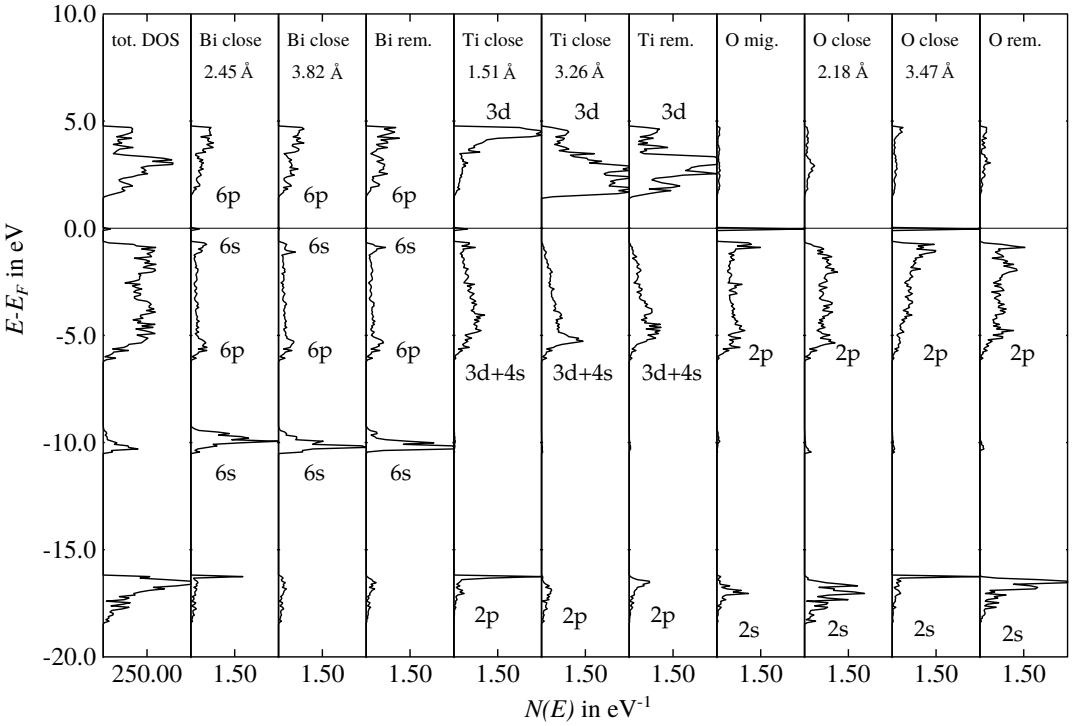

b) II Tetragonal path 1 (001) (low barrier)

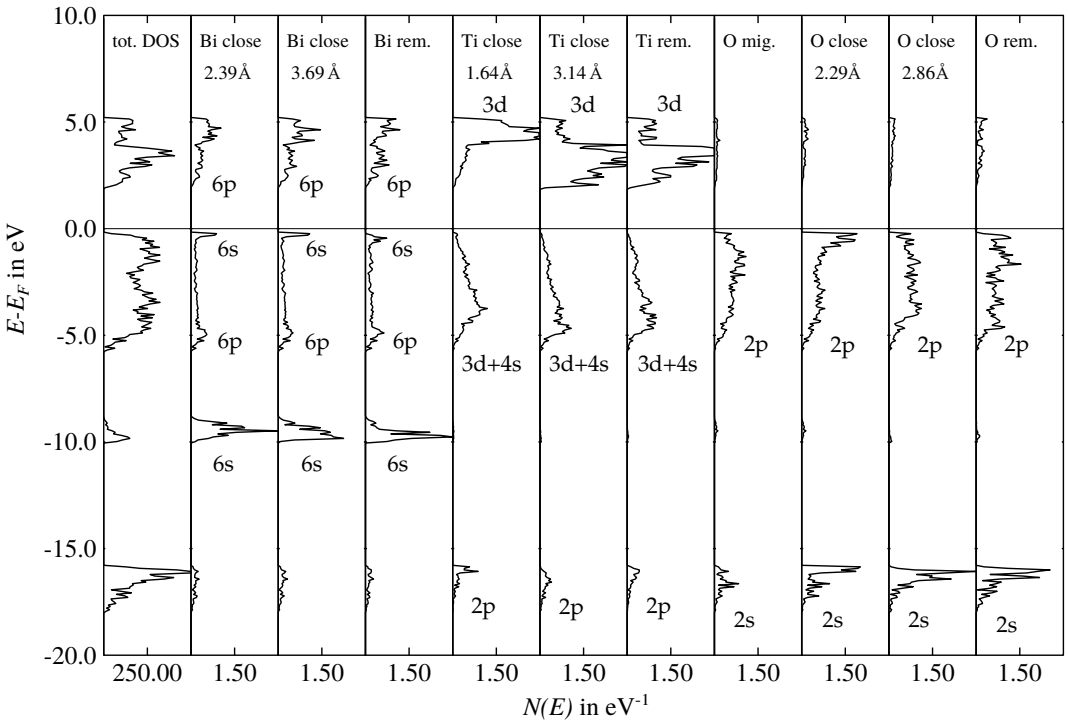

FIGURE 6.7: Electronic density of states for two tetragonal structures of Fig. 6.6 with **a)** a high oxygen migration barrier (structure I) **b)** a low migration barrier (structure II).

TABLE 6.1: Summary of the calculated oxygen vacancy migration barriers for the three investigated phases: rhombohedral (Fig. 6.3), orthorhombic (Fig. 6.5) and tetragonal (Fig. 6.6). Two different chemical orders are used: 111- and 001-order. Migration directions are along the [001]- and [010]-direction as drawn in Fig. 6.1. Values for back-hopping are given in brackets, when the migration barrier is asymmetric. All values are given for the "charged" case.

Migration barriers E_{mig} of a $V_O^{\bullet\bullet}$ oxygen vacancy in eV						
Phase	rhombohedral		orthorhombic		tetragonal	
Chemical order	111	001	111	001	111	001
Migration along [001] (path 1)	–	0.45-0.54 (0-0.1)	0.47 (0.33)	0.42-0.48 (0.36-0.40)	0.36	–
Migration along [001] (path 2)	–	0.61 (0.40)	0.53 (0.58)	1.03 (0.49)	0.40	–
Migration along [010] (path 3)	0.65	0.65 (0.55)	0.67 (0.55)	0.69 (0.75)	0.85	–
Migration along [010] (path 4)	0.59	0.58	0.47	1.11 (0.79)	0.89	–

tetragonal phase can be attributed to the appearance of electronic defect states originating from a dangling bond belonging to the migrating oxygen ion.
Migration barriers for three different phases (rhombohedral, orthorhombic and tetragonal) with two A-cation orders (111- and 001-order) were calculated. All obtained values for the "charged" cells (removal of one neutral oxygen ion and two electrons) for the migration of single $V_O^{\bullet\bullet}$ oxygen vacancy as drawn in Fig. 6.1 are summarized in **Tab. 6.1**. Energy barriers for back-hopping (migration in the opposite direction) are given in brackets.

6.4 Thermal expansion

So far, all calculations have been performed at the equilibrium volume at 0 K. However, since the temperature range over which the ionic conductivity is measured spans over approximately 500 K (from 400 K to 900 K), one has to think about influences of the thermal expansion on the migration barriers. The linear temperature expansion coefficient was determined to be $\alpha = 6 \cdot 10^{-6}\,\mathrm{K}^{-1}$ [42]. When the material is heated by 500 K, this leads to a linear expansion of 0.3% and an increase of volume of about 1%. However, since our DFT calculations are performed at 0 K and the conductivity measurements are done at up to 900 K, we study how the barriers change over an even larger volume change. Additionally, NBT has no constant value for the linear thermal expansion coefficient, but a value that varies from $\alpha = 4\,\mathrm{K}^{-1}$ to $8\,\mathrm{K}^{-1}$. Therefore, when we use an expansion coefficient of $8\,\mathrm{K}^{-1}$ and assume a temperature span of 1000 K, we reach volume increase in volume of 4.5%, compared to the ground state volume (labeled 0%). In the following, we do not study all three phases and possible migration paths, since we are only interested in the trends and thus we focus on the rhombohedral and the tetragonal T^- phases.

Rhombohedral

The migration barriers of the rhombohedral phase with 111-order are plotted in **Fig. 6.8a**. It can be seen that for path 1 the migration barriers decrease with increasing volume. This is an expected result, since the Bi-Na-Ti triangle, through which the oxygen is migrating, is widened. The volume increase of 4.5% leads to a migration barrier reduction. Unexpectedly, for path 2 the migration barrier does not change for different cell volumes. One possible explanation for this behavior is the rigidity of the covalent Ti-O bonds. As said above, in the rhombohedral ground state the Ti ion is displaced towards one face of the surrounding oxygen octahedron, which shortens three bond and lengthen three bonds. When now the volume is increased, the cell does not transform isotropically, but the Ti-O-O-O tetrahedron with shorter bonds stays rigid, whereas the Ti-O-O-O tetrahedron with longer bonds increase in bond lengths, as the bonds are weaker. This result indicates again that the properties and features of the system are extremely dependent on the symmetry of the local environment. All values of the calculations on the rhombohedral phase are summarized in **Tab. 6.2**.
When the structure has 001-order (**Fig. 6.8b**) the situation is different. We have seen that no energy barrier is present for path 1, when the vacancy hops from the mixed layer into

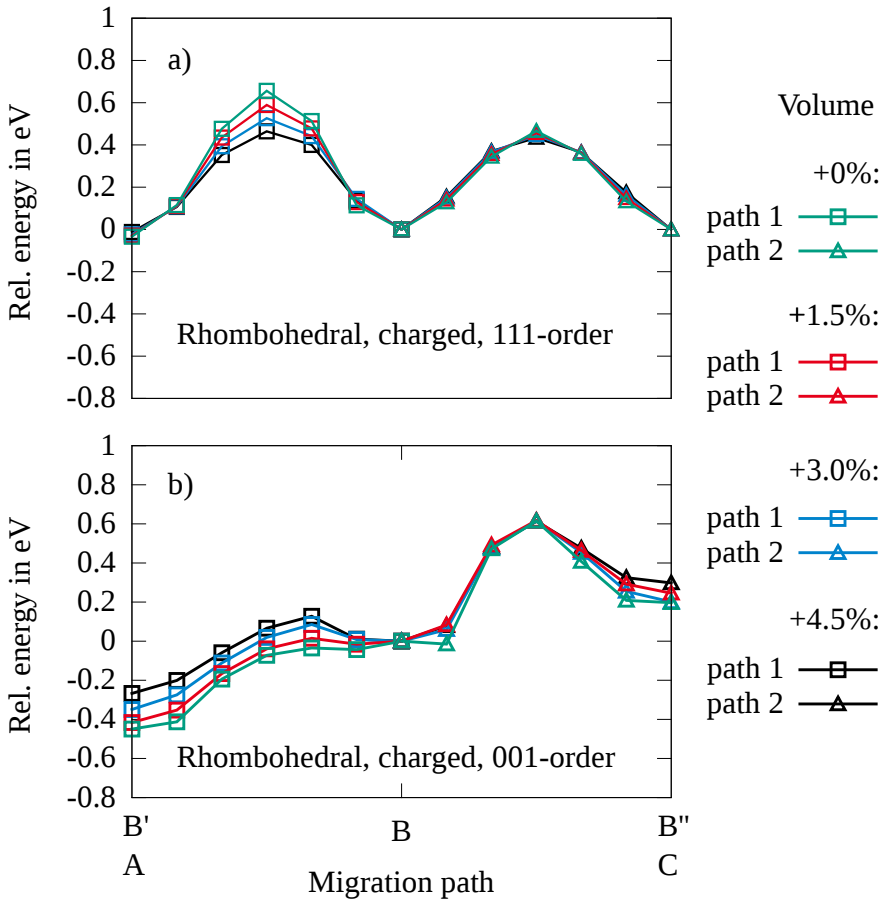

FIGURE 6.8: Volume dependent oxygen vacancy migration barriers of the rhombohedral phase with **a)** 111-order and **b)** 001-order.

TABLE 6.2: Summary of the volume dependent oxygen vacancy migration barriers for the rhombohedral phase. Two different chemical orders are used: 111- and 001-order. The migration paths are along the [001]- and [010]-direction as depicted in Fig. 6.1.

$V_O^{\bullet\bullet}$ migration barriers for the R phase in eV.				
Chemical order	111		001	
Paths	1	2	1	2
Volume 0%	0.66	0.47	0.45-0.54 (0-0.1)	0.61 (0.40)
Volume 1.5%	0.59	0.46	0.43	0.62 (0.41)
Volume 3%	0.53	0.45	0.43 (0.09)	0.62 (0.37)
Volume 4.5%	0.46	0.43	0.39 (0.13)	0.61 (0.31)

the Bi-layer. For an increasing volume a small migration barrier appears. At 4.5% the barrier for the mixed to Bi-layer reaches a height of 0.13 eV.
This finding is in contrast to the one of path 1 for the 111-order, where an increase in volume decreases the migration barrier. A possible explanation for this could be as follows: An increase in volume leads to a reduction of the octahedral tilt angle [89], which is coupled with a decreased displacement of the A- and B-cations. This shift toward the centers of the Ti-O octahedron and Bi-O cuboctahedron might increase the energy barrier for the case with 001-order.

Tetragonal

A somewhat simpler situation is given for the tetragonal phase, which has less A- and B- cation displacements and octahedral tilts and thus a higher symmetry. The migration barriers of the tetragonal structures with 111-order are shown in **Fig. 6.9a** for paths 1 and 2 and **Fig. 6.9b** for paths 3 and 4. However, as it can be seen in **Fig. 6.9a** for paths 1 and 2 the structures start to relax away from the tetragonal structures (due to displacing of Bi and Na away from the high symmetry values). By this, the initial and final states are

TABLE 6.3: Summary of the volume dependent oxygen vacancy migration barriers for the tetragonal phase. Two different chemical orders are used: 111- and 001-order. The migration paths are along the [001]- and [010]-direction as depicted in Fig. 6.1.

$V_O^{\bullet\bullet}$ migration barriers in the T^- phase in eV.				
Chemical order	111			
Paths	1	2	3	4
Volume 0%	0.36	0.40	0.85	0.89
Volume 1.5%	0.32	0.35	0.81	0.85
Volume 3%	0.26	0.30	0.75	0.79
Volume 4.5%	0.19	0.26	0.67	0.70

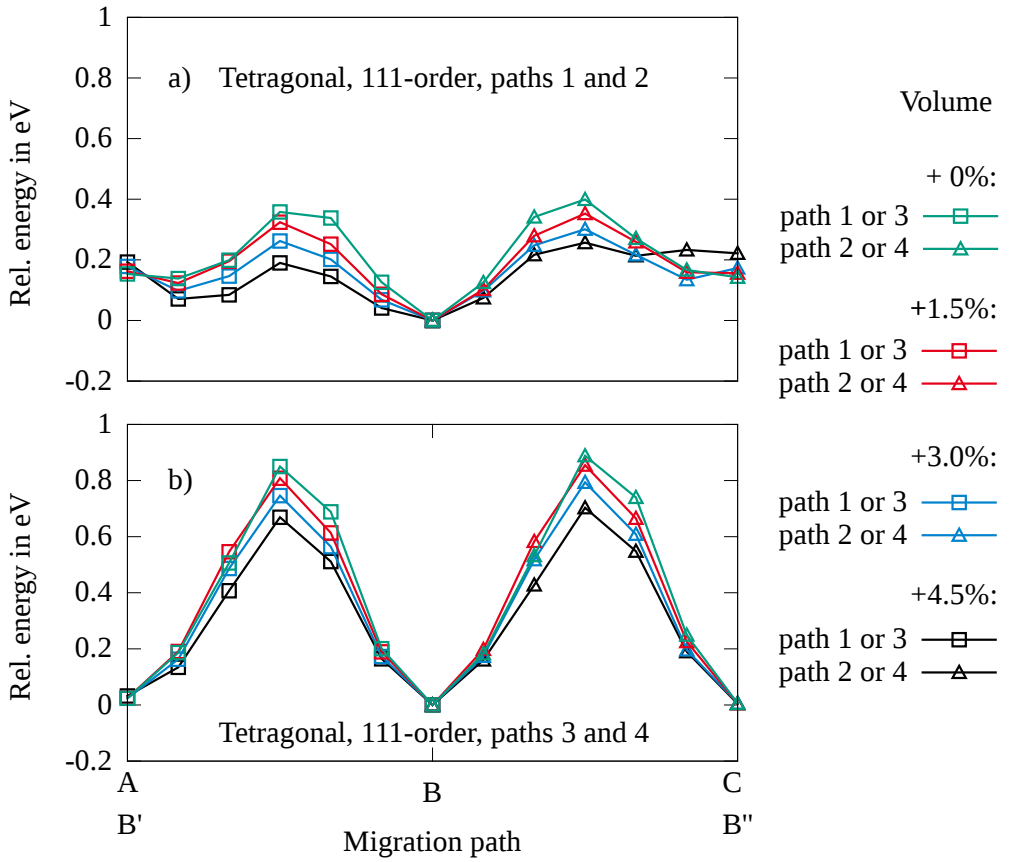

FIGURE 6.9: Oxygen vacancy migration barriers of the tetragonal T^{-} phase at four different volumes with 111-order and **a)** migration along the [001]-direction and **b)** migration along the [010]-direction.

no longer energetic minima and the determination of a barrier is less reliable. Thus, the obtained values cannot be taken for granted.

Paths 3 and 4 in **Fig. 6.9b** still show the same shape of the migration barrier. For an increase in volume from 0% to 1.5%, which relates to an increase in temperature of 500 K, we find a reduction in the barrier of about 0.05 eV. When going from 3% to 4.5% increase, the barriers decreases by 0.08 eV. Thus, a monotonic decrease in the migration barrier can be observed for all paths. The total change in migration barriers, when going from 0% (with around 0.87 eV) up to 4.5% (with 0.67 eV), is about 0.2 eV. These differences, ranging from 0.05 eV to 0.2 eV are significant, but are well below the experimentally observed change in the activation energy of more than 0.4 eV (see Fig. 3.10).

All values of the migration barrier calculations in the tetragonal phases are summarized in **Tab. 6.3**. The values of the calculations on the rhombohedral and tetragonal phases are plotted in **Fig. 6.10**. In summary, it can be seen that some migration barriers decrease, while others stay constant or increase. Thus, this again shows how different the two chemical orders behave.

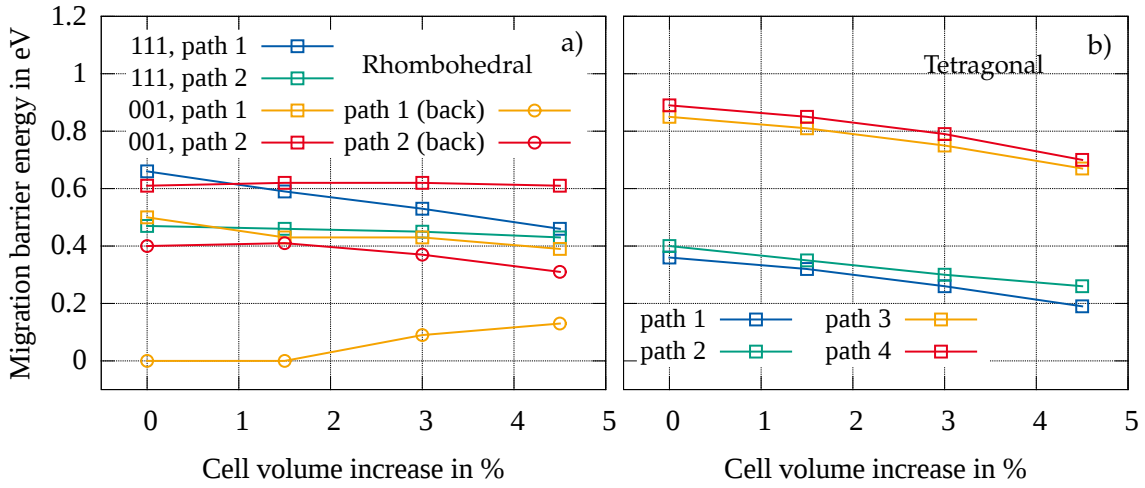

FIGURE 6.10: Volume dependent oxygen vacancy migration barrier heights for the **a)** rhombohedral and **b)** the tetragonal phase.

6.5 Summary

The results of the last chapter can be summarized by the following points:

- Oxygen vacancy migration barriers are different for the rhombohedral, orthorhombic and tetragonal phases, which differ in local tilt order and A-cation displacements. The difference in the lowest migration barriers is between 0.36 eV in the tetragonal and 0.59 eV in the rhombohedral phases, as was seen in Figs. 6.3 and 6.6.
- Because of the lower symmetry of the orthorhombic phase, the migration barriers show values in the range of 0.33 eV to 0.55 eV for the 111-order and up to 1.11 eV for the 001-order (Fig. 6.5).
- Differences in high and low migration barriers can originate from the strained interatomic distances between the migrating and neighboring oxygen ions (Fig. 6.7). This leads to dangling bonds, which create electronic defect states within the band gap.
- The oxygen vacancy migration from the mixed layer to the Bi-layer (only for structures with 001-order) show a very low migration barrier of 0 eV to 0.1 eV (Fig. 6.3). This low barrier should be reflected in the ion conductivity measurements, but there is no sign for such a high mobility, therefore a long-range order layered order of the A-cations can be ruled out. Oxygen vacancies prefer to reside in the Bi-layer, as this configuration shows the lowest formation energy (Fig. 6.3). Thus, trapping of oxygen vacancies in locally 001-ordered regions is possible.
- The shape and height of the migration barriers dependent on the charge of the system (Fig. 6.3). When a neutral oxygen vacancy is created, the migration barriers double in heights and certain aspects, like the very low barrier between the Bi- and mixed layer, vanish.
- The migration barriers are dependent on the volume of the cell (Tabs. 6.2 and 6.3). For the tetragonal phase, the barriers decrease monotonically with an increase in vol-

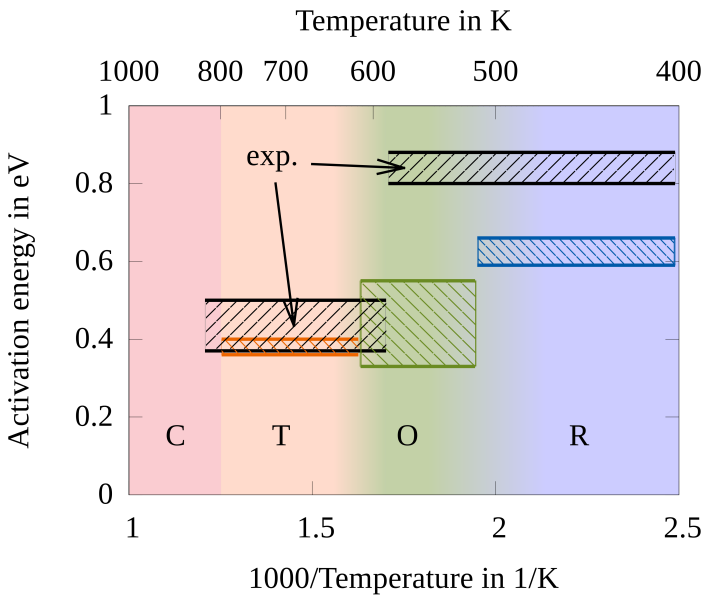

FIGURE 6.11: Experimental oxygen activation energies and calculated migration energies. Experimental data are taken from Li *et al.* [32]. Colors represent the temperature ranges of the cubic (red), tetragonal (orange), orthorhombic (green) and rhombohedral (blue) phases.

ume, as expected for a widening of the triangle consisting of two A-cations and Ti on the B-site, through which the migrating oxygen must squeeze. In the rhombohedral phase the situation is more complex. When the Ti-O bond length are rigid, the migration barriers are independent of the cell volume. For an increasing Ti-O bond length, the migration barriers decrease in height. However, the vanishing barrier for the hopping of the vacancy from the mixed layer into the Bi-layer develops a small barrier with increasing volume.

- Fig. 6.11 compares the migration barriers obtained in this study with the experimentally determined activation energies [32]. The four colored segments depict the temperature regions, where the cubic (red), tetragonal (orange), orthorhombic (green) and rhombohedral (blue) phases are present. A fade in color to the orthorhombic phase was drawn, since the phase transition temperatures are smeared over some range [80, 81]. The colored boxes give the range of the two lowest migration barriers from this study for each of the phases. The black boxes are the activation energies from the conductivity measurements over the temperature range from 400 K to 800 K. At 600 K a large change in activation energy is close to the temperature at which the transition from the orthorhombic to tetragonal phase was suggested [81]. The absolute values of around 0.6 eV in the rhombohedral and 0.4 eV in the orthorhombic phases are smaller than the experimental values of about 0.85 eV [32].

To explain the discrepancy between the experimentally observed change in the activation energies and the migration barriers obtained in this chapter, we inspect the association of dopants and oxygen vacancies in the next chapter.

7 Defect associates

Parts of this chapter have been published in Journal of Materials Chemistry A [317].

In the last chapter on the oxygen vacancy migration we used supercells which contained one single $V_O^{\bullet\bullet}$ oxygen vacancy. In this chapter we introduce additional point defects, in form of Mg and Ni dopants (that replace Ti on the B-site) and Bi vacancies. These point defects can form associates, when occupying lattice sites close to each other. The resulting associates are important when it comes to the migration of oxygen vacancies. For an oxygen ion to migrate, it additionally has to overcome the association energy that binds it to the dopant or Bi vacancy. Associates not only influence the oxygen migration, but also effect the ferroelectric properties, e.g. by domain pinning [178].
Here, we investigate if an association energy exists for the different possible associate complexes and if these energies can explain the difference in the experimentally observed activation energies for low and high temperatures as seen in Fig. 3.10. In the following set of calculations we focus on Mg and Ni doped NBT. We choose these elements, since these were used to enhance the ionic conductivity of NBT in experimental studies. Mg and Ni both have a valance charge of +2 and substitute Ti^{+4} on the B-site. Thus, oxygen vacancies $V_O^{\bullet\bullet}$ are created which compensate the charge. The $Do_{Ti}^{''}$ defects (where Do stands for the dopants Mg or Ni) can form polar defects when they associate with $V_O^{\bullet\bullet}$ defects. Therefore, in the next sections we calculate the binding energy of Mg and Ni dopants with oxygen vacancies.

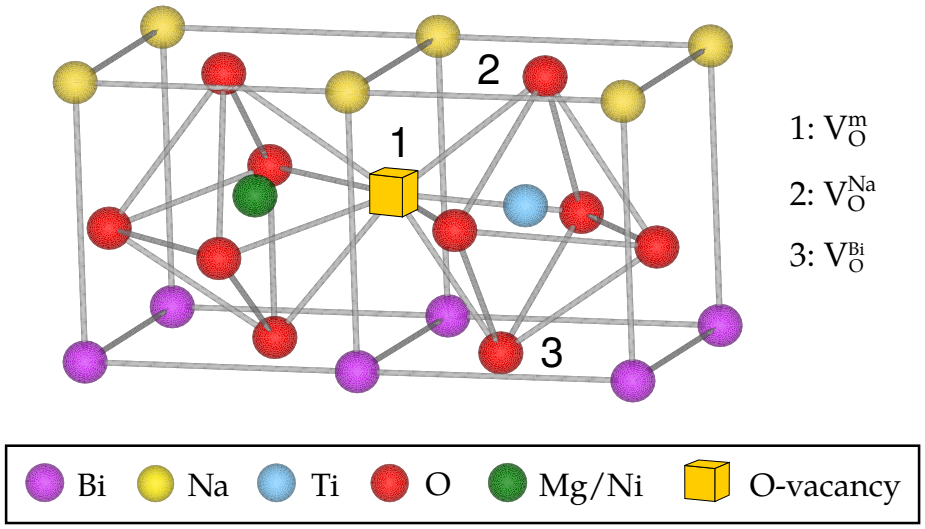

FIGURE 7.1: Positions of the oxygen vacancy $V_O^{\bullet\bullet}$ inside the 001-ordered NBT supercell. Only a 1×2×1 segment of the total 4×4×4 cell is shown. At position 1 the vacancy is situated in the mixed layer between the Bi and Na-layer, thus the label is given the superscript "m". Likewise, the superscript of position 2 and 3 refer to the Bi and the Na-layer.

Computational setup

The energy cut-off for all calculations was again set to 600 eV. Most cells have a size of 4×4×4 ≙ 64 $A'_{0.5}A_{0.5}BO_3$ unit cells (i.e 64 octahedra) and were thus large enough to reduce finite size effects [318]. A single k-point was set for all relaxations and the electric density of states were calculated with a doubling of the k-point density along each direction, resulting in a 2×2×2 k-point mesh. Some cells have a size 2×4×4 or a 4×4×2 and respectively a k-point mesh of 2×1×1 and 1×1×2. The 4×4×4 supercells contain 318 atoms for the calculations of $V_O^{\bullet\bullet}-V_{Bi}^{'''}$ associates and 319 atoms for the $V_O^{\bullet\bullet}-Do_{Ti}^{''}$ associates calculation, where for the dopant Do either Mg or Ni was used. To describe the different vacancies, the Kröger-Vink notation is used. A capital letter denotes the type of defect ("V" for a vacancy or "Mg" for Mg). The subscript gives the site at which the defect is located ("Ti" for a Ti site and "O" for an oxygen site). Superscripts give the relative charge of the defect, from the current charge to the previous charge, as bullets (positive), dashes (negative) and crosses (neutral). For example, Ti has a charge of +4 and Mg of +2, which leaves the resulting defects doubly negatively charged.

Fig. 7.1 explains the labeling of the oxygen vacancies situated at different sites in the NBT supercell. The figure shows an 1×2×1 segment of a 4×4×4 supercell with one dopant (Mg or Ni, green) at the B-site. Bi and Na are ordered in the layered 001-configuration, which results in different possible positioning of the oxygen vacancy (orange) within the oxygen octahedra (red). When the $V_O^{\bullet\bullet}$ is situated between the Bi and Na-layers (position 1) it is labeled V_O^m, where the superscript "m" stands for "mixed", since at this position it has two Bi and two Na ions as neighbors. If the vacancy was at position 2, it is labeled V_O^{Bi}, since it reside in the Bi-layer. The same applies for position 3, where the vacancy V_O^{Na} is within the Na-layer. For 111-order no distinction between positions 1, 2, 3 can be made. All oxygen site have 2 Bi and two Na as neighbors.

As long as the vacancy is at one of the six oxygen sites surrounding the dopant it is referred to as being a next neighbor (1NN). For vacancies situated further away, the labeling 2NN and 3NN respectively refers to the second and third next neighbor. Thus, the vacancy at position 1 is a 1NN and at positions 2 and 3 it a 2NN.

Further, **Fig. 7.1** shows the tilts of the oxygen octahedra. In the rhombohedral phase with $a^-a^-a^-$ tilt, the octahedra are tilted anti-phase-wise, but more importantly the B-site ions are displaced along the [111]-direction. For a structure with 111-order, this leads to three shorter and three longer Ti-O bond lengths. In a 001-ordered cell, where the oxygen ion are slightly displaced towards the Bi-layer, all Ti-O bonds have different lengths, varying from 1.82 to 2.07 Å. From this it becomes apparent that the definition of nearest neighbors is ambiguous. However, we stick to the definition sketched in **Fig. 7.1** and label all positions of the vacancies just as would be for a cell without tilts and displacements, even though keeping in mind that a distribution of bond lengths exist for each next neighbor shell. Therefore, in the following calculations we choose several positions within one next neighbor shell, to check for bond length dependencies of the binding energy.

A similar situation is given in the case of $V_{Bi}^{'''}$ and $V_O^{\bullet\bullet}$ associates. Since the bond lengths within a Bi-O cuboctahedron vary between 2.30 and 3.21 Å the definition of 1NN and the other shells is given for broad ranges of about 1 Å, as will be seen later.

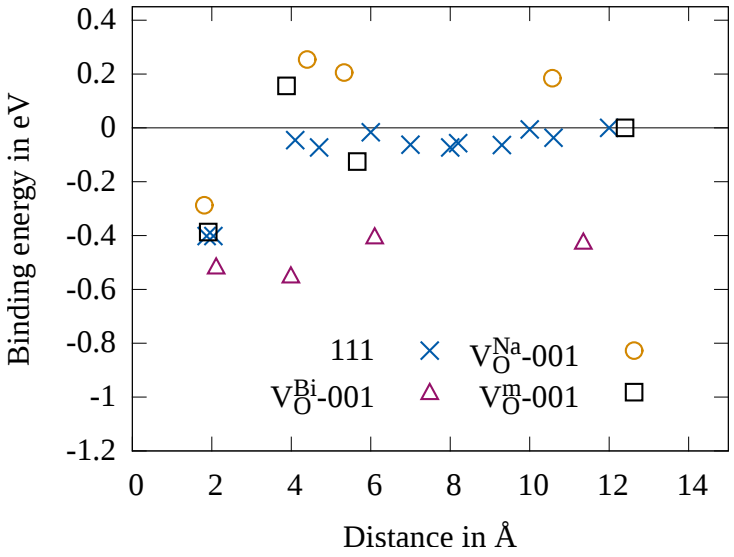

FIGURE 7.2: Binding energy for a $Mg_{Ti}^{''}$ dopant and a $V_O^{\bullet\bullet}$ oxygen vacancy in a 4×4×4 supercell for 111-order and 001-order.

7.1 Mg dopants

First, we look at the binding energies of a $Mg_{Ti}^{''}$ and a $V_O^{\bullet\bullet}$ defect, which are plotted in **Fig. 7.2** for 111- and 001-order. All energies are normalized to the energy of the furthest distance between oxygen and Mg vacancy. For the 111-order (blue crosses) only the energies of the two chosen 1NN positions show a significant deviation from the other energies of about -0.4 eV. From the 2NN positions on the energy is between -0.1 eV and 0 eV.
For 001-order the situation is different. When the oxygen vacancy V_O^{m} is situated within the mixed layer (black squares), the binding energy of the closest neighbor is also about -0.4 eV. When the oxygen vacancy V_O^{Na} is located in the Na-layer (orange circles), the binding energies are shifted upwards by 0.1 eV to 0.2 eV. Interestingly, no change in the binding energy can be found, when the oxygen vacancy V_O^{Bi} resides within the Bi-layer. Whether the oxygen vacancy is a next neighbor of the Mg dopant or further away, the energy is always about 0.5 eV below the energy of the mixed position. However, since no direct migration path from one position A in the Bi-layer to next A exists, a V_O^{Bi} vacancy has first to migrate to a V_O^{m} position, which requires an energy of about 0.5 eV. Therefore, an association energy of -0.35 eV to -0.5 eV for a $Mg_{Ti}^{''}$–$V_O^{\bullet\bullet}$ complex is present in Mg doped NBT, which is in line with the change in the activation energy of Fig. 3.10.
In the study of Koch *et al.* [172] it was suggested that a Mg conentration dependent association exists. Therefore, we study different arrangements of 2 $Mg_{Ti}^{''}$ and 1 $V_O^{\bullet\bullet}$ defect to mimic varying Mg concentrations. In three sets of calculations the 2 $Mg_{Ti}^{''}$ defects are next to each other, second next neighbors and third next neighbors. The distance of the $V_O^{\bullet\bullet}$ is given relative to the closest $Mg_{Ti}^{''}$ ion. **Fig. 7.3** shows the binding energies for the three data sets. It can be seen that the configuration with the 2 $Mg_{Ti}^{''}$ next to each other and the $V_O^{\bullet\bullet}$ far away has the highest energy. When the $V_O^{\bullet\bullet}$ approaches the Mg ions, the en-

ergy decreases, as already was seen in **Fig. 7.2**. However, when the Mg ions get separated, the association energy becomes smaller, since a dissolution $(Mg''_{Ti} - V_O^{\bullet\bullet})^{\times}$ complex requires less energy. Therefore, it appears that the association energy are dependent on the dopant concentration.
As said before, the association of a $(Mg''_{Ti}–V_O^{\bullet\bullet})^{\times}$ complex leads to a polarization that is directed along the bond between the two defects. The interaction between the defect inside the cell and its images beyond the boundaries may effect the association energies. Thus, next we study the influence of an anisotropic supercell by reducing the size of the supercell from 4×4×4 to 4×4×2 and 2×4×4. In the first variant the cell is cut along the [001]-direction, which is along the A-cation stacking, in a second variant along the [100]-

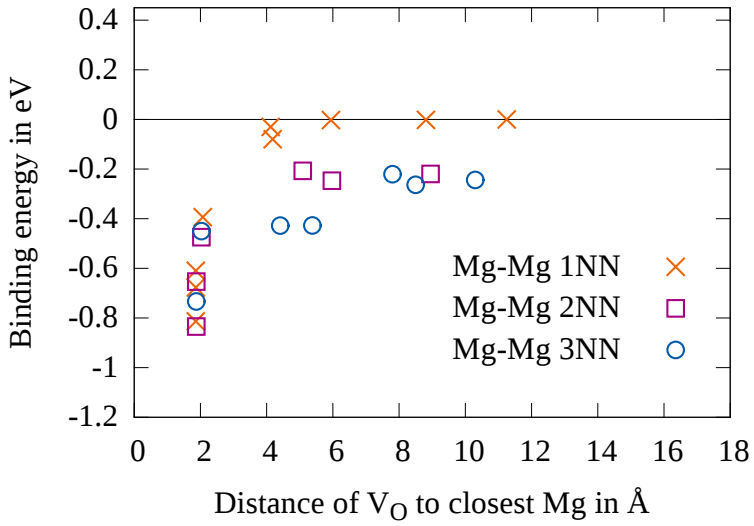

FIGURE 7.3: Binding energy for two Mg''_{Ti} dopants and a $V_O^{\bullet\bullet}$ oxygen vacancy for 111-order.

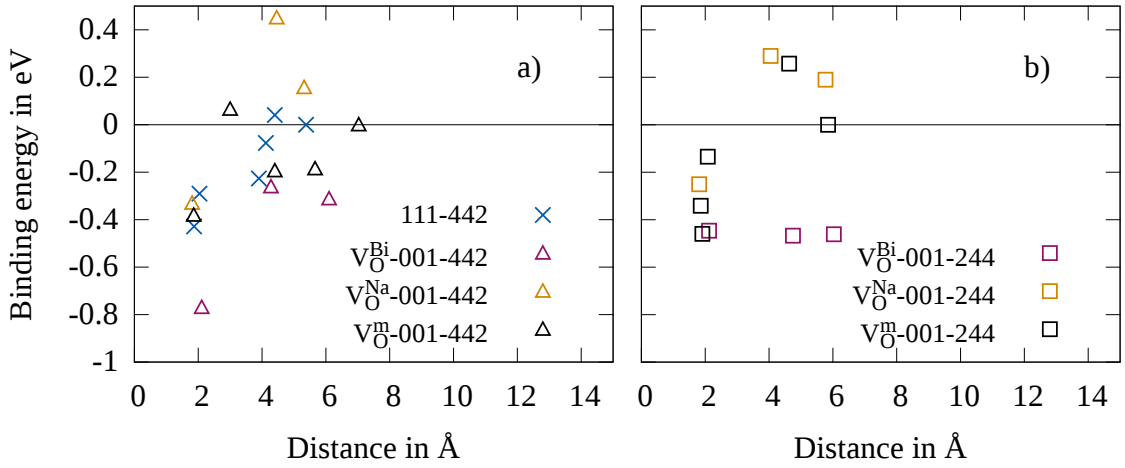

FIGURE 7.4: Binding energy for a Mg''_{Ti} dopant and a $V_O^{\bullet\bullet}$ oxygen vacancy in a **a)** 2×4×4 and **b)** 4×4×2 supercell for 111-order and 001-order.

TABLE 7.1: Binding energies of Mg''_{Ti}-$V_O^{\bullet\bullet}$ associates.

	Binding energies of Mg''_{Ti}-$V_O^{\bullet\bullet}$ associates in eV		
Supercell	444	442	244
111	-0.40	-0.29 – -0.43	–
001-Bi-layer	-0.51	-0.77	-0.45
001-Na-layer	-0.29	-0.33	-0.25
001-mixed-layer	-0.38	-0.38	-0.46

direction. In **Fig. 7.4** it can be seen that the trends for the 4×4×4 cells are approximately kept, however larger fluctuations in the binding energies are observed. The association energy for the 111-ordered cell and 001-order V_O^m defects are still around -0.4 eV and the Na-layer situated V_O^{Na} defects are still the most unfavorable, The biggest difference can be seen in the Bi-layer situated V_O^{Bi} defects. For the 4×4×2 in **Fig. 7.4a** a strong binding of about -0.8 eV for the 1NN oxygen vacancy is observed and a difference of 0.6 eV to the binding energies of other next neighbor shells. In contrast, in the 2×4×4 in **Fig. 7.4b** the binding energies of all next neighbor shells are around -0.4 eV, just as in the 4×4×4 case. All binding energies of the Mg''_{Ti}–$V_O^{\bullet\bullet}$ are summarized in **Tab. 7.1**.
Thus, the anisotropy of the supercell can have a huge impact on the obtained binding energies, as they fluctuate in the order of the association energy. Therefore, one has to be careful, when using supercells that deviate from the isotropic (cubic) cell.

7.2 Ni dopants

Next, we study the binding energies for a Ni dopant, just as in the case of Mg. The scenario is the same as for Mg and one can ask: does an association energy of the $(Ni''_{Ti}–V_O^{\bullet\bullet})^{\times}$ complex exist? But the transition metal Ni is somewhat a more complex ion than Mg and Ti. Whether the charge of Ni is 2+ or 3+, it still has 3d electrons, that need special consideration in DFT calculations. To model these strongly interacting d orbital electrons correctly, one has to add an energy correction term U (given in eV) onto a certain orbital that shifts the respective energy [261]. This is usually used to shift the band gap to the experimental value, but also used to correctly model bond energies. For these so-called "LDA+U" calculations we use a correction parameter of $U = 5$ eV that lies between the values of 4.5 eV and 6.9 eV from Refs. [321] and [322]. As a comparison we also set the parameter to $U = 0$ eV. Ni''_{Ti} – $V_O^{\bullet\bullet}$ binding energies are given in **Fig. 7.5** as orange triangles ($U = 0$ eV) and purple squares $U = 5$ eV. Additionally, the values for Mg dopants are plotted as blue crosses for comparison. Interestingly, the association energies vary from -0.2 eV for $U = 5$ eV to -0.8 eV for $U = 0$ eV. This huge difference in binding energies is larger than the association energy of -0.4 eV of Mg itself. Therefore, it becomes apparent that the choice of the U parameter is essential in determining the correct binding energy. Assuming that the U parameter of 5 eV is close to the correct value, one finds a binding energy of -0.2 eV that is much smaller than the change in the activation energy of the Ni-doped NBT sample in Fig. 3.10.

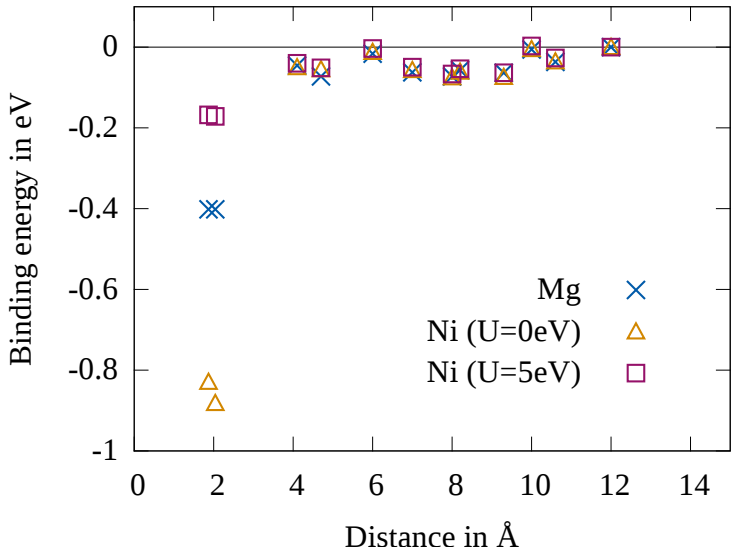

FIGURE 7.5: Binding energy for a Ni''_{Ti} dopant and a $V_O^{\bullet\bullet}$ oxygen vacancy.

7.3 Bi vacancies

As was seen in Fig. 3.10, the kink in the slope of the electric conductivity is also present for non-stoichiometric NBT. Bi and Na non-stoichiometric samples were investigated in several studies, mainly for their electric properties [323–326]. Secondary phases were found in 20% Na and Bi deficient NBT [323], but no secondary phases were reported for moderate doping concentrations of up to 5% [324, 325]. Thus, it can be expected that in the Bi-deficient samples of Li *et al.* the perovskite structure is retained. Still, as seen from Eq. 3.2, a loss in Bi leads to an increase of oxygen vacancies. Actually, for every two Bi vacancies, three oxygen vacancies are created. Therefore, complexes of these vacancies can occur, of which the $(V'''_{Bi} - V_O^{\bullet\bullet})'$ associate with one vacancy of each type is the simplest one. Just as in the previous calculation of the Mg and Ni dopants, we place the two defects at different distances from each other. As explained above, oxygen ions of the Bi-O cuboctahedron, have varying distances, due to the cation displacements and the octahedral tilts. Therefore, different Bi-O pairs can be removed within the 1NN shell.

Fig. 7.6a depicts the binding energies of a Bi and oxygen vacancy for the 1NN, 2NN and 3NN shells for a rhombohedral structure with 111- and 001-order. One of the first aspects that can be seen, is the large energetic difference between the different 1NN configurations. The energies vary by 0.3 eV in the 111-order and 0.6 eV in the 001-order. This is a remarkably high value, since the Bi-O bond is relatively weak [104].

For 111-order the binding energy is not the largest for the 1NN shell, but for the second nearest neighbor position (2NN). This behavior of the binding energy is different from what was seen by Erhart *et al.* in PT [179], where the configuration with the shortest distance between dopant and oxygen vacancy are the energetically lowest. From an electrostatic point of view the positively charged $V_O^{\bullet\bullet}$ oxygen vacancy and negatively charged V'''_{Bi} vacancy attract each other (**Fig. 7.6b**). However, since defects always produce a strain field in their surrounding, in certain cases these strain fields can repel each other, which drives defects

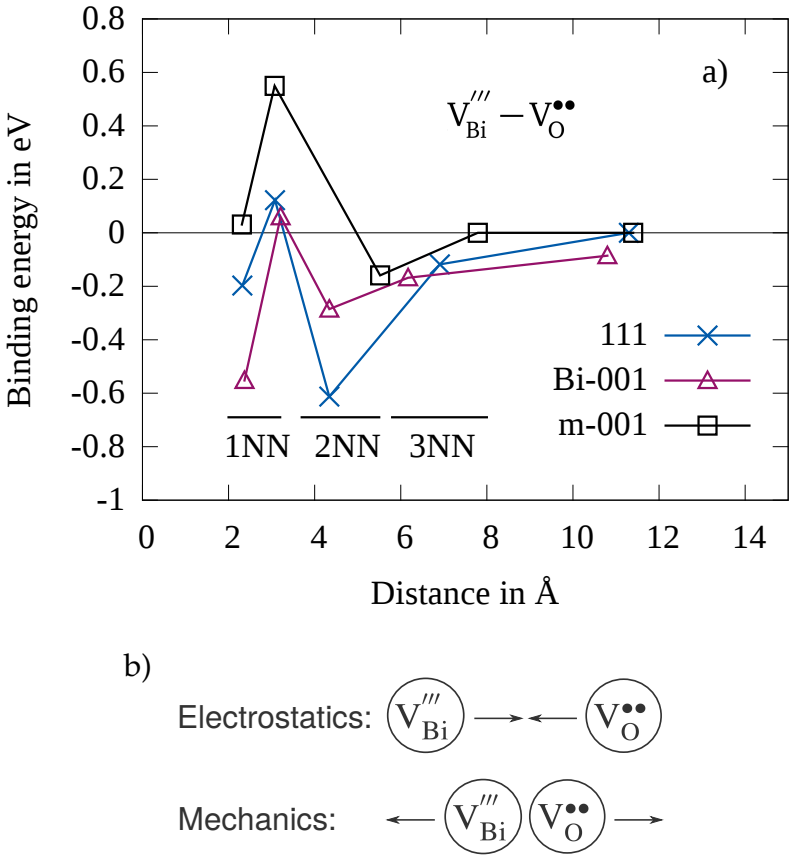

FIGURE 7.6: **a)** Binding energy for a $V^{\bullet\bullet}_{O}$ oxygen and a V'''_{Bi} Bi vacancy for 111- and 001-order for first nearest neighbor (1NN), second nearest neighbor (2NN) and third nearest neighbor (3NN) configurations. Lines are plotted as guide for the eyes.
b) Sketch of an explanation for the second nearest neighbor association energy of an oxygen and Bi vacancy. The differently charged vacancies attract each other, but can produce repulsive strain fields, which result in an energetic minimum for a 2NN configuration.

apart [327, 328]. Thus, a binding energy of about -0.5 eV can be found for 2NN associates, which is similar to the binding energy of the $(Mg''_{Ti} - V^{\bullet\bullet}_{O})^{\times}$ complex.
Fig. 7.7 compares the migration barriers obtained in this study with the experimentally determined activation energies [32]. The four colored segments depict the temperature regions where the cubic (red), tetragonal (orange), orthorhombic (green) and rhombohedral (blue) phases are present. A fade in color to the orthorhombic phase was drawn, since the phase transition temperatures are smeared over some range [80, 81]. The colored boxes give the range of the two lowest migration barriers from this study for each of the phases. The black boxes show the activation energies from the conductivity measurements over the temperature range from 400 K to 800 K [32]. At 600 K a large change in activation energy is close to the temperature at which the transition from the orthorhombic to tetragonal phase was suggested [81]. However, the calculated values of around 0.6 eV in the rhombohedral and 0.4 eV in the orthorhombic phases are smaller than the experimental values of about 0.85 eV. But, given the charge neutrality of the association and dissociation reaction of the $V^{\bullet\bullet}_{O}$ and Mg''_{Ti} defects [174], half of the association energy of -0.35 eV to -0.5 eV has to be added to the migration energy. Thus, the total activation energy coincides with the

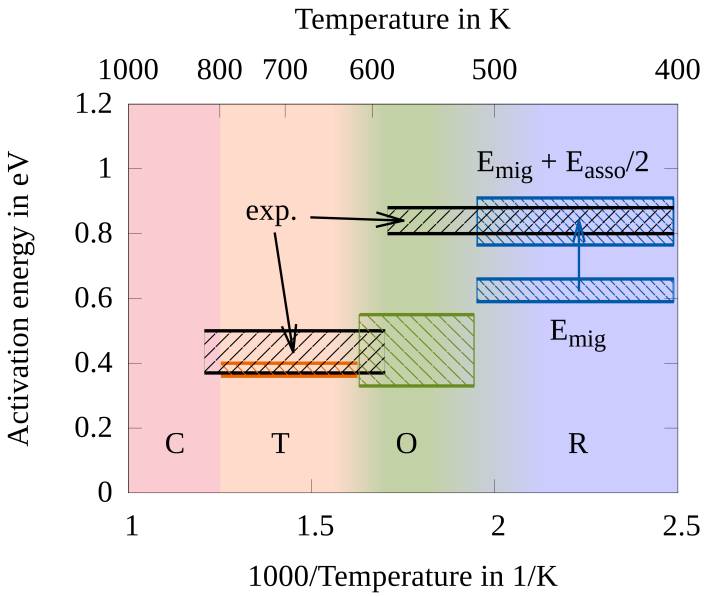

FIGURE 7.7: Calculated and experimental oxygen migration activation energies in NBT. Experimental data are taken from Ref. [32]. Colors represent the temperature ranges of the cubic (red), tetragonal (orange), orthorhombic (green) and rhombohedral (blue) phases. Activation energies at high temperatures are purely due to the migration energy. At lower temperatures the activation energy is a sum of the migration energy E_{mig} and half of the association energy E_{asso}.

experimental one (blue arrow). Therefore, the contribution of the association energy of the $(\mathrm{Mg}''_{\mathrm{Ti}}-\mathrm{V}_{\mathrm{O}}^{\bullet\bullet})^{\times}$ or $(\mathrm{V}'''_{\mathrm{Bi}}-\mathrm{V}_{\mathrm{O}}^{\bullet\bullet})'$ complex to the total activation energy are essential for reaching the experimentally obtained activation energy. At higher temperatures the migration energy is sufficient to explain the experimental activation energy and no association of the oxygen vacancy is required.

7.4 Summary

From the defect association calculations of this chapter we can conclude the following points:

- The association energies for $(\mathrm{Mg}''_{\mathrm{Ti}}\text{–}\mathrm{V}_{\mathrm{O}}^{\bullet\bullet})^{\times}$ complexes are about 0.37 eV to 0.5 eV (Fig. 7.2), which agrees with the experimentally determined change in the slope of the activation energies in the Arrhenius plot of the conductivity [32].
- The association energy for the $\mathrm{Mg}''_{\mathrm{Ti}}-\mathrm{V}_{\mathrm{O}}^{\bullet\bullet}$ appears to be dependent on the concentration of the Mg dopant. This is in line with the analytical model, presented in Ref. [172].
- $\mathrm{Ni}''_{\mathrm{Ti}}-\mathrm{V}_{\mathrm{O}}^{\bullet\bullet}$ complexes exhibit an association energy of 0.2 eV for an U correction parameter of 5 eV (Fig. 7.5). This value is lower than the change in the activation barrier

of the conductivity plot of around 0.6 eV in Fig. 3.10, However, when the U parameter is set to 0 eV, the binding energy increases to 0.8 eV. Thus, the correct choice of the U parameter (which is difficult to determine) is essential to obtain the real binding energy.

- The association of $(V_O^{\bullet\bullet} - V_{Bi}^{'''})'$ complexes in Bi-deficient NBT is somewhat more complex than for the Mg- and Ni-doped cases as it can be seen in Fig. 7.6. A second next neighbor configuration has the lowest binding energy, which might arise from the interplay of an attracting coulomb force and repulsive strain fields.
- Our observations suggest that only a combination of phase dependent association and migration energies can explain the large kink in the slope of the ionic conductivity. The results of chapters 6 and 7 are summarized in Fig. 7.7.

8 Electrocaloric effect in $BaTiO_3$

After having studied phase transformations, oxygen migration and defect associates of NBT in the previous chapters, this chapter deals with the ECE. It would be desirable to apply the following MC and MD models directly to NBT. But as we have seen, there are too many degrees of freedom, which can not be properly described, let alone octahedral tilts are very difficult to implement. Thus, we restrict ourselves in the MC model to a simple description of a relaxor and do not look at relaxors in the MD simulations at all.
The first aspect is to study whether relaxor RFE systems are able to enhance the EC temperature change and tune the usable temperature range, compared to ferroelectrics (FE) and antiferroelectrics (AFE). A second focus of this chapter is on the influence of polar defect dipoles on the ECE, since it has already been shown that defect dipoles can strongly alter the ECE [224]. The electrocaloric temperature change is studied by means of two methods: Monte Carlo (MC) and molecular dynamics (MD) based on an effective Hamiltonian. In the first part, the ECE is investigated via MC simulations of defect-free FE, AFE and relaxor-like systems (RFE) and afterwards defect dipoles are introduced. In the second part, the effective Hamiltonian MD is used to describe the ECE in BT for defect-free and defect containing systems. A relevant question for all calculations is whether a negative EC temperature change can be observed, as was in the experiments in AFEs [30, 218] and FEs containing polar defects [220, 224].

8.1 Monte Carlo simulations

[1] First, we describe how the different material classes RFE, FE and AFE are modeled within an Ising-like model. The Hamiltonian of this model was given in Eq. 4.33. As shown in **Fig. 8.1a**, the interaction strength between the polarization vectors is controlled by the Ising parameters J_{ij} which are Gaussian distributed around a mean value J_0 with a standard deviation of ΔJ. If all J_{ij} are positive, neighboring polarizations want to align and thus the material behaves as a ferroelectric. If J_{ij} are negative, polarizations align antiparallel and the material becomes antiferroelectric. Last, in the case that J_{ij} has both negative and positive values, the material behaves like a relaxor. For the first set of calculations, in which we focus on the Ising parameters, the random fields $\boldsymbol{h}$ are set to zero.
To illustrate the different behaviors the polarization-electric field hysteresis loops are given for the FE → RFE transition in **Fig. 8.1b** and the AFE → RFE transition in **Fig. 8.1c**. In **Fig. 8.1b** it can be seen that the FE system shows a large coercive field, which decreases with increasing ΔJ. The final curve (purple, $J_0 = 2$, $\Delta J = 5$) exhibits a much narrower hysteresis, as is expected for a relaxor material (compare with **Fig. 3.9**). A similar process can be found for the AFE system in **Fig. 8.1c**. The typical double S-curve vanishes for increasing ΔJ and finally results in a very narrow hysteresis, as it is expected for a RFE.

[1] The content of this section was mapped out in collaboration with Constanze Kalcher, who performed the simulations and created the figures.

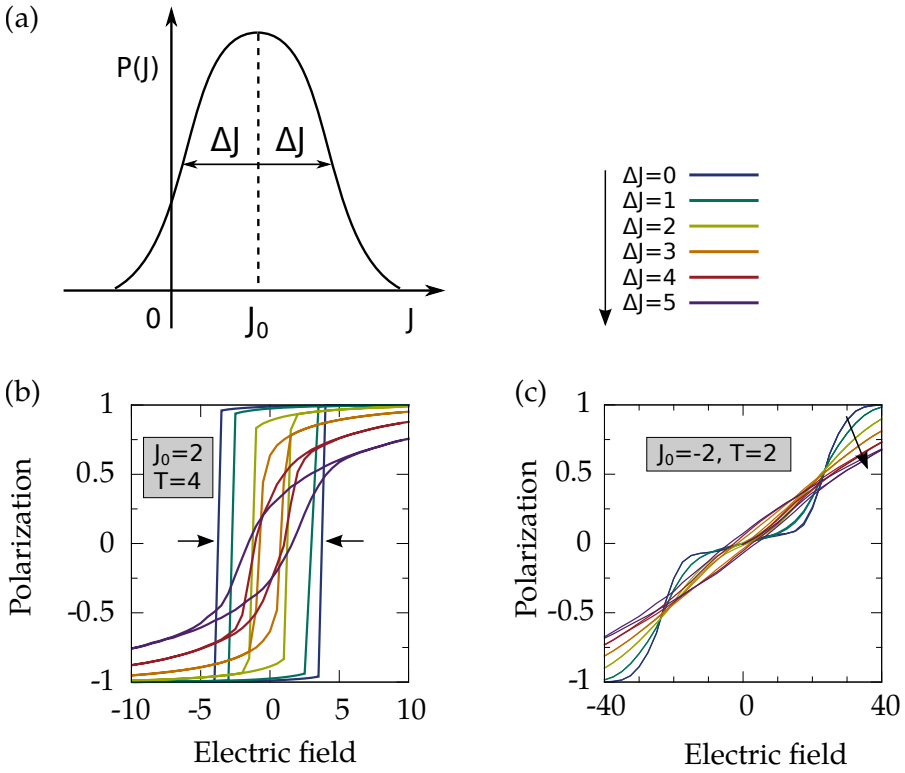

FIGURE 8.1: **a)** The Ising parameters J_{ij} have a gaussian distribution with a mean J_0 and a standard deviation of ΔJ. In **b)** polarization-electric field hysteresis curves for $J_0 = 2$ and varying ΔJ ($0 \geq \Delta J \geq 5$) are given to show the transition from the ferroelectric to the relaxor-like case. **c)** shows the transition from the antiferroelectric to relaxor-like case with $J_0 = -2$.

8.1.1 Defect-free

Figs. 8.2a shows the EC temperature change at different temperatures for various electric fields for an antiferroelectric system. As expected, a negative ECE can be observed in the AFE case (**Fig. 8.2a**) for a small value of the electric field and at lower temperatures. When the electric field change and the temperature is increased ($E > 40$ and $T > 7$ for $J_0 = -2$ and $\Delta T = 1$), the negative effect vanishes. The antiferroelectric system experiences a positive ECE only for higher electric fields or temperatures. For a relaxor-like case the temperature change is always positive (**Fig. 8.2b**).
To understand the origin of the negative ECE in antiferroelectrics, we study two dimensional slices of the polarization configurations at $T = 5$ (see circle in **Fig. 8.2a**) which are depicted in **Fig. 8.2c**. On the left, which shows the initial configuration at $E = 0$, the spins align antiparallel and thus have a small configurational entropy. If now a small field $E = 10$ is applied along the z-direction (**Fig. 8.2c** right), the polarization vectors partially align along the external field, which induces disorder and therefore increases the configurational entropy. Therefore the vibrational entropy decreases of Eq. 3.8 and the temperature of the sample goes down (negative ECE). In comparison, **Fig. 8.2d** illustrates the polariza-

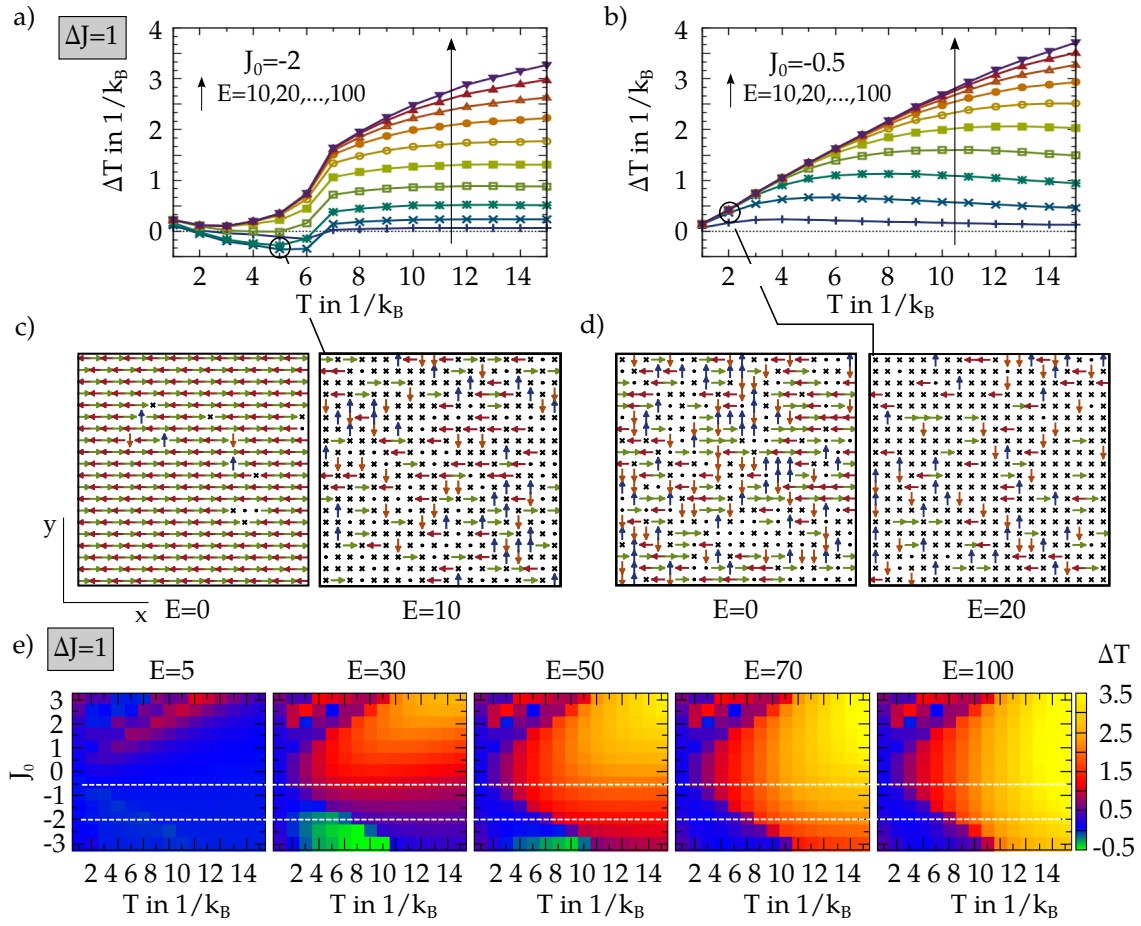

FIGURE 8.2: Electrocaloric temperature change for various electric fields in **a)** an antiferroelectric and **b)** a relaxor-like system. Two dimensional slices of the configurations of the polarization vectors are displayed in **c)** and **d)** for snapshots taken from **a)** and **b)**, respectively. The left figures in **c)** and **d)** show the configuration of the polarizations at zero field and the right figures show the configuration for small electric fields. **e)** Electrocaloric temperature change contour plots for J_0 varying from -3 (AFE) to 3 (FE) at different electric fields. The curves in **a)** and **b)** can be found as horizontal white lines at $J_0 = -0.5$ and -2.

tions in the initial $E = 0$ configuration (left) and at $E = 10$ (right), see circle in **Fig. 8.2b**. Here, due to the distribution of positive and negative Ising parameters disorder is already present in the system for no electric field. When the electric field is switched on, an alignment of the polarization vectors along the external field appears, which leads to a decrease in configurational entropy and an increase in temperature (positive ECE). Thus, the sign of the EC temperature change is different for the antiferroelectric and relaxor-like systems, which can be explained solely by the different dipole configurations.

Now, keeping $\Delta J = 1$ constant, we change the mean Ising parameter step-wise from -3 (AFE) through 0 (RFE) to +3 (FE) and examine the change in the ECE. **Fig. 8.2e** shows contour plots for five different electric fields in which the change in the temperature is given in colors. Blue indicates no or a small temperature change, red and yellow a large

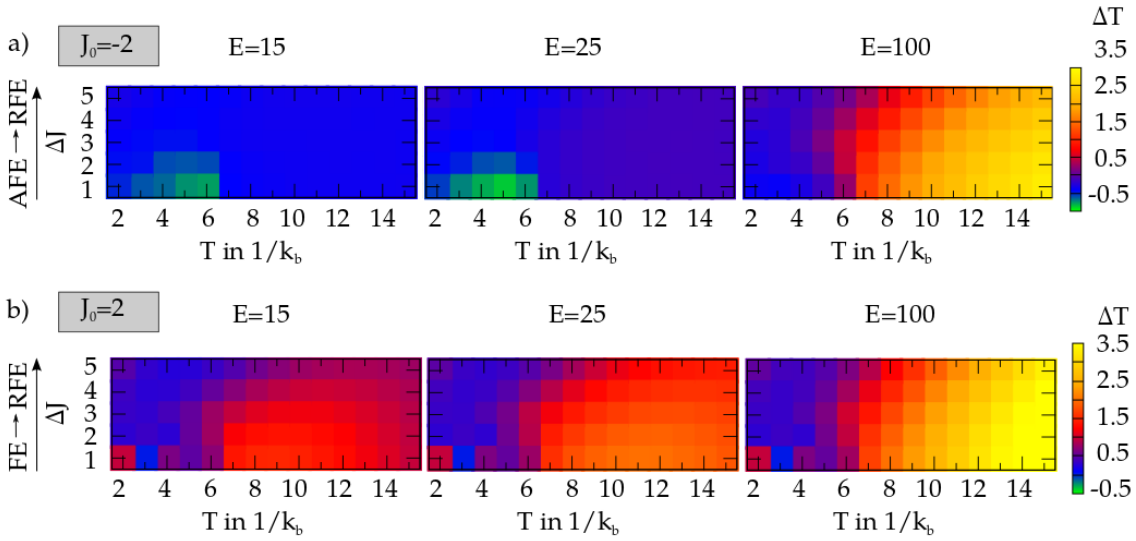

FIGURE 8.3: Electrocaloric temperature change for a transition of an **a)** antiferroelectric to a relaxor-like system and **b)** a ferroelectric to relaxor-like system by increasing ΔJ. As in Fig. 8.2, for the antiferroelectric system the negative temperature change disappears for $\Delta J \geq |J_0|$.

change and green a negative change. The horizontal dotted lines at $J_0 = -0.5$ and $J_0 = -2$ show the positions of the curves from **Fig. 8.2a** and **Fig. 8.2b**. It can be seen that the EC temperature change shifts continuously in temperature during the transition from the AFE to the FE case. For most temperatures, electric fields and J_0, a positive ECE is observed. Only when the number of positive Ising parameters is negligible (as in the AFE state) the negative temperature change can be observed. For higher electric fields the AFE case is similar to the FE case, although it has a slightly smaller maximum temperature change.
In the following, we investigate the transitions from the AFE to RFE and FE to RFE by changing the standard deviation of ΔJ and keeping J_0 fixed at -2 and +2, respectively.

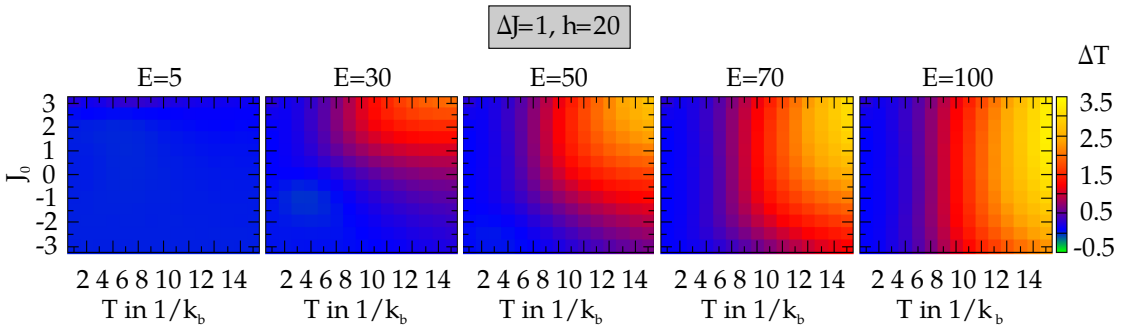

FIGURE 8.4: Electrocaloric temperature change for various Ising parameters J_0 and electric fields with random fields set to $|\boldsymbol{h}| = 20$. The random fields remove the negative temperature change in the antiferroelectric system (compare with Fig. 8.2e).

Fig. 8.3 shows how the EC temperature change evolves. The relaxor-like systems (large ΔJ) show either no ECE when a majority of J_{ij} is negative or a positive ECE for positive J_{ij}. However, the AFE system exhibits again the negative ECE in **Fig. 8.3a**, but the effect vanishes when the distribution is broader than the mean Ising parameter ($\Delta J \geq |J_0|$), as we have seen in **Fig.8.2e**. Thus, even if the Ising parameters are much smaller than zero in average, the negative ECE disappears when a certain number of ferroelectric interactions (positive J_{ij}) are present in the system. **Fig. 8.3b** shows that the achievable temperature change decreases when the system is transformed from a ferroelectric to a relaxor. In both cases the distribution width ΔJ becomes negligible for high electric fields, although the relaxor systems have a slightly reduced ΔT.
So far, we have not considered random fields in the calculation of the ECE. Even though Akbarzadeh *et al.* [147] stated that random fields (and random strains) do not significantly affect the ECE, random fields are an essential part in the description of relaxor ferroelectrics. Thus, in this section, the influence of random fields on FE, AFE and relaxor-like systems will be investigated. Comparing the cases of J_0 = -3, -2, ... , +2, +3 and fixed J_{ij} = -1 in Fig. 8.2e and the one with additional random fields in **Fig. 8.4**, one can see that random fields reduce the EC temperature change ΔT for all electric fields. In contrast to the antiferroelectric systems without random fields, much higher electric fields are needed to obtain the same electrocaloric temperature change. At intermediate electric fields the ECE is present only for the FE and relaxor-like systems, but not for the AFE system. Only for very high electric fields the random fields stop playing a role and the temperature change is similar for all systems and has the same magnitude as without random fields. Therefore, random fields contribute to disorder in the dipole configuration for the initial and the final states and are thus decrease the achievable maximum entropy change and therefore are detrimental to the ECE. Hence, for the following calculations we leave out random fields and set $|\boldsymbol{h}| = 0$.
In the next section we study the influence of static defect dipoles on the ECE.

8.1.2 Polar defects

In the last section we have shown that the negative temperature change exists when the system behaves as an antiferroelectric material. In this section we introduce defects which have polarizations that are not allowed to switch in direction or magnitude. **Fig. 8.5a** displays ΔT for a ferroelectric ($J_0 = 2$) and **Fig. 8.5b** for an antiferroelectric (J_0 =-2) system with defects parallel (par) and antiparallel (apar) to the external field. $\Delta J_0 = 0$ is fixed for both cases. Most importantly, a negative temperature change can be seen for the ferroelectric system at $E = 3$ when antiparallel oriented defects are present. This effect appears for defect concentrations of 10% or higher. The explanation for this effect is similar to the antiferroelectric system without defects from Fig. 8.2. At low electric fields the polarization vectors align parallel along the polarizations of the defects. When the electric field increases, some polarizations are able to flip and align along the external electric field. This leads to a decrease of order and thus an increase of the configurational entropy. When the electric field is raised to even higher values (see Fig. 8.5a at $E = 30$), most of the polarization vectors (not just a few) tend to align with the external field which again decreases the order and thus the entropy. For higher temperatures the negative effect vanishes since the system becomes disordered already in the initial state when no electric field is present.

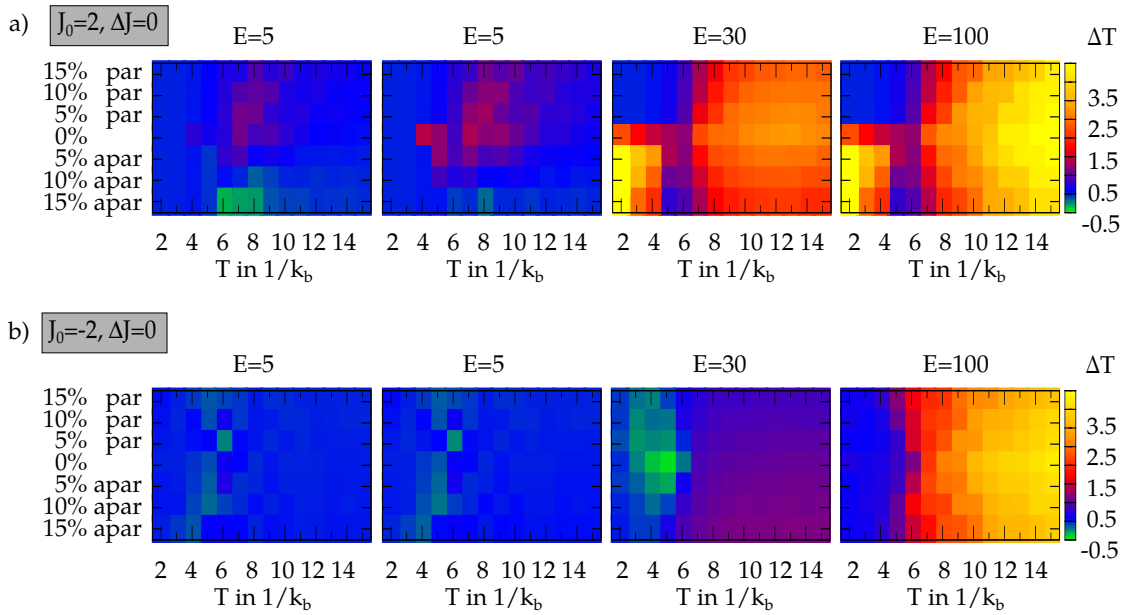

FIGURE 8.5: Electrocaloric temperature change for various concentrations of parallel (par) and antiparallel (apar) defects in **a)** a ferroelectric and **b)** an antiferroelectric system. The negative electrocaloric effect becomes visible for antiparallel defects in the ferroelectric and in the antiferroelectric system. The negative temperature change in the antiferroelectric system decreases with an increasing concentration of defects.

The application of the electric field leads to an ordering of the polarizations and therefore a positive ECE. At high electric fields the curve for the temperature change becomes similar to the system without defects (compare Fig. 8.5a and Fig. 8.2e).
In the antiferroelectric system the negative temperature change is the strongest when no defects are present, see $E = 3$ in **Fig. 8.5b**. Both parallel and antiparallel defects decrease the effect since any type of defect leads to an increase of the disorder of the polarization vectors in the initial state which lowers the change in total entropy when an electric field is applied.
In reality, defect dipoles are not static, but are able to reorient. This rearrangement and ordering of the polar defects are a reason for aging and fatigue in ferroelectrics [180, 183, 329]. Aging is the change in the material properties without changing the external conditions. Fatigue in contrast is the change in the material due to varying external conditions, like electric fields or strain. For the ECE the influence of the electric field on the polar defects are of importance. When the alternating external field has a high frequency compared to the switching times of the defect dipoles, they will rearrange and a higher concentration of parallel defects appear [179]. **Fig. 8.6** shows how the EC temperature change behaves for a ferroelectric system ($J_0 = 2$ and $\Delta J = 0$) with a defect concentration between 15% of parallel and 15% of antiparallel defects. As was seen in **Fig. 8.5a** a negative EC is present when antiparallel defects exist in a high concentration. The negative change in temperature persists up to a concentration of 10.5% antiparallel and 4.5% parallel, but only for very low fields. At slightly higher fields the number of antiparallel defects has to be even closer to 15% to retain the negative change. The effect vanishes for electric

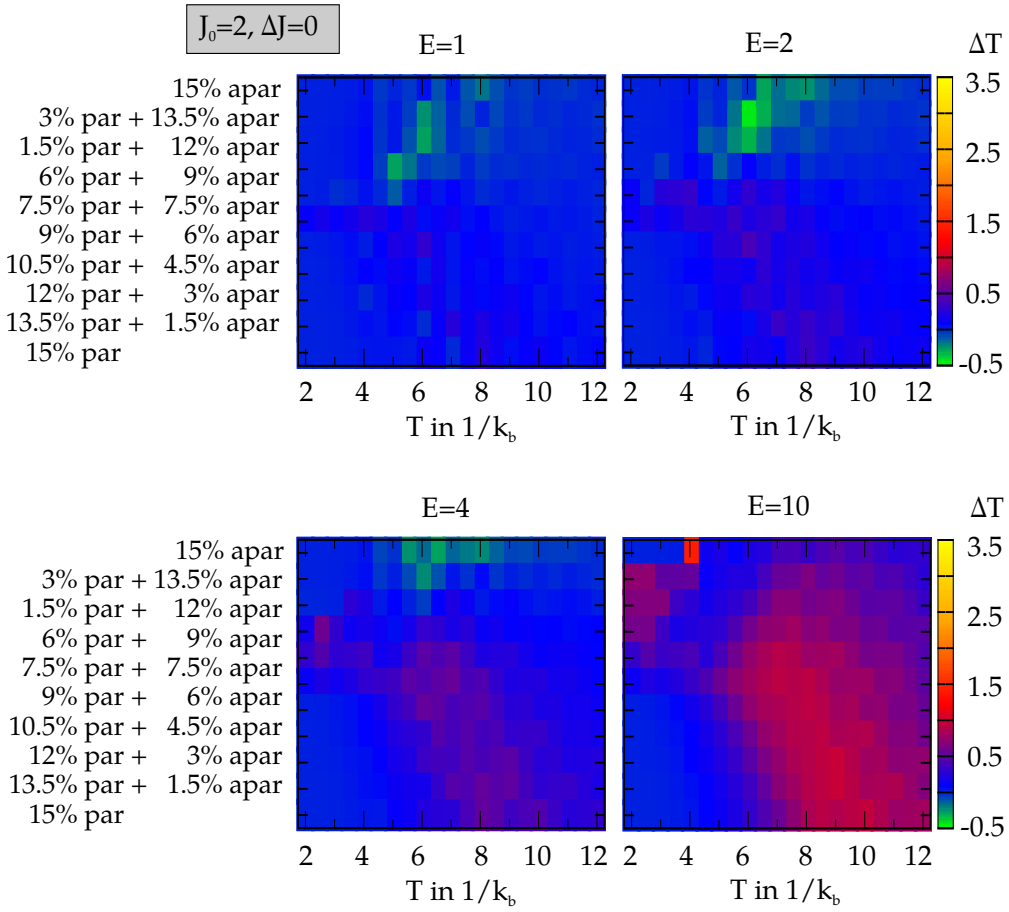

FIGURE 8.6: Electrocaloric temperature change in a fatiguing ferroelectric system. The system starts either in a configuration where all defects are aligned parallel (15% par) or antiparallel (15% apar) to the external field and ends in a configuration where the amount of parallel and antiparallel defects are equal (7.5% par and 7.5% apar).

fields larger than 10. When the system contains 7.5% of antiparallel and 7.5% of parallel defects, the negative EC disappears for all temperatures and electric fields. However, at intermediate fields and temperatures $T > 5$ the positive ECE appears. This fatigue effect may play a major role in all applications, where the negative ECE, arising from antiparallel oriented defect dipoles, is exploited.

The MC simulations of the previous subsection have investigated the trends of the ECE for FE, AFE ad RFE materials, with and without polar defects. Further, the Ising-like model is very simplistic and could not give any quantitative values, only trends could be obtained. In this section, we perform molecular dynamics simulations to study, whether the results from the MC calculations can also be seen in a model that is based on *ab initio* parameters and is thus closer to real systems.

Fig. 8.7 shows the EC temperature change ΔT for a range of 0% to 3% parallel defects of strength $0.5\,\mathrm{Cm}^{-2}$, which is in the same order as real dipole defects [31]. For 0% defects the feram calculations give values of around 6 K for the EC temperature change, which is much higher than the ones obtained from experiment for BT, where the values are $\Delta T \approx 1\,\mathrm{K}$ [229]. This is due to the fact that in the experimentally studied samples imperfections, domains and interfaces are present, whereas in the calculations a defect-free crystal lattice is used [300]. When 1% defect dipoles are present, the temperature change decreases slightly and the maximum peaks shift from 510 K to 610 K. For a higher defect concentration the EC peak shifts to even higher temperatures. These findings are in line with the ones obtained from the Ising-like calculations of Fig. 8.5 and from the Ginzburg-Landau MC calculations of Ma *et al.* [31].

When antiparallel defects are introduced into the system, the results are more complicated. **Fig. 8.8** shows the EC temperature change for three different defect dipole strengths. The temperature changes for a system without defects are given as reference. Firstly, in **Fig. 8.8a** weak defect dipoles of $0.25\,\mathrm{Cm}^{-2}$ are chosen. The introduction of 1% defects inverts the temperature change for temperatures in the range of 400 K to 470 K. However, a small

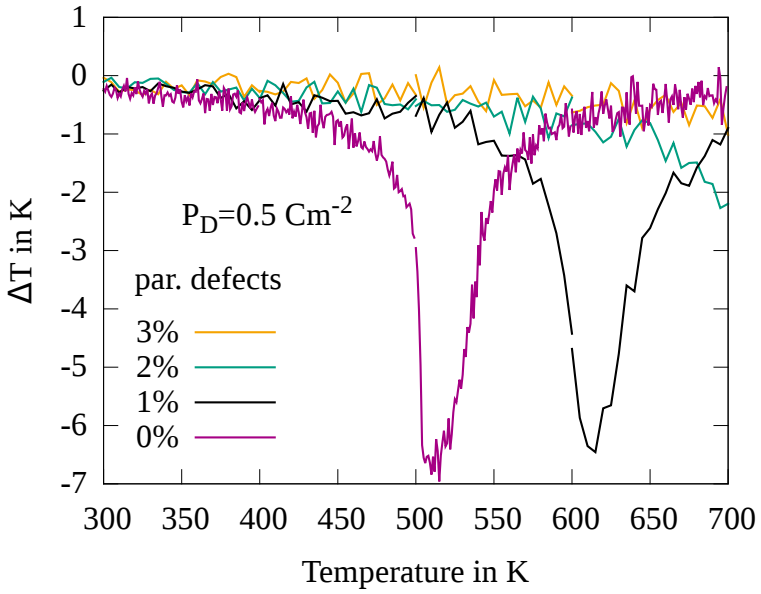

FIGURE 8.7: Electrocaloric temperature change ΔT in $BaTiO_3$ for different amount of defects oriented parallel to the external electric field. The electric field was decreased from $E = 100\,\mathrm{kV/cm}$ down to $E = 0\,\mathrm{kV/cm}$.

positive ECE is still present up to 400 K. These kind of sharp transitions have also been reported from MC calculation [31]. The shape of the 1% peak can be understood by looking at the temperature dependent polarization of the system in **Fig. 8.9a**, before and after the removal of the electric field. After the first equilibration phase in the $E = 100\,\mathrm{kV/cm}$ electric field, the polarization is directed along the external field, the z-direction, for all

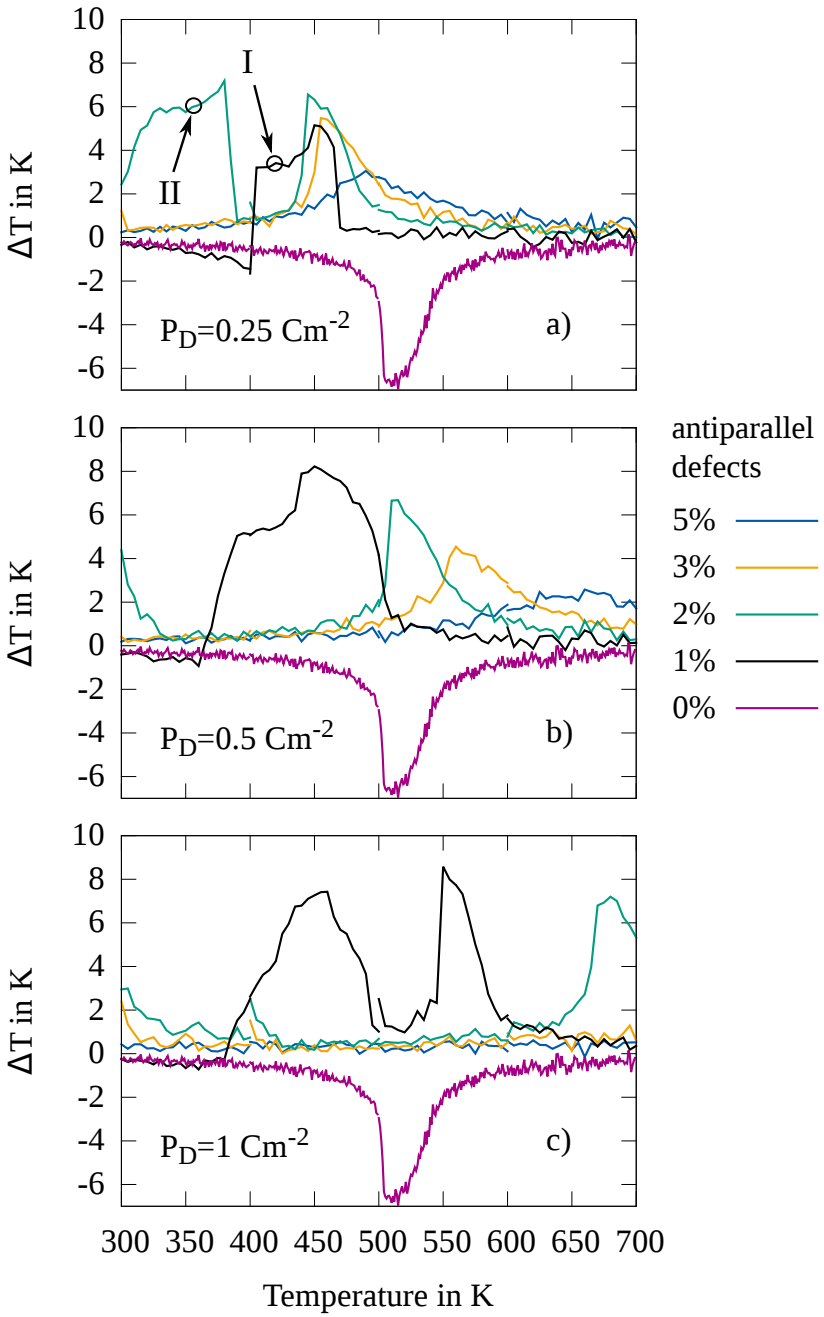

FIGURE 8.8: Electrocaloric temperature change ΔT in $BaTiO_3$ for different amount of defects oriented antiparallel to the external electric field with a defect polarization of **a)** 0.25 C/m^2, **b)** 0.5 C/m^2 and **c)** 1.0 C/m^2. The electric field was decreased from $E = 100\,\mathrm{kV/cm}$ down to $E = 0\,\mathrm{kV/cm}$. Polarization of systems labeled I and II are displayed in Fig. 8.9.

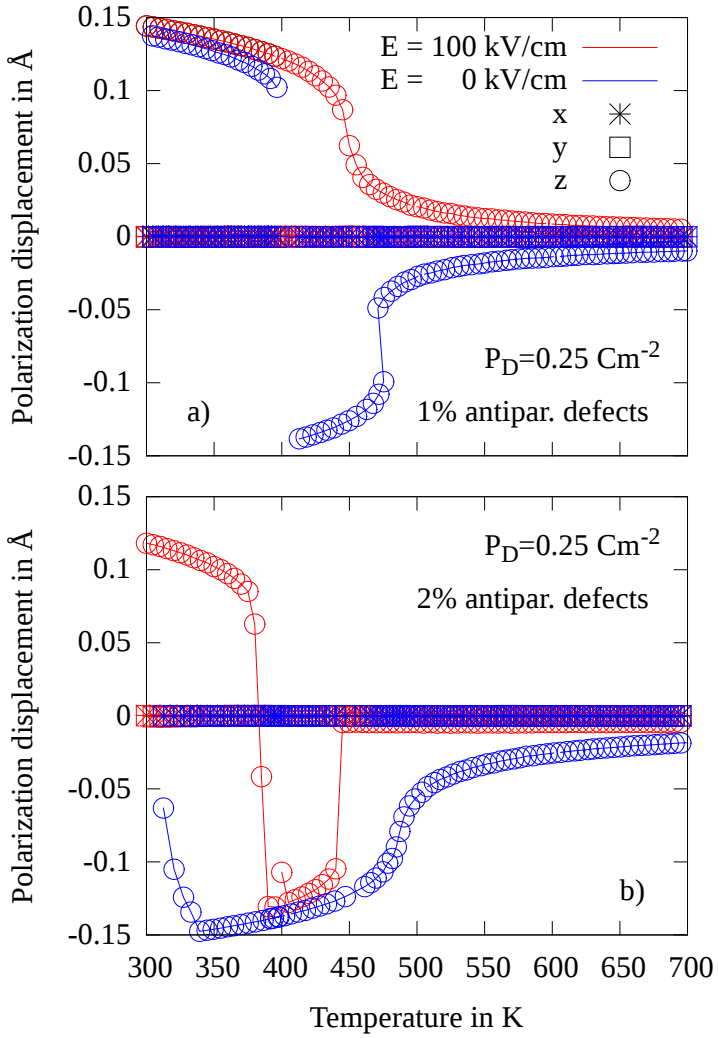

FIGURE 8.9: Temperature dependent polarization, before and after application of an electric field with defect dipole strengths of 0.25 C/m^2 and **a)** 1% and **b)** 2% defect dipoles. The electric field was decreased from $E = 100$ kV/cm down to $E = 0$ kV/cm.

temperatures. Up to 400 K, hardly any change in the polarization can be observed, when the electric field is turned off. Above 400 K, the thermal vibrations are large enough to flip the polarization vectors in the opposite direction, which then align along the antiparallel defect dipoles. At 470 K the transition to the cubic phase occurs, which reduces the total polarization of the system. Thus, the height of the EC peak depends on the difference in the polarization before and after the removal of the electric field.
For 2% antiparallel defects the negative ECE gets even larger and no positive ECE is visible anymore. Interestingly, a second negative EC peak appears at lower temperatures. This can again be explained by the polarization change, as seen **Fig. 8.9b**. In this case, the 2% antiparallel defects produce a large enough internal electric field, that the polarization switches into the negative z-direction, when no external electric field is present. The height in the EC peak is again given by the difference in the magnitudes of the polarization before and after removal of the electric field.

When the defect concentration is increased even further (>3%) the EC peak decreases and shifts slightly to higher temperatures.
The situation is similar when the strength of the defect dipoles is doubled to the value of 0.5 Cm^{-2}, which is displayed in **Fig. 8.8b**. The largest negative EC peak is observed for the system with 1% antiparallel defects. For 2% the peak shifts towards higher temperatures by 100 K. Also the peaks of 3% and 5% defects are shifted upwards. When the defect dipole strength is increased to 1.0 Cm^{-2} (**Fig. 8.8c**), the peaks again shift towards higher temperatures.
Thus, a delicate interplay between the external electric field and the internal electric field, arising from the defect dipoles, determines the resulting shape of the ECE. The strength of the internal electric fields depends on the concentration of the defect dipoles and their polarization strength. This result was also observed in the simple Ising-like simulations above and the Ginzburg-Landau based MC simulations [31].

8.3 Summary

The results of this chapter can be summarized as:

- Any introduction of disorder, either by random fields, a distribution of positive and negative Ising parameters (relaxor-like system) or introduction of polar defects decrease the magnitude of the ECE. The highest degree of order (lowest entropy), and thus the highest EC temperature change, can be achieved in ferroelectrics. Relaxor-like systems show a slightly reduced EC temperature change, but which are comparable in magnitude. This is in line with an experimental study [219] and one recent theoretical study [330].
- The 3D Ising-like model can reproduce the experimentally observed negative electrocaloric effect for antiferroelectric materials (Figs. 8.2 and 8.3). The negative effect exists only at low temperatures and small electric fields that disturb the antiferroelectric ordering.
- The ECE is strongly influenced by the presence of defect dipoles (Fig. 8.5). 1) The incorporation of defects parallel to the external field shifts the ECE peak to higher temperatures, but decreases the achievable temperature change. 2) For a ferroelectric system with polar defects, which polarizations are oriented antiparallel to the external field, a negative ECE is observed.
- The sign of the EC temperature change depends on whether the configurational entropy of the polarization vectors increases or decreases after the removal of the electric field. This is dependent on the relative strengths of the internal electric field (arising from defect dipoles) and the external electric field.
- When the system experiences fatigue (parallel and antiparallel defects are present at the same time), the negative ECE vanishes (Fig. 8.6).
- MC simulations (without strain coupling) and MD simulations (strain coupling included) agree qualitatively. From this, we conclude that strain-coupling is a minor aspect when investigating the ECE.

9 Conclusions

This work was separated into several parts. In the first part, first-principles DFT calculations were used to shed light on the atomistic kinetics of NBT, including phase transformations, oxygen vacancy migration and oxygen vacancy defect association. Secondly, we used MC and MD simulations to study the influence of polar defects on the electrocaloric effect in ferroelectrics, antiferroelectrics and relaxor ferroelectrics. The key results are summarized in the following.

Tilt kinetics and phase transformations in NBT.

- **The energy landscape is flat and PNRs can be small.**

  Octahedral tilt transformations and A-cation displacements both have energy barriers that are close to the room temperature thermal energy (Sec. 5.3). From nudged elastic band and *ab initio* MD calculations (Sec. 5.4) we found that oxygen ions exhibit the largest thermal displacement. In a first step octahedral tilt transformations occur, and in a second step a shift of the A-cations follow subsequently. This also implies that PNRs, i.e. regions with different octahedral tilt patterns and A-cation displacements, can be small, with sizes smaller than 200 Å, as we have seen in Sec. 5.5. From preliminary *ab initio* MD calculations [331] it appears that the size of PNRs (and distances between those) affect the time scale for octahedral tilt transformations, which could explain the frequency dependent dielectric response.

- **Chemical A-cation order matters.**

  Even though we investigated only two different chemical orders (the rock-salt 111-order and layered 001-order), we found plenty of differences between them. Not only is the ground state rhombohedral for the 111-order and orthorhombic for the 001-order, also phase transformation energy barriers are affected (Sec. 5.3). Further, 001-order allows for improper ferroelectricity, as several degrees of freedom (octahedral tilts and ferroelectric distortions) are present simultaneously. Octahedral tilt defects show smaller formation energies in regions with 001-order, compared to regions with 111-order (Sec. 5.5). Therefore, the chemical order determines the phase transition energies and thus the phase transition temperatures. This is in line with the proposed diffuse phase transition model for relaxor ferroelectrics that suggest spatially varying Curie temperatures. These local regions can also be understood as PNRs with different polarizations, since the A-cation displacement can create polarizations. Varying chemical order leads also to spatially different random electric and stress fields, because of the different distributions of charge and bond lengths.

- **Different phase sequences are energetically similar.**

  Although the three investigated phases (tetragonal, orthorhombic and rhombohedral) have distinctly different energies, the phase transition path from the low temperature rhombohedral phase to high temperature tetragonal phase is not unique. In Sec. 5.5 we found that formation energies of anti-phase tetragonal tilt defects in a rhombohedral phase are similar to those of orthorhombic tilt defects. This is

because in both cases the deformations of the oxygen octahedra at the interfaces remain small. However, an in-phase tetragonal phase distorts the oxygen octahedra strongly and leads to high tilt defect formation energies. Thus, the two transitions $R \rightarrow T^{-}$ and $R \rightarrow O \rightarrow T^{+}$ are both possible. Similarly, the transformation from the orthorhombic to the in-phase tilted tetragonal phase is more likely than the transformation to the anti-phase tilted tetragonal phase.

- **Bi and Na behave differently.**

  Because of the 6*s* lone-pair of Bi and their charge difference, Bi^{+3} and Na^{+1} interact with their surrounding in different ways, even though their ion radii are similar. In Sec. 5.2 we have seen that also octahedral tilt barriers are affected. The experimentally observed peculiar displacement behaviors of Bi and Na within their oxygen cuboctahedron could be confirmed in Sec. 5.6.

Oxygen migration and oxygen vacancy associates

- **Tilt phases, local symmetries, chemical order and cell volume strongly influence the oxygen migration barriers.**

  Oxygen migration barriers were obtained in Sec. 6. In the low temperature rhombohedral phase they vary between 0.50 eV and 0.66 eV (Tab. 6.1). In the lower symmetry orthorhombic structure the migration energies vary from 0.33 eV to 1.11 eV. The tetragonal phase has the lowest migration barriers with 0.36 eV. An increase in the supercell volume of up to 1.5% decreases the oxygen migration barrier by about 0.1 eV (Sec. 6.4).

- **Chemical order again matters.**

  When 001-order is present, oxygen vacancies prefer to reside within the Bi-layer (Sec. 6.1). For a short range 001-order this leads to a trapping of the oxygen vacancies. Additionally, no migration barrier exists for a hopping process from the mixed layer (with two Na and Bi as neighbors) into the Bi-layer. Therefore, if a long-range 001-order would be present, the oxygen vacancies would diffuse along the Bi-layer.

- **Oxygen vacancies form associates with Mg and Ni dopants.**

  Binding energies of associates of oxygen vacancies with Mg and Ni are obtained in Secs. 7.1 and 7.2. The association energies are 0.4 eV for Mg and range from 0.2 eV to 0.8 eV for Ni, depending on the *U* correction parameter of the DFT calculations.

- **Associates of oxygen vacancies and Bi vacancies are complex.**

  In contrast to the Mg''_{Ti}–$V_O^{\bullet\bullet}$ and Ni''_{Ti}–$V_O^{\bullet\bullet}$ associates, V'''_{Bi}–$V_O^{\bullet\bullet}$ associates do not have the lowest binding energy when they are next neighbors, but when they are second next neighbors (Sec. 7.3). The explanation for this might be due to a competition between the attractive coulomb force and the repulsive force from the arising strain fields.

- **Any introduction of disorder lowers the achievable EC temperature change.**

  Our calculations show that the highest EC temperature change is obtained in ferroelectric materials (Sec. 8.1). Any initial disorder (arising from random fields, defect dipoles or a distribution of positive and negative Ising parameters) reduces the maximum EC temperature change, since the overall change in entropy is reduced.

- **The ECE is strongly dependent on the strength, concentration and direction of polar defects.**

  The obtained EC temperature change is influenced by defect dipoles. Defect dipoles that are aligned along the external field (parallel defects) decrease the ECE, since the polarization close to the defects is pinned and cannot contribute to the configurational entropy change. Antiparallel to the external field oriented defects can create a negative ECE, in which the temperature decreases when the external field is turned on (Sec. 8.1.2).

- **Fatigue leads to a reduction of the ECE.**

  Since the on- and off-switching of an electric field will lead to a reorientation of the defect dipoles (Sec. 8.1.2), all effects that arise from ordered defect dipoles (such as the negative ECE or a shift in the application temperature) are reduced during the lifespan of the device (fatigue). Even when some defect dipoles are still oriented antiparallel to the external field, the negative ECE vanishes.

- **MC and MD models give similar results.**

  The simplistic Ising-like MC model and sophisticated MD simulations (based on an effective Hamiltonian) give the same qualitative trends for the ECE (Secs. 8.1 and 8.2). An increase in the defect concentration leads in both models to a decrease of the EC temperature change and a shift of the maximum ECE towards higher temperatures. Also MC simulations, based on a Ginzburg-Landau description of the free energy, show these trends [31]. Therefore, the main contributions to the ECE arise from the dipole-dipole interaction and the interaction of the individual polarization dipoles with the external electric field. Strain-coupling, short-range interaction (which leads to domain formations) do not alter the trends significantly.

10 Discussion

Now we want to discuss the obtained results, also regarding the shortcomings and limitations of the used methods. We also make some general remarks and statements.

First-principles studies of NBT

- **Restriction in supercell sizes.**

  The supercells of this study have a maximum size of 320 atoms (4×4×4) or 360 atoms (6×6×2) and further increases of the cell size is computational not feasible. This limits the cluster sizes of the tilt defect calculations of Sec. 5.5 to rather small clusters of nine tilt defects. Therefore, the extrapolated PNRs sizes of Sec. 5.5 have to be taken with care. The finite size of the 4×4×4 supercells can also affect the association energies, as was seen in the smaller 4×4×2 supercells (Sec. 7.1).

  The virtual crystal approximation [332, 333] would be a way to introduce a more complex A-cation distribution by averaging the atomic potentials of Na and Bi. These approximations, however, only work for ions that have similar properties. In NBT, Bi^{+3} and Na^{+1}, behave completely different. They have different charges and the displacements of those ions is different, due to the lone-pair of the Bi ion.

- **Restriction in cell size and runtimes in *ab initio* molecular dynamics.**

  Ab initio MD and phase transformation cells are limited to 2×2×2 supercells (40 atoms) and runtimes of up to 100 ps. These small box sizes prevent to make statements concerning interface effects or oxygen vacancy diffusion.

- **Slow ionic and electronic relaxation.**

  Due to the flat energy surface of NBT, ion relaxation calculations can take many ionic steps before convergence. Sometimes it is difficult to obtain convergence at all and a careful selection of the input parameters have to be chosen. This is especially the case for oxygen migration barriers and defect associates, which have a reduced cell symmetry. Switching to a GGA exchange-correlation potential (instead of the LDA potential) increased the time until convergence.

Electrocaloric effect

- **Small system sizes.**

  The Ising-like MC model suffers from a limited system size (less than 1000 sites). This prevents the study of large scale phenomena, like domains. It also decreases the obtained statistics and requires an increased number of simulation runs. An increase in the system size is not feasible computationally with the current status of the code.

- **Parameters for feram only available for ferroelectric $BaTiO_3$ and simple solid solution.**

  So far, only parameter sets for $BaTiO_3$, $SrTiO_3$ and $PbTiO_3$ are available for feram. As soon as a more complex system is investigated, like $Ba(Zr_xTi_{x-1})O_3$ for example, the set of parameters is difficult to obtain. The simplest approach for solid solutions is to average all parameters of the end members. However, for $Ba(Zr_xTi_{x-1})O_3$ this is not easily accomplished, since $BaZrO_3$ is paraelectric, which does not allow to determine some parameters like short range dipole-dipole interaction parameters. Further, octahedral tilts, as in NBT, are also out of the scope of the feram code.

11 Outlook

Here we want to give some possible continuations of this study.

Tilt kinetics and phase transformations

- **Metadynamics algorithm for structure search.**

  The obtained structures from the phase transformation calculations of NBT might not be the only stable structures. Nudged elastic band calculations give only the energetic most favorable path between two states. In constrast, metadynamics sample the entire energy landscape and can thus find other local minima. It can sample the energy landscape by following the soft mode of the ground state structure. Metadynamics are fully implemented in the software package cp2k [334] and some basic features of the metadynamics algorithms for VASP are built into the USPEX code [335].

- **Comparison of *ab initio* MD data to inelastic neutron scattering data.**

  In collaboration with Florian Pforr from the group of Prof. Wolfgang Donner at the Technische Universität Darmstadt, *ab initio* MD simulations of NBT will be analyzed and compared to neutron scattering data. These can be used to gain deeper knowledge of the dynamics responsible for the experimentally observed quasielastic and inelastic reflections.

- **MD simulation of NBT from the bond-valence model.**

  Classical interatomic MD potentials for NBT do not exist. However, the bond-valance model can account for chemical order, oxygen octahedra tilts and ionic interactions [283–287]. It has so far been used for the material $PbTiO_3$, but could be extended for NBT. These calculations would permit to calculate longer timescales and larger simulation boxes than within the *ab initio* MD calculations.

Ionic conductivity and defect associates

- **Phase dependent oxygen diffusion from kinetic Monte Carlo simulations.**

  With data of oxygen migration barriers and defect association energies, kinetic Monte Carlo simulations can be set up that are able to determine the diffusion of oxygen in NBT. From these, one can extract information on diffusion paths, phase dependent (and thus temperature dependent) activation energies, which then can be compared with experimentally obtained values.

- **Theoretic models for ion conductivity.**

  The in this work investigated factors that influence oxygen migration barriers (phase transitions, thermal expansion and defect association) could not ultimately explain the temperature dependent change in the activation energy observed in experiment [32]. Another approach to shed light in this problem, is to construct a theoretic model

of the ionic conductivity, based on the defect chemistry of point defects. Work on this approach is currently in progress within our group in collaboration with our experimental partners [172].

- **Migration barriers for doped NBT.**

  In this work oxygen migration barriers have been calculated only for oxygen vacancies contained in pure NBT. However, migration barriers might be influenced due to the presence of dopants and Bi vacancies.

- **Automatic calculation of defect formation energies.**

  Defect formation energies of the various possible defects are important to determine the concentration of the defect. This is relevant for oxygen vacancies and the ionic conductivity in NBT. The recently published code PyCDT [336] enables the user to automatically generate a large set of data on defect formations.

- **Different $V_{Bi}^{'''} - V_{O}^{\bullet\bullet}$ complexes.**

  The $(V_{Bi}^{'''} - V_{O}^{\bullet\bullet})^{'}$ associate, consisting of one oxygen vacancy and one Bi vacancy, was studied in this work. But this associate is charged, and other defect clusters may be more likely to exist. A neutral cluster would consist of three $V_{O}^{\bullet\bullet}$ and two $V_{Bi}^{'''}$ vacancies. Though, it is not clear how these defects should be arranged within a supercell. These large defect clusters could even lead to a transformation of the perovskite structure, which could influence the oxygen migration.

Electrocaloric effect

- **Thermal conductivity of contact and EC materials for the ECE.**

  So far, a large amount of time has been spent on finding a material, which maximizes the EC temperature change. However, also the aspect of heat conductivity is important, since only a high thermal conductivity ensures that the generated heat can be transferred to the heat sink. The thermal conductivity of the EC material at its interface to the substrate can be determined from DFT calculations [337].

- **Switchable defect dipoles.**

  In our MC and MD calculations, defect dipoles were static, i.e. did not change their direction or strength during the simulations. When some of the defect dipoles change direction during the electric field switching process, this could affect the ECE. Since the time scales of the switching of the electric field is in the order of seconds, the defect dipoles can reorient [338]. These switchable defect could be implemented in the MC, as well in the MD model.

- **Further development of the MC and MD models.**

  As discussed, both the MC and the MD code have certain limitation. One possible step for a further development would be the implementation of octahedra tilts in the feram code. A description of octahedral tilts based on Landau theory has been published [339]. This would give a more realistic description of materials which exhibit tilts of the octahedra, like PZT and maybe ultimately NBT.

12 Appendix

12.1 Structures

12.1.1 Structure parameters

Parameters for 111-ordered structures

Tilt	Crystal system and Symbol	Space group	Energy in eV (8 f.u.)	Pseudo-cubic lattice parameters in Å		
$a_0^0a_0^0c_0^+$	tetragonal (T^+)	$P4_2/mnm$	-328.83	$a = 7.532$	$b = 7.532$	$c = 7.785$
				$\alpha = 90.00°$	$\beta = 90.00°$	$\gamma = 90.00°$
$a_0^0a_0^0c_0^-$	tetragonal (T^-)	$I\bar{4}2m$	-329.11	$a = 7.540$	$b = 7.540$	$c = 7.770$
				$\alpha = 90.00°$	$\beta = 90.00°$	$\gamma = 90.00°$
$a_0^0c_0^-a_0^0$	tetragonal (T_b^-)	$I\bar{4}2m$	-329.11	$a = 7.544$	$b = 7.773$	$c = 7.544$
				$\alpha = 90.00°$	$\beta = 90.00°$	$\gamma = 90.00°$
$a^-a^-c_0^+$	orthorhombic (O)	$Pmn2_1$	-329.94	$a = 7.638$	$b = 7.638$	$c = 7.576$
				$\alpha = 90.00°$	$\beta = 90.00°$	$\gamma = 88.911°$
$a^-a^-a^-$	rhombohedral (R)	$R3$	-330.04	$a = 7.674$	$b = 7.674$	$c = 7.674$
				$\alpha = 89.52°$	$\beta = 89.52°$	$\gamma = 89.52°$

Parameters for 001-ordered structures

Tilt	Crystal system and Symbol	Space group	Energy in eV (8 f.u.)	Pseudo-cubic lattice parameters in Å		
$a_0^0a_0^0c_0^+$	tetragonal (T^+)	$P4/mbm$	-329.59	$a = 7.514$	$b = 7.514$	$c = 7.857$
				$\alpha = 90.00°$	$\beta = 90.00°$	$\gamma = 90.00°$
$a_0^0a_0^0c_0^-$	tetragonal (T^-)	$P4/nbm$	-329.74	$a = 7.516$	$b = 7.516$	$c = 7.836$
				$\alpha = 90.00°$	$\beta = 90.00°$	$\gamma = 90.00°$
$a_0^0c_0^-a_0^0$	tetragonal (T_b^-)	$Cmmm$	-330.03	$a = 7.539$	$b = 7.728$	$c = 7.621$
				$\alpha = 90.00°$	$\beta = 90.00°$	$\gamma = 90.00°$
$a^-a^-c_0^+$	orthorhombic (O)	$Pmc2_1$	-330.80	$a = 7.605$	$b = 7.605$	$c = 7.706$
				$\alpha = 90.00°$	$\beta = 90.00°$	$\gamma = 89.18°$
$a^-a^-a^-$	rhombohedral (R)	Pc	-330.52	$a = 7.661$	$b = 7.661$	$c = 7.700$
				$\alpha = 89.50°$	$\beta = 89.50°$	$\gamma = 89.63°$

Tetragonal T^+ (111-order)

- Tilt configuration: $a_0^0 a_0^0 c_0^+$
- Space group: *P4/mbm*
- $a = 5.326\,\text{Å}$, $b = 5.326\,\text{Å}$, $c = 7.786\,\text{Å}$
- $\alpha = 90.00°,\ \beta = 90.00°,\ \gamma = 90.00°$

atom type	Wyckoff position	x	y	z
Bi	2a	0.00000	0.00000	0.00000
Na	2b	0.00000	0.00000	0.50000
Ti	4d	0.00000	0.50000	0.25000
O1	8j	0.80791	0.80791	0.75445
O2	4c	0.00000	0.50000	0.00000

Tetragonal T^- (111-order)

- Tilt configuration: $a_0^0 a_0^0 c_0^-$
- Space group: *I4/mcm*
- $a = 5.331\,\text{Å}$, $b = 5.331\,\text{Å}$, $c = 7.770\,\text{Å}$
- $\alpha = 90.00°,\ \beta = 90.00°,\ \gamma = 90.00°$

atom type	Wyckoff position	x	y	z
Bi	2b	0.00000	0.00000	0.50000
Na	2a	0.00000	0.00000	0.00000
Ti	4d	0.00000	0.50000	0.25000
O1	8i	0.19163	0.19163	0.25719
O2	4c	0.00000	0.50000	0.00000

Tetragonal T_b^- (111-order)

- Tilt configuration: $a_0^0 a_0^0 c_0^-$
- Space group: *I4/mcm*
- $a = 5.334\,\text{Å}$, $b = 5.334\,\text{Å}$, $c = 7.773\,\text{Å}$
- $\alpha = 90.00°$, $\beta = 90.00°$, $\gamma = 90.00°$

atom type	Wyckoff position	x	y	z
Bi	2b	0.00000	0.00000	0.50000
Na	2a	0.00000	0.00000	0.00000
Ti	4d	0.00000	0.50000	0.25000
O1	8i	0.80842	0.80842	0.25720
O2	4c	0.00000	0.50000	0.00000

Orthorhombic O (111-order)

- Tilt configuration: $a_-^- a_-^- c_0^+$
- Space group: $Pmn2_1$
- $a = 7.576\,\text{Å}$, $b = 5.452\,\text{Å}$, $c = 5.349\,\text{Å}$
- $\alpha = 90.00°$, $\beta = 90.00°$, $\gamma = 90.00°$

atom type	Wyckoff position	x	y	z
Bi	2a	0.00000	0.80106	-0.01775
Na	2a	0.00000	0.27864	0.50246
Ti	4b	0.75227	0.25913	-0.00924
O1	4b	0.70957	-0.03195	0.22291
O2	4b	0.79217	0.54212	0.79489
O3	2a	0.00000	0.23542	0.07582
O4	2a	0.00000	0.73084	0.42234

Rhombohedral R (111-order)

- Tilt configuration: $a^-a^-a^-$
- Space group: *R3c*
- $a = 5.404\,\text{Å}$, $b = 5.404\,\text{Å}$, $c = 13.401\,\text{Å}$
- $\alpha = 90.00°,\ \beta = 90.00°,\ \gamma = 120.00°$

atom type	Wyckoff position	x	y	z
Bi	3a	0.00000	0.00000	0.27948
Na	3a	0.00000	0.00000	0.77142
Ti1	3a	0.00000	0.00000	0.00942
Ti2	3a	0.00000	0.00000	0.51185
O1	9b	0.65460	0.76306	0.07557
O2	9b	-0.00297	0.56329	0.24705

Tetragonal T^{+} (001-order)

- Tilt configuration: $a_0^0 a_0^0 c_0^+$
- Space group: *P4/mbm*
- $a = 5.313\,\text{Å}$, $b = 5.313\,\text{Å}$, $c = 7.857\,\text{Å}$
- $\alpha = 90.00°$, $\beta = 90.00°$, $\gamma = 90.00°$

atom type	Wyckoff position	x	y	z
Bi	2c	0.00000	0.50000	0.50000
Na	2d	0.00000	0.50000	0.00000
Ti	4e	0.00000	0.00000	0.23685
O1	8k	0.80444	0.30444	0.74112
O2	2a	0.00000	0.00000	0.00000
O3	2b	0.00000	0.00000	0.50000

Tetragonal T^{-} (001-order)

- Tilt configuration: $a_0^0 a_0^0 c_0^-$
- Space group: *I4/mcm*
- $a = 5.315\,\text{Å}$, $b = 5.315\,\text{Å}$, $c = 7.835\,\text{Å}$
- $\alpha = 90.00°$, $\beta = 90.00°$, $\gamma = 90.00°$

atom type	Wyckoff position	x	y	z
Bi	2c	0.75000	0.25000	0.00000
Na	2d	0.75000	0.25000	0.50000
Ti	4g	0.25000	0.25000	0.73749
O1	8m	-0.05583	0.05583	0.75907
O2	2b	0.25000	0.25000	0.50000
O3	2a	0.25000	0.25000	0.00000

Tetragonal T_b^- (001-order)

- Tilt configuration: $a_0^0 a_0^0 c_0^-$
- Space group: *I4/mcm*
- $a = 7.539\,\text{Å}$, $b = 7.728\,\text{Å}$, $c = 7.621\,\text{Å}$
- $\alpha = 90.00°,\ \beta = 90.00°,\ \gamma = 90.00°$

atom type	Wyckoff position	x	y	z
Bi	4j	0.00000	0.75440	0.50000
Na	4i	0.00000	0.75058	0.00000
Ti	8o	0.24833	0.00000	0.76173
O1	4l	0.00000	0.50000	0.69102
O2	4k	0.00000	0.00000	0.80139
O3	8m	0.25000	0.25000	0.72957
O4	4g	0.30447	0.00000	0.00000
O5	4h	0.18849	0.00000	0.50000

Orthorhombic O (001-order)

- Tilt configuration: $a^-\_a^-\_c_0^+$
- Space group: $Pmn2_1$
- $a = 7.706\,\text{Å}$, $b = 5.339\,\text{Å}$, $c = 5.416\,\text{Å}$
- $\alpha = 90.00°,\ \beta = 90.00°,\ \gamma = 90.00°$

atom type	Wyckoff position	x	y	z
Bi	2b	0.50000	0.25543	0.55402
Na	2a	0.00000	0.25397	0.49069
Ti	4c	0.76350	0.24348	0.01151
O1	4c	0.70641	0.46515	0.27553
O2	4c	0.77403	0.04905	0.69645
O3	2a	0.00000	0.31329	0.01353
O4	2b	0.50000	0.17718	-0.02524

Rhombohedral R (001-order)

- Tilt configuration: $a^-a^-a^-$
- Space group: *R3c*
- $a = 7.700\,\text{Å}$, $b = 5.400\,\text{Å}$, $c = 5.435\,\text{Å}$
- $\alpha = 90.00°$, $\beta = 90.71°$, $\gamma = 90.00°$

atom type	Wyckoff position	x	y	z
Bi	2a	0.75827	0.24759	0.44435
Na	2a	0.27228	0.24788	0.45555
Ti1	2a	0.01642	0.25447	-0.00988
Ti2	2a	0.48929	0.74654	0.46961
O1	2a	-0.04926	0.02357	0.73831
O2	2a	0.01765	0.45551	0.30419
O3	2a	0.24648	0.18455	0.00304
O4	2a	0.74593	0.31596	0.02526
O5	2a	0.46904	0.52473	0.21900
O6	2a	0.53389	-0.02391	0.76951

12.2.1 VASP

1. Phase transitions NEB (Sec. 5.3)

INCAR

```
ISTART  =  0
ICHARG  =  1
INIWAV  =  1
ISPIN   =  1
LPLANE  =  .TRUE.
EDIFF   =  1E-8
NELMIN  =  6
NELM    =  60
EDIFFG  =  -1E-2
NSW     =  60
ISIF    =  2
IBRION  =  1
MAXMIX  =  40
POTIM   =  0.3
IMAGES  =  11
SPRING  =  -05
PREC    =  ACCURATE
ENCUT   =  600
ADDGRID =  .TRUE.
LREAL   =  .FALSE.
ALGO    =  NORMAL
ISMEAR  =  0
SIGMA   =  0.01
LWAVE   =  .FALSE.
LCHARG  =  .FALSE.
```

KPOINTS

```
Automatic mesh
0               ! number of k-points = 0 ->automatic generation scheme
Gamma           ! generate a Gamma centered grid
4  4  4         ! subdivisions N_1, N_2 and N_3 along recipr. l. vectors
0. 0. 0.        ! optional shift of the mesh (s_1, s_2, s_3)
```

2. *Ab initio* molecular dynamics (Sec. 5.4)

INCAR

```
ISTART  =  0
ICHARG  =  1
INIWAV  =  1
ISPIN   =  1
LPLANE  =  .TRUE.
NCORE   =  12
EDIFF   =  1E-5
NELMIN  =  4
NELM    =  30
EDIFFG  =  -1E-2
ISIF    =  2
MAXMIX  =  40
POTIM   =  1
PREC    =  Normal
ENCUT   =  500
ADDGRID =  .TRUE.
LREAL   =  .FALSE.
ALGO    =  Normal
ISMEAR  =  0
SIGMA   =  0.01
IBRION  =  0
NSW     =  10000
NWRITE  =  1
LCHARG  =  .FALSE.
LWAVE   =  .FALSE.
TEBEG   =  400
TEEND   =  400
SMASS   =  0
```

KPOINTS

```
Automatic mesh
0               ! number of k-points = 0 ->automatic generation scheme
Gamma           ! generate a Gamma centered grid
1  1  1         ! subdivisions N_1, N_2 and N_3 along recipr. l. vectors
0. 0. 0.        ! optional shift of the mesh (s_1, s_2, s_3)
```

3. Tilt defects (Sec. 5.5)

INCAR

```
ISTART  =  0
ICHARG  =  1
INIWAV  =  1
ISPIN   =  1
LPLANE  =  .TRUE.
NPAR    =  5
EDIFF   =  1E-8
NELMIN  =  6
NELM    =  60
EDIFFG  =  -1E-2
NSW     =  10
ISIF    =  2
IBRION  =  1
MAXMIX  =  40
POTIM   =  0.4
PREC    =  ACCURATE
ENCUT   =  600
ADDGRID =  .TRUE.
LREAL   =  .TRUE.
ALGO    =  NORMAL
ISMEAR  =  0
SIGMA   =  0.01
LWAVE   =  .FALSE.
LCHARG  =  .FALSE.
```

KPOINTS

```
Automatic mesh
0              ! number of k-points = 0 ->automatic generation scheme
Gamma          ! generate a Gamma centered grid
1  1  1        ! subdivisions N_1, N_2 and N_3 along recipr. l. vectors
0. 0. 0.       ! optional shift of the mesh (s_1, s_2, s_3)
```

4. Oxygen migration NEB (Sec. 6)

INCAR

```
ISTART  =  0
ICHARG  =  1
INIWAV  =  1
ISPIN   =  1
LPLANE  =  .TRUE.
EDIFF   =  1E-8
NELMIN  =  6
NELM    =  40
EDIFFG  =  -1E-2
NSW     =  50
ISIF    =  2
IBRION  =  1
MAXMIX  =  40
POTIM   =  0.3
IMAGES  =  5
SPRING  =  -5
PREC    =  ACCURATE
ENCUT   =  600
ADDGRID =  .TRUE.
LREAL   =  .TRUE.
ALGO    =  NORMAL
ISMEAR  =  0
SIGMA   =  0.01
LWAVE   =  .FALSE.
LCHARG  =  .FALSE.
NELECT  =  2616
```

KPOINTS

```
Automatic mesh
0               ! number of k-points = 0 ->automatic generation scheme
Gamma           ! generate a Gamma centered grid
1  1  1         ! subdivisions N_1, N_2 and N_3 along recipr. l. vectors
0. 0. 0.        ! optional shift of the mesh (s_1, s_2, s_3)
```

5. Electronic density of states (Sec. 6.3)

INCAR

```
ISTART  =  0
ICHARG  =  1
INIWAV  =  1
ISPIN   =  1
LPLANE  =  .TRUE.
NCORE   =  12
EDIFF   =  1E-8
NELMIN  =  6
NELM    =  40
EDIFFG  =  -1E-2
NSW     =  0
ISIF    =  2
IBRION  =  1
MAXMIX  =  40
POTIM   =  0.3
PREC    =  ACCURATE
ENCUT   =  600
ADDGRID =  .TRUE.
LREAL   =  .FALSE.
ALGO    =  NORMAL
ISMEAR  =  -5
SIGMA   =  0.01
LORBIT  =  11
NEDOS   =  1872
LWAVE   =  .FALSE.
LCHARG  =  .FALSE.
NELECT  =  2616
```

KPOINTS

```
Automatic mesh
0               ! number of k-points = 0 ->automatic generation scheme
Gamma           ! generate a Gamma centered grid
2  2  2         ! subdivisions N_1, N_2 and N_3 along recipr. l. vectors
0. 0. 0.        ! optional shift of the mesh (s_1, s_2, s_3)
```

12.2.2 feram

```
method            = 'vs'
GPa               = -2.6
kelvin            = 300
mass_amu          = 38.24
acoustic_mass_amu = 46.44
bulk_or_film      = 'bulk'
L                 = 48 48 48
B11               = 126.731671475652
B12               =  41.7582963902598
B44               =  49.2408864348646
B1xx              = -185.347187551195 [eV/Angstrom^2]
B1yy              = -3.28092949275457 [eV/Angstrom^2]
B4yz              = -14.5501738943852 [eV/Angstrom^2]
P_k1              = -267.98013991724 [eV/Angstrom^6]
P_k2              = 197.500718362573 [eV/Angstrom^6]
P_k3              = 830.199979293529 [eV/Angstrom^6]
P_k4              = 641.968099408642 [eV/Angstrom^8]
P_alpha           = 78.9866142426818 [eV/Angstrom^4]
P_gamma           = -115.484148812672 [eV/Angstrom^4]
dt                = 0.002 [pico second]
n_thermalize      = $n_thermalize
n_average         = $n_average
n_coord_freq      = $n_coord_freq
external_E_field  = 0.00 0.00 0.00100000
distribution_directory = 'never'
P_kappa2          = 8.53400622096412
j =  -2.08403 -1.12904 0.68946 -0.61134 0.00000 0.27690 0.00000 [eV/Angstrom^2]
a0                =   3.98597    [Angstrom]
Z_star            =  10.33000
epsilon_inf       =   6.86915
init_dipo_avg     = 0.00  0.00  0.14   [Angstrom]
init_dipo_dev     = 0.06  0.06  0.04   [Angstrom]
```

feram (http://loto.sourceforge.net/feram/) is an *ab initio* based molecular dynamics simulator for bulk and thin-film ferroelectrics and relaxors [278–280], distributed under the GNU General Public License.

List of Figures

2.1 Usage of lead since 1960 and energy consumption in US households. 6
3.1 Measured real part of the dielectric permittivity ϵ' of NBT and Bi-deficient NBT ($Na_{0.48}Bi_{0.52}TiO_{2.98}$). 8
3.2 X-ray diffuse scattering pattern of NBT at hydrostatic pressure of 0.6 GPa. . . 9
3.3 Arrhenius-type plots of bulk conductivity of stoichiometric NBT, non-stoichiometric NBT and Mg-doped $NBTi_{0.98}Mg_{0.02}$. 9
3.4 Electric field and temperature dependences of the electrocaloric temperature change in NBT-6BT. 10
3.5 NBT phase diagram. 12
3.6 Two different representations of the perovskite $BaTiO_3$. 13
3.7 The different degrees of freedom in NBT. 13
3.8 111- and 001-A-cation order. 14
3.9 Comparison between ferroelectrics and relaxor ferroelectrics. 17
3.10 Electronic and ionic conductivity of stoichiometric, Bi-deficient, Ni-doped ($NBTi_{0.98}Ni_{0.02}$) and Mg-doped $NBTi_{0.98}Mg_{0.02}$. 21
3.11 The adiabatic electrocaloric cycle. 25
4.1 The employed computational methods of this work. 30
4.2 Electronic and atomic self-consistency cycle in DFT. 35
4.3 Sketch of the transition path of an octahedral tilt transformation. 37
4.4 Sketch of the nudged elastic band method for determination of the transition path. 38
5.1 The six possible chemical orders in NBT. 45
5.2 The four investigated tilt configurations viewed along the a-axis. 46
5.3 The four investigated tilt configurations viewed along the c-axis. 47
5.4 Illustration of the stepwise transformation from $a^0a^0c^+$ to $a^0a^0c^-$. 48
5.5 Transformation barriers for $a^0a^0c^+$ to $a^0a^0c^-$. 48
5.6 Tilting of two adjacent layers of oxygen octahedra in a 2×2×4 structure. . . . 49
5.7 Transformation energies for two adjacent layers in a 2×2×4 structure. 50
5.8 2×2×6 supercells with adjacent layers and separated layers. 50
5.9 Energy barrier for 2×2×6 supercells with adjacent layers and separated layers. 51
5.10 The five investigated structures and transformations between those. 52
5.11 Energies of the seven transformation paths for 111-order and 001-order. . . . 53
5.12 Root mean square displacement of Bi, Na, Ti and O ions. 56
5.13 Snapshot of an *ab initio* molecular dynamics run at 700 K. 56
5.14 Root mean square displacement of oxygen ions along different directions. . . 57
5.15 6x6x2 supercell with 111-order and an orthorhombic tilt phase defect in a rhombohedral tilted matrix. 58
5.16 Energies for two tilt defect clusters extrapolated to larger sizes. 59
5.17 Energies for various defect and matrix tilt combinations. 61
5.18 Displacements of Bi and Na along three different directions. 62
6.1 Oxygen vacancy migration paths within one oxygen octahedron. 67
6.2 The two used A-cation chemical orders and the oxygen vacancy migration paths. 68
6.3 Oxygen vacancy migration barriers in the rhombohedral phase for three different scenarios. 69

6.4 Sketch of NBT with few unit cell sized regions with 001-order. 70
6.5 Oxygen vacancy migration barriers for the orthorhombic phase. 71
6.6 Oxygen vacancy migration barriers for the tetragonal phase. 72
6.7 Electronic density of state plots for two tetragonal structures. 73
6.8 Volume dependent oxygen vacancy migration barriers of the rhombohedral phase. 75
6.9 Oxygen vacancy migration barriers of the tetragonal phase at four different volumes. 77
6.10 Volume dependent oxygen vacancy migration barrier heights for the rhombohedral and tetragonal phase. 78
6.11 Experimental oxygen activation energies and calculated migration energies. . 79
7.1 Positions of the oxygen vacancy $V_O^{\bullet\bullet}$ inside the 001-ordered NBT supercell. . . 80
7.2 Binding energy for a $Mg_{Ti}^{''}$ dopant and a $V_O^{\bullet\bullet}$ oxygen vacancy. 82
7.3 Binding energy for two $Mg_{Ti}^{''}$ dopants and a $V_O^{\bullet\bullet}$ oxygen vacancy. 83
7.4 Binding energy for a $Mg_{Ti}^{''}$ dopant and a $V_O^{\bullet\bullet}$ oxygen vacancy in a 2×4×4 and 4×4×2 supercell. 83
7.5 Binding energy for a $Ni_{Ti}^{''}$ dopant and a $V_O^{\bullet\bullet}$ oxygen vacancy. 85
7.6 Binding energy for a $V_O^{\bullet\bullet}$ oxygen and a $V_{Bi}^{'''}$ Bi vacancy and possible explanation for its second nearest neighbor association energy. 86
7.7 Calculated and experimental oxygen migration activation energies. 87
8.1 The Ising parameters and resulting hysteresis loops of the MC model. 91
8.2 EC temperature change and cell snapshots for an antiferroelectric and relaxor-like system. 92
8.3 EC temperature change for a transition of an antiferroelectric system and a ferroelectric system to relaxor-like systems. 93
8.4 EC temperature change for various Ising parameters with random fields. . . . 93
8.5 EC temperature change for various concentrations of parallel and antiparallel defects. 95
8.6 EC temperature change in a fatiguing ferroelectric system. 96
8.7 EC temperature change in $BaTiO_3$ for defects oriented parallel to the external electric field calculated with the effective Hamiltonian code feram. 97
8.8 EC temperature change in $BaTiO_3$ for defects oriented antiparallel to the external electric field. 98
8.9 Temperature dependent polarization, before and after application of an electric field. 99

List of Tables

4.1 Valence electrons used in the DFT calculations of this work. 36
5.1 Summary of the calculated values from the tilt defect section. 60
6.1 Summary of the calculated oxygen vacancy migration barriers. 74
6.2 Summary of the volume dependent oxygen vacancy migration barriers for the rhombohedral phase. 76
6.3 Summary of the volume dependent oxygen vacancy migration barriers for the tetragonal phase. 76
7.1 Binding energies of $Mg_{Ti}^{''}$-$V_O^{\bullet\bullet}$ associates. 84

List of symbols, abbreviations and constants

Used symbols

$\boldsymbol{a}$	Acceleration
c	Heat capacity
$\boldsymbol{E}$	External electric field
E_{diff}	Energetic difference between two phases per oxygen ion
E_{def}	Energetic cost to deform an octahedron
E_{mig}	Migration energy
E_{t}	Transition energy
$\boldsymbol{F}$	Force
g	Goldschmidt tolerance factor
Γ	Jump rate
h	Random field strength
H	Hamiltonian
J_{ij}	Ising parameter
k	Force constant
m	Mass
m_c	Mass of an atom core
m_e	Mass of an electron
n	Electron density
N	Size of tilt defect clusters (in number of octahedra)
O	Orthorhombic phase
$\boldsymbol{p}$	Impulse
$\boldsymbol{P}$	Polarization vector
P_{D}	Polarization of the defect dipole
ψ	Single electron wave function
Ψ	Wave function
q	Electron charge
Q	Core charge
$\boldsymbol{r}$	Spatial coordinate
r_A	Ionic radius of element A
r_B	Ionic radius of element B
r_X	Ionic radius of element X
R	Rhombohedral phase
$\boldsymbol{R}$	Spatial coordinate
s	Spring constant
S	Entropy
S_{t}	Total entropy
S_{d}	Dipolar (configurational) entropy
σ	Conductivity
t	Time
T	Temperature
T_{B}	Burns temperature

T_D	Depolarization temperature
T_f	Freezing temperature
T_m	Maximum dielectric constant temperature
T^*	Intermediate temperature
T^+	Tetragonal phase with in-phase tilts
T^-	Tetragonal phase with anti-phase tilts
$\boldsymbol{u}$	Polar soft mode vector
U	Internal energy
$\boldsymbol{v}$	Velocity
v	Single particle potential
V_{ext}	Electrons and cores interaction potential
V_H	Hartree potential
$V_{H,SIC}$	self-interaction corrected Hartree potential
V_{xc}	Electrons and cores interaction potential
$\boldsymbol{w}$	Acoustic displacement vector
$\xi(r, v)$	Friction term

Acronyms and Abbreviations

AFE	Antiferroelectric
BCZT	Barium calcium zirconium titanate $(Ba_xCa_{x-1})(Zr_yTi_{y-1})O_3$
BST	Barium strontium titanate $Ba_{0.5}Sr_{0.5}TiO_3$
BT	Barium titanate $BaTiO_3$
BZT	Barium zirconium titanate $Ba(Zr_xTi_{x-1})O_3$
DE	Differential equation
DFG	Deutsche Forschungsgemeinschaft
DFT	Density functional theory
DPT	Diffuse phase transition
DSC	Differential scanning calorimetry
EC	Electrocaloric
ECE	Electrocaloric effect
FE	Ferroelectric
f.u.	Formula unit
GGA	Generalized gradient approximation
HEG	Homogeneous electron gas
KBT	Potassium bismuth titanate $K_{0.5}Bi_{0.5}TiO_3$
KN	Potassium niobate $KNbO_3$
KNN	Potassium sodium niobate $(K_xNa_{x-1})NbO_3$
KSE	Kohn-Sham equation
LDA	Local density approximation
NBT	Sodium bismuth titanate $Na_{0.5}Bi_{0.5}TiO_3$
NBT-BT	Sodium bismuth barium titanate $Na_{0.5}Bi_{0.5}TiO_3$–$BaTiO_3$
NKBT	Sodium potassium bismuth titanate $(Na_xK_{1-x})_{0.5}Bi_{0.5}TiO_3$
PBZ	Lead barium zirconate $Pb_xBa_{1-x}ZrO_3$
PLZT	Lead lanthanum zirconium titanate $(Pb_xLa_{1-x})(Zr_yTi_{1-y})O_3$
PMN	Lead magnesium niobate $Pb(Mg_{1/3}Nb_{2/3})O_3$

PMN-PT	Lead magnesium niobate $Pb(Mg_{1/3}Nb_{2/3})O_3$–$PbTiO_3$
PNR	Polar nanoregion
PT	Lead titanate $PbTiO_3$
PZ	Lead zirconate $PbZrO_3$
PZT	Lead zirconium titanate $PbZr_xTi_{x-1}O_3$
RFE	Relaxor ferroelectrics
RMSD	Root mean square displacement
SE	Schrödinger equation
ST	Strontium titanate $SrTiO_3$
TEM	Transmission electron microscopy
TFD	Thomas-Fermi-Dirac
VASP	Vienna Ab-Initio Simulation Package
XRD	X-ray diffraction
YSZ	Yttria-stabilized zirconia $Zr_{1-x}Y_xO_{2-x/2}$

Useful constants

k_B	Boltzmann constant	$8.6173324(78) \cdot 10^{-5} \frac{eV}{K}$
1 Bohr	Atomic length	0.52917721092(17) Å
1 Hartree	Atomic energy	27.211385 eV
ϵ_0	Vacuum permittivity	$8.854187817 \cdot 10^{-12}$ Fm^{-1}
$\hbar$	Planck constant	$6.582119514(40) \cdot 10^{-16}$ eVs
1 eV	Electronvolts	$1.602176565(35) \cdot 10^{-19}$ J
		$\equiv 2.41796 \cdot 10^{14}$ Hz
		$\equiv 8.0655 \cdot 10^{3}$ cm^{-1}
		$\equiv 1.1604 \cdot 10^{4}$ K

References

[1] **J. Rödel, K. G. Webber, R. Dittmer, W. Jo, M. Kimura and D. Damjanovic**, *Transferring lead-free piezoelectric ceramics into application*, J. Eur. Ceram. Soc. **35**, 1659–1681 (2015).

[2] *US Environmental Protection Agency: Renewable Space Cooling*, Retrieved 5 May 2017.

[3] *Directive 2011/65/EU on the Restriction of the Use of Certain Hazardous Substances in Electrical and Electronic Equipment (Recast)*, Official Journal of the European Union **L174**, 88–100 (2011).

[4] *Directive 2012/19/EU on Waste Electrical and Electronic Equipment (Recast)*, Official Journal of the European Union **L197**, 38–71 (2012).

[5] *Commission Directive 2013/28/EU of 17 May 2013 amending Annex II to Directive 2000/53/EC of the European Parliament and of the Council on end-of-life vehicles Text with EEA relevance*, Official Journal of the European Union **L135**, 14–18 (2013).

[6] **B. G. S. B. C. for Sustainable Mineral Development**, *World mineral statistics archive*, Retrieved 5 May 2017.

[7] **S. Fähler, U. K. Rößler, O. Kastner, J. Eckert, G. Eggeler, H. Emmerich, P. Entel, S. Müller, E. Quandt and K. Albe**, *Caloric effects in ferroic materials: New concepts for cooling*, Adv. Eng. Mater. **14**, 10–19 (2012).

[8] *US Department of Energy: Air Conditioning*, Retrieved 5 May 2017.

[9] **A. S. Mischenko, Q. Zhang, J. F. Scott, R. W. Whatmore and N. D. Mathur**, *Giant electrocaloric effect in thin-film* $PbZr_{0.95}Ti_{0.05}O_3$, Science **311**, 1270–1271 (2006).

[10] **G. H. Haertling**, *Ferroelectric ceramics: History and technology*, J. Am. Ceram. Soc. **82**, 797–818 (1999).

[11] **T. Takenaka and H. Nagata**, *Present status of non-lead-based piezoelectric ceramics*, Key Engineering Materials **157**, 57–64 (1999).

[12] **Y. Saito, H. Takao, T. Tani, T. Nonoyama, K. Takatori, T. Homma, T. Nagaya and M. Nakamura**, *Lead-free piezoceramics*, Nature **432**, 84–87 (2004).

[13] **T. Shrout and S. Zhang**, *Lead-free piezoelectric ceramics: Alternatives for PZT?*, J. Electroceram. **19**, 113–126 (2007).

[14] **S. Zhang, R. Xia and T. R. Shrout**, *Lead-free piezoelectric ceramics vs. PZT?*, J. Electroceram. **19**, 251–257 (2007).

[15] **T. Takenaka, H. Nagata and Y. Hiruma**, *Current Developments and Prospective of Lead-Free Piezoelectric Ceramics*, Jpn. J. Appl. Phys. **47**, 3787 (2008).

[16] **J. Rödel, W. Jo, K. T. P. Seifert, E.-M. Anton, T. Granzow and D. Damjanovic**, *Perspective on the Development of Lead-free Piezoceramics*, J. Am. Ceram. Soc. **92**, 1153–1177 (2009).

[17] **P. K. Panda**, *Review: environmental friendly lead-free piezoelectric materials*, J. Mater. Sci. **44**, 5049–5062 (2009).

[18] **E. Aksel and J. L. Jones**, *Advances in lead-free piezoelectric materials for sensors and actuators*, Sensors **10**, 1935–1954 (2010).

[19] **T. Maiti, G. R. and A. S. Bhalla**, *Finite-Temperature Properties of $BaZr_xTi_{1-x}O_3$ Relaxors from First Principles*, J. Am. Ceram. Soc. **91**, 1769–1780 (2008).

[20] **W. Liu and X. Ren**, *Large Piezoelectric Effect in Pb-Free Ceramics*, Phys. Rev. Lett. **103**, 257602 (2009).

[21] **M. D. Maeder, D. Damjanovic and N. Setter**, *Lead Free Piezoelectric Materials*, J. Electroceram. **13**, 385–392 (2004).

[22] **Z. Kutnjak, J. Petzelt and R. Blinc**, *The giant electromechanical response in ferroelectric relaxors as a critical phenomenon*, Nature **441**, 956–959 (2006).

[23] **X. Liu and X. Tan**, *Giant Strains in Non-Textured $(Bi_{1/2}Na_{1/2})TiO_3$–Based Lead-Free Ceramics*, Adv. Mater. (2015).

[24] **M. E. Manley, D. L. Abernathy, R. Sahul, D. E. Parshall, J. W. Lynn, A. D. Christianson, P. J. Stonaha, E. D. Specht and J. D. Budai**, *Giant electromechanical coupling of relaxor ferroelectrics controlled by polar nanoregion vibrations*, Science Advances **2** (2016).

[25] **G. A. Samara**, *The relaxational properties of compositionally disordered ABO_3 perovskites*, J. Phys.-Condens. Matter **15**, R367 (2003).

[26] **R. Blinc**, *Advanced Ferroelectricity*, Oxford Univ Pr, Oxford, 2011.

[27] **F. L. Goupil, A. Berenov, A.-K. Axelsson, M. Valant and N. M. Alford**, *Direct and indirect electrocaloric measurements on <001>-$PbMg_{1/3}Nb_{2/3}O_3$–30$PbTiO_3$ single crystals*, J. Appl. Phys. **111**, 124109 (2012).

[28] **S.-G. Lu and Q. Zhang**, *Large electrocaloric effect in relaxor ferroelectrics*, J. Adv. Dielect. **02**, 1230011 (2012).

[29] **J. Peräntie, H. N. Tailor, J. Hagberg, H. Jantunen and Z.-G. Ye**, *Electrocaloric properties in relaxor ferroelectric (1-x)$Pb(Mg_{1/3}Nb_{2/3})O_4$–x$PbTiO_3$ system*, J. Appl. Phys. **114** (2013).

[30] **S. Uddin, G.-P. Zheng, Y. Iqbal, R. Ubic and J. Yang**, *Unification of the negative electrocaloric effect in $Bi_{1/2}Na_{1/2}TiO_3$–$BaTiO_3$ solid solutions by $Ba_{1/2}Sr_{1/2}TiO_3$ doping*, J. Appl. Phys. **114** (2013).

[31] **Y.-B. Ma, A. Grünebohm, K.-C. Meyer, K. Albe and B.-X. Xu**, *Positive and negative electrocaloric effect in $BaTiO_3$ in the presence of defect dipoles*, Phys. Rev. B **94**, 094113 (2016).

[32] **M. Li, M. J. Pietrowski, R. A. De Souza, H. Zhang, I. M. Reaney, S. N. Cook, J. A. Kilner and D. C. Sinclair**, *A family of oxide ion conductors based on the ferroelectric perovskite $Na_{0.5}Bi_{0.5}TiO_3$*, Nat. Mater. **13**, 31–35 (2014).

[33] **S. Sengodan, S. Choi, A. Jun, T. H. Shin, Y.-W. Ju, H. Y. Jeong, J. Shin, J. T. S. Irvine and G. Kim**, *Layered oxygen-deficient double perovskite as an efficient and stable anode for direct hydrocarbon solid oxide fuel cells*, Nat. Mater. **14**, 205–209 (2015), Letter.

[34] **G. A. Smolensky, V. A. Isupov, A. Agranoskaya and K. N.N.**, *New Ferroelectrics of Complex Composition. IV*, Sov. Phys. Solid State **2**, 2651 (1961).

[35] **K. Reichmann, A. Feteira and M. Li**, *Bismuth Sodium Titanate Based Materials for Piezoelectric Actuators*, Materials **8**, 5469 (2015).

[36] *DFG Priority Programme 1599 (SPP)*, Retrieved 5 May 2017.

[37] **J. Attfield**, *'A' cation control of perovskite properties*, Crystal Engineering **5**, 427–438 (2002).

[38] **G. King and P. M. Woodward**, *Cation ordering in perovskites*, J. Mater. Chem. A **20**, 5785–5796 (2010).

[39] **N. A. Benedek and C. J. Fennie**, *Why are there so few perovskite ferroelectrics?*, J. Phys. Chem. C **117**, 13339–13349 (2013).

[40] **Y. Hidaka, S. Tsukada and S. Kojima**, *Aging of Dielectric Properties in $Na_{0.5}Bi_{0.5}TiO_3$ Ceramics*, Ferroelectrics **376**, 134–139 (2008).

[41] **J. Kreisel, P. Bouvier, B. Dkhil, P. A. Thomas, A. M. Glazer, T. R. Welberry, B. Chaabane and M. Mezouar**, *High-pressure x-ray scattering of oxides with a nanoscale local structure: Application to $Na_{1/2}Bi_{1/2}TiO_3$*, Phys. Rev. B **68**, 014113 (2003).

[42] **I. P. Pronin, P. P. Syrnikov, V. A. Isupov, V. M. Egorov and N. V. Zaitseva**, *Peculiarities of phase transitions in sodium-bismuth titanate*, Ferroelectrics **25**, 395–397 (1980).

[43] **S. Vakhrushev, B. Kvyatkovskii, N. Okuneva, É. Plachenova and P. Syrnikov**, *Phase transitions in sodium-bismuth titanate*, ZhETF Pisma Redaktsiiu **35**, 111 (1982).

[44] **S. B. Vakhrushev, B. G. Ivanitskii, B. E. Kvyatkovskii, A. N. Maistrenko, R. S. Malysheva, N. M. Okuneva and N. N. Parfenova**, *Neutron scattering studies of the structure of sodium bismuth titanate*, Sov. Phys. Solid State **25**, 1504–6 (1983).

[45] **S. B. Vakhrushev, B. E. Kvyatkovskii, R. S. Malysheva, N. M. Okuneva, E. L. Plachenova and P. P. Syrnikov**, *Investigation of phase transitions in the ferroelectric crystal of $Na_{0.5}Bi_{0.5}TiO_3$ by means of neutron scattering*, Sov. Phys. Crys. **34**, 89–91 (1989).

[46] **G. O. Jones and P. A. Thomas**, *The tetragonal phase of $Na_{0.5}Bi_{0.5}TiO_3$ – a new variant of the perovskite structure*, Acta Cryst. **56**, 426–430 (2000).

[47] **G. O. Jones and P. A. Thomas**, *Investigation of the structure and phase transitions in the novel A-site substituted distorted perovskite compound $Na_{0.5}Bi_{0.5}TiO_3$*, Acta Cryst. **58**, 168–178 (2002).

[48] **P. A. Thomas, J. Kreisel, A. M. Glazer, P. Bouvier, Q. Z. Jiang and R. Smith**, *The high-pressure structural phase transitions of sodium bismuth titanate*, Z. Krist.-Cryst. Mater. **220**, 717–725 (2005).

[49] **A. M. Balagurov, E. Y. Koroleva, A. A. Naberezhnov, V. P. Sakhnenko, B. N. Savenko, N. V. Ter-Oganessian and S. B. Vakhrushev**, *The rhombohedral phase with incommensurate modulation in $Na_{1/2}Bi_{1/2}TiO_3$*, Phase Transit. **79**, 163–173 (2006).

[50] **R. Ranjan, V. Kothai, R. Garg, A. Agrawal, A. Senyshyn and H. Boysen**, *Degenerate rhombohedral and orthorhombic states in Ca-substituted $Na_{0.5}Bi_{0.5}TiO_3$*, Appl. Phys. Lett. **95**, 042904 (2009).

[51] **I. Jeong, C. Y. Park, D. J. Kim, S. H. Kim, B. K. Moon, W. Kim and C. W. Ahn**, *Neutron total scattering studies on A-site disorder in lead-free ferroelectric $Bi_{0.5}(Na_{1-x}K_x)_{0.5}TiO_x$*, Z. Krist.-Cryst. Mater. **226**, 150–154 (2011).

[52] **D. S. Keeble, E. R. Barney, D. A. Keen, M. G. Tucker, J. Kreisel and P. A. Thomas**, *Bifurcated polarization rotation in bismuth-based piezoelectrics*, Adv. Funct. Mater. **23**, 185–190 (2013).

[53] **E. Aksel, J. S. Forrester, J. C. Nino, K. Page, D. P. Shoemaker and J. L. Jones**, *Local atomic structure deviation from average structure of $Na_{0.5}Bi_{0.5}TiO_3$: Combined x-ray and neutron total scattering study*, Phys. Rev. B **87**, 104113 (2013).

[54] **B. N. Rao, R. Datta, S. Chandrashekaran, D. K. Mishra, V. Sathe, A. Senyshyn and R. Ranjan**, *Local structural disorder and its influence on the average global structure and polar properties in $Na_{1/2}Bi_{1/2}TiO_3$*, Phys. Rev. B **88**, 224103 (2013).

[55] **W. Ge, C. P. Devreugd, D. Phelan, Q. Zhang, M. Ahart, J. Li, H. Luo, L. A. Boatner, D. Viehland and P. M. Gehring**, *Lead-free and lead-based ABO_3 perovskite relaxors with mixed-valence A-site and B-site disorder: Comparative neutron scattering structural study of $(Na_{0.5}Bi_{0.5})TiO_3$ and $Pb(Mg_{1/3}Nb_{2/3})O_3$*, Phys. Rev. B **88**, 174115 (2013).

[56] **G. Deng, S. Danilkin, H. Zhang, P. Imperia, X. Li, X. Zhao and H. Luo**, *Dynamical mechanism of phase transitions in A-site ferroelectric relaxor $Na_{1/2}Bi_{1/2}TiO_3$*, Phys. Rev. B **90**, 134104 (2014).

[57] **H. Zhang, G. Deng, A. J. Studer, X. Li, X. Zhao and H. Luo**, *Neutron diffuse scattering of (1-x)$(Na_{0.5}Bi_{0.5})TiO_3$–x$BaTiO_3$ relaxor ferroelectric single crystals*, Scr. Mater. **86**, 5–8 (2014).

[58] **M. Matsuura, H. Iida, K. Hirota, K. Ohwada, Y. Noguchi and M. Miyayama**, *Damped soft phonons and diffuse scattering in $(Bi_{1/2}Na_{1/2})TiO_3$*, Phys. Rev. B **87**, 064109 (2013).

[59] **S. E. Park, S. J. Chung, I. T. Kim and K. S. Hong**, *Nonstoichiometry And The Long-Range Cation Ordering In Crystals Of $(Na_{1/2}Bi_{1/2})TiO_3$*, J. Am. Ceram. Soc. **77**, 2641–2647 (1994).

[60] **V. A. Shuvaeva, D. Zekria, A. M. Glazer, Q. Jiang, S. M. Weber, P. Bhattacharya and P. A. Thomas**, *Local structure of the lead-free relaxor ferroelectric $(K_xNa_{1-x})_{0.5}Bi_{0.5}TiO_3$*, Phys. Rev. B **71**, 174114 (2005).

[61] **S. Gorfman and P. A. Thomas**, *Evidence for a non-rhombohedral average structure in the lead-free piezoelectric material $Na_{0.5}Bi_{0.5}TiO_3$*, J. Appl. Cryst. **43**, 1409–1414 (2010).

[62] **P. Thomas, S. Trujillo, M. Boudard, S. Gorfman and J. Kreisel**, *Diffuse X-ray scattering in the lead-free piezoelectric crystals $Na_{1/2}Bi_{1/2}TiO_3$ and Ba-doped $Na_{1/2}Bi_{1/2}TiO_3$*, Solid State Sci. **12**, 311–317 (2010).

[63] **B. N. Rao, A. N. Fitch and R. Ranjan**, *Ferroelectric-ferroelectric phase coexistence in $Na_{1/2}Bi_{1/2}TiO_3$*, Phys. Rev. B **87**, 060102 (2013).

[64] **S. Gorfman, D. S. Keeble, A. Bombardi and P. A. Thomas**, *Topology and temperature dependence of the diffuse X-ray scattering in $Na_{0.5}Bi_{0.5}TiO_3$ ferroelectric single crystals*, J. Appl. Crystallogr. **48**, 1543–1550 (2015).

[65] **T.-M. Usher, I. Levin, J. E. Daniels and J. L. Jones**, *Electric-field-induced local and mesoscale structural changes in polycrystalline dielectrics and ferroelectrics*, Sci. Rep. **5**, 14678 (2015).

[66] **J. Yao, W. Ge, L. Luo, J. Li, D. Viehland and H. Luo**, *Hierarchical domains in $Na_{1/2}Bi_{1/2}TiO_3$ single crystals: Ferroelectric phase transformations within the geometrical restrictions of a ferroelastic inheritance*, Appl. Phys. Lett. **96**, 222905 (2010).

[67] **I. G. Siny, E. Husson, J. M. Beny, S. Lushnikov, E. Rogacheva and P. P. Syrnikov**, *Raman scattering in the relaxor-type ferroelectric $Na_{1/2}Bi_{1/2}TiO_3$*, Ferroelectrics **248**, 57–78 (2000).

[68] **J. Petzelt, S. Kamba, J. Fábry, D. Noujni, V. Porokhonskyy, A. Pashkin, I. Franke, K. Roleder, J. Suchanicz, R. Klein and G. E. Kugel**, *Infrared, raman and high-frequency dielectric spectroscopy and the phase transitions in $Na_{1/2}Bi_{1/2}TiO_3$*, J. Phys.: Condens. Matter **16**, 2719–2731 (2004).

[69] **J. Petzelt, D. Nuzhnyy, V. Bovtun, M. Paściak, S. Kamba, R. Dittmer, Šarunas Svirskas, J. Banys and J. Rödel**, *Peculiar Bi-ion dynamics in $Na_{1/2}Bi_{1/2}TiO_3$ from terahertz and microwave dielectric spectroscopy*, Phase Transit. **87**, 953–965 (2014).

[70] **D. K. Jackson, J. Toulouse and H. Luo**, *Phonon modes and central peaks in an A-site relaxor: A low-frequency Raman study of sodium bismuth titanate*, Phys. Rev. B **90**, 054108 (2014).

[71] **D. J. Ruth and B. Sundarakannan**, *Structural and raman spectroscopic studies of poled lead-free piezoelectric sodium bismuth titanate ceramics*, Ceram. Int. **42**, 4775 – 4778 (2015).

[72] **I. Aleksandrova, Y. Ivanov, A. Sukhovskiĭ and S. Vakhrushev**, *^{23}Na NMR in the relaxor ferroelectric $Na_{1/2}Bi_{1/2}TiO_3$*, Phys. Solid State **48**, 1120–1123 (2006).

[73] **P. B. Groszewicz, M. Gröting, H. Breitzke, W. Jo, K. Albe, G. Buntkowsky and J. Rödel**, *Reconciling Local Structure Disorder and the Relaxor State in $(Bi_{1/2}Na_{1/2})TiO_3$-$BaTiO_3$*, Sci. Rep. **6**, 31739 (2016).

[74] **B. N. Rao, L. Olivi, V. Sathe and R. Ranjan**, *Electric field and temperature dependence of the local structural disorder in the lead-free ferroelectric $Na_{0.5}Bi_{0.5}TiO_3$: An EXAFS study*, Phys. Rev. B **93**, 024106 (2016).

[75] **V. A. Isupov**, *Ferroelectric $Na_{0.5}Bi_{0.5}TiO_3$ and $K_{0.5}Bi_{0.5}TiO_3$ perovskites and their solid solutions*, Ferroelectrics **315**, 123–147 (2005).

[76] **C.-S. Tu, I. G. Siny and V. H. Schmidt**, *Sequence of dielectric anomalies and high-temperature relaxation behavior in $Na_{1/2}Bi_{1/2}TiO_3$*, Phys. Rev. B **49**, 11550–11559 (1994).

[77] **S.-E. Park, S.-J. Chung and I.-T. Kim**, *Ferroic Phase Transit. in $(Na_{1/2}Bi_{1/2})TiO_3$ Crystals*, J. Am. Ceram. Soc. **79**, 1290–1296 (1996).

[78] **J. Suchanicz**, *The low-frequency dielectric relaxation $Na_{0.5}Bi_{0.5}TiO_3$ ceramics*, Mater. Sci. Eng. B **55**, 114–118 (1998).

[79] **Y. Hiruma, H. Nagata and T. Takenaka**, *Thermal depoling process and piezoelectric properties of bismuth sodium titanate ceramics*, J. Appl. Phys. **105**, 084112 (2009).

[80] **V. Dorcet, G. Trolliard and P. Boullay**, *Reinvestigation of phase transitions in $Na_{0.5}Bi_{0.5}TiO_3$ by TEM. Part I: First order rhombohedral to orthorhombic phase transition*, Chem. Mater. **20**, 5061–5073 (2008).

[81] **G. Trolliard and V. Dorcet**, *Reinvestigation of phase transitions in $Na_{0.5}Bi_{0.5}TiO_3$ by TEM. Part II: Second order orthorhombic to tetragonal phase transition*, Chem. Mater. **20**, 5074–5082 (2008).

[82] **R. Beanland and P. Thomas**, *Imaging planar tetragonal sheets in rhombohedral $Na_{0.5}Bi_{0.5}TiO_3$ using transmission electron microscopy*, Scr. Mater. **65**, 440–443 (2011).

[83] **I. Levin and I. M. Reaney**, *Nano- and mesoscale structure of $Na_{1/2}Bi_{1/2}TiO_3$: A TEM perspective*, Adv. Funct. Mater. **22**, 3445–3452 (2012).

[84] **R. Beanland and P. A. Thomas**, *Symmetry and defects in rhombohedral single-crystalline $Na_{0.5}Bi_{0.5}TiO_3$*, Phys. Rev. B **89**, 174102 (2014).

[85] **E. Aksel, J. S. Forrester, J. L. Jones, P. A. Thomas, K. Page and M. R. Suchomel**, *Monoclinic crystal structure of polycrystalline $Na_{0.5}Bi_{0.5}TiO_3$*, Appl. Phys. Lett. **98**, 152901 (2011).

[86] **I. G. Siny, C.-S. Tu and V. H. Schmidt**, *Critical acoustic behavior of the relaxor ferroelectric $Na_{1/2}Bi_{1/2}TiO_3$ in the intertransition region*, Phys. Rev. B **51**, 5659–5665 (1995).

[87] **F. Pforr, M. Major, W. Donner, U. Stuhr and B. Roessli**, *Influence of tetragonal platelets on the dielectric permittivity of $0.964Na_{1/2}Bi_{1/2}TiO_3$–$0.036BaTiO_3$*, Phys. Rev. B **94**, 014105 (2016).

[88] **K. Sakata and Y. Masuda**, *Ferroelectric and antiferroelectric properties of $(Na_{0.5}Bi_{0.5})TiO_3$-$SrTiO_3$ solid solution ceramics*, Ferroelectrics **7**, 347–349 (1974).

[89] **M. Gröting, I. Kornev, B. Dkhil and K. Albe**, *Pressure-induced phase transitions and structure of chemically ordered nanoregions in the lead-free relaxor ferroelectric $Na_{1/2}Bi_{1/2}TiO_3$*, Phys. Rev. B **86**, 134118 (2012).

[90] **N. W. Thomas**, *The compositional dependence of octahedral tilting in orthorhombic and tetragonal perovskites*, Acta Crystallogr. Sect. B **52**, 16–31 (1996).

[91] **G. King, S. Thimmaiah, A. Dwivedi and P. M. Woodward**, *Synthesis and characterization of new $AA'BWO_6$ perovskites exhibiting simultaneous ordering of A-site and B-site cations*, Chem. Mat. **19**, 6451–6458 (2007).

[92] **M. Gröting**, *Ab-initio Calculations of the Relaxor Ferroelectric $Na_{1/2}Bi_{1/2}TiO_3$ and its Solid Solutions*, Ph.D. thesis, TU Darmstadt, 2013, http://tuprints.ulb.tu-darmstadt.de/3481/, Retrieved 5 May 2017.

[93] **M. W. Lufaso and P. M. Woodward**, *Jahn–Teller distortions, Cation Ordering and Octahedral Tilting in Perovskites*, Acta Cryst. **60**, 10–20 (2004).

[94] **R. E. Cohen**, *Origin of ferroelectricity in perovskite oxides*, Nature **358**, 136–138 (1992).

[95] **Y. Yoneda, H. Nagata and T. Takenaka**, *Local structure analysis of $Bi_{0.5}Na_{0.5}TiO_3$*, J. Korean Phys. Soc. **66**, 1339–1343 (2015).

[96] **M. Gröting, S. Hayn and K. Albe**, *Chemical order and local structure of the lead-free relaxor ferroelectric $Na_{1/2}Bi_{1/2}TiO_3$*, J. Solid State Chem. **184**, 2041–2046 (2011).

[97] **V. M. Goldschmidt**, *Die Gesetze der Krystallochemie*, Naturwissenschaften **14**, 477–485 (1926).

[98] **A. M. Glazer**, *The classification of tilted octahedra in perovskites*, Acta Cryst. **28**, 3384–3392 (1972).

[99] **H. T. Stokes, E. H. Kisi, D. M. Hatch and C. J. Howard**, *Group-theoretical analysis of octahedral tilting in ferroelectric perovskites*, Acta Cryst. **58**, 934–938 (2002).

[100] **D. I. Woodward and I. M. Reaney**, *Electron diffraction of tilted perovskites*, Acta Cryst. **61**, 387–399 (2005).

[101] **J. E. Daniels, W. Jo, J. Rödel, D. Rytz and W. Donner**, *Structural origins of relaxor behavior in a $0.96(Bi_{1/2}Na_{1/2})TiO_3$–$0.04BaTiO_3$ single crystal under electric field*, Appl. Phys. Lett. **98**, 252904 (2011).

[102] **D. L. Corker, A. M. Glazer, R. W. Whatmore, A. Stallard and F. Fauth**, *A neutron diffraction investigation into the rhombohedral phases of the perovskite series $PbZr_{1-x}Ti_xO_3$*, J. Phys.-Condes. Matter **10**, 6251 (1998).

[103] **X. Dai, Z. Xu and D. Viehland**, *Effect of Oxygen Octahedron Rotations on the Phase Stability, Transformational Characteristics, and Polarization Behavior in the Lead Zirconate Titanate Crystalline Solution Series*, J. Am. Ceram. Soc. **78**, 2815–2827 (1995).

[104] **A. Walsh, D. J. Payne, R. G. Egdell and G. W. Watson**, *Stereochemistry of post-transition metal oxides: revision of the classical lone pair model*, Chem. Soc. Rev. **40**, 4455–4463 (2011).

[105] **D. Schütz, M. Deluca, W. Krauss, A. Feteira, T. Jackson and K. Reichmann**, *Lone-Pair-Induced Covalency as the Cause of Temperature- and Field-Induced Instabilities in Bismuth Sodium Titanate*, Adv. Funct. Mater. **22**, 2285–2294 (2012).

[106] **D. Schütz and K. Reichmann**, *Complex bonding in perovskite ferroelectrics*, J. Ceram. Soc. Jpn. **122**, 231–236 (2014).

[107] **M. Ghita, M. Fornari, D. J. Singh and S. V. Halilov**, *Interplay between A-site and B-site driven instabilities in perovskites*, Phys. Rev. B **72**, 054114 (2005).

[108] **L. E. Cross**, *Relaxorferroelectrics: An overview*, Ferroelectrics **151**, 305–320 (1994).

[109] **A. Bokov and Z.-G. Ye**, *Recent progress in relaxor ferroelectrics with perovskite structure*, J. Mater. Sci. **41**, 31–52 (2006).

[110] **R. Blinc, V. Laguta, B. Zalar and J. Banys**, *Polar nanoclusters in relaxors*, J. Mater. Sci. **41**, 27–30 (2006).

[111] **G. Burns and F. Dacol**, *Glassy polarization behavior in ferroelectric compounds $Pb(Mg_{1/3}Nb_{2/3})O_3$ and $Pb(Zn_{1/3}Nb_{2/3})O_3$*, Solid State Commun. **48**, 853 – 856 (1983).

[112] **P. M. Gehring, H. Hiraka, C. Stock, S.-H. Lee, W. Chen, Z.-G. Ye, S. B. Vakhrushev and Z. Chowdhuri**, *Reassessment of the Burns temperature and its relationship to the diffuse scattering, lattice dynamics, and thermal expansion in relaxor $Pb(Mg_{1/3}Nb_{2/3})O_3$*, Phys. Rev. B **79**, 224109 (2009).

[113] **B. Dkhil, P. Gemeiner, A. Al-Barakaty, L. Bellaiche, E. Dul'kin, E. Mojaev and M. Roth**, *Intermediate temperature scale T^* in lead-based relaxor systems*, Phys. Rev. B **80**, 064103 (2009).

[114] **E.-M. Anton, W. Jo, D. Damjanovic and J. Rödel**, *Determination of depolarization temperature of $(Bi_{1/2}Na_{1/2})TiO_3$–based lead-free piezoceramics*, J. Appl. Phys. **110** (2011).

[115] **R. Pirc and R. Blinc**, *Vogel-Fulcher freezing in relaxor ferroelectrics*, Phys. Rev. B **76**, 020101 (2007).

[116] **C. W. Ahn, C.-H. Hong, B.-Y. Choi, H.-P. Kim, H.-S. Han, Y. Hwang, W. Jo, K. Wang, J.-F. Li, J.-S. Lee and I. W. Kim**, *A brief review on relaxor ferroelectrics and selected issues in lead-free relaxors*, J. Korean Phys. Soc. **68**, 1481–1494 (2016).

[117] **G. A. Smolenskii**, *Physical phenomena in ferroelectrics with diffused phase transition*, J. Phys. Soc. Jpn **28**, 26–37 (1970).

[118] **V. Kirillov and V. Isupov**, *Relaxation polarization of $PbMg_{1/3}Nb_{2/3}O_3$ (PMN)-A ferroelectric with a diffused phase transition*, Ferroelectrics **5**, 3–9 (1973).

[119] **L. E. Cross**, *Relaxor ferroelectrics*, Ferroelectrics **76**, 241–267 (1987).

[120] **J. I. Gittleman, B. Abeles and S. Bozowski**, *Superparamagnetism and relaxation effects in granular Ni-SiO_2 and Ni-A_2O_3 films*, Phys. Rev. B **9**, 3891–3897 (1974).

[121] **A. K. Tagantsev**, *Vogel-Fulcher relationship for the dielectric permittivity of relaxor ferroelectrics*, Phys. Rev. Lett. **72**, 1100–1103 (1994).

[122] **D. Viehland, M. Wuttig and L. Cross**, *The glassy behavior of relaxor ferroelectrics*, Ferroelectrics **120**, 71–77 (1991).

[123] **E. V. Colla, K. Sullivan and M. B. Weissman**, *Glassy aging in the relaxor-like ferroelectric $Na_{1/2}Bi_{1/2}TiO_3$*, J. Appl. Phys. **119** (2016).

[124] **V. Westphal, W. Kleemann and M. D. Glinchuk**, *Diffuse phase transitions and random-field-induced domain states of the "relaxor" ferroelectric $PbMg_{1/3}Nb_{2/3}O_3$*, Phys. Rev. Lett. **68**, 847–850 (1992).

[125] **Y. Imry and S.-K. Ma**, *Random-Field Instability of the Ordered State of Continuous Symmetry*, Phys. Rev. Lett. **35**, 1399–1401 (1975).

[126] **W. Kleemann**, *The relaxor enigma – charge disorder and random fields in ferroelectrics*, J. Mater. Sci. **41**, 129–136 (2006).

[127] **W. Kleemann**, *Random Fields in Relaxor Ferroelectrics – A Jubilee Review*, J. Adv. Dielect. **2**, 1241001 (2012).

[128] **D. Phelan, C. Stock, J. A. Rodriguez-Rivera, S. Chi, J. Leão, X. Long, Y. Xie, A. A. Bokov, Z.-G. Ye, P. Ganesh and P. M. Gehring**, *Role of random electric fields in relaxors*, Proc. Nat. Acad. Sci. **111**, 1754–1759 (2014).

[129] **A. Leschhorn and H. Kliem**, *Influence of thermal vibrations on polarization switching in the model of local fields*, J. Appl. Phys **121**, 014103 (2017).

[130] **H. Kliem and A. Leschhorn**, *Modeling relaxor characteristics in systems of interacting dipoles*, Physica B **503**, 167–173 (2016).

[131] **R. Pirc and R. Blinc**, *Spherical random-bond–random-field model of relaxor ferroelectrics*, Phys. Rev. B **60**, 13470–13478 (1999).

[132] **Z. Ye**, *Relaxor ferroelectric complex perovskites: structure, properties and phase transitions*, **155**, 81–122 (1998).

[133] **R. A. Cowley, S. N. Gvasaliya, S. G. Lushnikov, B. Roessli and G. M. Rotaru**, *Relaxing with relaxors: a review of relaxor ferroelectrics*, Adv. Phys. **60**, 229–327 (2011).

[134] **V. V. Shvartsman and D. C. Lupascu**, *Lead-Free Relaxor Ferroelectrics*, J. Am. Ceram. Soc. **95**, 1–26 (2012).

[135] **J. Hlinka**, *Do we need the ether of polar nanoregions?*, J. Adv. Dielect. **2**, 1241006 (2012).

[136] **I. Chen**, *Structural origin of relaxor ferroelectrics – revisited*, J. Phys. Chem. Solids **61**, 197–208 (2000).

[137] **G. Xu, Z. Zhong, H. Hiraka and G. Shirane**, *Three-dimensional mapping of diffuse scattering in $Pb(Zn_{1/3}Nb_{2/3})O_3$–$xPbTiO_3$*, Phys. Rev. B **70**, 174109 (2004).

[138] **J. Kreisel, P. Bouvier, B. Dkhil, B. Chaabane, A. M. Glazer, P. A. Thomas and T. R. Welberry**, *Effect of High Pressure on the Relaxor Ferroelectrics $Na_{1/2}Bi_{1/2}TiO_3$ (NBT) and $PbMg_{1/3}Nb_{2/3}O_3$ (PMN)*, Ferroelectrics **302**, 293–298 (2004).

[139] **P. Ganesh, E. Cockayne, M. Ahart, R. E. Cohen, B. Burton, R. J. Hemley, Y. Ren, W. Yang and Z.-G. Ye**, *Origin of diffuse scattering in relaxor ferroelectrics*, Phys. Rev. B **81**, 144102 (2010).

[140] **T. Egami**, *Local Structure of Ferroelectric Materials*, Ann. Rev. Mater. Res. **37**, 297–315 (2007).

[141] **B. P. Burton, E. Cockayne and U. V. Waghmare**, *Correlations between nanoscale chemical and polar order in relaxor ferroelectrics and the lengthscale for polar nanoregions*, Phys. Rev. B **72**, 064113 (2005).

[142] **S. Tinte, B. P. Burton, E. Cockayne and U. V. Waghmare**, *Origin of the relaxor state in $Pb(B_xB'_{1-x})O_3$ perovskites*, Phys. Rev. Lett. **97**, 137601 (2006).

[143] **A. Al-Barakaty, S. Prosandeev, D. Wang, B. Dkhil and L. Bellaiche**, *Finite-temperature properties of the relaxor $PbMg_{1/3}Nb_{2/3}O_3$ from atomistic simulations*, Phys. Rev. B **91**, 214117 (2015).

[144] **S. Prosandeev and L. Bellaiche**, *Effects of atomic short-range order on properties of the $PbMg_{1/3}Nb_{2/3}O_3$ relaxor ferroelectric*, Phys. Rev. B **94**, 180102 (2016).

[145] **I. Grinberg, Y.-H. Shin and A. M. Rappe**, *Molecular Dynamics Study of Dielectric Response in a Relaxor Ferroelectric*, Phys. Rev. Lett. **103**, 197601 (2009).

[146] **H. Takenaka, I. Grinberg and A. M. Rappe**, *Anisotropic Local Correlations and Dynamics in a Relaxor Ferroelectric*, Phys. Rev. Lett. **110**, 147602 (2013).

[147] **A. Akbarzadeh, R., S. Prosandeev, E. J. Walter, A. Al-Barakaty and L. Bellaiche**, *Finite-temperature properties of $Ba(Zr,Ti)O_3$ relaxors from first principles*, Phys. Rev. Lett. **108**, 257601 (2012).

[148] **A. Bussmann-Holder, A. R. Bishop and T. Egami**, *Relaxor ferroelectrics and intrinsic inhomogeneity*, EPL **71**, 249 (2005).

[149] **J. Macutkevic, J. Banys, A. Bussmann-Holder and A. R. Bishop**, *Origin of polar nanoregions in relaxor ferroelectrics: Nonlinearity, discrete breather formation, and charge transfer*, Phys. Rev. B **83**, 184301 (2011).

[150] **M. Sepliarsky and R. E. Cohen**, *First-principles based atomistic modeling of phase stability in PMN-xPT*, J. Phys.: Condens. Matter **23**, 435902 (2011).

[151] **Y. Ni, H. T. Chen, Y. P. Shi, L. H. He and A. K. Soh**, *Modeling of polar nanoregions dynamics on the dielectric response of relaxors*, J. Appl. Phys. **113** (2013).

[152] **N. W. Ashcroft and D. Mermin**, *Introduction to Solid State Physics*, 1976.

[153] **M. Li, H. Zhang, S. N. Cook, L. Li, J. A. Kilner, I. M. Reaney and D. C. Sinclair**, *Dramatic Influence of A-Site Nonstoichiometry on the Electrical Conductivity and Conduction Mechanisms in the Perovskite Oxide $Na_{0.5}Bi_{0.5}TiO_3$*, Chem. Mater. **27**, 629–634 (2015).

[154] **J. Kilner and R. Brook**, *A study of oxygen ion conductivity in doped non-stoichiometric oxides*, Solid State Ion. **6**, 237–252 (1982).

[155] **T. Ishigaki, S. Yamauchi, K. Kishio, J. Mizusaki and K. Fueki**, *Diffusion of oxide ion vacancies in perovskite-type oxides*, J. Solid State Chem. **73**, 179–187 (1988).

[156] **E. Aksel, H. Foronda, K. A. Calhoun, J. L. Jones, S. Schaab and T. Granzow**, *Processing and properties of $Na_{0.5}Bi_{0.5}TiO_3$ piezoelectric ceramics modified with La, Mn and Fe*, Funct. Mater. Lett. **3**, 45–48 (2010).

[157] **E. Aksel, J. S. Forrester, B. Kowalski, M. Deluca, D. Damjanovic and J. L. Jones**, *Structure and properties of Fe-modified $Na_{0.5}Bi_{0.5}TiO_3$ at ambient and elevated temperature*, Phys. Rev. B **85**, 024121 (2012).

[158] **S. Supriya, A. J. D. santos García, C. You and F. Fernández-Martinez**, *Analysis of Single and Binary Phases in Cerium Doped Sodium Bismuth Titanate -$Na_{0.5}Bi_{0.5}TiO_3$ Materials*, Energy Procedia **84**, 190–196 (2015).

[159] **V. Schmitt**, *Effect of Dopants on the Local Atomic Structure and Sintering Behavior of Bismuth Sodium Titanate*, Ph.D. thesis, Universität Bayreuth, 2014, http://epub.uni-bayreuth.de/77/, Retrieved 5 May 2017.

[160] **K. Thangavelu and S. Asthana**, *Monoclinic Cc -phase stabilization in magnetically diluted lead free $Na_{1/2}Bi_{1/2}$ TiO_3—Evolution of spin glass like behavior with enhanced ferroelectric and dielectric properties*, Mater. Res. Express **2**, 096301 (2015).

[161] **C.-M. Wang, L. Zhao, Y. Liu, R. L. Withers, S. Zhang and Q. Wang**, *The temperature-dependent piezoelectric and electromechanical properties of cobalt-modified sodium bismuth titanate*, Ceram. Int. **42**, 4268–4273 (2016).

[162] **D. Kirsever and H. Yilmaz**, *Electrical Properties of Lead-Free $Na_{1/2}Bi_{1/2}TiO_3$ Relaxor Ferroelectric Ceramics Doped with Hafnium or Zirconium*, J. Am. Ceram. Soc. **98**, 1858–1864 (2015).

[163] **D. E. Jain Ruth, M. Muneeswaran, N. V. Giridharan and B. Sundarakannan**, *Enhanced electrical properties in Rb-substituted sodium bismuth titanate ceramics*, Appl. Phys. A **122**, 1–7 (2016).

[164] **X. Liu, H. Fan, J. Shi, L. Wang and H. Du**, *Enhanced ionic conductivity of Ag addition in acceptor-doped $Bi_{0.5}Na_{0.5}TiO_3$ ferroelectrics*, RSC Adv. **6**, 30623–30627 (2016).

[165] **J. Huang, F. Zhu, D. Huang, B. Wang, T. Xu, X. Li, P. Fan, F. Xia, J. Xiao and H. Zhang**, *Intermediate-temperature conductivity of B-site doped $Na_{0.5}Bi_{0.5}TiO_3$-based lead-free ferroelectric ceramics*, Ceram. Int. **42**, 16798–16803 (2016).

[166] **M. Schie, A. Marchewka, T. Müller, R. A. D. Souza and R. Waser**, *Molecular dynamics simulations of oxygen vacancy diffusion in $SrTiO_3$*, J. Phys.-Condens. Matter **24**, 485002 (2012).

[167] **X. He and Y. Mo**, *Accelerated materials design of $Na_{0.5}Bi_{0.5}TiO_3$ oxygen ionic conductors based on first principles calculations*, Phys. Chem. Chem. Phys. **17**, 18035–18044 (2015).

[168] **M. Schie, R. Waser and R. A. D. Souza**, *A Simulation Study of Oxygen-Vacancy Behavior in Strontium Titanate: Beyond Nearest-Neighbor Interactions*, J. Phys. Chem. C **118**, 15185–15192 (2014).

[169] **R. A. De Souza**, *Oxygen Diffusion in $SrTiO_3$ and Related Perovskite Oxides*, Adv. Funct. Mater. **25**, 6326–6342 (2015).

[170] **R. A. De Souza, C. Voisin, H. Schraknepper, M. Teusner, M. Kessel, P. Dufour, C. Tenailleau and S. Guillemet-Fritsch**, *Complex diffusion behavior of oxygen in nanocrystalline $BaTiO_3$ ceramics*, Phys. Chem. Chem. Phys. **16**, 2568–2575 (2014).

[171] **M. Kessel, R. A. De Souza and M. Martin**, *Oxygen diffusion in single crystal barium titanate*, Phys. Chem. Chem. Phys. **17**, 12587–12597 (2015).

[172] **L. Koch, S. Steiner, K.-C. Meyer, I.-T. Seo, K. Albe and T. Frömling**, *Ionic conductivity of acceptor doped sodium bismuth titanate: influence of dopants, phase transitions and defect associates*, J. Mater. Chem. C, – (2017).

[173] **R. W. Balluffi, S. Allen and W. C. Carter**, *Kinetics of materials*, John Wiley & Sons, 2005.

[174] **R. Merkle and J. Maier**, *Defect association in acceptor-doped $SrTiO_3$: case study for $Fe'_{Ti}V_O^{\bullet\bullet}$ and $Mn''_{Ti}V_O^{\bullet\bullet}$*, Phys. Chem. Chem. Phys. **5**, 2297–2303 (2003).

[175] **G. E. Murch**, *The Nernst-Einstein equation in high-defect-content solids*, Philosophical Magazine A **45**, 685–692 (1982).

[176] **F. Yang, H. Zhang, L. Li, I. M. Reaney and D. C. Sinclair**, *High Ionic Conductivity with Low Degradation in A-Site Strontium-Doped Nonstoichiometric Sodium Bismuth Titanate Perovskite*, Chem. Mat. **28**, 5269–5273 (2016).

[177] **M. Dawber and J. F. Scott**, *A model for fatigue in ferroelectric perovskite thin films*, Appl. Phys. Lett. **76**, 1060–1062 (2000).

[178] **X. Ren**, *Large electric-field-induced strain in ferroelectric crystals by point-defect-mediated reversible domain switching*, Nat. Mater. **3**, 91–94 (2004).

[179] **P. Erhart, P. Träskelin and K. Albe**, *Formation and switching of defect dipoles in acceptor-doped lead titanate: A kinetic model based on first-principles calculations*, Phys. Rev. B **88**, 024107 (2013).

[180] **D. C. Lupascu**, *Fatigue in Ferroelectric Ceramics and related Issues*, vol. 61, Springer Science & Business Media, 2004.

[181] **D. C. Lupascu, Y. A. Genenko and N. Balke**, *Aging in ferroelectrics*, J. Am. Ceram. Soc. **89**, 224–229 (2006).

[182] **M. Zannen, A. Lahmar, B. Asbani, H. Khemakhem, M. El Marssi, Z. Kutnjak and M. Es Souni**, *Electrocaloric effect and luminescence properties of lanthanide doped $(Na_{1/2}Bi_{1/2})TiO_3$ lead free materials*, Appl. Phys. Lett. **107** (2015).

[183] **Y. A. Genenko, J. Glaum, M. J. Hoffmann and K. Albe**, *Mechanisms of aging and fatigue in ferroelectrics*, Mater. Sci. Eng. B **192**, 52–82 (2015).

[184] **Y. Xu and W. Y. Ching**, *Electronic structure of $(Na_{1/2}Bi_{1/2})TiO_3$ and its solid solution with $BaTiO_3$*, Philos. Mag. **80**, 1141–1151 (2000).

[185] **B. P. Burton and E. Cockayne**, *Prediction of the $[Na_{1/2}Bi_{1/2}]TiO_3$ ground state*, AIP Conference Proceedings **582**, 82–90 (2001).

[186] **R. Bujakiewicz-Korońska and Y. Natanzon**, *Determination of elastic constants of $Na_{0.5}Bi_{0.5}TiO_3$ from ab initio calculations*, Phase Transit. **81**, 1117–1124 (2008).

[187] **M. Bousquet, J.-R. Duclère, E. Orhan, A. Boulle, C. Bachelet and C. Champeaux**, *Optical properties of an epitaxial $Na_{0.5}Bi_{0.5}TiO_3$ thin film grown by laser ablation: Experimental approach and density functional theory calculations*, J. Appl. Phys. **107** (2010).

[188] **M. Zeng, S. W. Or and H. L. W. Chan**, *First-principles study on the electronic and optical properties of $Na_{0.5}Bi_{0.5}TiO_3$ lead-free piezoelectric crystal*, J. Appl. Phys. **107** (2010).

[189] **K. Dorywalski, N. Lemée, B. Andriyevsky, R. Schmidt-Grund, M. Grundmann, M. Piasecki, M. Bousquet and T. Krzyżyński**, *Optical properties of epitaxial $Na_{0.5}Bi_{0.5}TiO_3$ lead-free piezoelectric thin films: ellipsometric and theoretical studies*, Appl. Surf. Sci. (2016).

[190] **Y. Kitanaka, K. Yanai, Y. Noguchi, M. Miyayama, Y. Kagawa, C. Moriyoshi and Y. Kuroiwa**, *Non-180° polarization rotation of ferroelectric $(Bi_{0.5}Na_{0.5}TiO_3)$ single crystals under electric field*, Phys. Rev. B **89**, 104104 (2014).

[191] **M. K. Niranjan, T. Karthik, S. Asthana, J. Pan and U. V. Waghmare**, *Theoretical and experimental investigation of raman modes, ferroelectric and dielectric properties of relaxor $Na_{0.5}Bi_{0.5}TiO_3$*, J. Appl. Phys. **113**, 194106 (2013).

[192] **H. Lü, S. Wang and X. Wang**, *The electronic properties and lattice dynamics of $Na_{0.5}Bi_{0.5}TiO_3$: From cubic to tetragonal and rhombohedral phases*, J. Appl. Phys. **115**, 124107 (2014).

[193] **J. Pan, M. K. Niranjan and U. V. Waghmare**, *Aliovalent cation ordering, coexisting ferroelectric structures, and electric field induced phase transformation in lead-free ferroelectric $Na_{0.5}Bi_{0.5}TiO_3$*, J. Appl. Phys. **119** (2016).

[194] **K.-C. Meyer, M. Gröting and K. Albe**, *Octahedral tilt transitions in the relaxor ferroelectric $Na_{1/2}Bi_{1/2}TiO_3$*, J. Solid State Chem. **227**, 117–122 (2015).

[195] **L. Ju, C. Shi, L. Sun, Y. Zhang, H. Qin and J. Hu**, *Room-temperature magnetoelectric coupling in nanocrystalline $Na_{0.5}Bi_{0.5}TiO_3$*, J. Appl. Phys. **116** (2014).

[196] **M. Gröting and K. Albe**, *Theoretical prediction of morphotropic compositions in $Na_{1/2}Bi_{1/2}TiO_3$–based solid solutions from transition pressures*, Phys. Rev. B **89**, 054105 (2014).

[197] **Y. Zhang, J. Hu, F. Gao, H. Liu and H. Qin**, *Ab initio calculation for vacancy-induced magnetism in ferroelectric $Na_{0.5}Bi_{0.5}TiO_3$*, Comput. Theor. Chem. **967**, 284–288 (2011).

[198] **J. A. Dawson, H. Chen and I. Tanaka**, *Crystal structure, defect chemistry and oxygen ion transport of the ferroelectric perovskite, $Na_{0.5}Bi_{0.5}TiO_3$: insights from first-principles calculations*, J. Mater. Chem. A **3**, 16574–16582 (2015).

[199] **P. Kobeko and J. Kurtschatov**, *Dielektrische Eigenschaften der Seignettesalzkristalle*, Zeitschrift für Physik **66**, 192–205 (1930).

[200] **A. Karchevskii**, *Electrocaloric effect in polycrystalline barium titanate*, Soviet Physics-Solid State **3**, 2249–2254 (1962).

[201] **E. Hegenbarth**, *Studies of the electrocaloric effect of ferroelectricceramics at low temperatures*, Cryogenics **1**, 242–243 (1961).

[202] **P. D. Thacher**, *Electrocaloric Effects in Some Ferroelectric and Antiferroelectric $Pb(Zr,Ti)O_3$ Compounds*, J. Appl. Phys. **39**, 1996–2002 (1968).

[203] **G. Lombardo and R. O. Pohl**, *Electrocaloric effect and a new type of impurity mode*, Phys. Rev. Lett. **15**, 291–293 (1965).

[204] **B. A. Tuttle and D. A. Payne**, *The effects of microstructure on the electrocaloric properties of $Pb(Zr,Sn,Ti)O_3$ ceramics*, Ferroelectrics **37**, 603–606 (1981).

[205] **N. Novak, Z. Kutnjak and R. Pirc**, *High-resolution electrocaloric and heat capacity measurements in barium titanate*, EPL **103**, 47001 (2013).

[206] **X. Moya, E. Stern-Taulats, S. Crossley, D. González-Alonso, S. Kar-Narayan, A. Planes, L. Mañosa and N. D. Mathur**, *Giant electrocaloric strength in single-crystal $BaTiO_3$*, Adv. Mater. **25**, 1360–1365 (2013).

[207] **J. Wang, T. Yang, S. Chen, G. Li, Q. Zhang and X. Yao**, *Nonadiabatic direct measurement electrocaloric effect in lead-free $Ba,Ca(Zr,Ti)O_3$ ceramics*, J. Alloy. Compd. **550**, 561–563 (2013).

[208] **H.-J. Ye, X.-S. Qian, D.-Y. Jeong, S. Zhang, Y. Zhou, W.-Z. Shao, L. Zhen and Q. M. Zhang**, *Giant electrocaloric effect in $BaZr_{0.2}Ti_{0.8}O_3$ thick film*, Appl. Phys. Lett. **105** (2014).

[209] **M. Sanlialp, V. V. Shvartsman, M. Acosta, B. Dkhil and D. C. Lupascu**, *Strong electrocaloric effect in lead-free $0.65Ba(Zr_{0.2}Ti_{0.8})O_3$–$0.35(Ba_{0.7}Ca_{0.3})TiO_3$ ceramics obtained by direct measurements*, Appl. Phys. Lett. **106** (2015).

[210] **J. Koruza, B. Rožič, G. Cordoyiannis, B. Malič and Z. Kutnjak**, *Large electrocaloric effect in lead-free $K_{0.5}Na_{0.5}NbO_3$–$SrTiO_3$ ceramics*, Appl. Phys. Lett. **106** (2015).

[211] **Y. Bai, G.-P. Zheng and S.-Q. Shi**, *Abnormal electrocaloric effect of $Na_{0.5}Bi_{0.5}TiO_3$–$BaTiO_3$ lead-free ferroelectric ceramics above room temperature*, Mater. Res. Bull. **46**, 1866–1869 (2011).

[212] **W. Cao, W. Li, D. Xu, Y. Hou, W. Wang and W. Fei**, *Enhanced electrocaloric effect in lead-free NBT-based ceramics*, Ceram. Int. **40**, 9273–9278 (2014).

[213] **M. Dunce, E. Birks, J. Perantie, J. Hagberg, M. Antonova and A. Sternberg**, *Electrocaloric Effect in Ca-Modified $Na_{1/2}Bi_{1/2}TiO_3$–$SrTiO_3$–$PbTiO_3$ Solid Solutions*, IEEE Transactions on Ultrasonics, Ferroelectrics, and Frequency Control **61**, 1364–1367 (2014).

[214] **L. Luo, M. Dietze, C.-H. Solterbeck, M. Es-Souni and H. Luo**, *Orientation and phase transition dependence of the electrocaloric effect in $0.71PbMg_{1/3}Nb_{2/3}O_3$–$0.29PbTiO_3$ single crystal*, Appl. Phys. Lett. **101** (2012).

[215] **M. Valant, L. J. Dunne, A.-K. Axelsson, N. M. Alford, G. Manos, J. Peräntie, J. Hagberg, H. Jantunen and A. Dabkowski**, *Electrocaloric effect in a ferroelectric $Pb(Zn_{1/3}Nb_{2/3})O_3$-$PbTiO_3$ single crystal*, Phys. Rev. B **81**, 214110 (2010).

[216] **B. Rožič, M. Kosec, H. Uršič, J. Holc, B. Malič, Q. M. Zhang, R. Blinc, R. Pirc and Z. Kutnjak**, *Influence of the critical point on the electrocaloric response of relaxor ferroelectrics*, J. Appl. Phys. **110** (2011).

[217] **B. Peng, H. Fan and Q. Zhang**, *A Giant Electrocaloric Effect in Nanoscale Antiferroelectric and Ferroelectric Phases Coexisting in a Relaxor $Pb_{0.8}Ba_{0.2}ZrO_3$ Thin Film at Room Temperature*, Adv. Funct. Mater. **23**, 2987–2992 (2013).

[218] **J. Peräntie, J. Hagberg, A. Uusimäki and H. Jantunen**, *Electric-field-induced dielectric and temperature changes in a <011>-oriented $PbMg_{1/3}Nb_{2/3}O_3$-$PbTiO_3$ single crystal*, Phys. Rev. B **82**, 134119 (2010).

[219] **X.-C. Zheng, G.-P. Zheng, Z. Lin and Z.-Y. Jiang**, *Electro-caloric behaviors of lead-free $Bi_{0.5}Na_{0.5}TiO_3$–$BaTiO_3$ ceramics*, J. Electroceram. **28**, 20–26 (2012).

[220] **W. Geng, Y. Liu, X. Meng, L. Bellaiche, J. F. Scott, B. Dkhil and A. Jiang**, *Giant Negative Electrocaloric Effect in Antiferroelectric La-Doped $Pb(ZrTi)O_3$ Thin Films Near Room Temperature*, Advanced Materials **27**, 3165–3169 (2015).

[221] **I. Ponomareva and S. Lisenkov**, *Bridging the macroscopic and atomistic descriptions of the electrocaloric effect*, Phys. Rev. Lett. **108**, 167604 (2012).

[222] **F. L. Goupil, A.-K. Axelsson, L. J. Dunne, M. Valant, G. Manos, T. Lukasiewicz, J. Dec, A. Berenov and N. M. Alford**, *Anisotropy of the Electrocaloric Effect in Lead-Free Relaxor Ferroelectrics*, Adv. Energy Mater. **4**, 1301688 (2014).

[223] **R. Pirc, B. Rožič, J. Koruza, B. Malič and Z. Kutnjak**, *Negative electrocaloric effect in antiferroelectric $PbZrO_3$*, EPL **107**, 17002 (2014).

[224] **T. Zhang, W. Li, Y. Hou, Y. Yu, W. Cao, Y. Feng and W. Fei**, *Positive/negative electrocaloric effect induced by defect dipoles in PZT ferroelectric bilayer thin films*, RSC Adv. **6**, 71934–71939 (2016).

[225] **A. Grünebohm and T. Nishimatsu**, *Influence of defects on ferroelectric and electrocaloric properties of $BaTiO_3$*, Phys. Rev. B **93**, 134101 (2016).

[226] **C. Kalcher, K.-C. Meyer, A. Stukowski and K. Albe**, *Inverse electrocaloric effect in relaxor ferroelectrics*, in preparation.

[227] **M. Valant**, *Electrocaloric materials for future solid-state refrigeration technologies*, Prog. Mater. Sci. **57**, 980–1009 (2012).

[228] **M. Ožbolt, A. Kitanovski, J. Tušek and A. Poredoš**, *Electrocaloric refrigeration: Thermodynamics, state of the art and future perspectives*, Int. J. Refrig.-Rev. Int. Froid **40**, 174–188 (2014).

[229] **X.-S. Qian, H.-J. Ye, Y.-T. Zhang, H. Gu, X. Li, C. A. Randall and Q. M. Zhang**, *Giant electrocaloric response over a broad temperature range in modified $BaTiO_3$ ceramics*, Adv. Funct. Mater. **24**, 1300–1305 (2014).

[230] **Y. Zhou, Q. Lin, W. Liu and D. Wang**, *Compositional dependence of electrocaloric effect in lead-free (1-x)$Ba(Zr_{0.2}Ti_{0.8})O_3$–x$(Ba_{0.7}Ca_{0.3})TiO_3$ ceramics*, RSC Adv. (2016).

[231] **G. G. Guzmán-Verri and P. B. Littlewood**, *Why is the electrocaloric effect so small in ferroelectrics?*, APL Mater. **4** (2016).

[232] **J. Scott**, *Electrocaloric materials*, Annu. Rev. Mater. Res. **41**, 229–240 (2011).

[233] **R. Pirc, Z. Kutnjak, R. Blinc and Q. M. Zhang**, *Electrocaloric effect in relaxor ferroelectrics*, J. Appl. Phys. **110**, 074113 (2011).

[234] **T. Correia and Q. Zhang**, *Electrocaloric Materials*, Springer, 2014.

[235] **Y. Liu, J. F. Scott and B. Dkhil**, *Direct and indirect measurements on electrocaloric effect: Recent developments and perspectives*, Applied Physics Reviews **3** (2016).

[236] **S. Kar-Narayan, S. Crossley, X. Moya, V. Kovacova, J. Abergel, A. Bontempi, N. Baier, E. Defay and N. D. Mathur**, *Direct electrocaloric measurements of a multilayer capacitor using scanning thermal microscopy and infra-red imaging*, Appl. Phys. Lett. **102** (2013).

[237] **Y. Liu, H. Strozyk, B. Dkhil and E. Defay**, *Insight into electrocaloric cooling power in multilayer capacitors using infra-red camera*, Appl. Phys. Lett. **109** (2016).

[238] **S. G. Lu, B. Rožič, Q. M. Zhang, Z. Kutnjak, R. Pirc, M. Lin, X. Li and L. Gorny**, *Comparison of directly and indirectly measured electrocaloric effect in relaxor ferroelectric polymers*, Appl. Phys. Lett. **97** (2010).

[239] **R. Niemann, O. Heczko, L. Schultz and S. Fähler**, *Inapplicability of the maxwell relation for the quantification of caloric effects in anisotropic ferroic materials*, Int. J. Refrig.-Rev. Int. Froid **37**, 281–288 (2014).

[240] **C. Kalcher, A. Stukowski and K. Albe**, *From micro- to multi-canonical: Comparison of three Monte-Carlo Methods to calculate the Electrocaloric Effect*, in preparation.

[241] **Z. Kutnjak, B. Rožič and R. Pirc**, *Electrocaloric Effect: Theory, Measurements, and Applications*, John Wiley & Sons, Inc., 1999.

[242] **A. Devonshire**, *Theory of ferroelectrics*, Adv. Phys. **3**, 85–130 (1954).

[243] **G. Akcay, S. P. Alpay, J. V. Mantese and G. A. Rossetti**, *Magnitude of the intrinsic electrocaloric effect in ferroelectric perovskite thin films at high electric fields*, Appl. Phys. Lett. **90** (2007).

[244] **J. Zhang, S. P. Alpay and G. A. Rossetti**, *Influence of thermal stresses on the electrocaloric properties of ferroelectric films*, Appl. Phys. Lett. **98** (2011).

[245] **J. Zhang, I. B. Misirlioglu, S. P. Alpay and G. A. Rossetti**, *Electrocaloric properties of epitaxial strontium titanate films*, Appl. Phys. Lett. **100** (2012).

[246] **Y. Liu, X.-p. Peng, X. Lou and H. Zhou**, *Intrinsic electrocaloric effect in ultrathin ferroelectric capacitors*, Appl. Phys. Lett. **100**, 192902 (2012).

[247] **B. Li, J. B. Wang, X. L. Zhong, F. Wang, B. L. Liu, X. J. Lou and Y. C. Zhou**, *Enhancing the electrocaloric effect of $PbZr_{0.4}Ti_{0.6}O_3/PbTiO_3$ superlattices via composition tuning*, EPL **95**, 67004 (2011).

[248] **Y. Shi and A. Soh**, *Modeling of enhanced electrocaloric effect above the curie temperature in relaxor ferroelectrics*, Acta Mater. **59**, 5574–5583 (2011).

[249] **R. Pirc, Z. Kutnjak, R. Blinc and Q. M. Zhang**, *Upper bounds on the electrocaloric effect in polar solids*, Appl. Phys. Lett. **98**, 021909 (2011).

[250] **L. J. Dunne, M. Valant, A.-K. Axelsson, G. Manos and N. M. Alford**, *Statistical mechanical lattice model of the dual-peak electrocaloric effect in ferroelectric relaxors and the role of pressure*, J. Phys. D: Appl. Phys. **44**, 375404 (2011).

[251] **A.-K. Axelsson, F. Le Goupil, L. J. Dunne, G. Manos, M. Valant and N. M. Alford**, *Microscopic interpretation of sign reversal in the electrocaloric effect in a ferroelectric $PbMg_{1/3}Nb_{2/3}O_3$–$30PbTiO_3$ single crystal*, Appl. Phys. Lett. **102** (2013).

[252] **B. Li, J. B. Wang, X. L. Zhong, F. Wang and Y. C. Zhou**, *Room temperature electrocaloric effect on $PbZr_{0.8}Ti_{0.2}O_3$ thin film*, J. Appl. Phys. **107** (2010).

[253] **L. J. Dunne, M. Valant, G. Manos, A.-K. Axelsson and N. Alford**, *Microscopic theory of the electrocaloric effect in the paraelectric phase of potassium dihydrogen phosphate*, Appl. Phys. Lett. **93** (2008).

[254] **R. D. Shannon**, *Revised effective ionic radii and systematic studies of interatomic distances in halides and chalcogenides*, Acta Crystallogr. Sect. A **32**, 751–767 (1976).

[255] **G. H. Kwei, A. C. Lawson, S. J. L. Billinge and S. W. Cheong**, *Structures of the ferroelectric phases of barium titanate*, J. Phys. Chem. **97**, 2368–2377 (1993).

[256] **I. A. Kornev, L. Bellaiche, P.-E. Janolin, B. Dkhil and E. Suard**, *Phase diagram of $Pb(Zr,Ti)O_3$ solid solutions from first principles*, Phys. Rev. Lett. **97**, 157601 (2006).

[257] **V. S. Puli, A. Kumar, D. B. Chrisey, M. Tomozawa, J. F. Scott and R. S. Katiyar**, *Barium zirconate-titanate/barium calcium-titanate ceramics via sol–gel process: novel high-energy-density capacitors*, J. Phys. D: Appl. Phys. **44**, 395403 (2011).

[258] **B. Chaabane, J. Kreisel, B. Dkhil, P. Bouvier and M. Mezouar**, *Pressure-Induced Suppression of the Diffuse Scattering in the Model Relaxor Ferroelectric $PbMg_{1/3}Nb_{2/3}O_3$*, Phys. Rev. Lett. **90**, 257601 (2003).

[259] **Y. Guo, K.-i. Kakimoto and H. Ohsato**, *Ferroelectric-relaxor behavior of $(Na_{0.5}K_{0.5})NbO_3$-based ceramics*, J. Phys. Chem. Solids **65**, 1831–1835 (2004).

[260] **D. W. Baker, P. A. Thomas, N. Zhang and A. M. Glazer**, *Structural study of $K_xNa_{1-x}NbO_3$ (KNN) for compositions in the range $x = 0.24$–0.36*, Acta Crystallogr. Sect. B **65**, 22–28 (2009).

[261] **R. M. Martin**, *Electronic Structure: Basic Theory and Practical Methods*, Cambridge University Press, 2004.

[262] **C. A. Coulson**, *Present State of Molecular Structure Calculations*, Rev. Mod. Phys. **32**, 170–177 (1960).

[263] **D. M. Ceperley and B. J. Alder**, *Ground state of the electron gas by a stochastic method*, Phys. Rev. Lett. **45**, 566–569 (1980).

[264] **R. O. Jones and O. Gunnarsson**, *The density functional formalism, its applications and prospects*, Rev. Mod. Phys. **61**, 689–746 (1989).

[265] **J. P. Perdew, K. Burke and M. Ernzerhof**, *Generalized Gradient Approximation Made Simple*, Phys. Rev. Lett. **77**, 3865–3868 (1996).

[266] **K. M. Rabe, C. H. Ahn and J.-M. Triscone**, *Physics of Ferroelectrics: A Modern Perspective*, vol. 105, Springer Science & Business Media, 2007.

[267] **Z. Wu, R. E. Cohen and D. J. Singh**, *Comparing the weighted density approximation with the LDA and GGA for ground-state properties of ferroelectric perovskites*, Phys. Rev. B **70**, 104112 (2004).

[268] **Z. Wu and R. E. Cohen**, *More accurate generalized gradient approximation for solids*, Phys. Rev. B **73**, 235116 (2006).

[269] **G. Kresse and D. Joubert**, *From ultrasoft pseudopotentials to the projector augmented-wave method*, Phys. Rev. B **59**, 1758–1775 (1999).

[270] **P. E. Blöchl**, *Projector augmented-wave method*, Phys. Rev. B **50**, 17953–17979 (1994).

[271] **H. J. Monkhorst and J. D. Pack**, *Special points for brillouin-zone integrations*, Phys. Rev. B **13**, 5188–5192 (1976).

[272] **G. Henkelman, B. P. Uberuaga and H. Jónsson**, *A climbing image nudged elastic band method for finding saddle points and minimum energy paths*, J. Chem. Phys. **113**, 9901–9904 (2000).

[273] **D. Sheppard, P. Xiao, W. Chemelewski, D. D. Johnson and G. Henkelman**, *A generalized solid-state nudged elastic band method*, J. Chem. Phys. **136** (2012).

[274] **R. D. King-Smith and D. Vanderbilt**, *First-principles investigation of ferroelectricity in perovskite compounds*, Phys. Rev. B **49**, 5828–5844 (1994).

[275] **W. Zhong, D. Vanderbilt and K. M. Rabe**, *First-principles theory of ferroelectric phase transitions for perovskites: The case of $BaTiO_3$*, Phys. Rev. B **52**, 6301–6312 (1995).

[276] **U. V. Waghmare and K. M. Rabe**, *Ab initio statistical mechanics of the ferroelectric phase transition in $PbTiO_3$*, Phys. Rev. B **55**, 6161–6173 (1997).

[277] **D. Vanderbilt and W. Zhong**, *First-principles theory of structural phase transitions for perovskites: Competing instabilities*, Ferroelectrics **206**, 181–204 (1998).

[278] **J. Paul, T. Nishimatsu, Y. Kawazoe and U. V. Waghmare**, *Ferroelectric Phase Transitions in Ultrathin Films of $BaTiO_3$*, Phys. Rev. Lett. **99**, 077601 (2007).

[279] **T. Nishimatsu, U. V. Waghmare, Y. Kawazoe and D. Vanderbilt**, *Fast molecular-dynamics simulation for ferroelectric thin-film capacitors using a first-principles effective Hamiltonian*, Phys. Rev. B **78**, 104104 (2008).

[280] **T. Nishimatsu**, *feram*, Retrieved 5 May 2017.

[281] **T. Nishimatsu, M. Iwamoto, Y. Kawazoe and U. V. Waghmare**, *First-principles accurate total energy surfaces for polar structural distortions of $BaTiO_3$, $PbTiO_3$, and $SrTiO_3$: Consequences for structural transition temperatures*, Phys. Rev. B **82**, 134106 (2010).

[282] **M. C. Rose and R. E. Cohen**, *Giant electrocaloric effect around T_c*, Phys. Rev. Lett. **109**, 187604 (2012).

[283] **I. Grinberg, V. R. Cooper and A. M. Rappe**, *Relationship between local structure and phase transitions of a disordered solid solution*, Nature **419**, 909–911 (2002).

[284] **Y.-H. Shin, V. R. Cooper, I. Grinberg and A. M. Rappe**, *Development of a bond-valence molecular-dynamics model for complex oxides*, Phys. Rev. B **71**, 054104 (2005).

[285] **Y.-H. Shin, J.-Y. Son, B.-J. Lee, I. Grinberg and A. M. Rappe**, *Order-disorder character of $PbTiO_3$*, J. Phys.-Condens. Matter **20**, 015224 (2008).

[286] **S. Liu, I. Grinberg and A. M. Rappe**, *Development of a bond-valence based interatomic potential for $BiFeO_3$ for accurate molecular dynamics simulations*, J. Phys.-Condens. Matter **25**, 102202 (2013).

[287] **S. Liu, I. Grinberg, H. Takenaka and A. M. Rappe**, *Reinterpretation of the bond-valence model with bond-order formalism: An improved bond-valence-based interatomic potential for $PbTiO_3$*, Phys. Rev. B **88**, 104102 (2013).

[288] **M. P. Allen and D. J. Tildesley**, *Computer Simulation of Liquids*, Oxford University Press, 1989.

[289] **D. Frenkel and B. Smit**, *Understanding Molecular Simulation: From Algorithms to Applications*, vol. 1, Elsevier (formerly published by Academic Press), 2002.

[290] **H. C. Andersen**, *Molecular dynamics simulations at constant pressure and/or temperature*, J. Chem. Phys. **72**, 2384–2393 (1980).

[291] **J. Thijssen**, *Computational Physics*, Cambridge University Press, 2007.

[292] **S. Nosé**, *A unified formulation of the constant temperature molecular dynamics methods*, J. Chem. Phys. **81**, 511–519 (1984).

[293] **W. G. Hoover**, *Canonical dynamics: Equilibrium phase-space distributions*, Phys. Rev. A **31**, 1695–1697 (1985).

[294] **W. Shinoda, M. Shiga and M. Mikami**, *Rapid estimation of elastic constants by molecular dynamics simulation under constant stress*, Phys. Rev. B **69**, 134103 (2004).

[295] **S. Prosandeev, I. Ponomareva and L. Bellaiche**, *Electrocaloric effect in bulk and low-dimensional ferroelectrics from first principles*, Phys. Rev. B **78**, 052103 (2008).

[296] **S. Prosandeev, D. Wang, A. R. Akbarzadeh and L. Bellaiche**, *First-principles-based effective hamiltonian simulations of bulks and films made of lead-free Ba(Zr,Ti)O_3 relaxor ferroelectrics*, J. Phys.-Condens. Matter **27**, 223202 (2015).

[297] **S. Lisenkov and I. Ponomareva**, *Intrinsic electrocaloric effect in ferroelectric alloys from atomistic simulations*, Phys. Rev. B **80**, 140102 (2009).

[298] **E. Glazkova-Swedberg, J. Cuozzo, S. Lisenkov and I. Ponomareva**, *Electrocaloric effect in $PbZrO_3$ thin films with antiferroelectric-ferroelectric phase competition*, Comput. Mater. Sci. **129**, 44–48 (2017).

[299] **R. Herchig, C.-M. Chang, B. K. Mani and I. Ponomareva**, *Electrocaloric effect in ferroelectric nanowires from atomistic simulations*, Sci. Rep. **5**, 17294 (2015), 26612267.

[300] **S. Beckman, L. Wan, J. A. Barr and T. Nishimatsu**, *Effective Hamiltonian methods for predicting the electrocaloric behavior of $BaTiO_3$*, Mater. Lett. **89**, 254–257 (2012).

[301] **T. Nishimatsu, J. A. Barr and S. P. Beckman**, *Direct Molecular Dynamics Simulation of Electrocaloric Effect in $BaTiO_3$*, J. Phys. Soc. Jpn. **82**, 114605 (2013).

[302] **M. Marathe and C. Ederer**, *Electrocaloric effect in $BaTiO_3$: A first-principles-based study on the effect of misfit strain*, Appl. Phys. Lett. **104** (2014).

[303] **M. Marathe, A. Grünebohm, T. Nishimatsu, P. Entel and C. Ederer**, *First-principles-based calculation of the electrocaloric effect in $BaTiO_3$: A comparison of direct and indirect methods*, Phys. Rev. B **93**, 054110 (2016).

[304] **A. Grünebohm, M. Marathe and C. Ederer**, *Tuning the caloric response of $BaTiO_3$ by tensile epitaxial strain*, EPL **115**, 47002 (2016).

[305] **E. Ising**, *Beitrag zur Theorie des Ferromagnetismus*, Zeitschrift für Physik **31**, 253–258 (1925).

[306] **N. Metropolis, A. W. Rosenbluth, M. N. Rosenbluth, A. H. Teller and E. Teller**, *Equation of state calculations by fast computing machines*, J. Chem. Phys. **21**, 1087–1092 (1953).

[307] **M. Creutz**, *Microcanonical Monte Carlo Simulation*, Phys. Rev. Lett. **50**, 1411–1414 (1983).

[308] **V. D. Buchelnikov, V. V. Sokolovskiy, S. V. Taskaev, V. V. Khovaylo, A. A. Aliev, L. N. Khanov, A. B. Batdalov, P. Entel, H. Miki and T. Takagi**, *Monte Carlo simulations of the magnetocaloric effect in magnetic Ni–Mn–X (X = Ga, In) Heusler alloys*, J. Phys. D: Appl. Phys. **44**, 064012 (2011).

[309] **M. Ožbolt, A. Kitanovski, J. Tušek and A. Poredoš**, *Electrocaloric vs. magnetocaloric energy conversion*, Int. J. Refrig.-Rev. Int. Froid **37**, 16–27 (2014).

[310] **A. Chauhan, S. Patel and R. Vaish**, *Multicaloric effect in $Pb(Mn_{1/3}Nb_{2/3})O_3$–$32PbTiO_3$ single crystals: Modes of measurement*, Acta Mater. **97**, 17–28 (2015).

[311] **A. Kitanovski, J. Tušek, U. Tomc, U. Plaznik, M. Ozbolt and A. Poredoš**, *Magnetocaloric Energy Conversion*, vol. 565, Springer, 2015.

[312] **A. M. Tishin and Y. I. Spichkin**, *The Magnetocaloric Effect and its Applications*, CRC Press, 2016.

[313] **K.-C. Meyer, L. Koch and K. Albe**, *Phase transformations in the relaxor $Na_{1/2}Bi_{1/2}TiO_3$ studied by means of density functional theory calculations*, J. Am. Ceram. Soc. (2017).

[314] **D. Viehland, S. J. Jang, L. E. Cross and M. Wuttig**, *Freezing of the polarization fluctuations in lead magnesium niobate relaxors*, J. Appl. Phys. **68**, 2916–2921 (1990).

[315] **E. Bousquet, M. Dawber, N. Stucki, C. Lichtensteiger, P. Hermet, S. Gariglio, J.-M. Triscone and P. Ghosez**, *Improper ferroelectricity in perovskite oxide artificial superlattices*, Nature **452**, 732–736 (2008).

[316] **J. M. Rondinelli and C. J. Fennie**, *Octahedral rotation-induced ferroelectricity in cation ordered perovskites*, Adv. Mater. **24**, 1961–1968 (2012).

[317] **K.-C. Meyer and K. Albe**, *Influence of phase transitions and defect associates on the oxygen migration in the ion conductor $Na_{1/2}Bi_{1/2}TiO_3$*, J. Mater. Chem. A **5**, 4368–4375 (2017).

[318] **L. Zhang, B. Liu, H. Zhuang, P. Kent, V. R. Cooper, P. Ganesh and H. Xu**, *Oxygen vacancy diffusion in bulk $SrTiO_3$ from density functional theory calculations*, Comput. Mater. Sci. **118**, 309–315 (2016).

[319] **M. Saiful Islam**, *Ionic transport in ABO_3 perovskite oxides: a computer modelling tour*, J. Mater. Chem. **10**, 1027–1038 (2000).

[320] **B. P. Uberuaga and G. Pilania**, *Effect of Cation Ordering on Oxygen Vacancy Diffusion Pathways in Double Perovskites*, Chem. Mat. **27**, 5020–5026 (2015).

[321] **F. Zhou, M. Cococcioni, C. A. Marianetti, D. Morgan and G. Ceder**, *First-principles prediction of redox potentials in transition-metal compounds with* LDA$+U$, Phys. Rev. B **70**, 235121 (2004).

[322] **W.-B. Zhang, J. Li and B.-Y. Tang**, *Role of electronic correlation in high-low temperature phase transition of hexagonal nickel sulfide: A comparative density functional theory study with and without correction for on-site Coulomb interaction*, J. Chem. Phys. **138** (2013).

[323] **M. Spreitzer, M. Valant and D. Suvorov**, *Sodium deficiency in $Na_{0.5}Bi_{0.5}TiO_3$*, J. Mater. Chem. **17**, 185–192 (2007).

[324] **Y. S. Sung, J. M. Kim, J. H. Cho, T. K. Song, M. H. Kim, H. H. Chong, T. G. Park, D. Do and S. S. Kim**, *Effects of Na nonstoichiometry in $(Bi_{0.5}Na_{0.5+x})TiO_3$ ceramics*, Appl. Phys. Lett. **96**, 022901 (2010).

[325] **Y. S. Sung, J. M. Kim, J. H. Cho, T. K. Song, M. H. Kim and T. G. Park**, *Effects of Bi nonstoichiometry in $(Bi_{0.5+x}Na)TiO_3$ ceramics*, Appl. Phys. Lett. **98**, 012902 (2011).

[326] **J. Carter, E. Aksel, T. Iamsasri, J. S. Forrester, J. Chen and J. L. Jones**, *Structure and ferroelectricity of nonstoichiometric $(Na_{0.5}Bi_{0.5})TiO_3$*, Appl. Phys. Lett. **104**, 112904 (2014).

[327] **W. Cai and W. D. Nix**, *Imperfections in Crystalline Solids*, Cambridge University Press, 2016.

[328] **R. W. Balluffi**, *Introduction to Elasticity Theory for Crystal Defects*, Cambridge University Press, 2012.

[329] **J. F. Scott and M. Dawber**, *Oxygen-vacancy ordering as a fatigue mechanism in perovskite ferroelectrics*, Appl. Phys. Lett. **76**, 3801–3803 (2000).

[330] **Y. Shi, L. Huang, A. K. Soh, G. J. Weng, S. Liu and S. A. Redfern**, *Distinct scaling behaviors of giant electrocaloric cooling performance in low-dimensional organic, relaxor and anti-ferroelectrics*, arXiv preprint arXiv:1610.08448 (2016).

[331] **F. Pforr, K.-C. Meyer, M. Major, K. Albe, W. Donner, U. Stuhr, B. Roessli and A. Ivanov**, *Relaxation of dynamically disordered tetragonal platelets in the relaxor ferroelectric $0.964Na_{1/2}Bi_{1/2}TiO_3$–$0.036BaTiO_3$*, in preparation.

[332] **N. Ramer and A. Rappe**, *Application of a new virtual crystal approach for the study of disordered perovskites*, J. Phys. Chem. Solids **61**, 315–320 (2000).

[333] **N. J. Ramer and A. M. Rappe**, *Virtual-crystal approximation that works: Locating a compositional phase boundary in $Pb(Zr_{1-x}Ti_x)O_3$*, Phys. Rev. B **62**, R743–R746 (2000).

[334] **J. Hutter, J. VandeVondele and O. Schütt**, *cp2k*, Retrieved 5 May 2017.

[335] **A. R. Oganov**, *USPEX*, Retrieved 5 May 2017.

[336] **D. Broberg, B. Medasani, N. Zimmermann, A. Canning, M. Haranczyk, M. Asta and G. Hautier**, *PyCDT: A Python toolkit for modeling point defects in semiconductors and insulators*, arXiv:1611.07481v1 (2016).

[337] **J. Shiomi, K. Esfarjani and G. Chen**, *Thermal conductivity of half-Heusler compounds from first-principles calculations*, Phys. Rev. B **84**, 104302 (2011).

[338] **P. Erhart, R.-A. Eichel, P. Träskelin and K. Albe**, *Association of oxygen vacancies with impurity metal ions in lead titanate*, Phys. Rev. B **76**, 174116 (2007).

[339] **A. B. Harris**, *Landau theory of tilting of oxygen octahedra in perovskites*, Phys. Rev. B **85**, 174107 (2012).

Erklärung zur Dissertation

Hiermit versichere ich, die vorliegende Dissertation ohne Hilfe Dritter nur mit den angegebenen Quellen und Hilfsmitteln angefertigt zu haben. Alle Stellen, die aus Quellen entnommen wurden, sind als solche kenntlich gemacht. Diese Arbeit hat in gleicher oder ähnlicher Form noch keiner Prüfungsbehörde vorgelegen.

Darmstadt, den 30.8.2017

_____

(Kai-Christian Meyer)

Curriculum Vitae

M.Sc. Kai-Christian Meyer
Born on the 4th August 1987 in Frankfurt am Main, Germany

Education

09/2013 - 06/2017	**PhD Thesis:** Phase Transformation Kinetics and Oxygen Transport in the Relaxor Ferroelectric $Na_{1/2}Bi_{1/2}TiO_3$ studied by First-Principles Calculations
	Technische Universität Darmstadt, Germany
05/2011 - 08/2013	Studies: Physics
	Degree: **M.Sc. Physics**
	Thesis: Calculation of Spin-Lattice-Relaxation Time in heavy Ion irradiated LiF-Crystals
	Technische Universität Darmstadt, Germany
08/2010 - 01/2011	Aalto University, Espoo, Finland
10/2007 - 05/2011	Studies: Physics
	Degree: **B.Sc. Physics**
	Technische Universität Darmstadt, Germany
09/1998 - 06/2007	Secondary school: Otto-Hahn-Schule, Hanau, Germany

Peer-reviewed articles

1. *Phase transformations in the relaxor $Na_{1/2}Bi_{1/2}TiO_3$ studied by means of density functional theory calculations*
   K.-C. Meyer, L. Koch and K. Albe
   J. Am. Ceram. Soc. (2017)

2. *Ionic conductivity of acceptor doped sodium bismuth titanate: influence of dopants, phase transitions and defect associates*
   L. Koch, S. Steiner, **K.-C. Meyer**, I.-T. Seo, K. Albe and T. Frömling
   J. Mater. Chem. C, 2017

3. *Influence of phase transitions and defect associates on the oxygen migration in the ion conductor $Na_{1/2}Bi_{1/2}TiO_3$*
   K.-C. Meyer and K. Albe
   J. Mater. Chem. A 5, 4368–4375 (2017)

4. *Positive and negative electrocaloric effect in $BaTiO_3$ in the presence of defect dipoles*
   Y.-B. Ma, A. Grünebohm, **K.-C. Meyer**, K. Albe and B.-X. Xu
   Phys. Rev. B 94, 094113 (2016)

5. *Octahedral tilt transitions in the relaxor ferroelectric $Na_{1/2}Bi_{1/2}TiO_3$*
   K.-C. Meyer, M. Gröting and K. Albe
   J. Solid State Chem. 227, 117–122 (2015)

Oral presentations at international conferences

1. **MSE-Congress, Darmstadt, Germany (09/2016)**
   K.-C. Meyer, L. Koch and K. Albe
   Phase transitions in the relaxor-like sodium bismuth titanate studied by density functional theory calculations

2. **ISAF/ECAPD/PFM, Darmstadt, Germany (08/2016)**
   K.-C. Meyer, S. In-Tae, L. Koch, S. Steiner, T. Frömling and K. Albe
   Oxygen vacancy migration in sodium bismuth titanate studied by density functional theory calculations

3. **ElectroCeramics XV, Limoges, France (06/2016)**
   K.-C. Meyer, S. In-Tae, L. Koch, S. Steiner, T. Frömling and K. Albe
   Oxygen vacancy migration in sodium bismuth titanate studied by density functional theory calculations

4. **DPG-Frühjahrstagung, Regensburg, Germany (03/2016)**
   K.-C. Meyer, C. Kalcher, A. Stukowski and K. Albe
   Abnormal electrocaloric effect studied by lattice based Monte-Carlo simulations

5. **DPG-Frühjahrstagung, Berlin, Germany (03/2015)**
   K.-C. Meyer, M. Gröting and K. Albe
   Modelling of octahedral tilts in NBT by first-principles

6. **AMPERE NMR School, Zakopane, Poland (06/2013)**
   K.-C. Meyer, S. Quittek and F. Fujara
   Calculation of the spin-lattice-relaxation time in heavy ion irradiated LiF crystals

Poster presentations at international conferences

1. **ISAF/ECAPD/PFM, Darmstadt, Germany (08/2016)**
   K.-C. Meyer, L. Koch and K. Albe
   Phase transitions in the relaxor-like sodium bismuth titanate studied by density functional theory calculations

2. **DPG-Frühjahrstagung, Regensburg, Germany (03/2016)**
   K.-C. Meyer, M. Gröting and K. Albe
   Oxygen vacancy diffusion in sodium bismuth titanate studied by density functional theory calculations

3. **13th European Meeting on Ferroelectricity, Porto, Portugal (06/2015)**
   K.-C. Meyer, M. Gröting, C. Kalcher and K. Albe
   Octahedral tilt transitions in sodium bismuth titanate (NBT) by DFT calculations